UNIVERSIDAD DE CANTABRIA
Departamento de Física Moderna

y

C.S.I.C. - U.C.
Instituto de Física de Cantabria

Reconstrucción de la dinámica no lineal de sistemas caóticos con retraso mediante redes neuronales

Silvia Ortín González

Tesis doctoral

2009

UNIVERSIDAD DE CANTABRIA
Departamento de Física Moderna

y

C.S.I.C. - U.C.
Instituto de Física de Cantabria

Reconstrucción de la dinámica no lineal de sistemas caóticos con retraso mediante redes neuronales

Memoria presentada por la Ingeniera
Silvia Ortín González
para optar al título de Doctor en Ciencias Físicas

Realizada bajo la supervisión del
Dr. **Luis Pesquera González**
y del
Dr. **Ángel Valle Gutiérrez**
2009

Dr. Luis Pesquera González, Catedrático de la Universidad de Cantabria y Dr. Ángel Valle Gutiérrez, Profesor titular de la Universidad de Cantabria, certifican:

> Que la presente Memoria, titulada **"Reconstrucción de la dinámica no lineal de sistemas caóticos con retraso mediante redes neuronales"**, ha sido realizada, bajo su dirección, por Silvia Ortín González, y constituye su Tesis para optar al grado de Doctor por la Universidad de Cantabria. Asimismo emiten su conformidad para que dicha memoria sea presentada y tenga lugar, posteriormente, la correspondiente lectura.

Santander, a 1 de Diciembre de 2009

Fdo.: Dr. Luis Pesquera González Fdo.: Dr. Ángel Valle Gutiérrez

Agradecimientos

Vaya ahora mi agradecimiento a todos los que han contribuido de forma directa o indirecta al desarrollo de esta tesis. A lo largo de estos años he tenido la suerte de encontrarme con muchas personas que me han dedicado su tiempo y me han ofrecido su ayuda tanto personal como profesionalmente. Un sincero ¡gracias! a todos los que habéis estado ahí mientras escribía esta tesis.

En primer lugar me gustaría expresar mi gratitud a mis directores de tesis Luis Pesquera y Ángel Valle por haberme dado la oportunidad de realizar este trabajo, y sobre todo por la valiosa ayuda prestada y la disponibilidad mostrada en todo momento. Sin su apoyo este trabajo no habría sido posible. Me gustaría agradecer especialmente la dedicación, la paciencia y las provechosas e interesantes charlas mantenidas con Luis durante estos años.

También mi más sincera gratitud a José Manuel Gutiérrez, que es en cierto modo el responsable de que esta tesis sea una realidad, por sus ideas y que junto a Antonio Cofiño me ayudó a empezar en el complejo mundo de la redes neuronales.

A toda la gente que ha colaborado conmigo durante estos años y con los que he publicado artículos, parte de los cuales son la base de esta tesis.

Mi gratitud a todo el grupo de Física Estadística y No Lineal, en especial a mis compañeros de despacho con los que he trabajado y disfrutado de tantos buenos ratos. Me gustaría agradecer especialmente el apoyo y la ayuda que me han brindado a lo largo de estos años Ivan Szendro, Marta Sanchez de la Lama, Clara Picallo, Diego Pazó, Jorge Revelli, Cristina Primo y Ana Quirce.

I had a great academical opportunity to visit Prof. Laurent Larger at his Laboratory at Besançon, France. I appreciate the discussions and the excellent opportunity for me to learn more about experimental opto-electronics. I

would also like to thank him and all the people of his group for their hospitality during my stay.

Pasando a agradecimientos más personales, me gustaría dar las gracias a todos mis amigos, demasiados nombres para mencionarlos por separado, pero que han estado realmente siempre ahí para mí. Finalmente, estoy particularmente en deuda con mis padres y mi hermana por su inquebrantable apoyo y ánimo en todos los frentes. Sin ellos nada de esto podría haber sido ni remotamente posible.

Nonlinear dynamics reconstruction by neural networks of time-delay chaotic systems

A dissertation submitted in partial fulfillment of the requirements for the degree of Philosophy Doctor in Physics

by

Silvia Ortín González

Departamento de Física Moderna
Universidad de Cantabria

&

Instituto de Física de Cantabria
Consejo Superior de Investigaciones Científicas-Universidad de Cantabria

2009

Contents

Chapter 1

Motivations and outline

In the last years there has been an intense research in chaos-based communications. One of the original motivations for research in chaos-based communications arose from the ongoing need for methods to communicate information offering privacy and security. The understanding of chaotic dynamical systems leads to a natural application to "hide" information in the broadband spectrum of chaotic waveforms. Chaotic waveforms provide an additional layer or level of privacy beyond any conventional software-based cryptography that can be simultaneously part of the communication protocol. Moreover, the typically broadband spectrum of the chaotic signals is also desirable for applications that require robustness against interference, jamming and low detection probability.

Although great advances have been made in the field of chaos-based communications it is very difficult to determine the privacy offered by any specific scheme of chaotic communication. Some rules have been suggested to achieve a reasonable degree of security [Alvarez and Li 2006]. Methods to quantify the cryptanalysis of chaotic encryption schemes have been also proposed [Tenny and Tsimring 2004]. However, the analysis of the security of different chaotic communication systems is still a question that has to be addressed for practical applications in the field.

Many chaos-based encryption schemes have been proposed, and many of those schemes have been broken later on. It was early shown that low dimensional chaotic systems can be often cracked using standard nonlinear techniques [Pérez and Cerdeira 1995, Short and Parker 1998]. Higher dimensional systems, especially those involving hyperchaotic dynamics, are likely to provide improved security. Nonlinear time-delay systems can have chaotic attrac-

tors whose dimension increases with the delay time, reaching very high values [Farmer 1982]. It is then computationally difficult to reconstruct the nonlinear dynamics of these systems with time-series analysis techniques based on the standard embedding approach. However, it is possible to reconstruct the nonlinear dynamic of a single-variable time-delay system by using an embedding-like approach [Bünner et al. 2000a;b, Hegger et al. 1998]. This method works with a special embedding space that includes both short time and feedback-time delayed values of the system variable. It permits to reconstruct the nonlinear dynamics of a chaos time-delay system without having any a-priori knowledge about the equation that rule the system.

This thesis focuses on the reconstruction of the nonlinear dynamic of time-delay systems applying this special embedding. We use global nonlinear models (Neural Networks) instead of the local linear ones used by Bünner and coworkers. The global models present serious advantages over the local linear models, such as a smaller computation time to construct the model. We also carefully investigate the time delay identification from the time series, a crucial parameter to construct the special embedding vector. Finally we shall use the reconstructed models to show the vulnerability of the chaos-based communication system based on time-delay systems and to study the predictability of these systems.

We particulary focus on optical communication systems with delayed feedback. Optical communication system are very interesting because they offer the possibility of high transmission rates (range of Gbits) [Argyris et al. 2005, Uchida et al. 2005]. Moreover, semiconductor lasers subject to feedback provide simple ways of generating chaotic signals with high dimensional attractors. Two schemes based on all-optical and electro-optical feedback have been considered. We particulary concentrate our attention in electro-optical feedback system that present chaos in wavelength. These systems can be modelled by the Ikeda equation [Ikeda 1979, Ikeda and Matsumoto 1987] that has turned out to be a paradigm for the study of delayed chaotic system under variations of the nonlinear strength. The experiments were performed in the group of Prof. Laurent Larger (Université de Franche-Comté, Besançon, France). This particular system does not reach high transmission rates, but it permits to analyze the time delay identification and the nonlinear dynamics reconstruction for high dimensions and entropies. Therefore, we can use this system to determine the effect of these magnitudes in the nonlinear dynamics reconstruction and time delay identification.

Although we mainly focus on electro-optical feedback system, the techniques investigated in this thesis have a general applicability to scalar time-delay systems. In particular, we also study the Mackey-Glass system from

numerical and experimental data. These experiments were performed in the electronics laboratory at IFCA.

The thesis is outlined as follows:

In Chapter 2 (**Introduction**) we introduce and explain various concepts and terms that will be referred for the remainder of the thesis. The chapter starts with a general introduction to chaotic systems, followed by a closer look at chaos-based communications. We particulary focus on the security of these systems. The chapter finishes with a general description of the nonlinear time series analysis and the neural networks.

In Chapter 3 (**Time delay identification**) we study the identification of the time delay from numerical and experimental time series of semiconductor lasers subject to optoelectronic and optical feedback. To this aim we use different techniques. The identification of the time delay is a key step in the reconstruction of the nonlinear dynamics. We analyze semiconductor lasers subject to one and two fixed time-delays. We apport original contributions based on the development of adapted methods to identify multiples fixed time delays. Finally, we also develop a new technique based on the standard ones to identify the periodic time delay and we apply this method successfully to the experimental time series of a semiconductor laser with optoelectronic feedback.

In Chapter 4 (**Nonlinear dynamics reconstruction of time-delay systems**) we reconstruct the nonlinear dynamics of time-delay chaotic systems from time series using neural networks. In this chapter we use a new type of modular neural network based on the structure of time-delay systems. We analyze the advantages of the modular versus the standard neural networks and the effect of the nonlinear strength and the time delay on the nonlinear dynamic reconstruction. We have particulary focused on two time-delay chaotic systems: the Mackey-Glass system and the semiconductor lasers subject to optoelectronic feedback. For the latter system, the nonlinear dynamics is reconstructed when the system is subjected to one or two fixed time delays. Experimental nonlinear dynamics reconstruction of the semiconductor chaotic wavelength laser subject to optoelectronic feedback are shown for the first time.

In chapter 5 (**Prediction of time-delay nonlinear systems**) we study the forecasting horizon of a Mackey-Glass system using standard prediction techniques and the anticipated synchronization. We use neural networks models of the original system obtained from numerical and experimental time series. On the other hand, we also show that convective instabilities appear in chains of identical replicas of a time-delay system synchronized without anticipation. We characterize these convective instabilities.

In chapter 6 (**Unmasking messages encoded by time-delay chaotic systems**) we construct an unauthorized receiver using neural networks from the transmitted signal of a chaos-based optical communication system. The chaotic carrier is generated by a semiconductor laser subject to optoelectronic feedback. We show that the unauthorized receiver can recover the message from numerical and experimental transmitted signals.

In chapter 7 (**Concluding remarks and open questions**) we close the thesis with a summary and discussion of the presented research topics, concluding with some suggestions for future research.

Chapter 2

Introduction

In this chapter we will take a short tour of the field of chaos based communication and nonlinear time series analysis. We introduce and explain various concepts and terms that will be referred in this thesis. We begin with an overview of chaotic systems, before focusing on the topic of chaos based communications. We specially concentrate on optical chaotic communications using semiconductor lasers subject to delayed feedback. Then, we go into some of the issues concerning the privacy of these communication systems and introduce the nonlinear time series analysis as a general approach to recover the nonlinear dynamics of the chaotic system. Finally, among the different methods to reconstruct the nonlinear dynamics we point out the neural networks and give some basic concepts related to them.

It is outside the scope of this thesis to give a complete overview of the field of chaos based communications, or to exhaustively consider all the possible approaches that can be chosen to tackle the aforementioned issues. A more comprehensive treatment of the chaotic systems can be found in [Hilborn 2000, Ott 2002, Pikovsky et al. 2001, Strogazt 1994]. Regarding the optical chaotic communications and semiconductor lasers, one can look at [Ohtsubo 2007, Uchida et al. 2005]. A good reference for nonlinear time series analysis is [Kantz and Schreiber 1997]. Finally, an extensive information about neural networks can be obtained from [Castillo et al. 1999, Haykin 2001, Kecman 2001].

2.1 Chaotic systems

Chaos has generated a great deal of attention in the scientific community in the last decades. Although Henri Poincaré was the precursor of the chaos theory in 19th century, the big development of chaos research was in the last seventies with the advent of modern digital computing. The modern theory of chaos has been constructed with the contributions of many investigators [see Hilborn 2000, Ott 2002, Strogazt 1994, for a survey].

Chaos designates a class of dynamical behavior. The asymptotic behavior of a dynamical system as time approaches infinity, can be a fixed point, a periodic or quasi-periodic solution or chaos. It is well known that a dynamical system consists of a set of possible states, together with a rule that determines the present state in terms of past states. The rule must be deterministic, which means that one can determine the present state uniquely from the past states. If the rule is applied at discrete times, it is called a discrete-time dynamical system, also called maps. The continuous-time dynamical system is essentially the limit of discrete systems with smaller updating times. The evolution rule in that case becomes a set of differential equations.

The phase space of a dynamical system is a mathematical space with orthogonal coordinate directions representing each of the variables needed to specify unambiguously the instantaneous state of the system. The number of degrees of freedom of a dynamical system is the dimension of its phase space, i.e., the number of variables needed to completely describe the system. The phase space can be finite-dimensional (as in ordinary differential equations and mappings) or infinite-dimensional, as in partial differential equations and delay differential equations. The attractor is the set in the phase space formed by the non-transient trajectories of the system. The dimension of the attractor gives an estimation of the number of the active degrees of freedom for the system and it is an important feature for the nonlinear dynamics reconstruction based on embedding techniques as we shall see later (see section 2.6). Thus, the dimension of the attractor is smaller than the dimension of the full phase space.

Necessary conditions for chaos are the nonlinearity of the system and dimension larger than two when the system is described by ordinary differential equations (Poincare-Bendixon theorem). Chaos in one dimensional system is only possible if the system is discrete (maps).

There is a lack of a general definition of chaotic systems, however they share three essential properties. First, they are very sensitive to initial conditions, i.e., nearby trajectories of a given variable separate exponentially fast. Second, they can display a highly aperiodic behavior which looks random, and third,

despite the last feature, they are deterministic. It is worth noting that because of their random-like behavior, chaotic signals have impulse-like autocorrelation functions and white wideband power spectra.

Several methods and measures are available to recognize and characterize chaotic systems [see Kantz and Schreiber 1997]. One of the most important measures to quantify chaos are the Lyapunov exponents. As above mentioned, the sensitivity to initial conditions is a distinctive feature of chaotic behavior. Initially arbitrary close points in the phase space produce markedly different trajectories. Characteristically, trajectories in chaotic systems diverge exponentially and Lyapunov exponents are a measure of the average rate of the exponential divergence of two trajectories. For a N-dimensional dissipative system there are N Lyapunov exponents, since the divergence of the trajectories can occur in any direction of the system. The largest Lyapunov exponent represents the largest rate of exponential divergence. Chaotic systems have at least one positive Lyapunov exponent, i.e., at least in one direction the difference of the trajectories grows in an exponential way.

Another important quantifier of a chaotic system is the metric entropy, also known as Kolmogorov-Sinai (KS) entropy. The KS entropy measures the average loss of information rate, or equivalently is inversely proportional to the time interval over which the future evolution can be predicted. It can be interpreted as a measure of unpredictability of a dynamical system. The KS entropy is zero for periodic systems, positive for chaotic systems and infinite for a stochastic/random process. Moreover, the KS entropy is connected with the Lyapunov exponents by the Pessin's theorem. Roughly speaking the theorem says that the KS entropy is equal to the sum of the positive Lyapunov exponents.

These two dynamical quantifiers (Lyapunov exponents and KS entropy) play a very important role in the predictability of the chaotic systems. The long-time prediction in a chaotic system is impossible due to the exponential growth of the nearby trajectories that is measured by the Lyapunov exponents. Therefore, the limit for the predictability of a chaotic system is related to the largest positive Lyapunov exponent. The prediction time, T, can be estimated by inverse of the largest Lyapunov exponent, λ, as $T \sim \lambda^{-1}$. On the other hand, the KS entropy is a measure of how great our failure to predict the future state will be; the larger the entropy, the larger the unpredictability of the system.

The two above methods of quantifying chaos (Lyapunov exponents and KS entropy) focus on the dynamics (evolution in time) of trajectories in the phase space. However, one can also pay attention to the geometric features of the attractors. The geometry of chaotic attractors can be complex and diffi-

cult to describe. It is therefore useful to have quantitative characterizations of such geometrical objects. Perhaps the most basic characterization is the dimension of the attractor. One way to estimate the attractor dimension is by the Kaplan-Yorke conjecture, that states that the dimension of a strange attractor can be approximated from the spectrum of Lyapunov exponents. Such a dimension has been called the Kaplan-Yorke (or Lyapunov) dimension.

2.2 Chaotic Synchronization

Synchronization is an ubiquitous phenomenon, which can be encountered in a lot of scientific disciplines [Pikovsky et al. 2001]. Synchronization in dynamical systems was introduced by Christiaan Huygens in 1665. He observed that two pendulum clocks which are suspended on the same support, display perfectly out of phase oscillations. The clocks did influence each other through imperceptible movements of the common support.

The idea of chaos synchronization between two nonlinear systems was proposed by Pecora and Carroll [1990]. After their proposal, synchronization phenomena in various chaotic systems including lasers have been reported.

If two nonlinear chaotic systems operate independently, the two systems never show the same output because of the sensitivity of chaos to the initial conditions. However, when a small portion of a chaotic output from one nonlinear system is sent to the other, the two systems synchronize with each other and show the same output under certain conditions of the system parameters. This scheme is called chaos synchronization.

The drive signal necessary to achieve synchronization in coupled systems can go in all directions, but here we only consider the case of unidirectional coupling, that is the way that has more applications in communications. In the case of unidirectional coupling, the system which sends the synchronization signal is indistinctly referred to as the emitter, the drive or the master system; the system which receives this synchronization signal and thereby tries to track the dynamics of the emitter is referred to as the receiver, the response or the slave system.

There are different ways to characterize the synchronization. One is related to the relationship achieved between the master and slave variables. Another is concerned to the way the synchronization state is reached. In order to explain the different ways to characterize the synchronization, let us consider two autonomous N dimensional chaotic systems of the form:

$$\dot{\mathbf{x}} = f(\mathbf{x})$$
$$\dot{\mathbf{y}} = g(\mathbf{y})$$

where $\mathbf{x} = (x_1, ...x_n)$ and $\mathbf{y} = (y_1, ...y_n)$ are N-dimensional vectors describing the state of the master and slave system, respectively. Note that master and slave may not be identical systems.

Concerning the functional relations in trajectories between the master and the slave, the most well-known synchronization schemes are:

- Identical or complete synchronization: refers to a perfect locking of chaotic trajectories of the master and slave so, $\lim_{t\to\infty} \|\mathbf{x}(t) - \mathbf{y}(t)\| = 0$. The identical synchronization is sensitive to the mismatch between the master and slave system [Ashwin et al. 1994, Brown et al. 1994, Kouomou et al. 2004]. Therefore, it has been proposed to use the identical synchronization as a method to validate nonlinear models obtained from chaotic data [Aguirre et al. 2006, Brown et al. 1994]. This approach shall be used through this thesis.

- Generalized synchronization is defined as the existence of a functional relationship (G) between the states of the master and slave [Rulkov et al. 1995], $\lim_{t\to\infty} \|G(\mathbf{x}(t)) - \mathbf{y}(t)\| = 0$.

- Lag synchronization implies that there is a time shift between the evolution of the master and slave system, where the slave lags the state of the master, $\lim_{t\to\infty} \|\mathbf{y}(t) - \mathbf{x}(t-\tau)\| = 0$.

- Anticipated synchronization implies that there is a time shift between the evolution of the master and slave system, but in this case the slave is anticipating the state of the master, $\lim_{t\to\infty} \|y(t) - x(t+\tau)\| = 0$. It is a rather counterintuitive phenomenon, that has been proposed as a way to increase the predictability of chaotic systems by using chains of anticipated synchronized slaves [Voss 2001a]. However, it has been recently shown that this scheme is unstable to propagating perturbations. The spatiotemporal character of the coupled chain introduces a convective like instability into the synchronization manifold [Mendoza et al. 2004]. We shall show in chapter 5 that convective instabilities also appear in chains of identical synchronized time-delay chaotic systems due to the time delay. Moreover, we shall analyze the predictions obtained from the anticipated synchronization scheme using a chain of slave neural networks that model the master system.

- Phase synchronization is defined as the locking of the phases of the state variables, whereas the amplitudes evolve freely and remain chaotically uncorrelated [Rosenblum et al. 1996].

The above presented schemes determine the relationship between master and slave systems once the synchronization state has been reached. To obtain a synchronization state, several schemes have been presented in the literature. One of the more widespread is the diffusive coupling proposed by Pyragas [1993]:

$$\dot{\mathbf{y}} = g(\mathbf{y}) + k_c(x_1 - y_1) \tag{2.1}$$

where k_c is the coupling parameter or the strength of the perturbation. For identical systems, a synchronous solution of equation (2.1) exists in a mathematical sense. In other words, the synchronized state $\mathbf{x}$=$\mathbf{y}$ is a fixed point of the system which can be stabilized by the coupling term for a sufficiently large strength k_c. The diffusive coupling is very general and applicable to most kinds of nonlinear dynamical systems.

2.3 Chaos on communications

There has been significant interest in recent years in exploiting chaotic dynamics in communications. Their special properties (sensitive dependence on initial conditions, random-like behavior and continuous broadband power spectrum) have emerged in several applications in the communication field. One of the most outstanding is the chaotic communications based on chaos synchronization.

In the communication field, spread-spectrum communications are well known techniques that are used in many commercial applications, such as the code division multiple access (CDMA) protocol used in the Global Positioning System (GPS) and in the third generation of mobile telephones. The main concept behind the spread spectrum systems is a broadband transmitted signal that occupies a bandwidth which is much larger than the message/data/information bandwidth. The key idea for the exploitation of spread-spectrum signals in communications is to increase the robustness against disturbances affecting narrow frequency ranges, i.e. multipath propagations and interfering signals.

Chaotic signals, with their inherent wideband characteristic, are natural candidates for spreading narrowband information. In chaos-based communications the broadband coding signal is a chaotic waveform generated at the

physical layer instead of algorithmically. These chaos based communication systems have all the advantages of the standard spread spectrum techniques regarding the robustness of communication channels to interferences with narrowband disturbances. From a fundamental point of view, using waveforms generated by deterministic chaotic systems to carry information in a robust manner is a generalization of standard communication systems. Additionally, chaotic carriers offer a certain degree of intrinsic privacy in the data transmission as we shall see in section 2.5.

In chaos based communications using synchronization, the message is somehow hidden into the noise-like output of a chaotic emitter and sent to the receiver via a public channel. The receiver thanks to the synchronization phenomenon, performes a nonlinear filtering process, intended to generate locally a message-free chaotic signal, which is then used to recover the message from the encoded transmitted signal. This nonlinear filtering process is known as the chaos-pass-filtering phenomenon. That is, the receiver only couples to the chaotic component of the transmitted signal.

Therefore, the two basic requirements of chaos based communications using synchronization are a system able to generate a chaotic waveform and the synchronization. The synchronization process is the key of the chaotic communication system.

Concerning the way the message is embedded into the chaotic signal, a great number of different modulation and demodulation schemes have been proposed for chaotic communications based on chaos synchronization. Nonetheless, only some of them have been implemented. Depending on how the message signal is encoded and decoded, the modulation schemes can be categorized into three classes: chaos masking (CMA), chaos modulation (CMO) and chaos shift keying (CSK) (see figure 2.1).

- Chaos Masking (CMA): In the additive chaos masking or chaos masking the message signal is added to the chaotic carrier outside the transmitter. Assuming that the receiver dynamics synchronizes only with the chaotic carrier, the message is recovered by a simple substraction between the transmitted signal and the output of the receptor. This procedure works well when synchronization is not very sensitive to perturbations in the drive signal. In particular the amplitude of the message must be small enough with respect to the carrier, in order to reproduce a good quality of a decoded message and to hide the message into the chaotic carrier.

- Chaos Modulation (CMO): In the chaos modulation, the message is mixed nonlinearly with the chaotic carrier. This means that the message signal affects directly the dynamics of the chaotic carrier. The

original chaotic signal together with the message conforms a new chaotic signal and, therefore, the message may essentially have a large amplitude. However, the message must not be so large that it may completely change the dynamics of the original chaotic system. Moreover, the message itself may even explicitly appear in the transmission signal. For these reasons a message with small amplitude is usually used in CMO.

- Chaos Shift Keying (CSK): The chaotic shift keying also known as chaotic switching was designed to transmit digital message signals. In almost all proposed methods, the basic principle is to map digital symbols to different chaotic basis signals, which are produced from a dynamical system using different values of a bifurcation parameter or from different dynamical systems. In the most simple scheme, presented in figure 2.1(c), the digital message is used to switch the transmitted signal between two statistically similar chaotic attractors, which are respectively used to encode bit 0 and bit 1 of the message signal. These two attractors are generated by two chaotic systems with the same structure and different parameters. The difference between the two chaotic states in the CSK system must be very small, since the message can be easily estimated from the attractors when the difference of chaotic oscillations between the two states is too large. In the receiver each state is detected by the technique of chaos synchronization. For practical use of this system, we must take into account the transient time required for the synchronization between the receiver and transmitter.

The possibility of secure communications based on chaos synchronization was pointed out by Pecora and Carroll [1991] in their seminal paper about chaos synchronization in nonlinear systems. The first experimental demonstration of chaos communication schemes were made in electronic circuits [Cuomo and Oppenheim 1993, Cuomo et al. 1993, Halle et al. 1993, Kocarev et al. 1992, Parlitz et al. 1992, Volkovskii and Rul'kov 1993]. In 1993 Cuomo and Oppenheim proved experimentally, using electronic circuits that it is possible to mask and recover a message by using chaos synchronization. However, the bandwidth of this system was inherently limited by its electronic nature (few KHz). This successful experience was a breakthrough suggesting the use of optical systems to increase the bandwidth available for information transmission to the gigahertz range.

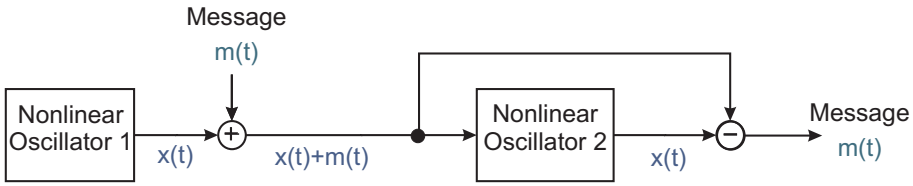

(a) Chaos Masking

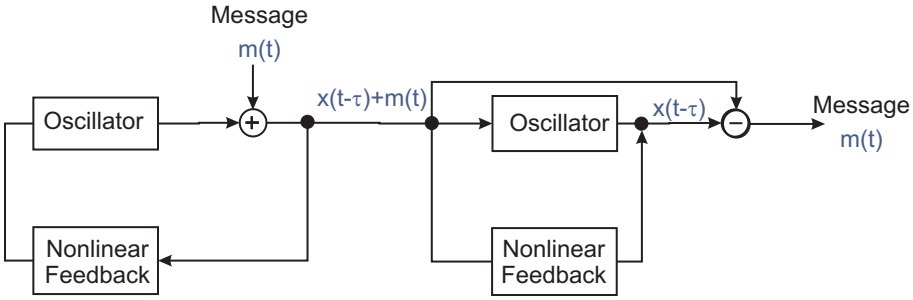

(b) Chaos Modulation

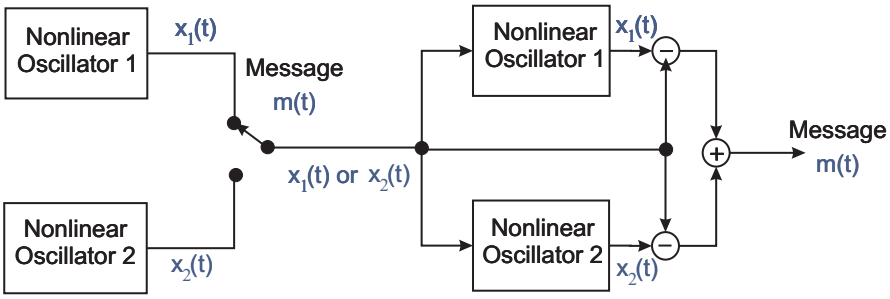

(c) Chaos Shift Keying

Figure 2.1: General examples of CMA (a), CMO (b) and CSK (c) modulation schemes

2.4 Chaotic optical communications

Researchers from different groups around the world have been trying to develop optical communication systems exploiting chaos. One of the major motivations for using lasers is that optical chaotic systems offer the possibility of high-speed data transfer.

The two necessary conditions for chaotic optical communications are the optical chaotic generator and the synchronization between the transmitter and receiver laser. Methods to lead lasers to chaos are numerous: as early emphasized, two necessary conditions are nonlinearity and threefold dimensionality. Hence, when the nonlinearity of the laser (system) is not strong enough, an external nonlinear element can be introduced. Along the same line, when the dimensionality of the laser system is not high enough, it can be increased by parameter modulation or by delayed feedback loops. The first to show chaotic behavior in lasers was Haken [1975]. After that, chaos has been theoretically and experimentally encountered in almost all types of lasers (solid-state, gas, semiconductor, etc...).

The other essential ingredient of chaos based-communication systems is synchronization. In laser systems, synchronization was experimentally demonstrated for first time in CO_2 lasers [Sugawara et al. 1994] and solid state lasers [Roy and Thornburg 1994]. After that, many theoretical and experimental investigations for chaos synchronization in various laser systems including semiconductor lasers were published. In laser systems, to obtain a unidirectionally synchronization a small portion of the output from one of variables is sent to the slave laser from the master. Identical chaos synchronization is very sensitive to parameter mismatches between the master and slave systems [Kouomou et al. 2004]. Laser chaos synchronization was experimentally complicated by the difficulty to build almost identical lasers. For example, even for semiconductor lasers coming from the same wafer, we can not expect exactly the same oscillation frequencies for the master and slave under the same injection current.

In theory, the message can be encoded on the amplitude, frequency (phase) or polarization of a light wave. However, the first two options are the most extensively studied. The first experimental demonstrators of chaos based communication systems were built by Van Wiggeren and Roy [1998] using erbium-doped fiber ring-lasers, and by Larger et al. [1998a] using the wavelength chaos generated with a semiconductor laser. Both methods used the CMO technique to encode the transmitted message.

Semiconductor lasers are specially interesting for communication purposes because they are the emitters in modern telecommunication systems using

optical fibers. Therefore, much attention has been devoted to the application of synchronization of semiconductor lasers to chaos communication. Among others methods, semiconductor lasers can be driven to chaos when they are subject to optical injection, current modulation, optical feedback or optoelectronic feedback. Particularly interesting are the lasers with time-delay feedback because they can display a highly hyperchaotic behavior, that is, very complex temporal oscillations characterized by hundreds of positive Lyapunov exponents [Ahlers et al. 1998]. The feasibility of optical chaotic communication with such lasers was independently proposed by Mirasso et al. [1996] and by Annovazzi-Lodi et al. [1996]. A milestone in the field of chaos based communication systems using semiconductor lasers subject to delayed feedback was the successful field experiment reported by Argyris et al. [2005]. They obtained transmission rates at 1 Gb/s over a network of 120 Km of optical fiber in the metropolitan area of Athens, Greece. The corresponding recovered message exhibited BER values lower than 10^{-7}.

As far as semiconductor lasers are concerned, there are two delayed systems that are commonly used to obtain chaos. The first one studied in detail by Lang and Kobayashi [1980], corresponds to the situation where a fraction of the delayed output radiation of a semiconductor laser is fed back into the active region layer. The second one was proposed by Ikeda [1979], Ikeda and Matsumoto [1987], and consists in a continuous-wave laser whose output light propagates in a nonlinear cavity. In both cases hyperchaos can be generated. Moreover, the geometric dimension of the attractor increases linearly with time delay. In the following we present both systems in more detail.

2.4.1 Semiconductor lasers with optical feedback

The equations that are generally used to describe single-mode semiconductor lasers subject to coherent optical feedback are the ones proposed by Lang and Kobayashi [1980] for the complex electric field $E(t)$ and the carrier number inside the cavity $N(t)$:

$$\frac{dE(t)}{dt} = \frac{1+i\alpha}{2}[G - \frac{1}{\tau_p}]E + \kappa E(t-\tau)e^{-i\Omega\tau} \tag{2.2a}$$

$$\frac{dN(t)}{dt} = \frac{I}{e} - \frac{N}{\tau_s} - G|E|^2 \tag{2.2b}$$

where $G = g(N - N_t)/(1 + \varepsilon|E|^2)$ is the optical gain, g is the differential gain, N_t is the carrier number at transparency, ε is the gain saturation coefficient, α is the linewidth enhancement factor, τ_p is the photon life-time in the cavity,

τ_s is the carrier life time in the cavity, Ω is the frequency of the free running laser, I is the pump current, κ is the feedback coefficient and τ is the external cavity round-trip. Note that the Lang-Kobayashi model only includes the feedback effect after one roundtrip in the external cavity. Therefore, it may not be valid in regimes of strong optical feedback where multiple reflections in the external cavity should be accounted for.

Let us point out that in the semiconductor lasers subject to coherent optical feedback, the feedback is linear and nonlinearities come from the laser itself. The presence of the relaxation oscillations in semiconductor lasers gives rise to complex dynamics when the laser is perturbed by external disturbances. The relaxation oscillation frequency characterizes the time scale for exchange of energy between the electric field and the population inversion. The relaxation oscillation frequencies for semiconductor lasers are in the GHz range. Under moderate feedback rates the semiconductor lasers show chaotic behavior and sometimes evolve into unstable oscillations in a coherence collapse state (CC) where the laser linewidth is broadened greatly. On the other hand, one typical instability in a semiconductor laser subject to optical feedback is the phenomenon known as low frequency fluctuations (LFFs). In this case, the laser output power shows frequent irregular dropouts having frequencies from MHz to hundred of MHz. Usually, LFFs occurs for pump current rates around the laser threshold.

For systems described by equations (2.2), Vicente et al. [2005] have numerically demonstrated that the Kaplan-Yorke dimension increases linearly with the delay time so very large dimensionality can be achieved (see figure 2.2 left). However, they have also found that the KS entropy saturates as the delay time increases (see figure 2.2 right). Although the system has more positive Lyapunov exponents as the time delay is increased, they have a very small amplitude. Moreover, the largest positive Lyapunov exponent decreases for increasing delay times. Therefore, although the system has a larger dimensionality when increasing the delay, its behavior does not become more unpredictable.

Semiconductor lasers with optical feedback have been frequently used as chaotic generators. In this type of communication chaotic system, two different configurations (open-loop and closed-loop) can be used to obtain the synchronization (see figure 2.3). In the closed-loop configuration both emitter and receiver lasers are subject to optical feedback. By contrast, in the open-loop configuration only the emitter laser is subjected to optical feedback. In general, the open-loop configuration is less sensitive to parameter mismatch than the close-loop one, since the former does not require feedback in the re-

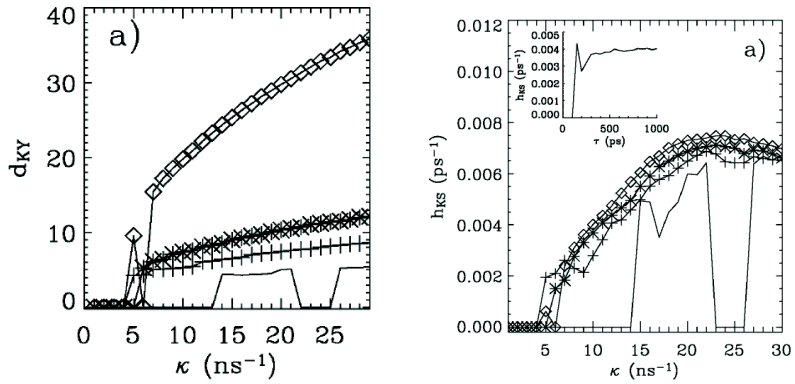

Figure 2.2: Left (Right): Kaplan-Yorke dimension (Kolmogorov-Sinai entropy) as a function of the feedback strength for $\tau = 100$ ps (solid), $\tau = 200$ ps (crosses), $\tau = 300$ ps (asterisks), and $\tau = 1000$ ps (diamonds). The inset panel of the right figure shows the Kolmogorov-Sinai entropy as a function of the delay time for a fixed feedback $\kappa = 10$ ns^{-1}. The figures have been taken from [Vicente et al. 2005].

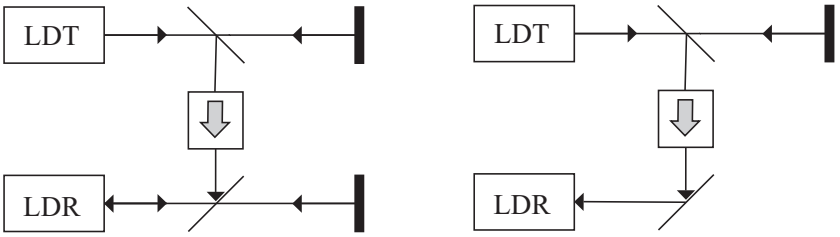

Figure 2.3: Schematic diagram of chaos synchronization systems in semiconductor lasers with optical feedback. Left: closed-loop configuration. Right: open-loop configuration. LDT: transmitter laser, LDR: receiver laser.

ceiver (and hence no tuning of feedback parameters in the receiver is needed at all).

2.4.2 Semiconductor lasers with electro-optical feedback

Chaotic behavior can be also induced when the light emitted by a semiconductor laser goes through an optoelectronic feedback loop containing a nonlinear optical device. In these type of systems, the chaotic dynamics is determined by the nonlinear optical device in the loop, not by the laser itself. The laser is a linear component.

The dynamics of these type of systems can be described by a delay differential equation where the feedback is modelled by a nonlinear function, whose transfer characteristic has at least a maximum or a minimum in the variable range.

The first experimental demonstration of chaotic communications based on semiconductor lasers with electro-optical feedback using CMO for message encoding was performed by Goedgebuer et al. [1998a], Larger et al. [1998a]. This system exhibits a nonlinearity in wavelength that is implemented by a birefringent plate (see 3.4.1 for more details). Similar experimental setup was also investigated for CSK modulation scheme in [Cuenot et al. 2001]. More recently, data transmission with a cryptosystem based on Mach-Zehnder modulators has been reported [Goedgebuer et al. 2002]. Here, the semiconductor laser with electro-optical feedback produces chaos in intensity. Optoelectronic phase chaos generators have been also reported [Larger et al. 2005].

In the chaotic communication systems considered in [Goedgebuer et al. 1998a, Larger et al. 1998a], the dynamical behavior of the chaotic carrier can be described by the following delay differential equation:

$$x(t) + T\frac{dx(t)}{dt} = \beta \sin^2(x(t-\tau) - \phi) \tag{2.3}$$

where $x(t)$ is the wavelength, T is the response time of the system, τ is the delay time in the optoelectronic feedback, and ϕ is the feedback phase. β determines the strength of the feedback as well as the strength of the nonlinearity. The regime of oscillations in wavelength depends on the value of the parameter β. The system can display chaotic behavior for $\beta > 2.1$, but this threshold value depends on the feedback phase. As the feedback strength β increases the influence of the phase decreases and for $\beta > 5$ the dynamics is independent of ϕ [Vicente et al. 2005]. The number of extreme values of the $\sin^2$ nonlinear function increases also with β.

It has been shown numerically for the system described by equation (2.3) that increasing the time delay produces a linear increment in the number of positive Lyapunov exponents but their values also decrease linearly [Vicente et al. 2005]. Hence, the KS entropy is independent of the value of the time delay for sufficiently large values of the feedback strength (see figure 2.4 right). The KS entropy has only a linear growth with the feedback strength. On the other hand, the Kaplan-Yorke dimension (an estimation of the attractor dimension) grows linearly with both the feedback delay time and the feedback intensity (see figure 2.4 left), in accordance with the results obtained for other systems described by delay differential equations (DDE) as the Mackey-Glass system [Farmer 1982].

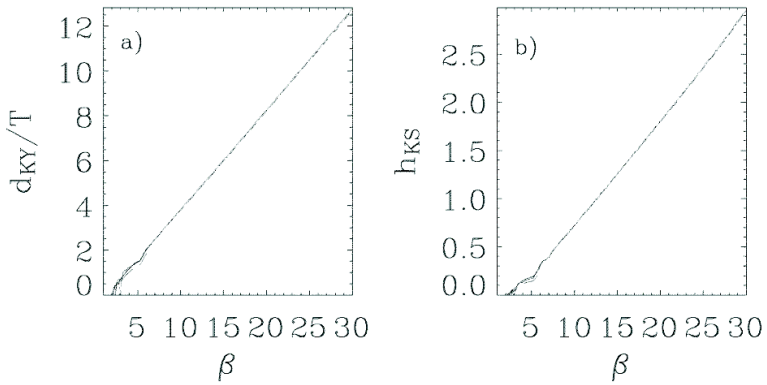

Figure 2.4: (a) Kaplan-Yorke dimension as a function of the feedback strength for $\tau = 5$, 10, 20, 50, 100 and 250 scaled with the delay time. (b) Kolmogorov-Sinai entropy as a function of the feedback strength for $\tau = 5$, 10, 20, 50, 100 and 250. In both panels, the curves corresponding to different delay times overlap indicating the almost perfect scaling of the dimension and the entropy. The figures have been taken from [Vicente et al. 2005].

2.5 Security of chaos-based communication systems

One of the main points to develop chaos-based communication systems is the promise of enhancing the security of the system. Nonetheless, it is worth highlight that using a chaotic carrier to dynamically encode information does not preclude the use of more traditional digital encryption schemes as well. Dynamical encoding with a chaotic waveform can thus be considered as an additional layer of encryption.

Nowadays, a growing proportion of data requires a high level of confidentiality while they are transmitted. Security of information in public or opened transmission channels is a key challenge in modern telecommunication networks. Until now, secure data transmission by conventional communication systems is based on mathematical algorithms. The operating principle of these systems is to take a message which has to be secretly transmitted, convolute it with a given pattern (key) supposed to be known by the emitter and the receptor of the message, and thereby obtain a new signal which can be safely sent in a public communication channel. If the system is properly designed, only the receptor (the one knowing how to deconvolute the message) can have access to the originally encrypted message. Actually, this is the description of a secret-key encryption. However, with this approach, two persons who

did not knew each other before can not communicate securely. The public-key cryptography circumvents the drawbacks of the secret key encryption. In public-key cryptography, each user has two keys, one public key and one private. The public key may be widely distributed, which can be freely intercepted by whoever, while the private key is kept secret. Both keys are related mathematically, but the private key cannot be practically derived from the public key (recovering the secret key from the public one remains a quasi-untractable mathematical problem). The messages encrypted with the public key can be decrypted only with the corresponding private key. However, Shor [1994] demonstrated that quantum computers may break all of our commonly used public-key algorithms. Moreover, breaking cryptographic mechanisms depends on the available computing power and taking into account the growing computation capacities and grid availability there is a strong hint that the era of public key cryptosystems will one day come to an end.

Consequently, there is a need to turn towards new alternatives able to strengthen software cryptography. Hardware cryptosystems, that is, cryptosystems relying on the physical properties of emitters and receivers, are good candidates. One advantage of hardware cryptosystems is that they are fully compatible with their software counterpart, in the sense that data can first be encrypted by software, and later encrypted again by hardware, thereby providing additional security. The more promising techniques in hardware encryption are quantum cryptography and chaos communication.

The idea behind the quantum cryptography is that two people communicating using a quantum channel can be absolutely sure no one is eavesdropping. Based on Heisenberg's uncertainty principle, one can not measure quantum information without disturbing it, and that disturbance alerts authorized users to the eavesdropper's presence. Nowadays, quantum cryptography or more exactly, Quantum Key Distribution (QKD) [Bennett and Brassard 1984, Ekert 1991] is only used to produce and safely distribute a key, not to transmit any message data. This key can then be used with any chosen encryption algorithm to encrypt (and decrypt) a message, which can then be transmitted over a standard communication channel. Quantum Key Distribution is currently widely investigated and even has yet reached the stage of reliable field applications and there are even some commercially available quantum cryptosystems. These QKD cryptosystems exploit the quantum mechanical properties of light particles (photons) to verify and certify that the information-photon has not been eavesdropped upon or intercepted. The photons are subsequently used to generate and exchange secrets (keys) between two remote sites through an optical fibre link, confirming thus their secrecy. However, QKD has quite severe limitations: it can not encrypt information

in real time, and until now, the distance over which keys can be exchanged is limited by several tens of kilometers and the key generation rate is very low (several tens of KHz).

Another interesting hardware cryptosystem is chaos-based communication, presented in the previous sections. The dependence on the initial condition of chaotic systems and the complexity of irregular behavior suggest the application of chaos in secure communications. In chaos based secure communications the objective is to use the apparently random oscillations of a chaotic system to hide a message. Encryption therefore relies on the unpredictability of chaotic systems.

Privacy in chaotic communication systems results from the fact that the receiver must posses the same configuration and parameter settings that the transmitter. Important aspects of receiver design are the number of parameters that have to be matched for information recovery and the precision required for parameter matching.

Therefore, in case of hardware attack, an eavesdropper must have the proper hardware and parameter settings in order to decode and recover the message. The decryption of the message is possible only when the emitter and receiver systems are almost perfectly identical: if it is not the case, synchronization does not occur and chaos-pass filtering becomes inoperant. It is expected that an eventual eavesdropper trying to build a chaotic receiver identical to the emitter would have to face this parameter mismatch problem, which impedes a proper extraction of the encrypted message.

However, it is also possible to make a software attack. Understanding the software attack as the possibility to eavesdrop and analyze the transmitted signal to detect and extract the hidden message. It was early shown that the hidden message can be unmasked by the dynamical reconstruction of the chaotic signal using nonlinear time series techniques [Short 1994; 1996] or other methods [Pérez and Cerdeira 1995, Rulkov et al. 1995, Yang et al. 1998a;b;c] in some low dimensional chaotic systems with few positive Lyapunov exponent. After the publication of these results in low-dimensional chaos-based communication systems, the employment of highly dimensional chaotic systems has been proposed to improve the security of these systems [Kocarev and Parlitz 1995, Peng et al. 1996].

A prominent class of dynamical systems that can have high dimensions and many positive Lyapunov exponents are nonlinear systems with time-delay feedback. These systems are wide spread in nature. There are many practical examples from physics, biology, economic and other fields. Within this rather broad class of systems, one can find the Ikeda equation [Ikeda 1979] modelling the passive optical resonator system, the Lang-Kobayashi equations [Lang and

Kobayashi 1980] describing semiconductor lasers with optical feedback or the Mackey-Glass equation [Mackey and Glass 1977] modelling the production of red blood cells. From a mathematical point of view, time delay feedback systems are usually modelled by delay differential equations (DDE). Although the physically meaningful models are continuous time systems, one will usually construct models which are discrete in time, the delayed maps (DM). In fact, the way DDE are implemented on digital computers is precisely by constructing a suitable DM and, more important, DM are the natural models to be reconstructed from experimental signals recorded with a finite sampling rate.

Nonetheless, in spite their high dimensionality, chaotic communication systems based on time delayed feedback systems have been broken by nonlinear time series analysis when the structure of the equation is known [Ponomarenko and Prokhorov 2002, Prokhorov and Ponomarenko 2008, Robilliard et al. 2006, Udaltsov et al. 2003, Zhou and Lai 1999].

2.6 Nonlinear time series analysis

In the first stages, the unpredictability of the chaotic signal suggested that chaotic communication systems may be totally secure. However, the underlying dynamics is deterministic, so that it is natural to ask whether some technique exists which is able to reproduce the observed dynamics. It was early demonstrated that these systems can be broken by nonlinear time series analysis [Abarbanel et al. 1994, Short and Parker 1998].

The methods of nonlinear time series analysis have been developed in close parallelism to the research in nonlinear dynamical systems defined by low dimensional ordinary differential equations (ODES). The bulk of them is based on the reconstruction of a vector space from the time record of a suitable observable. This vector space is equivalent to the original phase space of the system. For instance, in a laser system, the most common variable one can measure is the total intensity of the light output.

Nonlinear time series analysis is based on the assumption that the underlying dynamics of the recorded time series is deterministic. Then, the embedding method or the embedding theorem [Casdagli et al. 1991, Packard et al. 1980, Sauer et al. 1991, Takens 1981] states that the knowledge of sufficient values of a single scalar variable at a sequence of times allows to reconstruct the dynamics of the attractor. The standard embedding techniques describe only the dynamics in the attractor itself. More precisely, having a time series $x(t)$ measured with a sampling time δt, the method to reconstruct the attractor requires

the creation of the embedding vector $\mathbf{V} = (x(t), x(t-\tau_e), \ldots, x(t-(m-1)\tau_e))$, where m is the embedding dimension and τ_e is the embedding lag, an integer multiple of δt. In theory, the reconstruction of the nonlinear dynamics of the attractor is possible with $m > 2D_F$, where D_F is the dimension of the attractor.

However, the direct reconstruction of attractors from scalar data through time delay embedding using Takens theorem is clearly limited to low dimensional systems. A recent estimate [Olbrich and Kantz 1997] shows that the minimal number of points required for a clear manifestation of determinism is related to e^{hD_F}, where D_F is the dimension of the attractor and h is the Kolmogorov-Sinai entropy. In practice, attractors with dimensions larger than 5 can hardly be recognized by time series analysis using Takens theorem, since otherwise an unrealistic large amount of data and an unrealistically low noise-level would be required.

As early emphasized, it has been well established that time-delay feedback systems are able to exhibit high-dimensional chaotic attractors with many positive Lyapunov exponents. In these type of systems, the corresponding phase space is infinite dimensional, as an infinite set of independent numbers are required to specify the initial condition that is a generic function defined on the interval $[-\tau, 0]$, with τ being the delay time. In practice, however, high frequency components are almost absent and thus a finite number of variables are enough to parameterize the asymptotic solutions. On the other hand, the fractal dimension D_F can be made arbitrarily large as it has been established that D_F is proportional to τ for sufficiently large τ [Farmer 1982]. Thus the direct reconstruction of the system by the time delay embedding techniques runs into severe problems.

Nonetheless, it has been demonstrated that it is possible to reconstruct the dynamics of scalar time delay systems (i.e. systems involving a single variable) with high dimensional attractors by exploiting the particular structure of time-delay systems without taking into account the embedding theorems [Bezruchko et al. 2001, Bünner et al. 1996a;b, Ellner et al. 1997, Ponomarenko and Prokhorov 2002, Prokhorov et al. 2005, Robilliard et al. 2006, Udaltsov et al. 2003, Voss and Kurths 1997; 1999, Zhou and Lai 1999]. A method based on the projection of the phase space to suitable chosen subspaces has been extended to multi-variate delay systems, but a multi-variate measurement is required [Bünner et al. 1997].

The basic approach in the above mentioned cases is to consider that the structure of the equations that govern the time-delay systems is known, and only the functions and the parameters of the equations remain unknown. The

parameters and functions are estimated with parametric or non-parametric methods from the time series.

Nevertheless, these techniques fail when the structure of the equations that govern the system are unknown. In these cases, the nonlinear dynamics reconstruction by the embedding theorem is a more flexible approach, because one does not need to know so much a-priori information about the system under study.

Once the attractor is reconstructed by the embedding theorem, a model can be constructed by using the embedding vector. A faithful time series model can be used for many purposes, such as prediction, noise reduction and control, or to create artificial data which shares, for example, the power spectrum, distribution of values, attractor dimension, entropy and Lyapunov exponents of the original data. The general approach to construct the model is to estimate the next value of our observable time series $\hat{x}(t+\tau_e) = F(\mathbf{V})$, where $\mathbf{V}$ is the corresponding embedding vector. The value of $\hat{x}(t+\tau_e)$ is a unique function of its m previous values where m is the embedding dimension.

There are different choices to construct the general form of the function F from the time series, $x(t)$. Two of the most commonly used approaches are local methods in the phase space and global nonlinear models. In both cases, the free parameters are optimized by minimizing a cost function.

The local methods work by partitioning the embedding space into neighborhoods where the dynamics can be appropriately described by a linear model. Thus given a point in the embedded space the closest neighbors to such a point must be found. Among the local methods the most well known is the local linear fits. A common difficulty of local methods is the long computational times required by the searching for close neighbors in the embedding space and the effort to assemble the local linear models.

To overcome the problems of the local methods we can use global nonlinear models. The basic idea behind the nonlinear models is to find an appropriate F to model the true function on the whole attractor. A very popular strategy is to take F to be a linear superposition of basis functions (kernels), $F = \sum_{i=1}^{k} \alpha_i \Phi_i$. The k basis functions Φ_i are kept fixed during the fit and only the coefficients α_i are varied. There is a large variety of global nonlinear models such as neural networks, radial basis networks, wavelet-based models, support vector machines and so on.

Recently, Bünner et al. [2000a;b], Hegger et al. [1998] have demonstrated that it is possible to reconstruct the dynamics of scalar time delay systems (i.e. systems involving a single variable) with a local linear model by an embedding-like approach. This method works with a special "embedding" space which include both short-time and feedback-time delayed values of the variable. In

this way, the dynamics is recovered in a space with a dimension smaller than the attractor's dimension.

In this thesis we apply this special-like "embedding" to reconstruct the nonlinear dynamics of time-delay systems with global nonlinear models to exploit the advantages of the global models over the local ones. In our particular case, we will use neural networks models. Moreover, all the above mentioned methods developed to recover the nonlinear dynamics of time delay systems (parametric or non-parametric) take advantage of the particular structure of these systems. To this aim it is essential to know the time delay of the system. Therefore, a successfully recovery of the time delay from the time series is required. This question is studied in detail in chapter 3.

2.7 Neural networks

Artificial Neural Networks (NN) are mathematical models obtained from data. NN models are universal approximators in the sense that they can theoretically approximate any function to any degree of accuracy. They have been widely applied to a large number of problems in many different fields.

Neural Networks consist of a large number of simple processors (called neurons) with many interconnections. The strength of the connection or link between two neurons is called the weight. The values of the weights are the network parameters that have to be determined by the learning procedure in NNs. The neurons are organized into layers. Neural networks are nonparametric models and their parameters have no particular meaning in relation to the problems to which they are applied.

There are many different types of NNs. The choice of a particular type of NN depends on the kind of problem to be solved. The most famous and well-known NN is the multilayer Feed-forward network (FFNN) also called multilayer perceptron.

Multilayer Feed-forward networks consists of an input layer, an output layer and M hidden layers (HL) of neurons. Each neuron of one layer can receive only inputs of the neurons of the previous layer (see figure 2.5). Through this thesis, we refer to this type of architecture as FFNN(a:b), indicating a FFNN with two hidden layers with a and b neurons, respectively. Other notations found in the literature refers to this type of NN as (j:a:b:i), where j and i represents the number of inputs and outputs of the multilayer perceptron.

The typical output neuron, z_i, computes the weighted sum of its n inputs signals, x_j $(j = 1, 2, ...n)$ plus a bias or offset term θ_i and generates an output value given by:

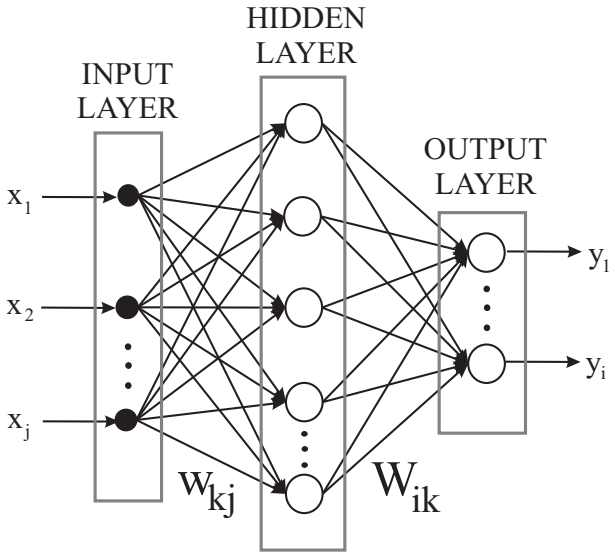

Figure 2.5: Example of a Multilayer Feed-forward NN with j inputs, i outputs and one hidden layer with k neurons: FFNN(k)

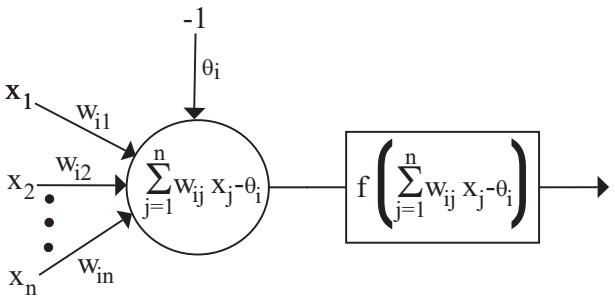

Figure 2.6: Schematic of a neuron

$$z_i = f(\sum_{j=1}^{n} w_{ij}x_j - \theta_i) \tag{2.4}$$

where f is the activation function and w_{ij} is the weight associated with the jth input (see figure 2.6). The weights w_{ij} can have positive or negative values.

For each output, y_i, the FFNN calculates a function $y_i = F_i(x_1, ...x_n)$ of the inputs. For example, the outputs of the multilayer NN plotted in figure 2.5 are given by:

$$y_i = f(\sum_k W_{ik} f(\sum_j w_{kj} x_j - \theta_k) - \theta_i) \tag{2.5}$$

In the case of general regression, the main task of the NN is to model the underlying function between the given inputs and outputs and to filter out the disturbances contained in the noisy training data set. As above mentioned, NNs learns from a set of training data and the learning procedure is one of the most important task of the nonlinear modelling with the NNs.

2.7.1 Learning process

The learning process consists on adjusting the connection weights of the NN so the NN can model the underlying function from a finite set of measurements or observations. The weights of the NN that have to be adjusted constitute the parameters of the NN. There are many different ways and various learning algorithms to adapt and change the weights.

Depending on the information that is available to the network the methods of learning can be classified in supervised or unsupervised learning. The unsupervised learning is outside the scope of this thesis, and for the remainder of this section we will focus on the supervised learning. In supervised learning the network is provided with the correct output for every input pattern. Hence, the learning problem is setting as follows: there is some unknown nonlinear dependency $\mathbf{y} = F(\mathbf{x})$ between some high-dimensional input vector $\mathbf{x}$ and scalar or vector output $\mathbf{y}$. The network is given a desired output $(y_{p1}, ..., y_{pm})$ for each input pattern $(x_{p1}, ...x_{pn})$. During the learning process, the actual output generated by the network $(\hat{y}_{p1}, ..., \hat{y}_{pm})$ may not equal the desired output. Weights are modified to allow the network to produce answers as close as possible to the known correct answer. Normally, the weights are obtained minimizing some cost functions that measure the difference between the desired output and the NN output. In the neural network field, the most widely criterion for the estimation of model parameters is the sum of error squares (if the data are corrupted with Gaussian noise with zero mean, minimization of the sum of error squares results in the same parameters as maximization of the likelihood function).

One of the main problems of the NN is that the cost function depends nonlinearly upon weights. This means that the error hypersurface is generally not a convex function with guaranteed minimum. There are many different learning algorithms to optimize the weights by minimizing the cost function. In this thesis, we will use the Levenberg-Marquardt algorithm [Hagan et al. 1996] that is based on the gradient descent along the error surface. This

algorithm appears to be the fastest method for training moderate-sized feed-forward neural networks (up to several hundred weights). In the general case, where the error hypersurface are plenty of local minima, all that can be done is to start at a number of random (or somehow well chosen) initial places, then go until find a local minimum each time. Then, one selects the lowest of the found local minima, and takes the corresponding weights vector as the best one. This implies that the NNs do not assure the global minima of the error hypersurface and depending on the initial conditions that minima can not be found.

2.7.2 Some aspects of NN design

The most important issues in designing feed-forward networks are the number of hidden layers, the number of neurons in a hidden layer, the type of activation functions and the size of the training set. Few theoretical results provide a guidelines for selecting these parameters in practice. There are many aspects in designing feed-forward networks that must be determined by trial and error. Recall that both the number of input and output neurons are in general determined by the nature of the problem.

One of the first decisions is to choose the number of hidden layers. Although it is possible to design a multilayer perceptron with an arbitrary number of hidden layers, theoretical results and simulations in different fields have demonstrated that there is no need to have more than two hidden layers. Feed-forward NNs with one or two hidden layers are theoretically able to approximate any continuous function to any degree of accuracy [Cybenko 1989, Kurkova 1992]. It is difficult to say which topology is better. The rule of thumb is to try first to solve the problem with only one layer and if it is necessary to add a second hidden layer.

The number of neurons in a hidden layer and their activation functions are the most important design parameters with respect to the model abilities of NNs. In practical applications of NNs one should build and train many different NNs structures and then pick the best one. To choose the number of neurons in hidden layers, two extreme solutions should be avoided: filtering out the underlying function (not enough HL neurons) and modelling the noise or "over-fitting" the data (too many HL neurons). On the other hand, the activation functions for the output layer neurons are typically linear or sigmoidal. Concerning the choice of the activation function of the hidden layer there is not a definitive answer. Any nonlinear, smooth, differentiable and preferable non-decreasing function can be used, ensuring the universal approximation capacity of a specific network. The sigmoidal function is the

favorite activation function. The most popular sigmoid functions are: the logistic function defined by $f(x) = 1/(1 - e^{-cx})$ and the hyperbolic tangent function defined by $f(x) = \tanh(cx)$, that yield output values in the range [-1,+1]. In both cases c is the slope parameter. It is generally recognized that the tangent hyperbolic always gives better approximation properties so people tends to use it.

Finally, it is also necessary to determine the number of training patterns needed to train the network to guarantee a valid generalization. Generalization refers to the capacity of a neural network to give correct answers on previously unseen data (this means, how will the network performs on data not included in the training set). Too few training data may cause "over-fitting" (wherein the network performs well on the training data set, but poorly on previously unseen data). To avoid this, it is important to make a cross validation of the model. The given data set can be divided into two parts, one destinated to the training of the NN and the other to the test. When the test error is much higher than the training error, there is a problem of over-fitting. Typically if the number of training data is higher than the number of neurons then there is not over-fitting. On the other hand, the quality of weight estimation depends upon the noise level and the size of the data set. Clearly, the higher the noise level and more complex the underlying function to be modelled, the more training data are needed.

To sum up, the main advantages of NNs are that they have the property of learning from the data, can approximate any multivariate nonlinear function, do not require deep understanding of the problem and are robust to the presence of noisy data. Nonetheless, NNs also present some disadvantages. For instance, the NNs do not increase our knowledge about the system and little guidance is offered about the NN structure or optimization procedure, or the type of NN to use for a particular problem. Moreover, they are prone to bad generalizations (data over-fitting) and offer multiple solutions but nothing assure you that the best solution for the problem is reached. In addition, NNs suffer from problems in convergence and longer training times for high dimensional input spaces. It is also addressed that the generalization ability decreases in huge NNs. The modular neural networks (MNNs) seem very promising for tackling the two last problems.

The idea behind the modular neural networks (MNNs) is the division of a complex problem into simpler tasks. A modular neural network is a neural network characterized by a series of neural networks moderated by some intermediary. Each independent neural network serves as a module and operates on separate inputs to accomplish some subtask of the task the network hopes

to perform. The task the module has to learn is in general easier than the whole task of the network. The intermediary takes the outputs of each module and processes them to produce the output of the network as a whole. The modules do not interact with each other. The architecture of a single module is simpler and the subnetworks are smaller than a standard NN network. One of the major benefits of modular neural networks is the ability to reduce the size of the network, since the computation time depends on the number of neurons and their connections.

Chapter 3

Time delay identification

In this chapter, we study how to identify the time delay in semiconductor lasers subject to optical and optoelectronic feedback. These systems have been considered as appropriate candidates for secure chaotic communications systems because they provide a simple way of generating high-dimensional chaotic carriers [Vicente et al. 2005].

However, several studies have demonstrated that it is possible to extract the nonlinear dynamics of certain chaotic nonlinear delayed systems once the time delay is known [Bezruchko et al. 2001, Bünner et al. 2000a;b; 1997; 1996a;b, Ellner et al. 1997, Hegger et al. 1998, Ponomarenko and Prokhorov 2002, Prokhorov et al. 2005, Prokhorov and Ponomarenko 2008, Robilliard et al. 2006, Udaltsov et al. 2003, Voss and Kurths 1997; 1999, Zhou and Lai 1999]. The extraction of the dynamics can only be performed if the value of the delay of the system is known . Therefore, time delay is a key parameter in order to ensure the confidentiality of a chaotic communication system.

Through this chapter we analyze the time delay identification of semiconductor lasers subject to optical and optoelectronic feedback in depth. We also pay attention to several modifications (like variable time delays or the inclusion of a second delay) proposed to avoid time delay identification.

The chapter is organized as follows. In section 3.1, we detail several techniques to extract the time delay from time series. Section 3.2 deals with the time delay extraction (from numerical simulations and experiments) in systems based on all-optical feedback with one and two delays. In sections 3.3 and 3.4 we study the time delay identification in systems based on optoelectronic feedback with one and two delays from numerical and experimental data, respectively. The experimental data are obtained from a semiconductor

laser with optoelectronic feedback that presents chaos in wavelength. In section 3.5 we extract the time delay of the optoelectronic feedback system from experimental data when the time delay is a periodic function. Finally, section 3.6 is devoted to the conclusions.

3.1 Techniques to identify the time delay from time series

Multiples methods have been developed to identify the time delay of scalar or vectorial delay systems from a time series $x(t)$. These type of system can be described by the following delay differential equation:

$$h(\dot{\mathbf{x}}(t)) = \mathbf{F}(\mathbf{x}(t), x_1(t-\tau)) \tag{3.1}$$

where $\mathbf{x} = (x_1, \ldots, x_N)$, $h(\dot{\mathbf{x}}(t))$ is usually equal to $T\dot{\mathbf{x}}(t)$, being T the response time of the system, F is some nonlinear function and τ represents the time delay. In the following, the bold type letter indicates vectors.

Among the reported methods to identify the time delay from time series, we can find the autocorrelation function [Lepri et al. 1994, Ohira and Sawatari 1997, Siefert 2007], the mutual information [Locquet et al. 2006, Udaltsov et al. 2005], the minimal forecast error [Bünner et al. 2000a;b, Fowler and Kember 1993, Hegger et al. 1998], the minimal value of information entropy [Tian and Gao 1997], various measure of complexity of the projected time series [Bünner et al. 1998; 1997; 1996a;b, Kaplan and Glass 1993], regression analysis [Ellner et al. 1997, Voss and Kurths 1997; 1999] and statistical analysis of time intervals between extrema in the time series [Bezruchko et al. 2001, Ponomarenko and Prokhorov 2002, Prokhorov et al. 2005, Prokhorov and Ponomarenko 2008].

In the following, we describe in some detail the most widespread methods used to extract the time delay from time series. Posteriorly, we use these methods to identify the time delay of semiconductor lasers subject to optical or optoelectronic feedback.

3.1.1 Autocorrelation Function

The autocorrelation function (AF) of a signal $x(t)$, is defined as:

$$c(\nu) = \frac{1}{\sigma^2}\langle (x(t) - \langle x(t)\rangle)(x(t-\nu) - \langle x(t)\rangle)\rangle \tag{3.2}$$

where $\langle\rangle$ implies averaging over time and $\sigma = \langle (x(t) - \langle x(t) \rangle)^2 \rangle^{1/2}$. Note that $c(\nu) = c(-\nu)$ and $c(0) = 1$.

The AF reflects the linear correlations of the variables $x(t)$ and $x(t-\nu)$. It is well established that the autocorrelation of signals from deterministic chaotic systems decays with increasing ν and the time delay can be estimated for the first peak or valley of the AF [Lepri et al. 1994]. However, as the AF only measures the linear relationship between x and $x(t-\nu)$, the detection of the time delay fails in systems with high nonlinearities. Moreover, the autocorrelation function leads to an overestimation of the delay time due to the finite reaction time of the system [Bünner et al. 1998].

3.1.2 Mutual information

The mutual information is based on Shannon's entropy and takes into account the nonlinear correlations. Given two discrete variables X and Y with joint probability distribution function, $P_{XY}(x,y)$, and marginal probability distribution functions $P_X(x)$ and $P_Y(y)$, the mutual information can be defined as:

$$I(X;Y) = \sum_{x \epsilon X} \sum_{y \epsilon Y} P_{XY}(x,y) \ln\left(\frac{P_{XY}(x,y)}{P_X(x) P_Y(y)}\right) \tag{3.3}$$

The mutual information measures the amount of information that can be obtained about one variable X by observing another variable Y. The delayed mutual information (DMI) is the special case when Y is the process X sampled at times $t-\nu$, and the calculation of the mutual information is performed for different delays ν. A nonlocal time dependence appears as a peak in the DMI of delayed systems when $\nu = \tau$. In the special case of $\nu = 0$ the expression yields the Shannon entropy of the data distribution. The mutual information takes always positive values.

Unlike the autocorrelation function, the DMI measures the nonlinear dependency between $x(t)$ and $x(t-\nu)$ and the time delay can be estimated for highly nonlinear systems. However, the time delay given by the DMI is also overestimated due to the response time of the system.

Hereafter, we shall present other techniques to extract the time delay that are not affected by the response time of the system. Nevertheless, the time delay identification by the DMI and the AF is more immune to the presence of noise.

3.1.3 Filling factor method

The filling factor method (FF) relies on the existence of a functional relationship between $\mathbf{x}(t)$ and $x_1(t-\tau)$ (see equation (3.1)). In this case, the trajectory projected on the space $(\mathbf{x}(t), x_1(t-\nu), \dot{\mathbf{x}}(t))$ is restricted to a line when $\nu = \tau$. However, with $\nu \neq \tau$, the trajectory is no longer restricted to a line and fills a great part of the space. This makes possible to detect the time delay of the system, τ, by measuring the complexity of the projected trajectory as a function of ν. This method also permits in some cases the reconstruction of the nonlinear dynamics of the system [Bünner et al. 1997; 1996a]. There are different ways to quantify the complexity of the projected trajectory [Bünner et al. 1996a;b, Zhou and Lai 1999], but one of the most well-known is the filling factor method [Bünner et al. 1998; 1997].

The filling factor of the projected trajectory of a N-order time-delay system is computed by covering the $(\mathbf{x}(t), x_1(t-\nu), \dot{\mathbf{x}}(t))$ space with P cubes of dimension $(2N+1)$. The filling factor is the number of cubes, which are visited by the projected trajectory at least one time, normalized to the total number of cubes, P. The filling factor analysis is performed under variation of ν.

The filling factor is minimal for small values of ν as a result of local correlations in time. When $\nu = \tau, 2\tau, ...n\tau$, the filling factor shows local minima with decreasing amplitude indicating nonlocal correlations in time due to the time delay.

One of the drawbacks of the FF method is that the time derivative of $\mathbf{x}(t)$ has to be estimated from the time series. The estimation of time derivatives from experimental time series is sensitive to additional noise. Moreover, the sampling rate has to be fine enough to allow the estimation of time derivatives with the help of adequate interpolating procedures. To save computation time, the filling factor can be measured over the space $(\mathbf{x}(t_{ext}), x_1(t_{ext}-\nu))$, where $\mathbf{x}(t_{ext})$ corresponds to the extrema of the time series. In this way we reduce the dimension of the cubes to $N+1$.

The value of the time delay given by the FF method is not overestimated by the time response of the system. Furthermore, the filling factor method works for highly nonlinear system, although the minimum at τ decreases in amplitude as the nonlinearity of the system increases. The main shortcoming of this method is its sensitivity to noise, as it is necessary to evaluate the extrema or the derivative of the time series.

3.1.4 Time distribution of extrema

The time distribution of extrema (TDE) method is based on a statistical analysis of time intervals between extrema in the time series [Bezruchko et al. 2001, Ponomarenko and Prokhorov 2002], [Prokhorov et al. 2005, Prokhorov and Ponomarenko 2008]. To identify the time delay, we count the number N of pairs of extrema in $x(t)$ that are separated in time by ν, normalized to the total number of extrema. $N(\nu)$ is an estimation of the probability to find a pair of extrema in $x(t)$ separated by ν given a sufficiently number of extrema.

Let us explain in more detail why the time delay can be estimated from $N(\nu)$ following the explanation given in [Ponomarenko and Prokhorov 2002]. We consider the equation (3.1) with N = 1 (the scalar case) and $h(\dot{x}(t)) = T\dot{x}(t)$ for the sake of clarity. In this case, the time derivative of such equation is given by:

$$T\ddot{x}(t) = \frac{\partial F(x(t), x(t-\tau))}{\partial x(t)}\dot{x}(t) + \frac{\partial F(x(t), x(t-\tau))}{\partial x(t-\tau)}\dot{x}(t-\tau) \tag{3.4}$$

The probability to find pairs of extrema in $x(t)$ separated by ν when $\nu = \tau$ is maximal for $T = 0$ and minimal when $T \neq 0$.

If $T = 0$ and $\dot{x}(t) = 0$, then most probably $\dot{x}(t-\tau) = 0$. Consequently, almost each extremum of $x(t)$ is separated by a time τ of another extremum. As a result $N(\nu)$ shows a maximum at $\nu = \tau$.

On the other hand, if $T \neq 0$, the maximum of $N(\nu)$ shifts from τ to larger values and can be found at $\tau + \tau_s$. The value of τ_s depends on T. In this case, if $\dot{x}(t) = 0$, typically, $\ddot{x}(t) \neq 0$. Thus, according to equation (3.4), $\dot{x}(t-\tau) \neq 0$. Then a minimum in $N(\nu)$ should appear at $\nu = \tau$.

The TDE can be used to estimate the time delay in highly nonlinear system since the statistics of extrema is independent of the nonlinearity of the system. However, the analysis of the time distribution of extrema can be difficult in presence of noise. The noise induces spurious extrema randomly distributed. Therefore, the noise increases the number of extrema and the probability to find a pair of extrema in time series separated in time by τ. However, for moderate noise levels this probability is smaller than the probability to find a pair of extrema separated in time by $\nu \neq \tau$. In data heavily corrupted by noise, since the maximum of $N(\nu)$ is more pronounced than the minimum, its location can be used as an upper estimate of τ. This implies that under high noise levels, the estimated time delay with this method is affected by the time response of the system. Moreover, this method requires long time series, in order to have enough statistics, particularly in presence of noise where the length of the time series can be crucial.

Time distribution of extrema method for systems with multiple delays

The analysis of the time distribution of extrema can be also used to estimate multiple time delays [Prokhorov et al. 2005]. We consider a system described by the equation:

$$T\dot{x}(t) = F(x(t), x(t-\tau_1), x(t-\tau_2)) \tag{3.5}$$

The time derivative of equation (3.5) is given by:

$$T\ddot{x}(t) = \frac{\partial F}{\partial x(t)}\dot{x}(t) + \frac{\partial F}{\partial x(t-\tau_1)}\dot{x}(t-\tau_1) + \frac{\partial F}{\partial x(t-\tau_2)}\dot{x}(t-\tau_2) \tag{3.6}$$

In general $x(t)$ has mainly quadratic extrema, and therefore, at the extrema points $\dot{x}(t) = 0$ and $\ddot{x}(t) \neq 0$. Hence, if $\dot{x}(t) = 0$ we have:

$$T\ddot{x}(t_{ext}) = \frac{\partial F}{\partial x(t_{ext}-\tau_1)}\dot{x}(t_{ext}-\tau_1) + \frac{\partial F}{\partial x(t_{ext}-\tau_2)}\dot{x}(t_{ext}-\tau_2) \tag{3.7}$$

When $\dot{x}(t)$ and $\dot{x}(t-\tau_1)$ or $\dot{x}(t)$ and $\dot{x}(t-\tau_2)$ vanish simultaneously, a special relationship between $\ddot{x}(t)$ and $\dot{x}(t-\tau_i)$ should be fulfilled. Then this corresponds to an event with low probability. As a result, the number of extrema separated in time by τ_1 and τ_2 must be appreciably less than the number of extrema separated in time by other values of ν. Thus, $N(\nu)$ has pronounced minima at $\nu = \tau_1$ and $\nu = \tau_2$ corresponding to the two time delays of equation (3.5).

3.1.5 Forecasting error of a model

The forecasting error of a model that approximate the original system can be used to retrieve the time delay. This method has been proposed by Hegger et al. [1998] to identify the time delay and also to reconstruct the nonlinear dynamics of the system [Bünner et al. 2000a;b]. They construct a local linear model from the available time series. The output of their model is given by $\hat{x}(t+\delta t) = a_t + b_t x(t) + c_t x(t-\nu)$, where a_t, b_t and c_t are the coefficients of the local linear approximations and δt is the sampling period. To identify the time delay, they evaluate the error given by the difference between $x(t)$ and $\hat{x}(t)$ under variations of ν. When $\nu = \tau$, the averaged forecasting error of the model has a minimum.

Based on the same approach, we have proposed to use a simpler global model instead of a local linear one [Lee et al. 2005, Ortín et al. 2005]. In this

way, we avoid the problems associated with local linear models (see 2.6). This global model is described by:

$$\begin{aligned}\hat{x}(t+\delta t) &= W(x(t), x(t-\delta t), ..., x(t-m_1\delta t), \\ &\quad x(t-\nu+m_2\delta t), ..., x(t-\nu), ..., x(t-\nu-m_2\delta t)) \end{aligned} \quad (3.8)$$

where W can be a linear or nonlinear function. As in the case of the local linear models, a minimal forecast error is expected when $\nu = \tau$. The optimal values for m_1 and m_2 are obtained by trial and error. As a rule of thumb, large m_1 and m_2 values should be avoided.

The main advantage of using a linear function is the simplicity of the model. In this case, the equation (3.8) can not reproduce the dynamics of the original system and the forecasting error takes high values. However, it is enough to identify the time delay for weakly nonlinear systems. Global nonlinear functions are necessary to identify the time delay in highly nonlinear system.

We have considered linear and nonlinear models. In the first case, our method is nothing but linear least squares fitting technique. In the second case the nonlinear function is obtained by using neural networks. In the latter case, the Neural Network model has been used to identify the time delay and also to extract the nonlinear dynamics of optoelectronics feedback system (see chapter 4).

The principal disadvantage of the global nonlinear model to identify the time delay is the long required computation times. However, the forecasting error of model is not affected by the response time of the system. Therefore it can be used in combination with other method (such as DMI) to refine the estimated time delay.

Finally, it is worth pointing out that this method under low and moderate noise is more robust than the filling factor method or the time distribution of extrema method. Nonetheless, for data heavily corrupted by noise, the DMI and the autocorrelation function yield better results.

3.2 Semiconductor lasers with all optical feedback

Previous works on time delay identification in external cavity semiconductor-based lasers (ECSLs) have shown that the time delay can be easily extracted from the laser light output by standard identification methods as the ones presented in the previous section [Bünner et al. 1998, Lee et al. 2005, Locquet et al. 2006].

To complicate the time delay identification, it has been suggested the inclusion of additional cavities in ECSLs [Lee et al. 2004]. In that work, it was shown on basis of the Lyapunov exponents and dimensions of the chaotic attractor, that the complexity of the dynamics is greater for double delay than for single delay systems. However, it has been demonstrated that even in the presence of multiple feedback loops it is possible to identify the time delays of the ECSLs [Bünner et al. 1998, Lee et al. 2005, Locquet et al. 2006]

Recently, it has been proved that a simple ECSL with a single optical feedback could, with a careful choice of parameters, hide its time-delay when standard methods are employed [Rontani et al. 2007]. Interestingly, the region of laser and feedback parameters where such a difficult time-delay identification occurs does not necessarily correspond to the situation where the chaos complexity (dimension and entropy) is high.

In this section, we study the time delay identification in the ECSLs applying the methods described in the previous section. Our purpose is to determine the more adequate methods to retrieve the time delay. The section is organized as follows. In subsections 3.2.1 and 3.2.2, we extract the time delay from numerical simulations of a ECSL with one and two feedback loops, respectively. In subsection 3.2.3, the time delay is identified from experimental time series of ECSLs with one and two times delays. In subsection 3.2.4, we analyze the estimation of the time delay in ECSLs with low feedback rates. Finally, the conclusions about time delay identification in semiconductor laser with all-optical feedback are presented in subsection 3.2.5.

3.2.1 One delay systems

In this section, we simulate the behavior of a single-mode semiconductor laser with a single external optical feedback with the following delay differential equations [Mulet 2003]:

$$\frac{dE(t)}{dt} = \frac{1}{2}(1+i\alpha)[G(t)-k]E(t) + \kappa e^{-i\Omega\tau}E(t-\tau) + \sqrt{2\beta_{sp}\gamma_e N}\xi(t) \quad (3.9a)$$

$$\frac{dN(t)}{dt} = pJ_{th} - \gamma_e N - G(t) \mid E(t) \mid^2 \quad (3.9b)$$

where $E(t) = E_1 + iE_2$ is the complex amplitude of the electrical field, $N(t)$ is the total carrier density, α is the linewidth enhancement factor, $G(t) = g(N - N_t)/(1 + \varepsilon \mid E \mid^2)$ is the optical gain, g is the differential gain, N_t is the carrier number at transparency, ε is the gain saturation coefficient, k is the cavity decay rate, κ is the feedback strength, τ is the external cavity

round trip, Ω is the frequency of the free running laser, p is the pumping factor, J_{th} is the threshold current and γ_e is the carrier recombination rate. β_{sp} is the spontaneous emission coefficient and ξ is the spontaneous emission noise that represents a complex Gaussian white noise with zero mean and time correlation given by $\langle \xi(t)\xi^*(s)\rangle = 2\delta(t-s)$.

We consider the following parameters values: $\alpha = 3$, $g = 2.76 \times 10^{-6}$ ns^{-1}, $N_t = 1.51 \times 10^8$, $\varepsilon = 3 \times 10^{-7}$, $k = 158$ ns^{-1}, $\kappa = 5$ ns^{-1}, $\tau = 2.3$ ns, $\gamma_e = 1.66$ ns^{-1} and $\beta_{sp} = 5 \times 10^{-7}$. For these parameters, when the pumping factor is 1.3 the system works in the CC regime and when $p = 1$ in the LFF regime (see section 2.4.1).

To identify the time delay we analyze the intensity time series $I(t) = E_1(t)^2 + E_2(t)^2$, sampled each 0.05 ns over 500 ns. The sampling time has been chosen to match the available experimental sampling times.

First, we extract the time delay of the system with the autocorrelation function and the delayed mutual information. The results are presented in figure 3.1 (a and b) for the LFF and CC regimes. The time delay is located at the peak with higher amplitude, although peaks with decreasing amplitudes also appear at multiples of the time delay. The estimated time delay with both methods is $\hat{\tau} = 2.35$ ns, within the error of 0.05 ns due to the sampling time.

We also estimate the time delay with the filling factor method and the forecasting error of a global linear model (see figure 3.1 (c and d)). The estimated time delay with these methods is $\hat{\tau} = 2.35$ ns, the same as the one obtained from the AF and DMI. These methods are not affected by the response time of the system. Therefore, the overestimation of the time delay given by some methods (like the AF or the DMI) due to the finite reaction time of the system, is insignificant respect to the time delay value. We conclude that the response time of the ECSLs is negligible compared to the time delay value. Moreover, the time delay identification is possible in the LFF and CC regimes with methods that only take into account the linear correlations between $x(t)$ and $x(t-\tau)$, such as the AF and the forecasting error of a global linear model. The only appreciable difference is that the peaks or valleys that identify the time delay have sharper width and smaller amplitude in the CC regime than in the LFF regime.

Finally, it is worth to mention that two different time scales (the relaxation oscillations period τ_{RO} and the time delay τ) coexist in the ECSLs. The effect of τ_{RO} on the time delay identification is more noticeable in the AF for the LFF regime. In this case, apart from the peaks due to the time delay, we find small peaks and valleys located at multiples of $\pm\tau_{RO}/2$ (see figure 3.1 (a_1)).

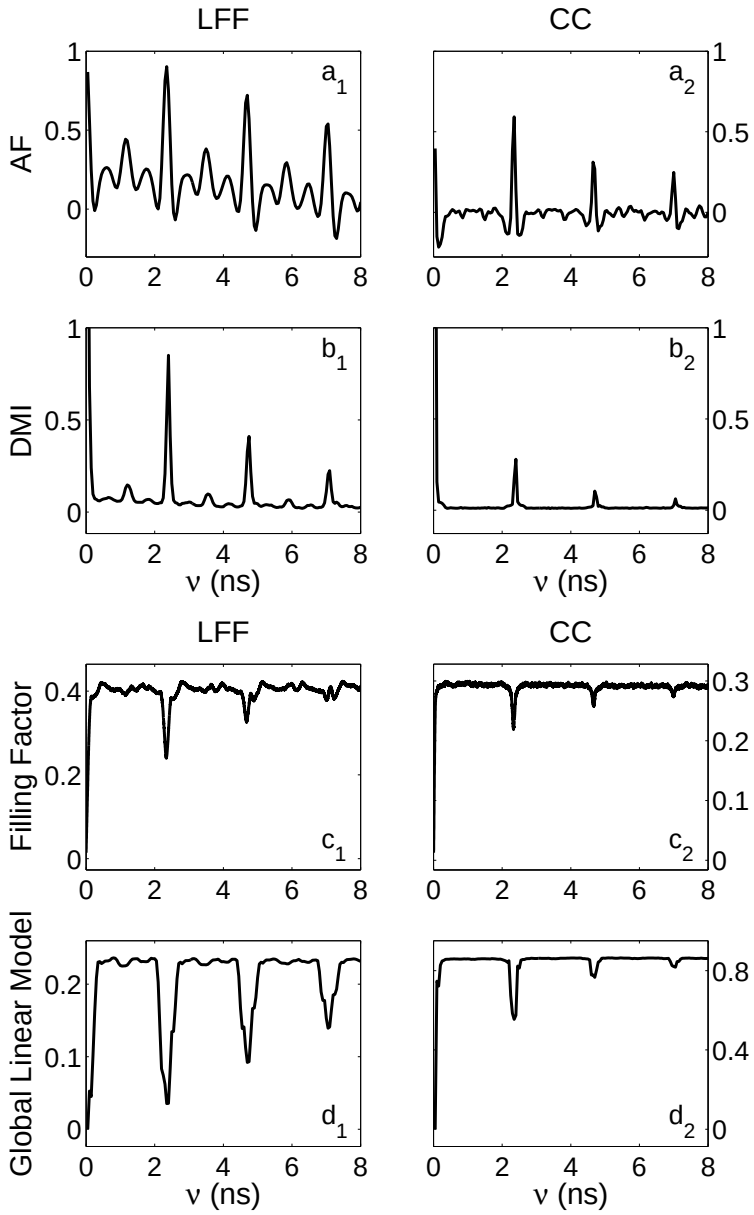

Figure 3.1: From top to bottom: the autocorrelation function (AF), the delayed mutual information (DMI), the filling factor and the forecasting error of a global linear model of the laser output intensity of an ECSL with single feedback, $\tau = 2.3$ ns. Left: LFF regime. Right: CC regime.

These peaks due to τ_{RO} can blur the identification of the time delay when the feedback strength is low [Rontani et al. 2007].

3.2.2 Two-delay systems

Now, we study if the inclusion of a second delay can affect the time delay extraction in ECSLs. The behavior of a semiconductor laser with two external optical feedbacks is simulated using a trivial generalization of the delay differential equations that rules the one delay case (equations (3.9)):

$$\begin{aligned}\frac{dE(t)}{dt} =& \frac{1}{2}(1+i\alpha)[G(t)-k]E(t) + \kappa_1 e^{-i\Omega\tau_1}E(t-\tau_1) + \\ &+ \kappa_2 e^{-i\Omega\tau_2}E(t-\tau_2) + \sqrt{2\beta_{sp}\gamma_e N}\xi(t) \qquad (3.10a)\\ \frac{dN(t)}{dt} =& pJ_{th} - \gamma_e N - G(t) \mid E(t) \mid^2 \qquad (3.10b)\end{aligned}$$

A second delay term is included in the electric field equation. The operational parameters are the same as in the single delay case, with $\kappa_1 = \kappa_2 = \kappa$. The first time delay is $\tau_1 = 2.3$ ns (the same as in the single delay case) and the second time delay is $\tau_2 = 4$ ns.

We find that it is possible to identify the two time delays using the same techniques that work in the single delay case. The DMI for the ECSL with two delays is plotted in figure 3.2. Comparable results are obtained with other methods of identification. As can be observed, the two peaks with higher amplitudes indicate the two time delays of the system. Peaks of lower amplitude also appear at the linear combinations of both time delays, $m\tau_1 \pm n\tau_2$ with m and n integer numbers. Among these peaks, the stronger one always corresponds to the sum of the time delays $\tau_1 + \tau_2$. As in the single delay case the effect of the response time is negligible. Likewise, the amplitude and the width of the peaks decrease in the CC regime respect to the LFF regime. Therefore, some of the $m\tau_1 \pm n\tau_2$ combinations are no noticeable in the CC regime.

Next, we study the particular case $\tau_2 = 2\tau_1$, with $\tau_1 = 2.3$ ns and $\tau_2 = 4.6$ ns. Here, the DMI plotted in figure 3.3 is very similar to the DMI of the single delay case (see figure 3.1 (b_1 and b_2)). The linear combinations $m\tau_1 \pm n\tau_2$ are always multiples of τ_1 and conceal the existence of the second delay. The results hold for other techniques of identification. The same happens for $\tau_2 = 3\tau_1$. By contrast, in the case $\tau_2 = 4\tau_1$, the peak in τ_2 is higher than the others and it is possible to guess the existence of the second delay from the DMI.

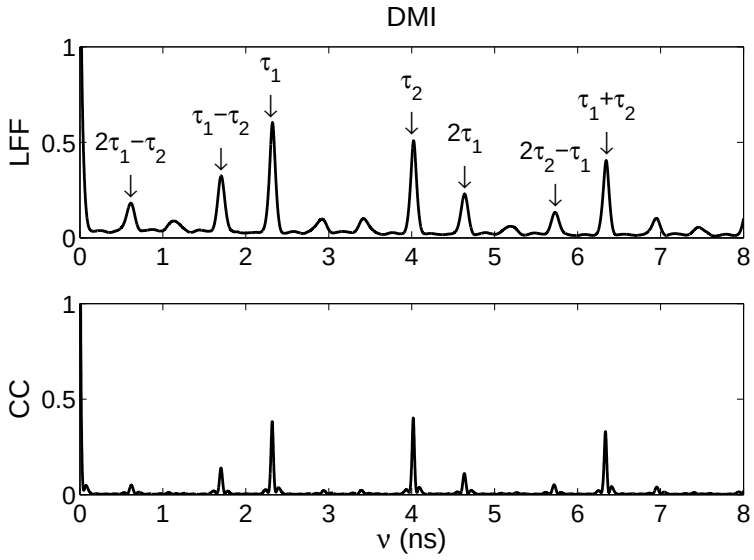

Figure 3.2: The delayed mutual information for the LFF (top) and CC regime (bottom) of the laser output intensity of an ECSL with two delays $\tau_1 = 2.3$ ns and $\tau_2 = 4$ ns.

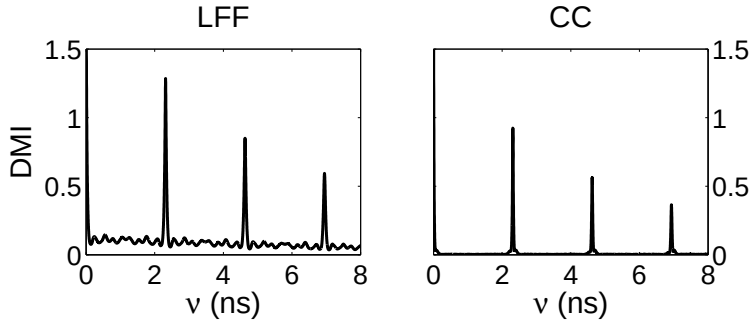

Figure 3.3: The delayed mutual information for the LFF (left) and CC regime (right) of the laser output intensity of an ECSL with two delays $\tau_1 = 2.3$ ns and $\tau_2 = 4.6$ ns.

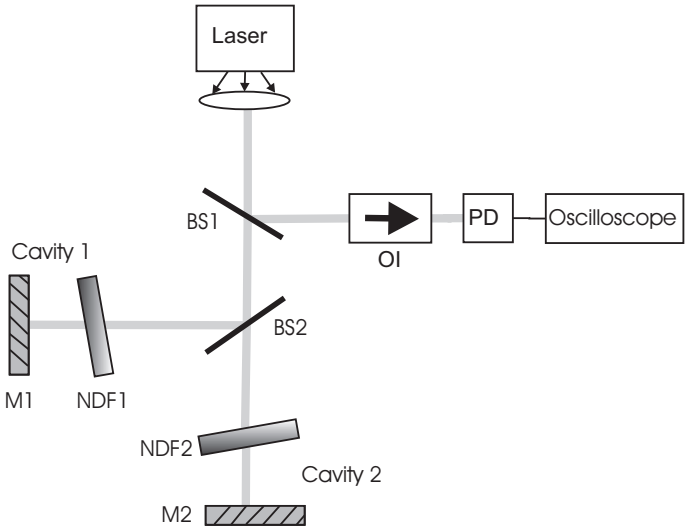

Figure 3.4: Schematic experimental setup of a ECSL with two feedbacks. BS: beam splitter, M:Mirror, OI: optical isolator, NDF: neutral density filter, PD: photodetector.

3.2.3 Experiments

Until now, we have studied the time delay extraction in ECSLs with numerical simulations. Hereafter, we analyze the time delay identification from experimental measurements of a semiconductor laser subject to single and double optical feedback.

The experimental setup is shown schematically in figure 3.4 [Lee et al. 2005]. A Fabry-Perót type diode laser emitting at 1550 nm is used as the optical source. The laser operates at 24.1 °C. The laser threshold current is 12.35 mA. The drive current is 12.5 mA for the case A and 24.7 mA for the case B. The emission of the laser is collimated by an aspheric lens. The system has two external-cavities: Cavity 1 and Cavity 2. The cavities are formed using mirrors M1 and M2. The beam splitter BS1 is used to couple the laser to the photodetector PD. BS2 is used to separate the laser output in two arms for double optical feedback through M1 and M2. The neutral density filters NDF1 and NDF2 are adjusted to give a 3% optical feedback intensity of the laser output for each cavity. The optical isolator OI eliminates back-reflection with a -40 dB isolation. The 12 GHz photodetector PD enables detection of the chaotic laser output at high frequencies. A 20 GS/s oscilloscope is used to record the photodetector outputs. The sampling time of the recorded

time series is 50 ps. Experiments have been performed for different cavity lengths L1 and L2. The experimental time delay has been estimated from the cavity length. More information about the experimental setup can be find in reference [Lee et al. 2005].

First, we study the single delay configuration (only one cavity) with a time delay of $\tau = 2.3$ ns. The intensity time series and the spectra of the cases A and B with single feedback are plotted in figure 3.5. A wider spectrum is obtained for case B (see figure 3.5(b)).

Clearly, the time delay of the system can be estimated as the inverse of the frequency difference between two consecutive peaks of the spectrum. The time delay can be also extracted with the autocorrelation function and the delayed mutual information. Both are depicted in figure 3.6. The biggest peak indicates the estimated time delay of the system $\hat{\tau} = 2.35$ ns for A and B cases. Peaks with decreasing amplitude also appear at multiples of the time delay. The peaks due to the time delay are surrounded for the DMI by small peaks at multiples of $\pm\tau_{RO}/2$. In the AF peaks and valleys are located at multiples of $\tau_{RO}/2$. The relaxation oscillation period (τ_{RO}) is 0.67 ns for case A and 0.2 ns for case B. The effect of τ_{RO} is more noticeable for the case B. These experimental results support the conclusions obtained with the numerical simulations.

Regarding the double delay system, it has been demonstrated with simulations and experiments [Bünner et al. 1998, Lee et al. 2005, Locquet et al. 2006] that the time delay can be extracted with the same methods used to extract the single time delay. Next, we study the identification of the time delay in the double feedback system for the same cases that have been analyzed with numerical simulations in the previous subsection.

The intensity time series and the spectra of an ECSL with two delays, $\tau_1 = 2.3$ ns and $\tau_2 = 4$ ns are plotted in figure 3.7. The intensity time series of one (figure 3.5(a)) and two delays seem similar. Nonetheless, in the two delays case, the spectrum (see figure 3.7(b)) does not yield any conclusion about the time delays of the system. Numerous peaks appear related with both delays and their linear combinations. Therefore, the identification of the time delays from the spectrum is difficult or even impossible in the double delay case. Here, to extract the time delays, other methods as the AF or DMI are necessary. The AF and DMI are shown in figure 3.8. In both cases, the two biggest peaks indicate the two delays of the system. Peaks at the linear combination of both delays also appear, but only the peaks located at $\tau_1 \pm \tau_2$ are noticeable in this case. The numerical results obtained in the previous subsection are in agreement with the experimental ones. However, note that the AF and DMI of the numerical simulations present more peaks due to the

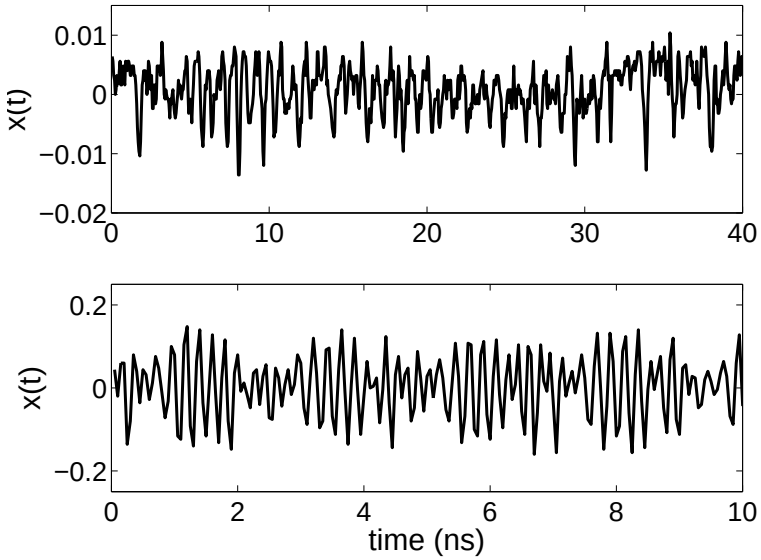

(a) Experimental time series. Top: case A ($I/I_{th} = 1$). Bottom: case B ($I/I_{th} = 2$)

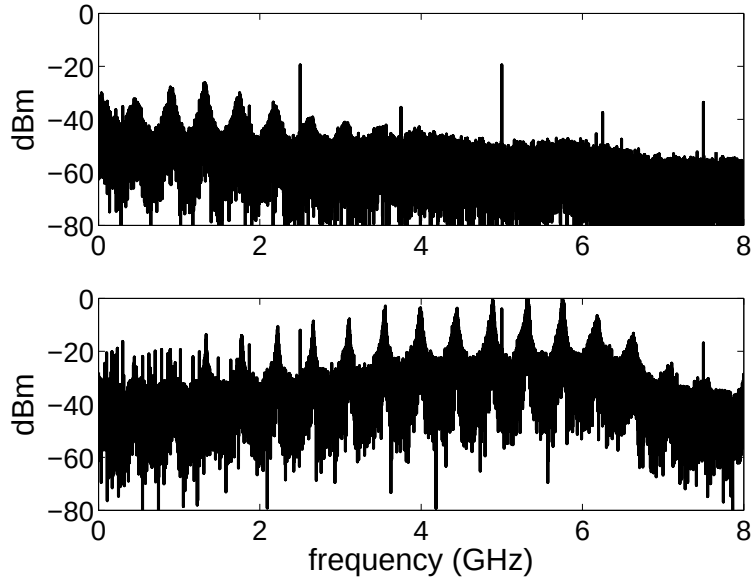

(b) Spectra of the experimental time series. Top: case A ($I/I_{th} = 1$). Bottom: case B ($I/I_{th} = 2$)

Figure 3.5: Experimental intensity time series and spectra of an ECSL with $\tau = 2.3$ ns.

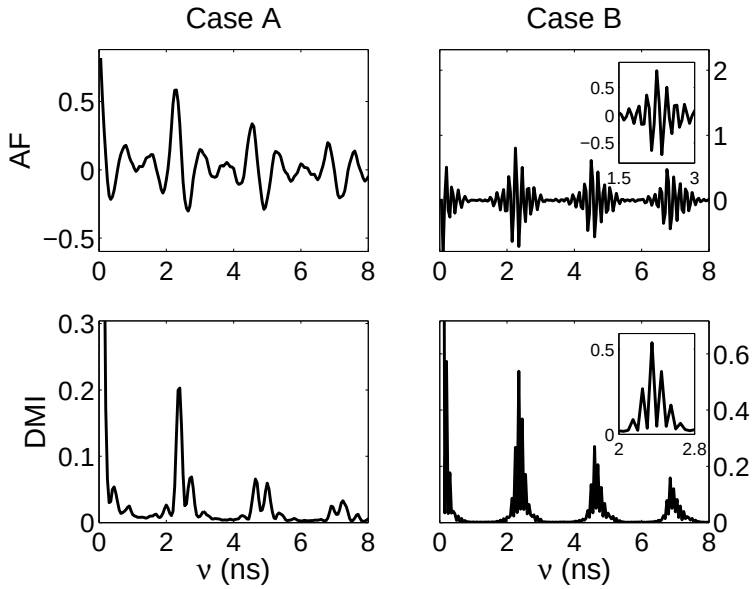

Figure 3.6: Autocorrelation function (top) and the delayed mutual information (bottom) of the experimental time series of an ECSLs with $\tau_1 = 2.3$ ns for case A ($I/I_{th} = 1$) (left) and B ($I/I_{th} = 2$) (right).

linear combinations of both delays. Here, the presence of another type of noise different from spontaneous emission can affect the presence of the linear combination peaks.

Now, we study two special situations, $\tau_2 = 2\tau_1$ ($\tau_1 = 2.3$ ns and $\tau_2 = 4.6$ ns) and $\tau_2 = 3\tau_1$ ($\tau_1 = 2.3$ ns and $\tau_2 = 6.9$ ns). The simulations of these cases have shown that it is not possible to guess the existence of the second delay from the results of the different techniques of identification. However, in the DMI of the experimental time series (plotted in figure 3.9 for case B) the marker located at τ_2 has higher amplitude than the marker at τ_1. This permits to guess the presence and value of both delays. We have checked that similar results are obtained for case A and other identification techniques. The delay located at the higher marker could have a higher feedback rate due to the difficulty to obtain experimentally identical feedbacks rates for both delays.

Finally, we analyze the two time delays identification when both delays are very close. When the two delays are close enough, the peaks located at each time delay converge into a single peak, making difficult or even impossible the distinction between both time delays. To illustrate this point, we plot the DMI

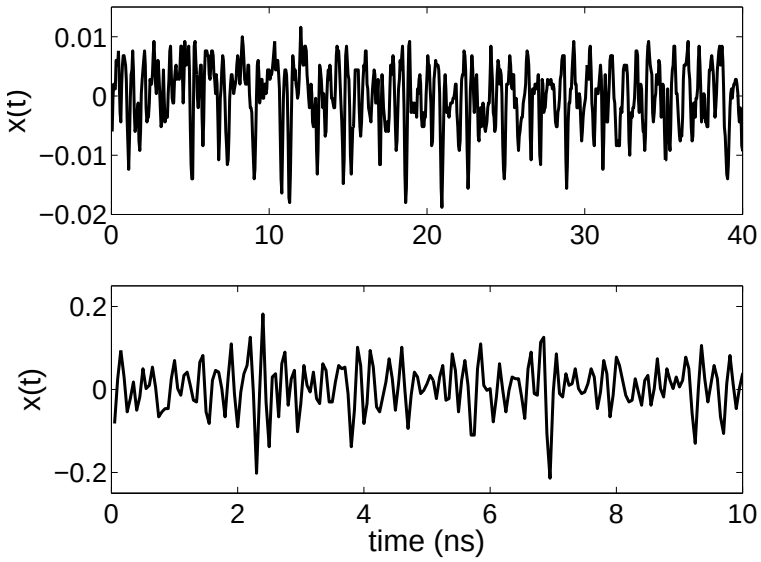

(a) Experimental time series. Top: case A ($I/I_{th} = 1$). Bottom: case B ($I/I_{th} = 2$)

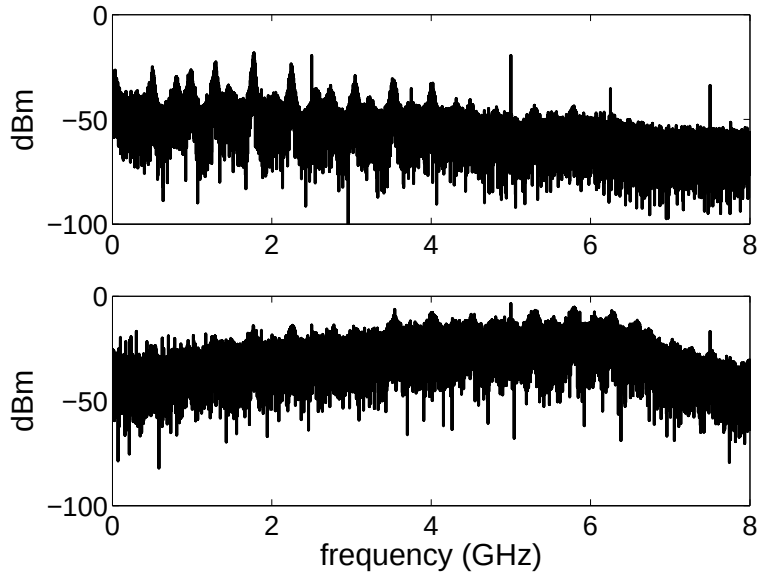

(b) Spectra of the experimental time series. Top: case A ($I/I_{th} = 1$). Bottom: case B ($I/I_{th} = 2$)

Figure 3.7: Experimental intensity time series and spectra of an ECSL with $\tau_1 = 2.3$ ns and $\tau_2 = 4$ ns.

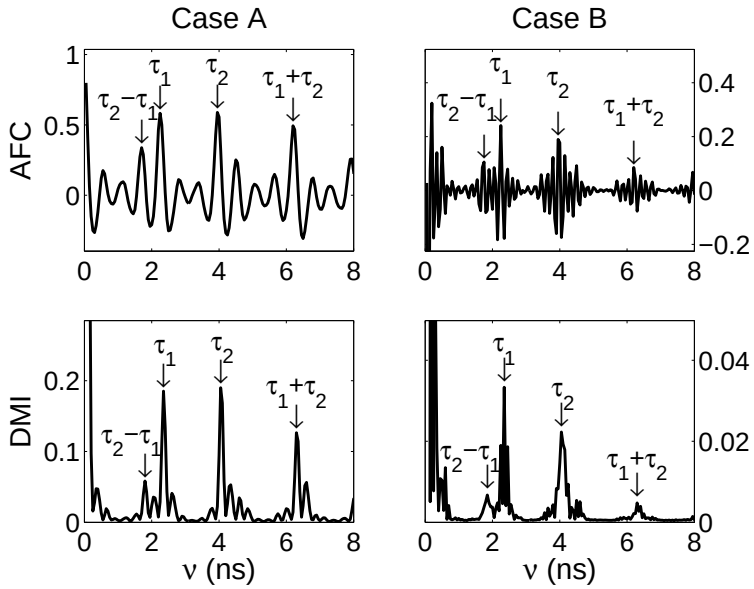

Figure 3.8: Autocorrelation function (top) and the delayed mutual information (bottom) of the experimental time series of an ECSLs with $\tau_1 = 2.3$ ns and $\tau_2 = 4$ ns for case A ($I/I_{th} = 1$) and B ($I/I_{th} = 2$).

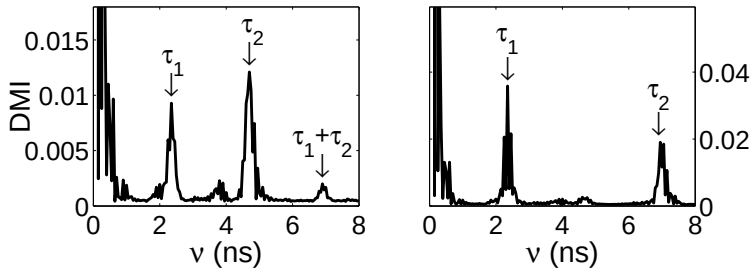

Figure 3.9: Right (Left): Delayed mutual information of the experimental time series of an ECSL with $\tau_1 = 2.3$ ns and $\tau_2 = 4.6$ ($\tau_2 = 6.9$) ns. Case B ($I/I_{th} = 2$).

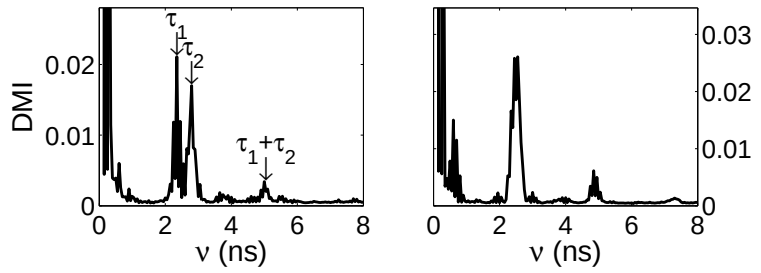

Figure 3.10: Right (Left): Delayed mutual information of the experimental time series of an ECSL with $\tau_1 = 2.3$ ns and $\tau_2 = 2.5$ ($\tau_2 = 2.7$) ns. Case B ($I/I_{th} = 2$).

when $\tau_1 = 2.3$ ns and $\tau_2 = 2.7$ ns for the B case in figure 3.10 (left). Here, both time delays are still identified without problem, although both peaks are very close. However, if $\tau_1 = 2.3$ ns and $\tau_2 = 2.5$ ns (figure 3.10 (right)), both peaks have converged into a single one. Evidently the possibility to distinguish both delays is subordinated to the sampling rate of the time series. If we increase the sampling period to 100 ps, it is impossible to distinguish the two peaks even with $\tau_1 = 2.3$ ns and $\tau_2 = 2.7$ ns. Comparable results and conclusions are obtained with other identification techniques.

3.2.4 Low feedback rates

Until recently, ECSLs with a single optical feedback were considered as weakly secure systems in terms of time-delay identification. In the previous section, we have demonstrated that the time delays can be extracted with standard techniques in the case of single and double delay feedback. However, it has been shown recently that a simple ECSL with a single optical feedback could, with a careful choice of parameters, hide its time-delay when standard methods are employed [Rontani et al. 2007].

The time delay identification in ECSLs strongly depends on the operational parameters of the ECSL, specially on the feedback rate, κ. The feedback rate controls the optical power reinjected in the laser cavity. As a result, it drives the contribution of the delayed intensity $I(t-\tau)$ in the time-evolution of $I(t)$. Therefore, the stronger the feedback rate, the more important the information shared between $I(t-\tau)$ and $I(t)$ will be. At large feedback rates, the time delay can be estimated with standard identification techniques (see previous subsections). However, when the feedback rate is weak, a large variety of scenarios has been reported [Rontani et al. 2009]. These scenarios are largely

dependent on the choice of the pumping factor, p, as well as the choice of the time-delay value in comparison with the relaxation oscillation period τ_{RO}. Two scenarios that difficult the time delay identification have been found. First, for low feedback rates and significant separation between τ and τ_{RO}, the presence of peaks or troughs at multiples of $\tau_{RO}/2$ makes the identification difficult. Second, when the feedback rates are low and the values of τ and τ_{RO} are close. In this case, it has been proved that it is not possible to identify the time delay by the DMI or the AF [Rontani et al. 2007; 2009]. No significant peak appears close to the delay value in the autocorrelation function or in the delayed mutual information.

These difficult identifications find their origin in the specific nonlinear dynamics and timescales appearing in the ECSL in its bifurcation cascade leading to chaos. Indeed, at weak feedback rates the chaos keeps reminiscence of the time-scales involved in the early stage of the laser dynamics, such as the undamped relaxation oscillation time-scale and possibly period-doubling and quasi-periodic dynamics. The time-delay estimators then exhibit complex modulated shapes showing these different laser dynamics timescales [Rontani et al. 2009].

In this subsection, we discuss the robustness of the time-delay concealment in the second scenario. The simulations have been carried out with the equations and parameters values presented in [Rontani et al. 2009]. The equations that rule the ECSL are basically the same as the equations described by (3.9). The parameters values of the system are: $\alpha = 5$, $g = 7.5 \times 10^{-6}$ ns^{-1}, $N_t = 3 \times 10^8$, $\varepsilon = 2.5 \times 10^{-7}$, $k = 500$ ns^{-1}, $\gamma_e = 0.5$ ns^{-1} and $\beta_{sp} = 2 \times 10^{-6}$.

First, we consider the case of a feedback strength, $\kappa = 2$ GHz, $\tau = 1$ ns and $\tau_{RO} = 0.75$ ns. The autocorrelation function and the delayed mutual information for this case are depicted in figure 3.11(a) (top). The valley (peak) with maxima amplitude in the AF (DMI) is positioned at $\tau_{RO}/2$. We do not observe any significant peak at the time delay value. Other identification techniques have been tested and do not give more insight about the time-delay value. For example, we plot in figure 3.11(a) (bottom) the results given by the forecasting error of a global nonlinear model and the analysis of time extrema distribution. The global nonlinear model consists on a modular neural network with two modules: the non-feedback module has only one linear neuron and the feedback module is a FFNN(6:3). The inputs for the non-feedback and feedback modules are $I(t - \tau_e)$ and $(I(t - \nu + \tau_e), I(t - \nu), I(t - \nu - \tau_e))$, respectively. The embedding time, τ_e, is 5 ps.

Now, we increase the feedback rate to $\kappa = 5$ GHz. As in the previous case, the time delay can not be inferred from the autocorrelation function, the delayed mutual information or the forecasting error of a global nonlinear

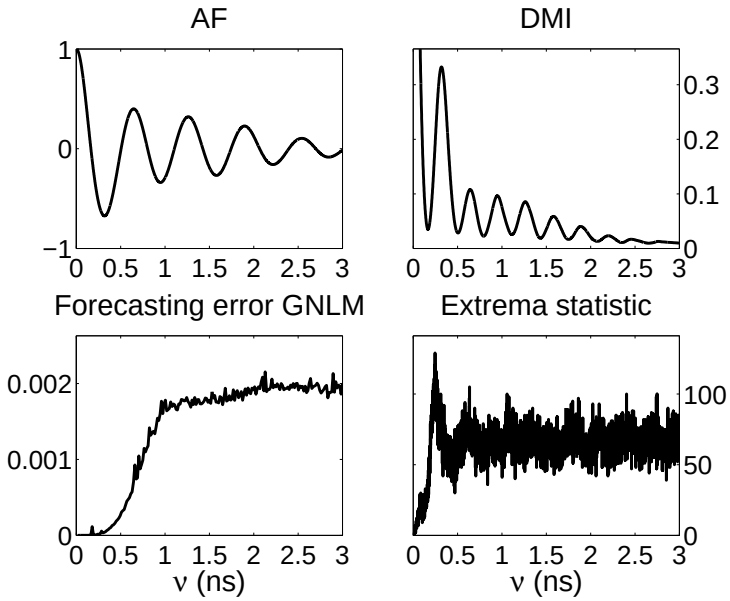

(a) $\gamma = 2$ GHz

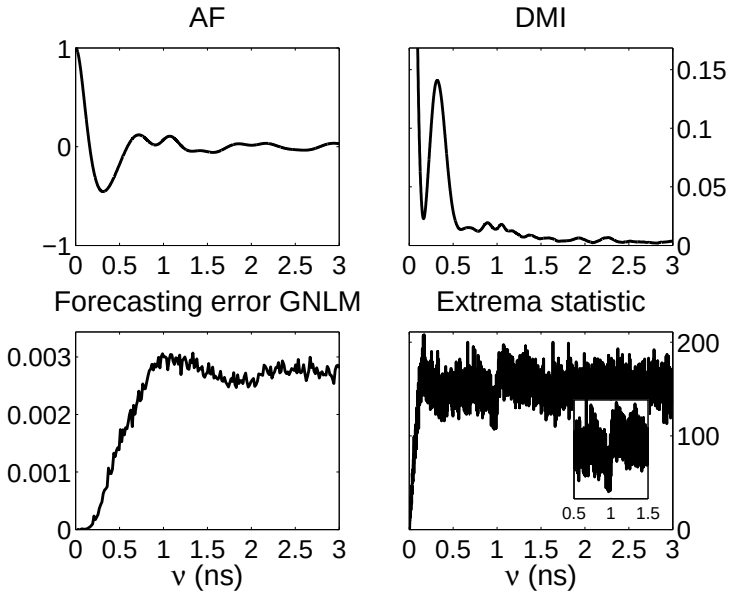

(b) $\gamma = 5$ GHz

Figure 3.11: Autocorrelation function (AF), Delayed mutual information (DMI), forecasting error of a global nonlinear model (GNLM) and analysis of time distribution of extrema of an ECSL with $\tau = 1$ ns and $\tau_{RO} = 0.75$ ns.

model (see figure 3.11(b)). Only a valley (peak) at $\tau_{RO}/2$ appears in the AF (DMI) as in the previous case. However, the analysis of time series extrema shows a small minimum at the time delay value. Therefore, as the feedback rate is increased, the first method that shows the time delay is the statistics of the time interval between extrema. It retrieves the time delay value for low feedbacks rates where the other methods fail.

In conclusion, it has been shown that independently from the method of identification, if the operational parameters of the ECSL are carefully chosen, the time-delay signature remains hidden. The low feedback rate is a critical condition. The parameter set that avoids the time delay identification is limited to a small range with very low feedback rates, low pumping rates and a close relationship between τ and τ_{RO}. This parameter choice yields a chaotic regime that is close to the regular one. In principle, this is not the most suitable regime for secure optical communications.

3.2.5 Conclusions

It has been shown, that the time delays of an ECSL with single or double feedback can be extracted from numerical and experimental time series using standard identification techniques when the system has large feedback rates. In this case, we have demonstrated that the estimated time delay with different techniques is similar.

At large feedback rates, the time delay identification is only ambiguous when two cavities are considered and both delays are multiples or have close values. If both delays are close enough, the markers that identify the two delays can converge into a single one. The minimum distance between delays to avoid this situation depends on the sampling time of the time series. In these cases, close and multiples time delays, the relevance of both delays in the reconstruction of the nonlinear dynamics has to be addressed. The proximity or relationship of both delays can make possible the nonlinear reconstruction knowing only the approximate time delay given by the identification techniques.

At low feedback rates, the time delay identification can be compromised. A careful choice of a low feedback rate, low pumping power and small distance between τ_{RO} and τ avoid the time delay identification with the standard techniques. However, the range of parameters that conceals the time delay extraction is very small. Moreover, in spite of the successful time delay concealment, the complexity of the chaos (dimensions and entropy) generated in this case is not very suitable for secure optical communications.

3.3 Semiconductor lasers with optoelectronic feedback

In the optoelectronic feedback system the laser operates in the linear regime. Therefore, the laser dynamics can not be used to hide the time delay as in the all optical case. However, the entropy of systems with optoelectronic feedback increases with the feedback strength, whereas it saturates for all-optical feedback systems [Vicente et al. 2005] (see chapter 2, section 2.4). Hence, the behavior might be more unpredictable for chaotic carriers based on optoelectronic feedback.

In spite of the high nonlinearity that can reach the semiconductor laser subject to a single optoelectronic feedback, the time delay can be easily retrieved from the time series with the standard techniques. In this section we particulary study the effect of the nonlinearity and the response time of the system on the time delay identification. Following the trail of the all optical feedback system, we also analyze if the inclusion of additional delays can difficult the time delay identification. We study two different double delay implementations, serial and parallel. In both cases, we extract the time delay, although the serial configuration requires the employment of more elaborated methods to identify both time delays.

This section is structured as followed. In subsection 3.3.1 we analyze the time delay identification of a single optoelectronic feedback system for different response times and nonlinearity strengths of the system. In subsection 3.3.2 we study the effect of the noise on the time delay identification. Subsection 3.3.3 is devoted to the time delay extraction with double feedback for two different configurations, serial and parallel. Finally, conclusions are presented in section 3.3.4.

3.3.1 One delay systems

We study the time delay identification in a semiconductor laser subject to a single optoelectronic feedback. The system can be modelled by the well-known Ikeda delay differential equation [Goedgebuer et al. 1998a;b, Vicente et al. 2005]:

$$T\dot{x}(t) = -x(t) + \beta \sin^2(x(t-\tau) - \phi) \tag{3.11}$$

where T is the response time or the finite reaction time of the system, β is the nonlinearity strength as well as the feedback strength, τ is the time delay and ϕ is the phase shift. The feedback strength is a particularly interesting param-

eter because both the entropy of the chaotic signal and the dimension of the chaotic attractor increase with β [Vicente et al. 2005]. System configurations that correspond to large values of β are therefore particularly interesting for encryption purposes.

The equation (3.11) is simulated with an Adams Moulton predictor corrector scheme [Press et al. 1992] and a time integration step of 0.01. To study the effect of the nonlinearity strength and the response time of the system on the time delay identification, we carry out numerical simulations of the equation (3.11) with $\beta = 5$ (low nonlinearity strength) and $\beta = 50$ (high nonlinearity strength), for $T = 1$ and $T = 40$. The phase and the time delay are always $\phi = 0.26\pi$ and $\tau = 100$. We have checked that our results hold for different phase shifts and time delays.

The length of the time series is one million points, sampled at $T/100$, where T is the response time of the system. This sampling time ensures that the discretization reproduces faithfully the characteristics of the continuous-time system even for $\beta = 50$. The dynamics of the system is faster for high nonlinearities and low response times (see figure 3.12). However, both values of β, 5 and 50, are studied using the same sampling time, although the dynamics of $\beta = 5$ can be faithfully reproduced with a larger sampling time. We will follow a similar approach to analyze the experimental data (see section 3.4). In figure 3.12 the numerical simulated time series are plotted. Note that the mean value and the standard deviation increase with the nonlinearity strength of the system.

Hereafter, we apply the different methods described in section 3.1 to identify the time delay of the system ruled by equation (3.11). The estimated time delay, $\hat{\tau}$, by the different methods is presented in table 3.1. The time delay is estimated by the position of the peak (or valley) with maximum (minimum) amplitude. Peaks (or valleys) with decreasing amplitudes also appear at multiples of $\hat{\tau}$. The amplitude of these markers (peaks or valleys) decreases with increasing nonlinear strengths. This can lead to the disappearance of the markers at the integer multiples of the time delay for high nonlinearity strengths. However, it has been tested that the marker at τ does not disappear even for $\beta = 100$.

The first methods applied to identify the delay are the delayed mutual information and the autocorrelation of the time series (plotted in figure 3.13). The AF only takes into account linear correlations between $x(t)$ and $x(t-\nu)$. When the system is highly nonlinear ($\beta = 50$), no trace of the time delay is found in the autocorrelation function (see figure 3.13(a) (b_1 and b_2)).

As we can observe from table 3.1, the AF and the DMI always overestimate the time delay of the system. This is due to the response time of the system,

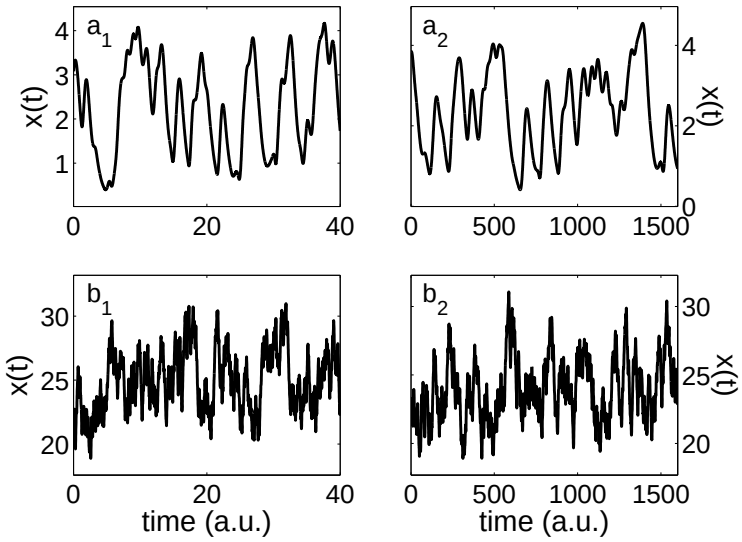

Figure 3.12: Time series of a semiconductor laser subject to optoelectronic feedback. The system is ruled by equation (3.11) with parameters $\tau = 100$ and $\phi = 0.26\pi$. a_1: $\beta = 5$ and $T = 1$. a_2: $\beta = 5$ and $T = 40$. b_1: $\beta = 50$ and $T = 1$. b_2: $\beta = 50$ and $T = 40$.

	$T = 1$		$T = 40$	
	$\beta = 5$	$\beta = 50$	$\beta = 5$	$\beta = 50$
AF	100.5	-	181.2	-
DMI	100.4	100.06	116	102.4
FF	100	100	100	100
TDE	100	100	100	100
GLM	100	-	100	-
GNLM	100	100	100	100

Table 3.1: Estimated time delay from the numerical time series by different techniques. The time delay is $\tau = 100$.

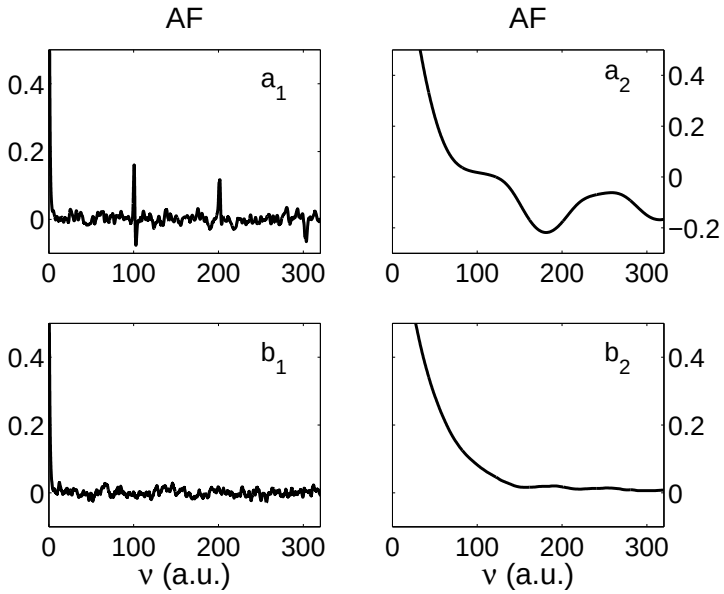

(a) Autocorrelation Function

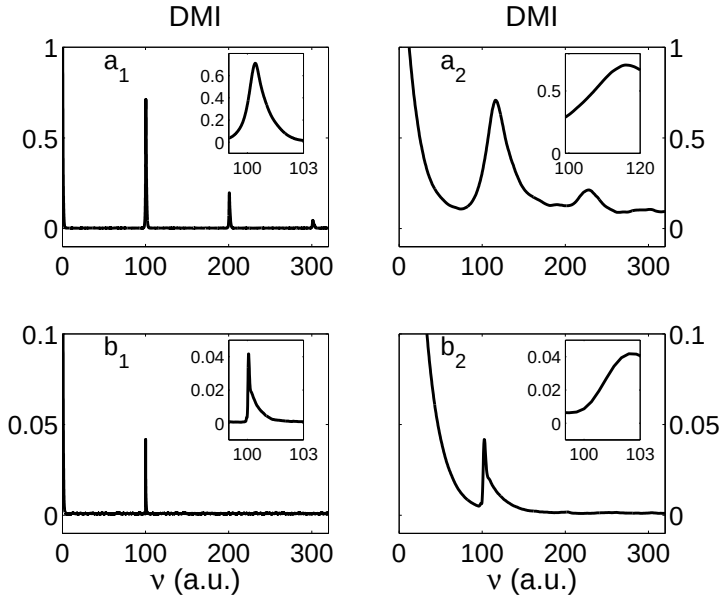

(b) Delayed Mutual Information

Figure 3.13: The parameters of the system are $\tau = 100$ and $\phi = 0.26\pi$. a_1: $\beta = 5$ and $T = 1$. a_2: $\beta = 5$ and $T = 40$. b_1: $\beta = 50$ and $T = 1$. b_2: $\beta = 50$ and $T = 40$.

T. The overestimation is more noticeable for low nonlinearities strengths. In these cases, the estimated time delay is approximately $\hat{\tau} \simeq \tau + T/2$. For higher β, the nonlinear dynamics rules the system and the effect of the linear dynamics (governed by the response time) is less appreciable. Therefore, when the response time is small compared to the time delay of the system, as in the all optical system, the overestimation can be neglected. However, when the response time is comparable with the time delay, the AF and the DMI are not suitable techniques to extract the time delay.

Other techniques, as the filling factor method or the statistics of the time interval between extrema do not overestimate the time delay due to T (see figure 3.14). However, both methods require an accurate localization of the extrema of the time series to obtain $\hat{\tau} = \tau$ (see table 3.1). The accurate localization of the extrema can be difficult when the system is affected by noise and/or the sampling time is too large. In the filling factor method, if we evaluate the complexity of the trajectory in the space $(x(t), x(t-\nu))$, (taking into account all the points not only the extrema), the results are comparable to the ones obtained from the DMI.

Finally, the time delay can be also retrieved from the forecasting error of a model. We have used simple global linear and nonlinear models. The global linear model is basically a least squared fitting. The global nonlinear model is a modular neural network, MNN(2:2) (see chapter 4 for more details about the MNN). In both cases the inputs of the models are $x(t)$, $x(t-\nu-\delta t)$,$x(t-\nu)$,$x(t-\nu+\delta t)$, where δt is the sampling time. The error is evaluated under variations of ν. A minimum appears at the value of the time delay. Nonetheless, the global linear model, as the AF, can only identify the time delay for low nonlinearity strengths (see table 3.1). A global nonlinear model is necessary to extract the time delay of highly nonlinear system (see figure 3.15).

Let us point out that, as general rule, we try to use the simpler model capable to identify the time delay in order to reduce the computational time. This factor is particulary important for the global nonlinear models. To reduce the long computational times of global nonlinear models, this method can be used in combination with a faster one (as the DMI), to reduce the searching range. Furthermore, it is also worth mentioning that we have also used modular neural networks to reconstruct the nonlinear dynamics of optoelectronic feedback systems (see chapter 4).

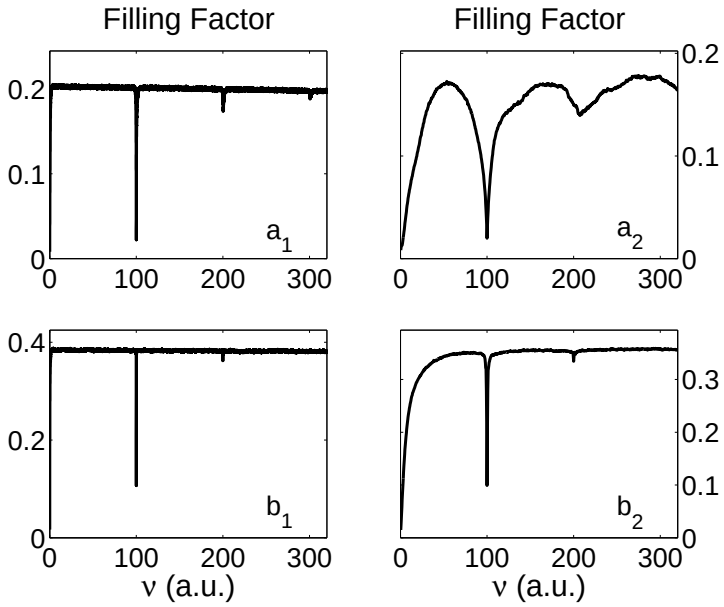

(a) Filling Factor

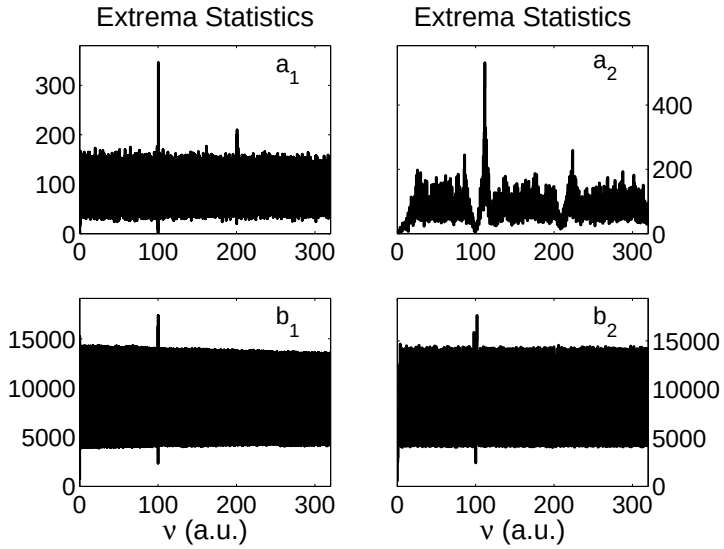

(b) Time distribution of extrema

Figure 3.14: The parameters of the system are $\tau = 100$ and $\phi = 0.26\pi$. a_1: $\beta = 5$ and $T = 1$. a_2: $\beta = 5$ and $T = 40$. b_1: $\beta = 50$ and $T = 1$. b_2: $\beta = 50$ and $T = 40$.

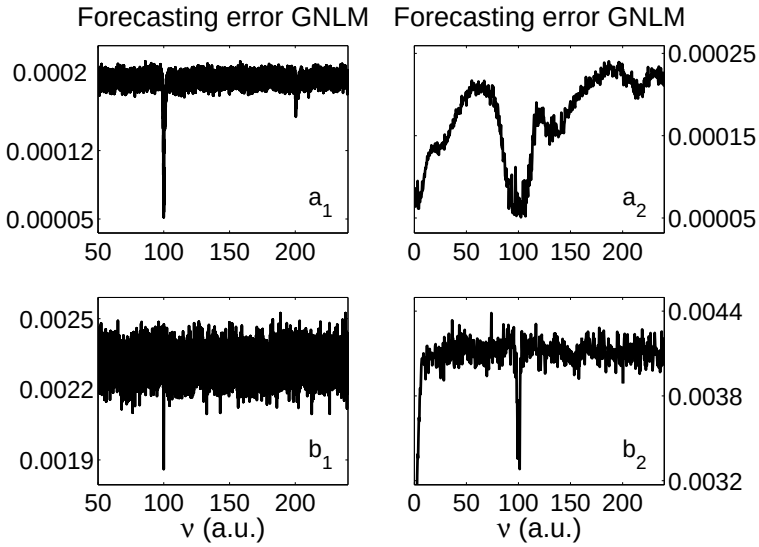

Figure 3.15: Forecasting error of a global nonlinear model that consists on a MNN(2:2). The parameters of the system are $\tau = 100$ and $\phi = 0.26\pi$. a_1: $\beta = 5$ and $T = 1$. a_2: $\beta = 5$ and $T = 40$. b_1: $\beta = 50$ and $T = 1$. b_2: $\beta = 50$ and $T = 40$.

3.3.2 Robustness of the time delay identification

The results presented in the previous subsection have been obtained from a free noise system, with long time series and sampling times that ensure a faithful capture of the system dynamics. Nonetheless, when some of the above conditions are not fulfilled, the estimation of the time delay can be difficult.

To study the performance of the identification techniques described in section 3.1 in presence of noise, a white gaussian noise is added to the time series. The white gaussian noise has zero mean and its standard deviation is the noise amplitude. Its autocorrelation function is a delta function centered at $\nu = 0$. Hence, the effect of this type of noise is negligible on the autocorrelation function or the delayed mutual information, even for high noise amplitudes.

By contrast, under moderate noise levels, the time delay estimated by the filling factor method and the statistics of extrema is overestimated by the response time of the system, given similar results as the DMI. The FF and TDE evaluate the extrema of the time series to extract the time delay. The overestimation is due to the spurious extrema that appear in the time series induced by the noise. In the case of the analysis of the extrema statistics, these spurious extrema increase the intervals of extrema separated by the time delay.

This leads to the disappearance of the minimum at τ. To a certain point, this effect can be counteracted with longer time series to improve the statistics.

A possible solution is filtering the noise of the time series. Under moderate noise amplitude it is possible to smooth the time series and use the smoothed time series to calculate the filling factor and the statistics of the interval between extrema. This technique works well under low and moderate noise levels (see section 3.4). Otherwise, the extrema of the smoothed time series do not correspond to the original extrema points.

The forecasting error of a global model is the unique method of those studied before that in presence of moderate noise levels does not overestimate the time delay of the system due to the response time. However, models with more parameters and training points are required to estimate the time delay in presence of noise. This yields longer computational times.

Other points to take into account in the estimation of the time delay from a time series are the length and the sampling time of the time series. In general, the shorter time series, the lower amplitude has the markers that identify the time delay. Furthermore, the filling factor and the analysis of the interval between extrema are not the best options to identify the time delays from short time series. These methods only evaluate the extrema of the time series, then short time series reduces the statistic of extrema. Regarding the sampling of the time series, it is possible to identify the time delay from time series sampled so that they do not reproduce faithfully the characteristics of the continuous-time system. Evidently, the accuracy of the time delay depends on the sampling time. The error in the time delay estimation can not be lower than the sampling time.

3.3.3 Two-delay systems

Optoelectronic systems with multiples delays have been proposed to increase the security of the system [Lee et al. 2004]. In the following, we investigate whether the additional delays can difficult the time delay extraction in the optoelectronic system.

The two-delay chaotic generator used in this work can be modelled by the following delay differential equation,

$$x(t) + T\frac{dx(t)}{dt} = G(x(t-\tau_1), x(t-\tau_2)) \tag{3.12}$$

where $x(t)$ is the dynamical variable, τ_1 and τ_2 are the time delays, G is a nonlinear function and T is the response time of a low pass filter which limits the dynamics of the system. This equation can also describe the generator

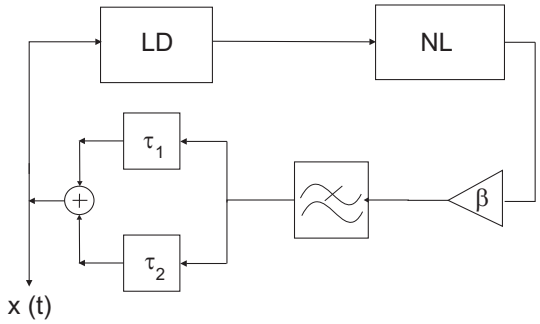

(a) Serial configuration

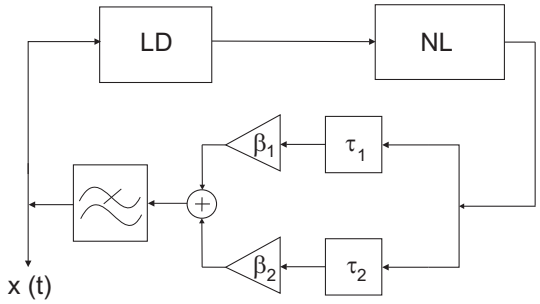

(b) Parallel configuration

Figure 3.16: Block diagram of a chaotic generator with two delays. The elements of system are the Laser Diode [LD], the nonlinear element [NL], the delay lines [τ_1 and τ_2], the amplifier [β] and the low pass filter.

of wavelength chaos reported in [Goedgebuer et al. 1998a;b, Larger et al. 1998a;b], but with some additional feedback loops.

Two different configurations, serial and parallel, regarding the way the nonlinear function is applied to the delayed terms are considered. The block diagrams of both configurations are presented in figure 3.16.

In the parallel configuration the nonlinear function is applied to each delayed term separately:

$$G_p[x(t-\tau_1), x(t-\tau_2)] = \beta_1 \sin^2\left(x(t-\tau_1) - \phi_1\right) + \beta_2 \sin^2\left(x(t-\tau_2) - \phi_2\right) \tag{3.13}$$

By contrast, in the serial configuration the nonlinear function is applied to the sum of the delayed terms,

$$G_s[x(t-\tau_1), x(t-\tau_2)] = \beta \sin^2\left(x(t-\tau_1) + x(t-\tau_2) - \phi\right) \tag{3.14}$$

In both cases, the parameter β determines the strength of the feedback as well as the strength of the nonlinearity, τ_1 and τ_2 are the delays of the system and ϕ is the phase shift.

When both time delays take similar values, $\tau_1 \approx \tau_2 \approx \tau$, in the parallel configuration the nonlinear function can be written as $G_p = (\beta_1+\beta_2)\sin^2(x(t-\tau))$. In the serial case, $x(t)+T\dot{x}(t) = \beta \sin^2(2x(t-\tau))$ and defining a variable $y(t) = 2x(t)$ we obtain a new differential equation, $y(t) + T\dot{y}(t) = 2\beta \sin^2(y(t-\tau))$. Therefore, in the two delays case, the upper bond of the effective nonlinear strength is approximately 2β when $\beta_1 = \beta_2 = \beta$. Likewise, regarding the entropy of the system, both configurations have the same entropy when $\phi_1 = \phi_2 = \phi$. In the parallel configuration the entropy is the same when $\phi_1 - \phi_2 = 0 = \pi/2$ and slightly higher if $\phi_1 - \phi_2 = \pi/4$ [Pazó 2009].

The simulations of the equation (3.12) have been carried out using the Adams-Bashforth-Moulton predictor-corrector scheme [Press et al. 1992] with a time integration step of 0.01 for both configurations (the same as in the one delay case). The time series of both configurations with parameters $\beta_1 = \beta_2 = \beta = 15$, $\tau_1 = 100$ and $\tau_2 = 215$ are plotted in figure 3.17. The system is working in the chaotic regime for the chosen parameters. The mean and the variance of x are higher for the parallel case.

Parallel configuration

The parallel configuration with two feedback loops have been experimentally implemented using coherence modulation techniques [Lee et al. 2004].

In the parallel configuration it is possible to extract the delays using the same techniques employed for single delay systems [Prokhorov et al. 2005, Siefert 2007]. For example, we plot in figure 3.18 the delayed mutual information and the filling factor when $\phi_1 = \phi_2 = 0.26\pi$, $\beta_1 = \beta_2 = 15$, $\tau_1 = 100$ and $\tau_2 = 215$ (there is not a rational relationship between τ_1 and τ_2). Two peaks (valleys) of approximately the same amplitude appear in the DMI (FF) at the value of the time delays τ_1 and τ_2. An additional peak (valley) emerges at $\tau_2 - \tau_1$. Its amplitude respect to the markers at τ_1 and τ_2 depends of the method of identification. Comparable results are obtained with the rest of the identification techniques.

Now, let us explain the presence of the peak at $\tau_2 - \tau_1$. For the sake of clarity, we consider $T = 0$. Then the delay differential equation for the parallel configuration can be written as:

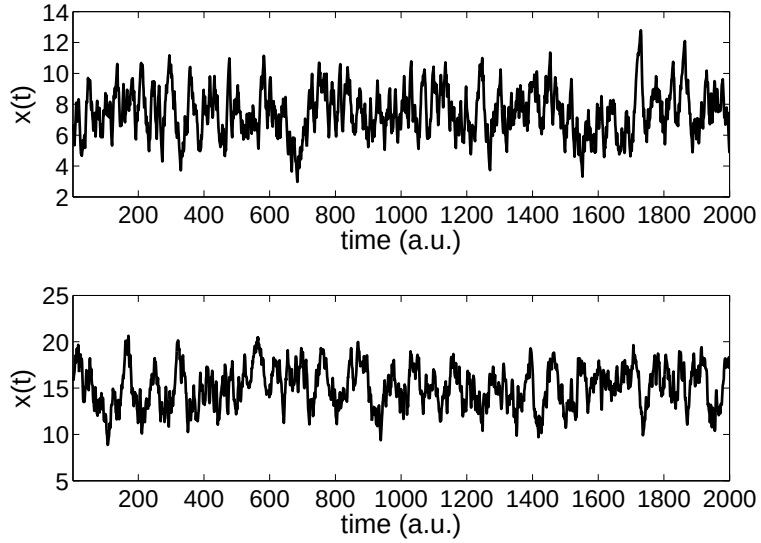

Figure 3.17: The time series for serial (top) and parallel (bottom) configurations. The parameters of the chaotic generator are $T = 1$, $\beta_1 = \beta_2 = \beta = 15$, $\phi_1 = \phi_2 = \phi = 0.26\pi$, $\tau_1 = 100$ and $\tau_2 = 215$. The sampling time is 0.01.

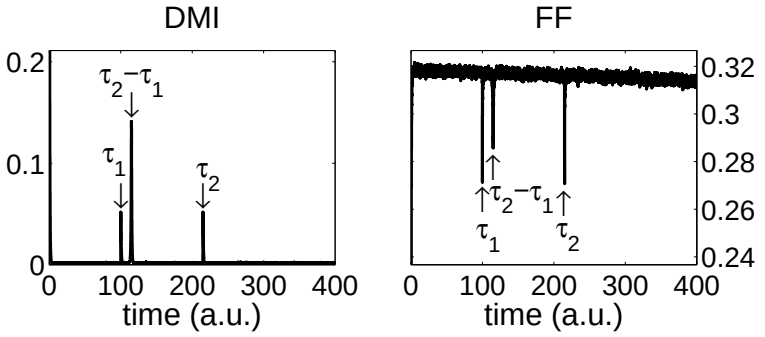

Figure 3.18: The mutual delayed information (left) and the filling factor (right) of an optoelectronic feedback system with two delays in the parallel configuration. The parameters of the system are $\beta_1 = \beta_2 = 15$, $\phi_1 = \phi_2 = 0.26\pi$, $T = 1$, $\tau_1 = 100$ and $\tau_2 = 215$.

$$x(t) = \beta_1 f_1(x(t-\tau_1)) + \beta_2 f_2(x(t-\tau_2)) \tag{3.15}$$

Next, we evaluate this equation at time $(t-(\tau_2-\tau_1))$:

$$x(t-(\tau_2-\tau_1)) = \beta_1 f_1(x(t-\tau_2)) + \beta_2 f_2(x(t-2\tau_2+\tau_1)) \tag{3.16}$$

Equating $x(t-\tau_2)$ from (3.15) and inserting in (3.16), $x(t-(\tau_2-\tau_1))$ and $x(t)$ are related by:

$$x(t-(\tau_2-\tau_1)) = \beta_2 f_2(x(t-(2\tau_2-\tau_1))) + \beta_1 f_1[f_2^{-1}(\frac{x(t)}{\beta_2} - \frac{\beta_1}{\beta_2} f_1(x(t-\tau_1)))] \tag{3.17}$$

When $f_1 = f_2 = f = \sin^2$ and $\phi_2 = \phi_1$, equation (3.17) can be expressed as:

$$x(t-(\tau_2-\tau_1)) = \beta_2 f(x(t-(2\tau_2-\tau_1))) + x(t)\frac{\beta_1}{\beta_2} - \frac{\beta_1}{\beta_2} f(x(t-\tau_1)) \tag{3.18}$$

demonstrating that exits a linear relationship between $x(t)$ and $x(t-(\tau_2-\tau_1))$, that cause the appearance of the peak (valley) at $(\tau_2-\tau_1)$ in the DMI (FF).

Another interesting scenario might be when $\phi_2-\phi_1$ is $\pi/2$ or $\pi/4$. When $\phi_2-\phi_1 = \pi/2$, $f_1 = 1-f_2$. Replacing this in equation (3.17), also appears a linear relationship between $x(t)$ and $x(t-(\tau_2-\tau_1))$:

$$x(t-(\tau_2-\tau_1)) = -\frac{\beta_1}{\beta_2}x(t) + \frac{\beta_1^2}{\beta_2} f_1(x(t-\tau_1)) + \beta_1 + \beta_2 f_2(x(t-2\tau_2+\tau_1)) \tag{3.19}$$

Therefore, the DMI when $\phi_2-\phi_1$ is $\pi/2$ (see figure 3.19 (left)) is very similar to the case $\phi_2-\phi_1 = 0$ (see figure 3.18 (left)) and a clear peak appears at $(\tau_2-\tau_1)$. However, when $\phi_2-\phi_1 = \pi/4$, there is not a linear relationship between $x(t)$ and $x(t-(\tau_2-\tau_1))$. In this case the DMI does not show any peak at $(\tau_2-\tau_1)$ (see figure 3.19 (right)). These conclusions hold for other techniques used to identify the time delay.

On the other hand, the behavior respect to the nonlinearity strength is the same as in the one delay case (increasing nonlinearities imply sharper and small markers). In the optoelectronic feedback system with the parallel configuration we can also analyze what happens if the nonlinear strength is different for both delays. To illustrate our results we use the DMI, but all the

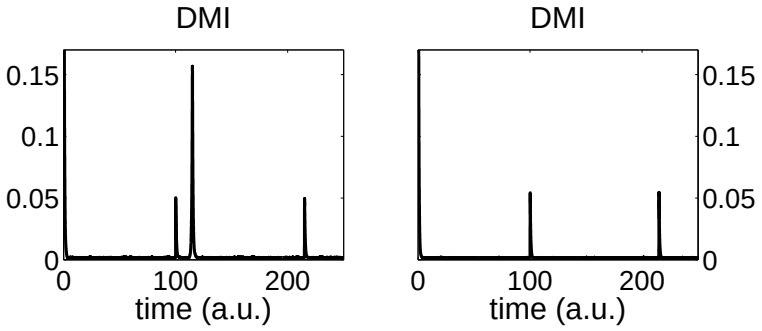

Figure 3.19: The mutual delayed information of a optoelectronic feedback system with two delays in the parallel configuration. Right (Left): $\phi_2 - \phi_1 = \pi/4(\pi/2)$. The rest of the parameters of the system are $\beta_1 = \beta_2 = 15$, $T = 1$, $\tau_1 = 100$ and $\tau_2 = 215$.

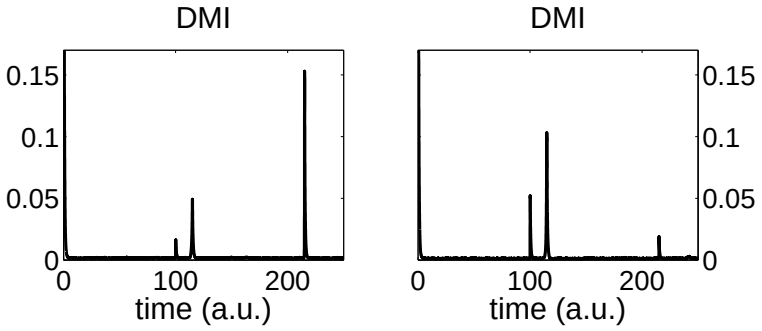

Figure 3.20: The delayed mutual information of a optoelectronic feedback system in the parallel configuration. Right (Left): $\beta_2 = 25\,(5)$. The rest of the parameters of the system are $\beta_1 = 15$, $T = 1$, $\phi_2 = \phi_1 = 0.26\pi$, $\tau_1 = 100$ and $\tau_2 = 215$.

identification techniques described in this thesis lead to the same conclusions. We show in figure 3.20 the DMI when $\beta_1 = 15$, and $\beta_2 = 5$ and 25. Just as expected, the peak associated with the time delay with lower (higher) nonlinearity strength increases (decreases) its amplitude.

Finally, we also study the time delay identification when both delays are integers multiples ($\tau_2 = 2\tau_1$) and have a similar value ($\tau_2 \approx \tau_1$). The delayed mutual information for these two cases is depicted in figure 3.21. When both delays are close enough the two peaks that indicate the time delays converge into a single peak. The DMI of the one and two delays case when $\tau_2 = 2\tau_1$ are qualitatively similar (compared figures 3.13(b) and 3.21 (left), respectively).

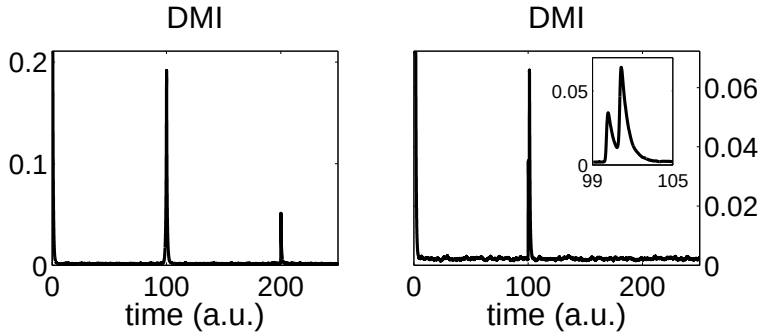

Figure 3.21: The delayed mutual information of a optoelectronic feedback system in the parallel configuration. Right (Left): $\tau_2 = 101\,(200)$. The rest of the parameters of the system are $\beta_1 = \beta_2 = 15$, $T = 1$, $\phi_2 = \phi_1 = 0.26\pi$ and $\tau_1 = 100$.

To sum up, we have found that the conclusions obtained for the identification of the two delays in the optoelectronic system with parallel configuration are similar to ones obtained for the all optical feedback system with two delays. In both cases the time delays can be retrieved with the same standard techniques that work for the one delay case. Likewise, peaks at linear combinations of both time delays appear. In the optoelectronic case, the main peak due to the linear combination of both delays is located at $\tau_2 - \tau_1$, while in the all optical case the main linear combination correspond to $\tau_1 + \tau_2$.

Through this subsubsection, the results have been illustrated with the delayed mutual information. Similar results are obtained with other methods of identification. Moreover, in the two-delay case we have checked that the effect of the response time is the same as in the one delay case.

Serial configuration

The time delays of the optoelectronic system with double feedback in the serial configuration can be extracted with the standard methods when the nonlinearity strength of the system is low (for example $\beta = 5$). When the nonlinearity strength increases, the standard procedures to identify the time delays start to fail. For $\beta = 15$ it is not possible to identify the time delays with the delayed mutual information, the forecasting error of a global nonlinear model or local linear models [Locquet et al. 2006]. The filling factor method and the analysis of the extrema distribution show small markers located at the time delays of the system (see figure 3.22 (top)). However, the time delay identification with these methods is not robust. Low noise levels,

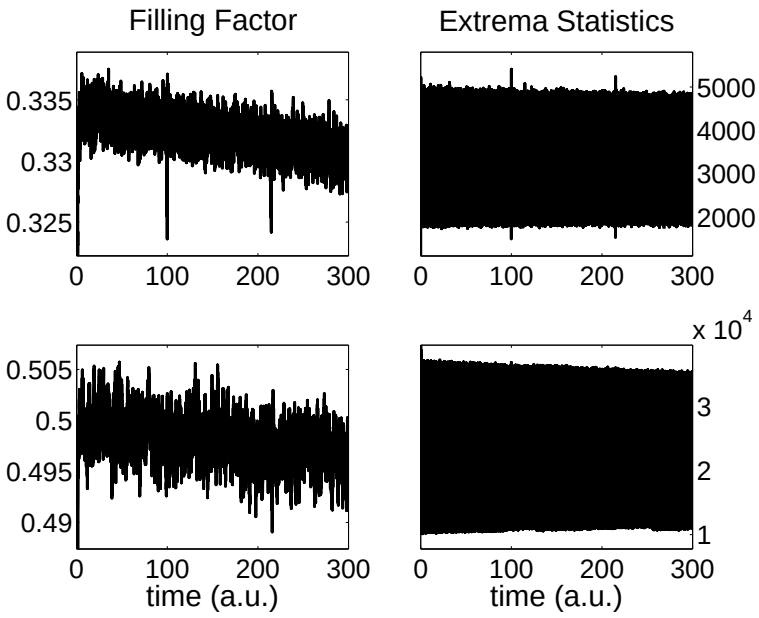

Figure 3.22: The filling factor (left) and the statistics of the time interval between extrema (right) of a optoelectronic feedback system with two delays in the serial configuration. Top: free noise system. Bottom: Additive gaussian noise whose standard deviation is 1% of the amplitude of the time series. The parameters of the system are $\beta = 15$, $T = 1$, $\phi = 0.26\pi$, $\tau_1 = 100$ and $\tau_2 = 215$.

higher nonlinearities, shorter time series or even longer sampling times make impossible the time delay identification (see figure 3.22 (bottom)).

In the double feedback systems, the equation (3.12) only guarantees the existence of structure in the four dimensional space $(\dot{x}(t), x(t), x(t-\tau_1), x(t-\tau_2))$ or in the three dimensional space $(x(t_{ext}), x(t_{ext}-\tau_1), x(t_{ext}-\tau_2))$ when only the extrema points are considered. It is not guaranteed, however, that a projection on a lower-dimensional space leads to an identifiable object. This depends on the system considered. In the parallel configuration, each nonlinear function depends only of one time delay yielding some structure in the $(x(t_{ext}), x(t_{ext}-\tau_i))$ space. To identify the time delays in the serial case, we propose to generalize the filling factor method and the forecasting error of the global models to work in the space $(x(t_{ext}), x(t_{ext}-\tau_1), x(t_{ext}-\tau_2))$. Hence, in the modified filling factor method the trajectory is evaluated in the space $(x(t_{ext}), x(t_{ext}-\nu_1), x(t_{ext}-\nu_2))$ for the extrema of $x(t)$. In the global model,

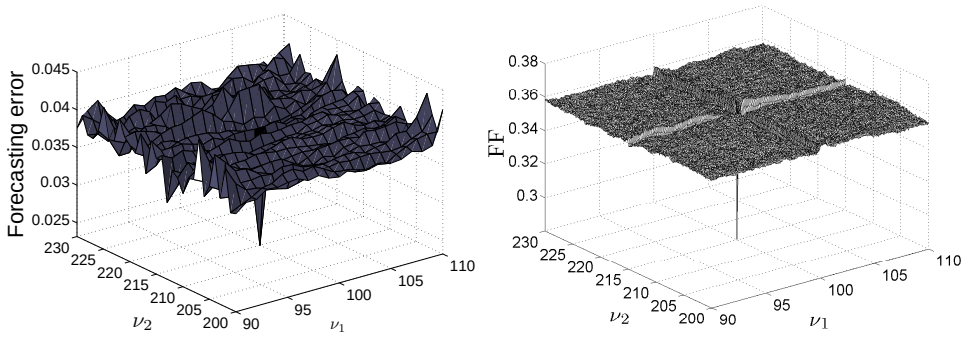

Figure 3.23: The modified filling factor (right) and the forecasting error of a GNLM adapted for two delays (left) of an optoelectronic feedback system with two delays in the serial configuration. The parameters of the system are $\beta = 15$, $T = 1$, $\phi = 0.26\pi$, $\tau_1 = 100$ and $\tau_2 = 215$.

now we have inputs delayed by both delays so the output of the model is given by:

$$\begin{aligned}\hat{x}(t+\delta t) &= W(x(t), x(t-\delta t), ..., x(t-m_1\delta t),\\ &\quad x(t-\nu_1+m_2\delta t), ..., x(t-\nu_1), ..., x(t-\nu_1-m_2\delta t),\\ &\quad x(t-\nu_2+m_2\delta t), ..., x(t-\nu_2), ..., x(t-\nu_2-m_2\delta t)) \quad (3.20)\end{aligned}$$

The results obtained with these modified methods are depicted in figure 3.23. In both cases a minimum appears when $\nu_1 = \tau_1$ and $\nu_2 = \tau_2$. The robustness of the modified filling factor and the forecasting error of the GNLM is similar to that of the one delay case. Note that the computational time of the modified methods respect to the standard ones is much higher due to the fact that we have to sweep two values instead of one.

3.3.4 Conclusions

We have shown that the time delays of optoelectronic feedback systems subject to one or two fixed time delays can be identified from numerical time series. The addition of a second delay does not avoid the time delay identification. Two different configurations have been analyzed for the two-delay case, serial and parallel. In the parallel configuration it is possible to extract the delays using the same techniques that work for single delay systems. However, in the serial case these techniques fail and we have developed some adapted methods

to identify the time delay in this configuration too. The basic idea of these methods is to sweep the two delays of the system. The main drawback of the modified methods is the increment of the computational time respect to the standard ones.

We have also studied the effect of the nonlinearity and the response time of the system on the identification of the time delay with the different techniques described in section 3.1. For increasing nonlinearity strengths, the general behavior is a dismissing amplitude of the marker that estimates the time delay. On the other hand, the response time of the system affects the accuracy of the estimated time delay by the DMI and the AF. These methods overestimate the time delay particularly when the nonlinearity is low and the response time of the system is comparable to the time delay. Moreover, if the system is not free noise, then the filling factor method and the analysis of time interval between extrema also overestimate the time delay due to the response time. In these latter cases, we have checked that under moderate level noise, the filtering of the time series can avoid or decrease this effect. The only method that does not overestimate the time delay of the system due to the response time is the forecasting error of a global nonlinear model. However, this method always implies long computational times.

3.4 Experiments: optoelectronic feedback system

After analyzing the time delay identification in a semiconductor laser with optoelectronic feedback from numerical time series, now we apply these techniques to experimental time series.

In subsection 3.4.1 we describe in detail the experimental setup. The chaotic experimental generator shows chaos in wavelength. This system offers a high flexibility compared to other optical systems. This feature permits us to analyze the time delay identification from the experimental time series under a large variation of parameters such as the response time and the nonlinearity. The same experimental setup will be used to study the reconstruction of the nonlinear dynamics and the unauthorized decoding of a message in chapters 4 and 6, respectively.

Finally, in subsections 3.4.2 and 3.4.3 we retrieve the time delay from the experimental time series of a semiconductor laser with optoelectronic feedback with one and two delays.

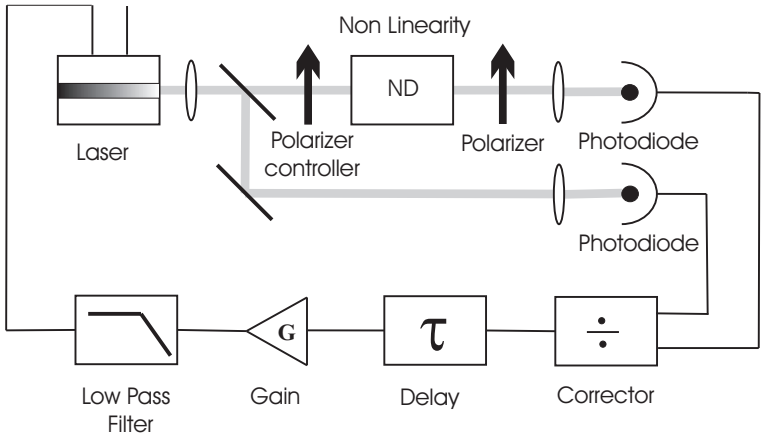

Figure 3.24: Experimental Setup.

3.4.1 Experimental setup

The chaotic experimental generator considered in this work is depicted in figure 3.24 [Goedgebuer et al. 1998a;b, Larger et al. 1998a;b]. It consists of a wavelength-tunable distributed-Bragg-reflector (DBR) semiconductor laser with a feedback loop. The feedback loop contains an optical component that exhibits a nonlinearity in wavelength, a delay line, an amplifier and a first-order low-pass filter. An electronic corrector is also included in the loop to achieve constant wavelength-independent optical power at the laser output.

After the nonlinear element the variable output power is converted into an electric current by a photodiode, and the current in turn is injected into the tunable-wavelength laser diode. As a consequence, the delayed feedback induces chaotic fluctuations in the laser wavelength for adequately chosen control parameters.

In the two-electrode DBR semiconductor laser, the wavelength is fixed at a given value Λ_0 by adjusting a couple of bias currents (I_{act}, I_{DBR}) on each of the electrodes. The wavelength can be tuned electronically around Λ_0 by varying current I_{DBR}, while keeping I_{act} constant. The I_{act} determine the output power of the laser. The variation range of the wavelength is small enough to ensure that the DBR laser always oscillates in a single longitudinal mode.

The nonlinearity in wavelength is induced by the birefringent plate whose fast and slow axes are oriented at 45° to two crossed linear polarizers. The

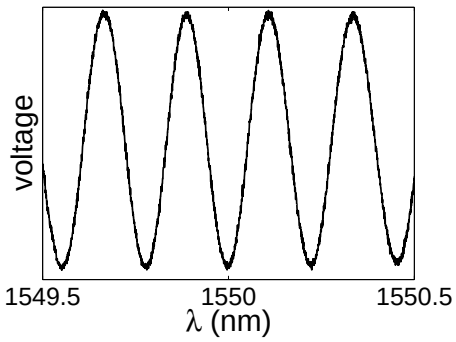

Figure 3.25: Nonlinear function generated by the birefringent plate in an open loop configuration.

intensity detected by the photodetector is a $\sin^2$ nonlinear function of the wavelength emitted by the laser diode (see figure 3.25).

The delay module consists of a First-In First-Out (FIFO) memory of 2048x9 bits that stores 2048 data in queue order so the first input element goes out the first. The FIFO module is plotted in detail in figure 3.26. The signal is digitized with a 12 bits analog-to-digital (AD) converter to store the data in the FIFO memory. When the data go out of the FIFO memory, they are converted again to an analog signal using a 12 bits digital-to analog (DA) converter. The clock frequency f_{clk} is given by an external clock with a frequency $f_{in} = 4f_{clk}$. The clock frequency is limited to a maximum value of 5 MHz by the AD and DA converters. A minimum clock frequency of 1 MHz is considered to avoid aliasing. When the clock frequency is fixed the time delay is given by $(2048+6)/f_{clk}$, where the extra small delay of $6/f_{clk}$ is due to a sort of buffer located inside the device. The time delay in this experimental setup takes values between 0.4 and 2 ms.

The wavelength of the chaotic carrier can be described by the following time-delay differential equation:

$$T\frac{d\lambda(t)}{dt} = -\lambda(t) + \beta_\lambda \sin^2\left(\frac{\pi D}{\Lambda_0^2}\lambda(t-\tau) - \phi\right) \tag{3.21}$$

where λ is the wavelength deviation from the center wavelength Λ_0, D is the optical path difference of the birefringent plate which constitutes the nonlinearity, ϕ is the feedback phase, τ is the time delay, T is the response time of the feedback loop, given by the cut-off frequency of a the first-order low-pass filter and β_λ is the feedback strength. The feedback strength can be adjusted through the gain G of an amplifier in the loop. The regime of oscillations

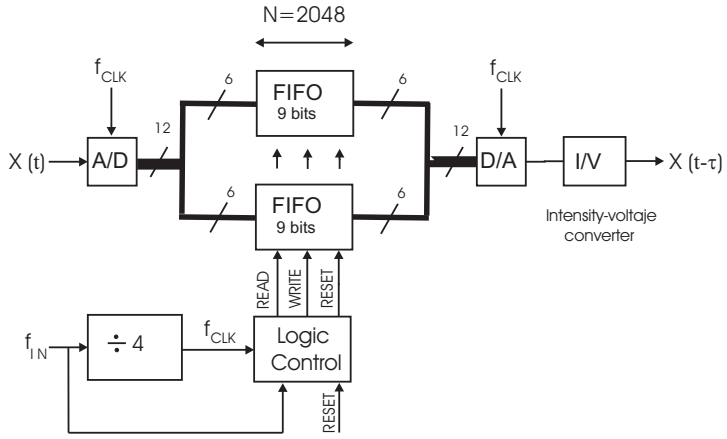

Figure 3.26: Detailed FIFO module.

in wavelength depends on the value of the parameter β_λ, which determines the strength of the feedback as well as the strength of the nonlinearity. In dimensionless units this parameter is given by $\beta = \pi D \beta_\lambda / \Lambda_0^2$. The number of extreme values of the $\sin^2$ nonlinear function increases also with β. In the following the system parameters are set to operate in the chaotic regime. Note that equation (3.21) can be normalized to the Ikeda delay differential equation (3.11) presented in the section 3.3.

3.4.2 One delay systems

In this subsection, we analyze the single time delay identification from the experimental time series generated by the chaotic generator explained above. The experimental time series have been recorded with a high end digital storage oscilloscope with 8 bits for the analog-digital conversion. The value of the time delay has been estimated from the FIFO parameters to be around 1.655 ms. We have checked that similar results are obtained for different time delay values.

Two different cases are studied: a nonlinear function with 2-3 extrema (low nonlinearity) and 6 extrema (moderate nonlinearity). Moreover, two different values of the cut-off frequency of the low-pass filter are considered, 20 KHz and 200 Hz, leading to response times of 8 μs and 800 μs, respectively. The sampling time is in both cases approximately one hundred times lower than the response time of the system. This means, a 10 Msampl/s for T=8 μs and

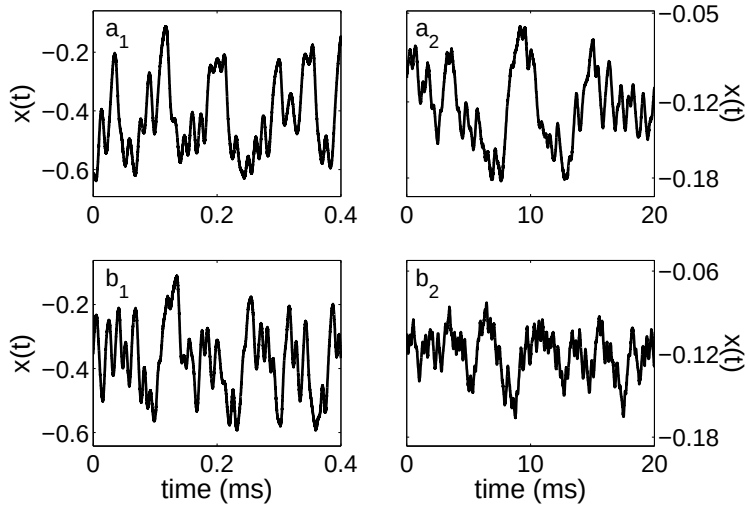

Figure 3.27: Experimental time series of an optoelectronics feedback system with $\tau = 1.655$ ms. Different nonlinearities and response times are plotted. a_1: Low nonlinearity strength and $T = 8\,\mu s$. b_1: Moderate nonlinearity strength and $T = 8\,\mu s$. a_2: Low nonlinearity strength and $T = 800\,\mu s$. b_2: Moderate nonlinearity strength and $T = 800\,\mu s$. The sampling time is 10 μs for $T = 800$ μs and 0.1 μs for $T = 8$ μs.

0.1 Msampl/s for T=800 μs. The length of the recorded time series is always of one million points. In figure 3.27 the experimental time series are depicted.

Contrary to the simulations results, the autocorrelation function of the experimental time series and the forecasting error of a global linear model do not give any indication of the time delay of the system for low nonlinearity strengths (nonlinear functions with 2-3 extrema). The reason might be the presence of noise (not only additive white gaussian noise).

A rough estimation of the noise of the time series can be made by subtracting the original time series (normalized to mean zero and variance unity) and an averaged version of it. The basic idea is to compare each point of the original signal with an average of the neighborhoods points. We calculate the noise of the system as the difference between the original and the smoothed signal. With this method we estimate a $SNR \simeq 32$ (31) dB when $T = 8$ (800) μs. The SNR is calculated as $20 \log(\sigma_\lambda / \sigma_{s\lambda-\lambda})$, where σ_λ and $\sigma_{s\lambda-\lambda}$ are the standard deviation of the original signal and the smoothed signal minus the original one, respectively. The normalized original time series and its average is plotted in figures 3.28(a) and 3.28(b) for $T = 800$ μs and $T = 8$ μs, respectively.

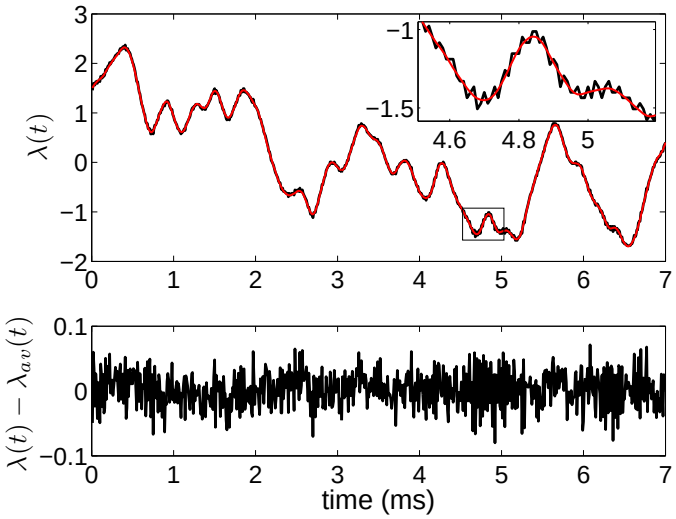

(a) $T = 800\ \mu s$

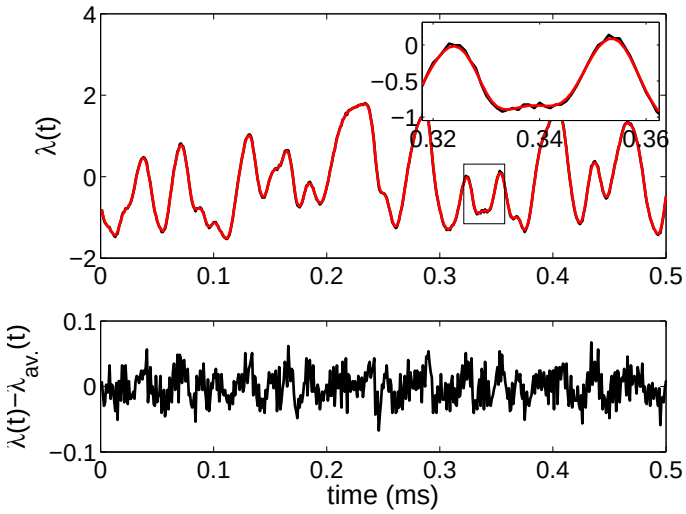

(b) $T = 8\ \mu s$

Figure 3.28: (a, b): Top panel: The normalized experimental time series (black) and its average (red). Bottom panel: the difference between the normalized experimental time series and its average. a (b): The time series has been generated by a chaotic generator with $\tau = 2080$ (476) μs, $T = 800$ (8) μs and a nonlinear function with 5 (2) extrema. The sampling period is 10 (1) μs. The average is over 31 (3) μs. $\lambda(t)$ is measured in volts.

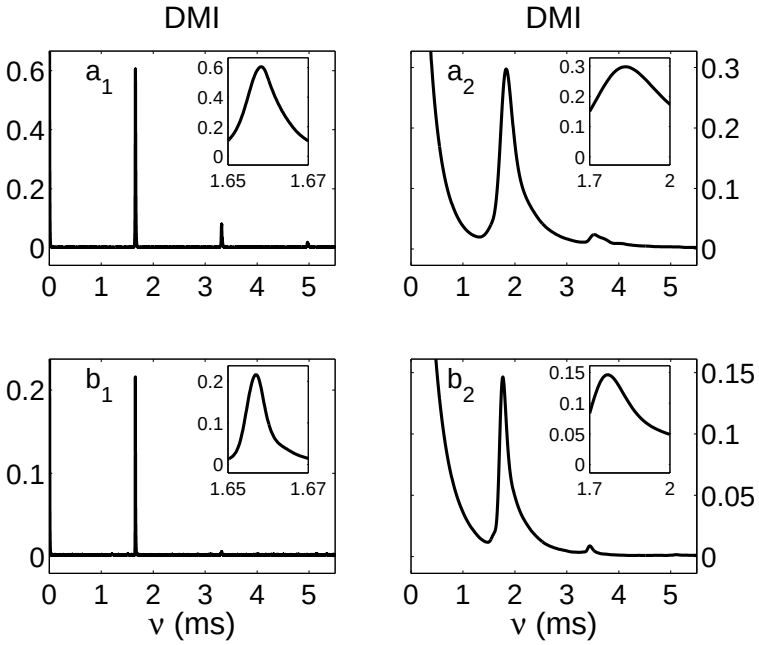

Figure 3.29: The delayed mutual information for the experimental time series with $\tau = 1.655$ ms. Different nonlinearities and response times are analyzed. a_1: Low nonlinearity strength and $T = 8\,\mu s$. b_1: Moderate nonlinearity strength and $T = 8\,\mu s$. a_2: Low nonlinearity strength and $T = 800\,\mu s$. b_2: Moderate nonlinearity strength and $T = 800\,\mu s$.

On the other hand, the location of the highest peak of the delayed mutual information (plotted in figure 3.29) estimates the time delay of the system. Lower amplitude peaks appear at multiples of the time delay. As happened with the numerical results, the amplitude of the peaks decreases as the nonlinearity strength increases. Moreover, the estimated time delay given by the DMI method is also overestimated due to the response time of the system (see table 3.2). The influence of the response time in the estimated time delay is more noticeable for high T and low nonlinearities. For high nonlinearities the influence of the response time in the dynamics of the system decreases, in parallel with the decreasing influence of the linear dynamics.

Next, we plot the filling factor and the statistic of the time interval between extrema of the experimental time series in figure 3.30. In both cases the estimated time delay is also affected by the response time of the system (see table 3.2). This is consequence of the spurious extrema that appear in the

	$T = 8\mu s$		$T = 800\mu s$	
	Low β	High β	Low β	High β
DMI	1.658 ms	1.657 ms	1.83 ms	1.77 ms
FF	1.657 ms	1.656 ms	1.76 ms	1.7 ms
GNLM	1.654 ms	1.654 ms	1.655 ms	1.655 ms
TDE	1.65 ms	1.652 ms	1.56 ms	1.6 ms
FF (smooth)	1.654 ms	1.654 ms	1.655 ms	1.655 ms
TDE (smooth)	-	-	1.655	1.655

Table 3.2: Estimated time delay from different techniques from the experimental time series. The experimental estimated time delay is 1.655 ms.

time series originated by the noise. The time delays estimated with the FF method, the absolute maximum of $N(\nu)$ (where $N(\nu)$ is the statistic of the time interval between extrema) and the DMI are similar. In the TDE, the absolute minimum of $N(\nu)$ should provide an accuracy time delay estimation but the extrema induced by the noise lead to an underestimation of the time delay (see table 3.2).

Under low and moderate noise, the forecasting error of a model is the only time delay identification technique of the ones studied in this thesis whose results are not affected by the response time of the system. We apply the same global nonlinear model used in the simulations to the experimental time series. The results are shown in figure 3.31 and table 3.2. The main shortcoming of this method is the long computational times. The computational time increases for long time delays, short sampling times and large number of parameters of the model. Systems with higher nonlinearity strengths and noise require more parameters. To minimize the computational time, this method can be used in combination with simpler ones, like the delayed mutual information. Once we have an estimation of the time delay, the range of the values near the estimated time delay can be swept with a global model to obtain a better approximation of the time delay.

Even with this approach, the computational time can be too long. A possible solution to avoid or decrease the effect of the noise is to filter the experimental time series. As previously mentioned, one simple way of filtering part of the noise is to smooth the data. Smoothing is achieved by averaging the signal around each point (the number of the nearby points used to average

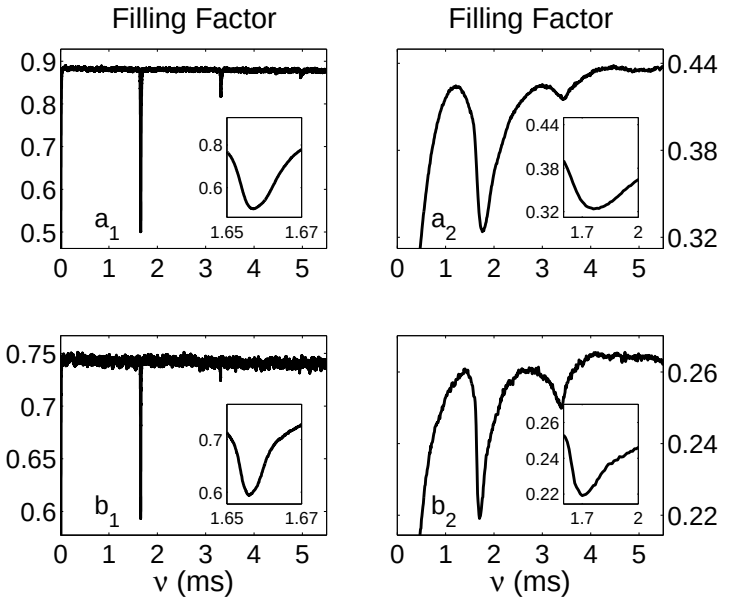

(a) Filling Factor

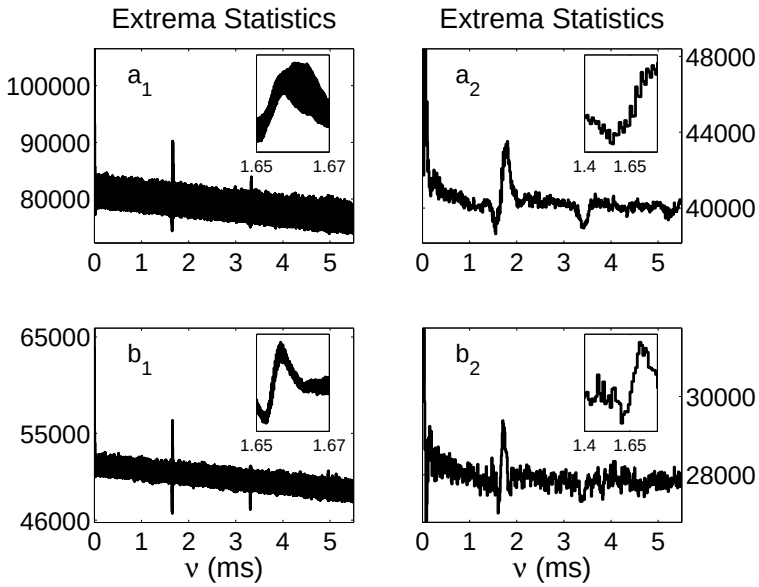

(b) The time distribution of extrema

Figure 3.30: The experimental time series has $\tau = 1.655$ ms. Different nonlinearities and response times are analyzed. a_1: Low nonlinearity strength and $T = 8\,\mu s$. b_1: Moderate nonlinearity strength and $T = 8\,\mu s$. a_2: Low nonlinearity strength and $T = 800\,\mu s$. b_2: Moderate nonlinearity strength and $T = 800\,\mu s$.

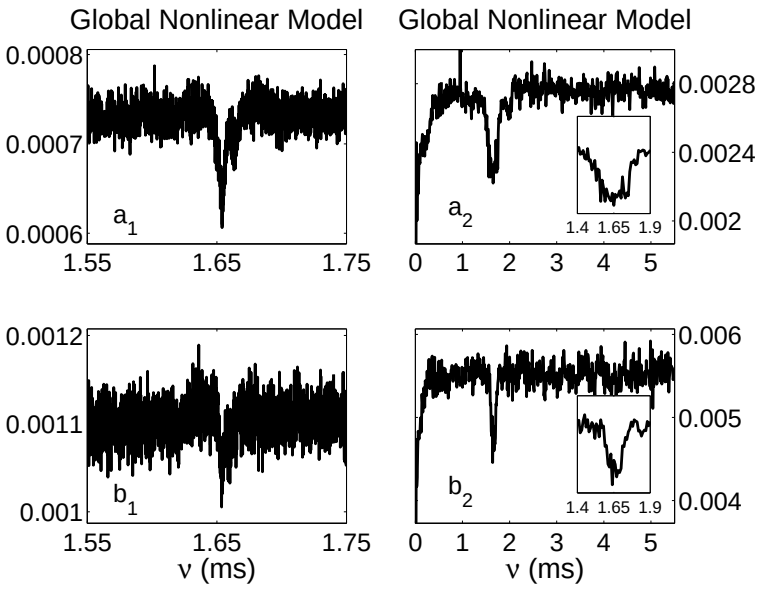

Figure 3.31: The forecasting error of a neural network model for the experimental time series with $\tau = 1.655$ ms. Different nonlinearities and response times are analyzed. a_1: Low nonlinearity strength and $T = 8\,\mu s$. b_1: Moderate nonlinearity strength and $T = 8\,\mu s$. a_2: Low nonlinearity strength and $T = 800\,\mu s$. b_2: Moderate nonlinearity strength and $T = 800\,\mu s$.

depends on the sampling time and the dynamics of the particular system). Under low and moderate noise, the extrema of the smoothed time series are located at the same points that the extrema of the free noise time series. Under high noise levels there is not a good resemblance between the smoothed and the free noise time series and this simple technique is not valid. We plot in figure 3.32 the filling factor and the statistics of the time interval between extrema of the smoothed time series. The overestimation of the time delay due to the effect of the response time of the system has been eliminated (see table 3.2). Nonetheless, when $T = 8\ \mu s$ the number of extrema of the smoothed time series is insufficient to apply with success the analysis of the time interval between extrema. In this particular case, longer time series are necessary. The effect of the low number of extrema can be also noticed in the filling factor that presents valleys with lower amplitude than for the original time series.

To conclude, in the experimental optoelectronic feedback system we can estimate the time delay with accuracy and avoid the effect of the response time of the system by using a global nonlinear model. However, the computational

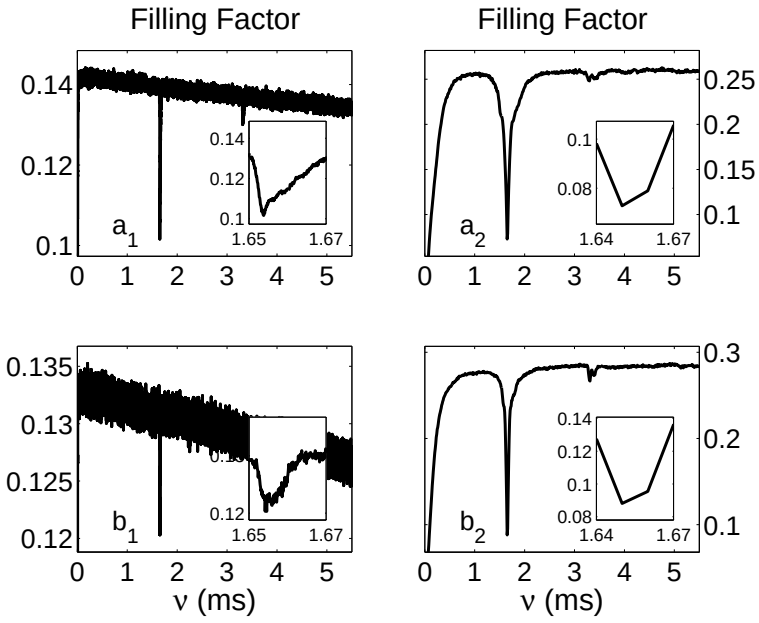

(a) Filling Factor

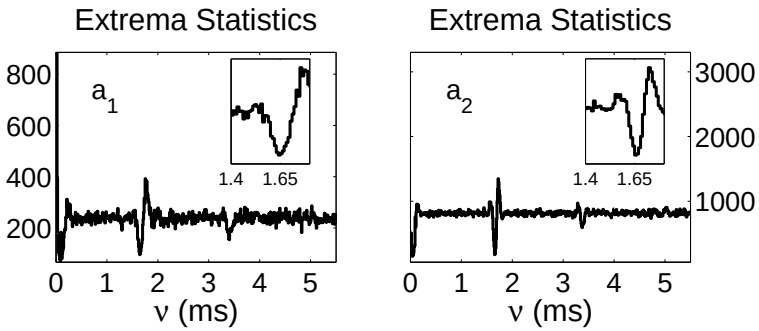

(b) The time distribution of extrema

Figure 3.32: The smoothed experimental time series has $\tau = 1.655$ ms. Different nonlinearities and response times are analyzed. a_1: Low nonlinearity strength and $T = 8\,\mu s$. b_1: Moderate nonlinearity strength and $T = 8\,\mu s$. a_2: Low nonlinearity strength and $T = 800\,\mu s$. b_2: Moderate nonlinearity strength and $T = 800\,\mu s$.

time is too long. Other effective methods are also the filling factor and the time distribution of extrema methods once part of the noise of the original time series has been filtered. This technique works well under low and moderate levels of noise. On the other hand, higher nonlinearity strengths (nonlinear function with more extrema) imply lower peaks or valleys located at the time delay of the system. Note that similar results and conclusions were reached with the numerical simulations in the previous section. Finally, it is worth mentioning that the time delay of the system can be extracted from time series with larger sampling times than the ones used in this section.

3.4.3 Two-delay systems

It is possible to add a second delay line to the experimental setup presented in subsection 3.4.1. The experimental setup of the two delays chaotic experimental generator is plotted in figure 3.33. The two delays chaotic experimental generator can be described by the following time-delay differential equation:

$$T\frac{d\lambda(t)}{dt} = -\lambda(t) + \beta_{\lambda_1}\sin^2(\frac{\pi D}{\Lambda_0^2}\lambda(t-\tau_1) - \phi_1) + \beta_{\lambda_2}\sin^2(\frac{\pi D}{\Lambda_0^2}\lambda(t-\tau_2) - \phi_2) \tag{3.22}$$

Due to the experimental implementation the nonlinearity strength β_{λ_2} is always higher than β_{λ_1}. This experimental case fits the parallel two-delay case presented in the simulations (see section 3.3.3).

The behavior of the time delay extraction with respect to the nonlinearity strength of the system is the same as in the one delay case. Taking this into account, in the two-delay experimental case we only study the time delay identification with the higher nonlinearity strength than can be reached by the present experimental setup. From previous sections, we know that this scenario is the most complicated to identify the time delay since the amplitude of the markers located at the time delay decreases for increasing nonlinearity strength.

First, we analyze the case of $T = 8\ \mu s$ when the experimental measured time delays are $\tau_1 = 0.41$ ms and $\tau_2 = 2.05$ ms. The recorded experimental time series has one million points sampling each 1 μs, demonstrating that it is possible to retrieve the time delay with sampling times longer than 0.1 μs (one delay case). The experimental time series corresponding to this case are plotted in figure 3.34.

We find that both delays of the system can be extracted using the one delay standard techniques (see figure 3.35). Due to $\beta_{\lambda_2} > \beta_{\lambda_1}$, the marker located at τ_2 is always lower than the marker at τ_1. A marker at $\tau_2 - \tau_1$ also

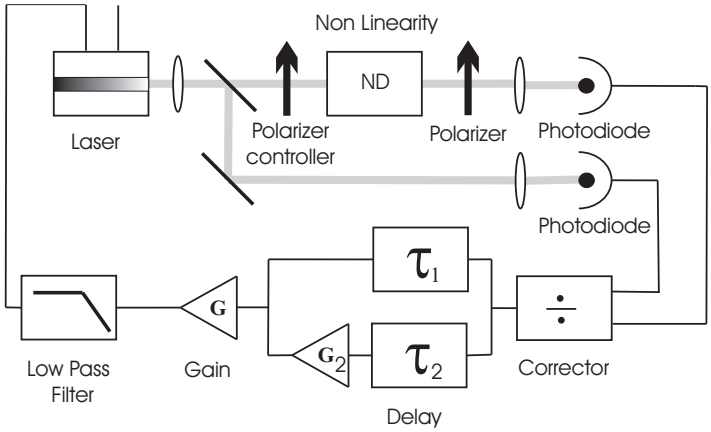

Figure 3.33: Experimental setup of the chaos in wavelength with two delay lines.

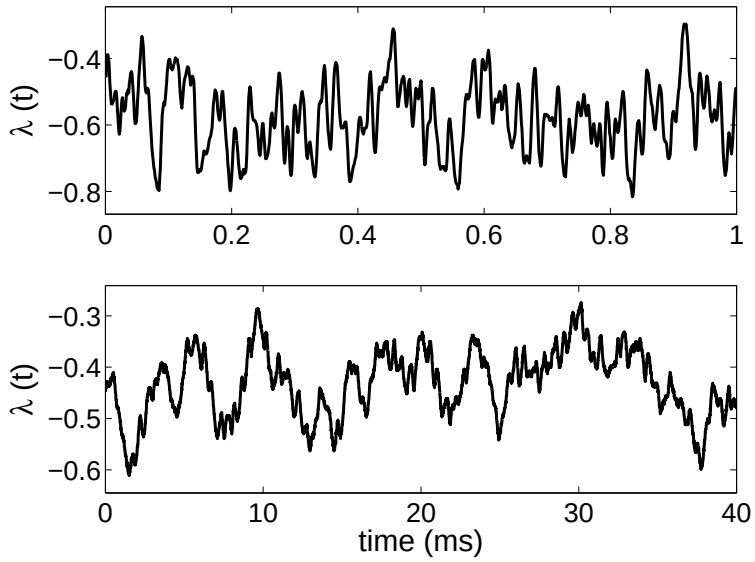

Figure 3.34: Experimental time series of an optoelectronics feedback system with two delays. Top (Bottom): The parameters of the system are $T = 8$ (800) μs, τ_1=0.41 (1.17) ms and τ_2=2.05 (1.64) ms. The sampling time is 1 (10) μs. In both cases high nonlinearity strength is considered.

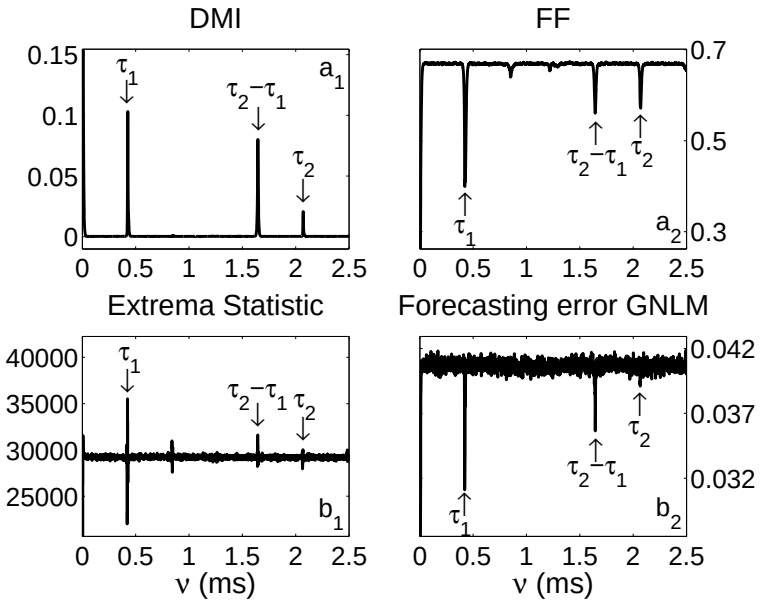

Figure 3.35: Time delay identification of a two-delay experimental system using different methods. a_1: DMI. a_2: Filling Factor. b_1: Statistics of the interval between extrema. b_2: Forecasting error of a modular neural network with 1 non-feedback input, 3 feedbacks inputs, 6:3 neurons in the feedback module. The parameters of the system are $T = 8\ \mu s$, high nonlinearity strength, $\tau_1 = 0.41$ ms and $\tau_2 = 2.05$ ms.

appears. This marker is even higher than the second delay one for most of the cases. Similar results and conclusions were obtained with the numerical simulations (see section 3.3.3).

As in the simulations, we study the time delay extraction in three special cases: τ_1 is very close to τ_2, $\tau_2 = 2\tau_1$ and $\tau_2 = 3\tau_1$. The delayed mutual information for these three cases is depicted in figure 3.36. The conclusions hold for other time delay identification techniques. Total agreement with the simulations conclusions is obtained. When both delays are close enough, the two peaks that indicate the time delays converge into a single peak, making impossible to distinguish both time delays. The DMI of the case $\tau_2 = 2\tau_1$ are qualitatively similar to the DMI of the one delay case (see figure 3.29). This does not occur when $\tau_2 = 3\tau_1$.

Finally, we can also analyze the two time delays case with $T = 800$. The DMI and the filling factor are plotted in figure 3.37 when the time delays are $\tau_1 = 1.17$ ms and $\tau_2 = 1.64$ ms. In both cases the sampling time is 10 μs.

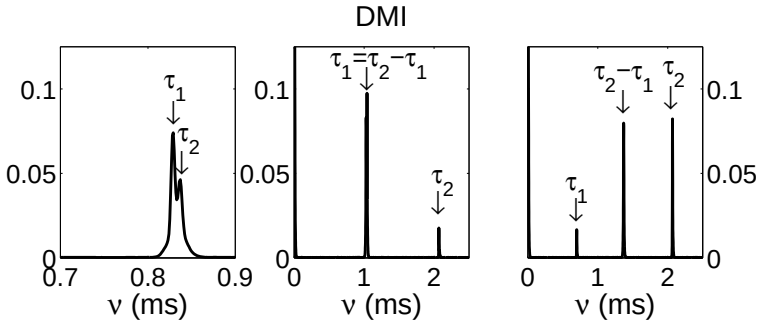

Figure 3.36: The DMI of experimental time series with T = 8 μs and high nonlinearity strength. Left: $\tau_1 = 0.811$ ms and $\tau_2 = 0.819$ ms. Middle: $\tau_1 = 1.025$ ms and $\tau_2 = 2.05$ ms Right: $\tau_1 = 0.683$ ms and $\tau_2 = 2.05$ ms.

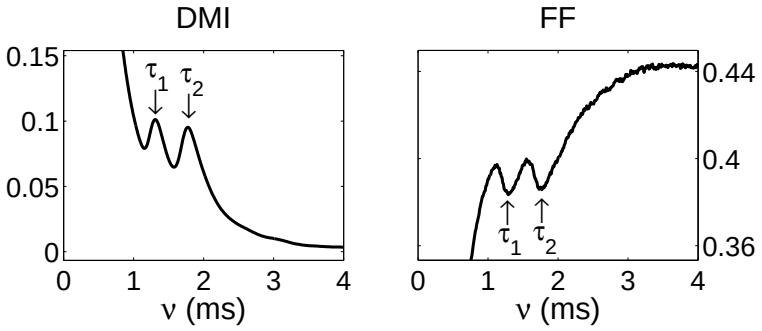

Figure 3.37: Left (Right): DMI (FF) of experimental time series with two time delays. The parameters of the system are $T = 800$ μs, high nonlinearity strength, $\tau_1 = 1.17$ ms and $\tau_2 = 1.64$ ms.

Here, the peaks (valleys) that estimated the time delay appear in the region where the effect of the linear correlations have not yet disappeared. The peak at $\tau_2 - \tau_1$ is concealed due to the linear correlations. Clearly, the time delays are overestimated due to the response time as in the one delay case. The same solutions proposed in the one delay case to avoid this overestimation can be applied to the two delays case.

3.5 Periodic time delay

We have demonstrated in the previous sections that the optoelectronic feedback system with one and several fixed delays is vulnerable from the point of view of time delay identification. To enhance the security of the system, it has been proposed [Kye et al. 2004] to use a variable time delay to hide it from an eavesdropper.

Following this approach, we study the extraction of a periodic time delay from the experimental time series. In the chaotic wavelength transmitters based on a DBR laser subject to optoelectronic feedback (see subsection 3.4.1), the value of the time delay is given by a FIFO memory (see figure 3.26). When fixed delays are considered, the f_{clk} of the FIFO memory is fixed. The experimental periodic time delay, $\tau(t)$, can be easily obtained by periodic modulation of the clock frequency. The modulated clock frequency, f_{clk}, is given by:

$$f_{clk}(t) = f_0 + \Delta f \psi(t) \tag{3.23}$$

where f_0 is the clock frequency is absence of modulation, Δf is the amplitude of modulation, $\psi(t)$ is a periodic function of period T=1/F and F is the modulation frequency.

Depending on the clock frequency modulation (Δf, $\psi(t)$, F), different functions for the periodic time delay, $\tau(t)$, are obtained. First, in subsection 3.5.1 we analyze the function obtained for the time delay, both from a theoretical model and from experimental data. In subsection 3.5.2 we study the case of a periodic time delay with square wave modulation for the clock frequency. The period of the time delay is obtained from the mutual information. Finally, in subsection 3.5.3 we show that the periodic time delay function of the chaotic carrier can be extracted from experimental data by applying a modified filling factor method. A sinusoidal periodic function for the clock frequency is considered for the delay. Different periods and modulation depths are considered.

3.5.1 Periodic time delay function

Let us examine first the simplest case, a square-wave modulation of the clock frequency between two values f_1 and f_2, such that $f_1 > f_2$.

In theory, the maximum and minimum time delays that the system can reach are $\tau_i = 2048/f_i (i = 1, 2)$, and correspond to the two clock frequencies f_1 and f_2. We first consider that the modulation frequency F is small, such that, $\tau_i (i = 1, 2)$ are smaller than T/2. T = 1/F is the modulation period. When the clock frequency is changed from f_1 to f_2, it takes a time τ_2 to replace the data

stored in the FIFO memory (sampled with the rate f_1) by the data sampled with the rate f_2. Then the value of the time delay increases linearly from τ_1 to τ_2 in a time τ_2 with a slope $(f_1 - f_2)/f_1$. A similar situation occurs when the clock frequency is changed from f_2 to f_1, and the time delay decreases linearly from τ_2 to τ_1 in a time τ_1, but with a greater slope $(f_1 - f_2)/f_2$. However, when the modulation frequency F is large, such that T/2 is smaller than τ_2, the maximum time delay that can be reached, $\tau_2 - (\tau_2 - \tau_1)(1 - T/(2\tau_2))$, is smaller than τ_2.

Following these guidelines we have developed a model that simulates the periodic time delay $\tau(t)$ as function of the clock frequency. We show in figure 3.38 (left) and figure 3.39 (left) the time delay function for square-wave and sinusoidal modulation, respectively. It can be seen that the time delay for square-wave modulation has an increasing slope smaller than the decreasing one. Moreover, in these figures the minimum frequency clock is 1 MHz. This leads to a maximum time delay of 2 ms applying the FIFO formula $(2054/f_{clk})$. For small values of the modulation frequency this maximum time delay is reached (see figure 3.38). For larger values of the modulation frequency the range of the delay values decreases, and the maximum time delay is smaller than 2 ms (see figure 3.39). These results are in agreement with the previous discussion.

We have also performed experimental measurements to obtain the time delay function. The experimental time delay function is obtained by the following procedure. A periodic triangular signal with a period $T_{in} = 50$ ms greater than T has been used as input of the FIFO delay module. The output signal is then given by $V_{ou}(t) = V_{in}(t - \tau(t))$. The time delay function can be obtained from $(V_{in} - V_{ou})/A$ (or $(V_{ou} - V_{in})/A$) using a half-period with increasing (or decreasing) input signal, where A = 70 mV/ms is the slope of the triangular input signal. Data acquisition is performed for all the cases of modulated time delay with a 8 bits resolution oscilloscope and a sampling time of 10 μs. The results obtained for square-wave and sinusoidal modulation are shown in figures 3.38 (right) and 3.39 (right), respectively. The time delay functions measured in this way are similar to the ones obtained from the model. In the case of sinusoidal modulation the range of the delay values is similar for both experimental and theoretical results. However, for the square-wave modulation the range of the delay values obtained from the model is 0.3 ms smaller than the range obtained from the experimental measurements. We note that the measurements in this subsection were performed at the end of the experimental work with the modulated time delay. It seems that the FIFO memory performance has become worse, and that the delay module was not working properly during these measurements.

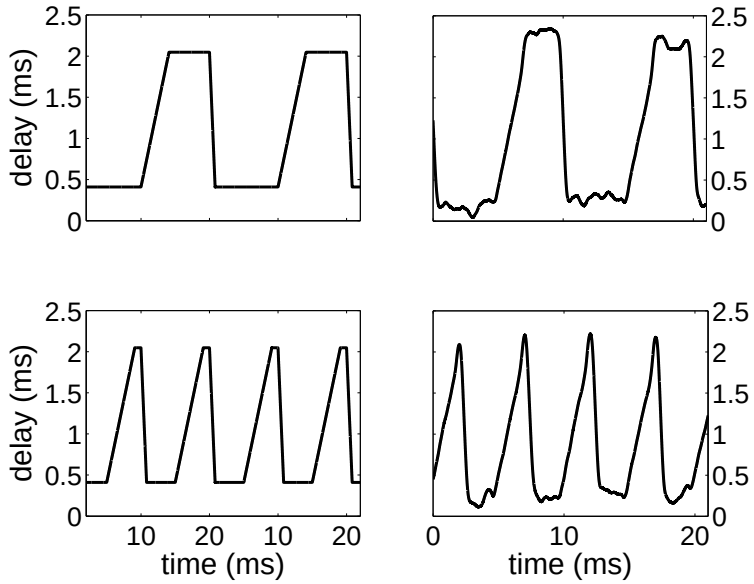

Figure 3.38: Periodic delay time obtained from model (left) and experiment (right) for square-wave modulation of the clock frequency between 1 and 5 MHz with modulation frequencies F = 100 (top) and 200 (bottom) Hz.

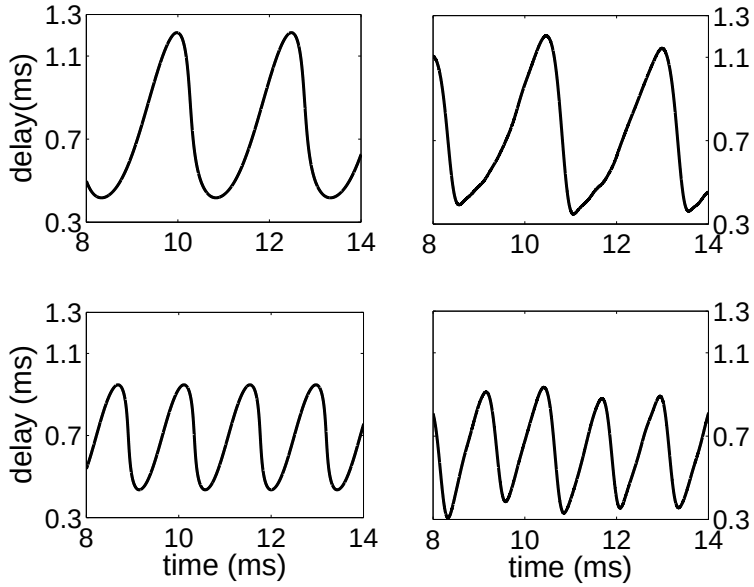

Figure 3.39: Periodic delay time obtained from model (left) and experiment (right) for sinusoidal modulation of the clock frequency between 1 and 5 MHz with modulation frequencies F = 400 (top) and 700 (bottom) Hz.

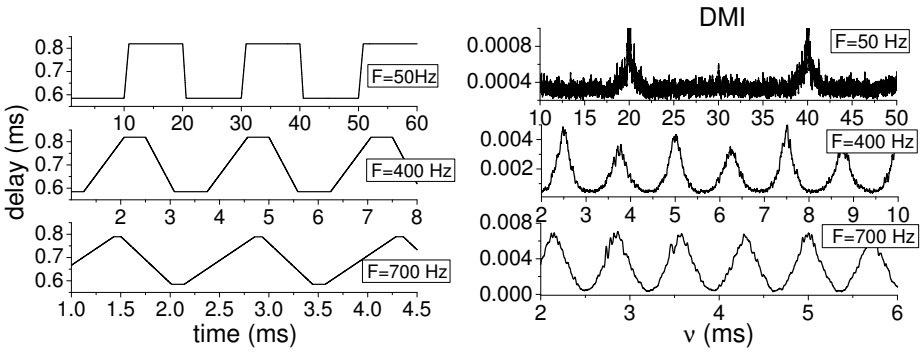

Figure 3.40: Right: Delayed Mutual information of the experimental time series for square-wave modulation with the clock frequency around $f_0 = 3$ MHz, $\Delta f = 1.25$ MHz and low nonlinearity. Left: Simulations of $\tau(t)$ for square-wave modulation with the clock frequency around $f_0 = 3$ MHz and $\Delta f = 1.25$ MHz. From top to bottom, different modulation frequencies: F = 50 (top), 400 (middle) and 700 (bottom) Hz.

3.5.2 Square-wave modulation

Now, we consider a square-wave modulation of the clock frequency:

$$f_{clk}(t) = f_0 + \Delta f \, \mathrm{sgn}(\sin(2\pi F t)), \tag{3.24}$$

where $\mathrm{sgn}(x)$ is the sign function, that gives 1 (-1) for positive (negative) values of x, Δf is the modulation amplitude, F is the modulation frequency and $f_0 = 3$ MHz. We name $f_1 = f_0 + \Delta f$ and $f_2 = f_0 - \Delta f$.

The modulation frequency can be obtained from the delayed mutual information of the experimental time series. We have found that the DMI exhibits a modulation with maxima at multiples of the modulation period T = 1/F (see figure 3.40 (right)). These maxima in the statistical link between $\lambda(t)$ and $\lambda(t + nT)$ are due to the fact that the time delay is the same for both variables. When the modulation frequency is increased the maxima also appear at multiples of T/2. This is related to the shape of $\tau(t)$ (see figure 3.40 (left)). Similar behavior is obtained for the DMI of $\tau(t)$.

The amplitude of the modulation of the DMI function decreases when the amplitude and/or the frequency modulation of the clock frequency decrease. Then for small clock frequency modulation amplitudes and low frequencies it is difficult to extract the modulation frequency F (see figure 3.41). Note that for small modulation frequencies it is necessary to use longer time series.

On the other hand, for low modulation frequencies the DMI gives also information about the two values of the time delay, $\tau_i = 2054/f_i (i = 1, 2)$,

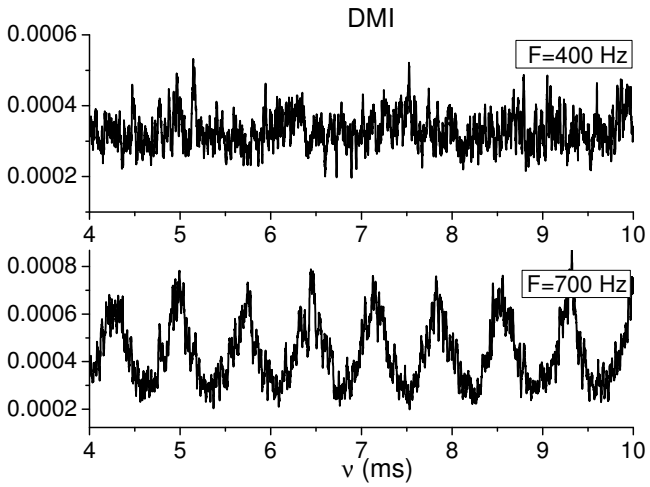

Figure 3.41: Delayed mutual information for square-wave modulation of the clock frequency around $f_0 = 3$ MHz for low nonlinearity, modulation amplitude of 0.25 MHz and modulation frequencies F = 400 (top) and 700 (bottom) Hz.

that correspond to the two clock frequencies (see figures 3.42 and 3.43). For low modulation frequencies the time delay function is similar to a square-wave function (see figure 3.40 (left)) with only two values τ_1 and τ_2 for the delay. Then the statistical link between $\lambda(t)$ and $\lambda(t-\nu)$ is maximum when $\nu = \tau_i (i = 1, 2)$ (see figure 3.43). When the modulation frequency is increased the peak amplitude at τ_1 and τ_2 decreases, and the values of the mutual information for times between τ_1 and τ_2 increase (see figure 3.43). For large modulation frequencies the time delay function is similar to a triangular function (see figure 3.40 (left)). Then the range of the delay values is given by the interval between τ_1 and τ_2, and the mutual information gives information about this range. It is also found that the statistical link given by the DMI decreases when the nonlinearity is increased (see figure 3.43).

3.5.3 Sinusoidal modulation

In this subsection we consider a sinusoidal modulation of the clock frequency of the form:

$$f_{clk}(t) = f_0 + \Delta f \sin(2\pi F t) \tag{3.25}$$

where Δf is the amplitude modulation, F is the modulation frequency and $f_0 = 2.25$ MHz.

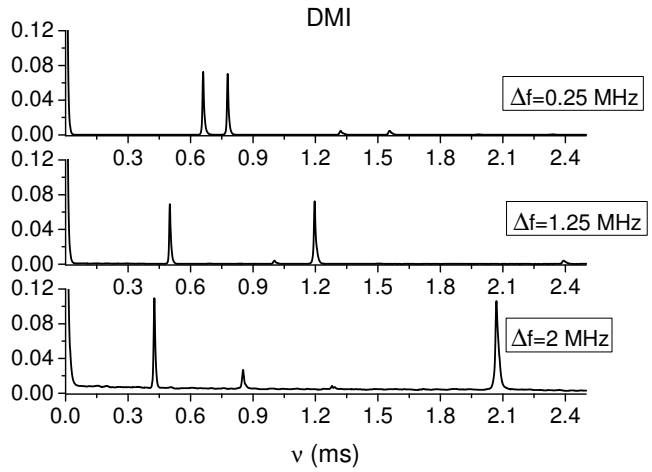

Figure 3.42: Delayed mutual information for square-wave modulation with the clock frequency around $f_0 = 3$ MHz , F = 50 and for low nonlinearity. From top to bottom different modulation amplitudes: $\Delta f = 0.25$ (top), 1.25 (middle) and 2 (bottom) MHz.

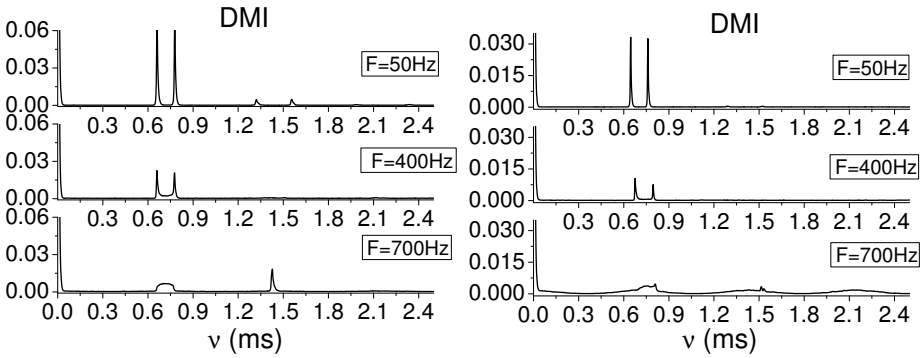

Figure 3.43: Delayed mutual information for square-wave modulation around $f_0 = 3$ MHz for $\Delta f = 0.25$ MHz and different modulation frequencies: F = 50 (top), 400 (middle) and 700 (bottom) Hz. Left: low nonlinearity. Right: high nonlinearity.

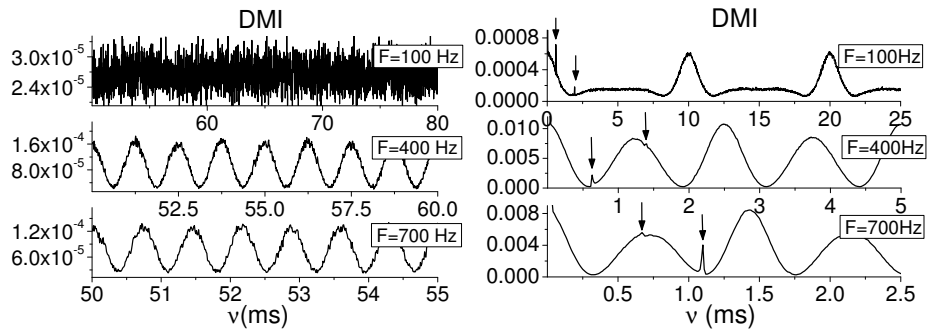

Figure 3.44: Delayed mutual information for sinusoidal modulation of the clock frequency around $f_0 = 2.25$ MHz for $\Delta f = 1.25$ MHz and different modulation frequencies: F = 100 (top), 400 (middle) and 700 (bottom) Hz. Left (Right): Low (High) nonlinearity. The arrows correspond to the maximum and minimum values of the time delay function.

As in the square-wave modulation case, the delayed mutual information exhibits a modulation with maxima at multiples of the modulation period T = 1/F. The maxima appear also at multiples of T/2 for small Δf, and when F is increased for large Δf (see figures 3.44 and 3.45). As in the square-wave modulation case this behavior is related to the shape of $\tau(t)$. It is also found that the DMI modulation amplitude decreases when F decreases (see figures 3.44 and 3.45). Then for small clock frequency modulation amplitudes and low frequencies it is more difficult to extract the modulation frequency F.

In addition, the DMI also informs us about the range of the time delay function. In figure 3.46 we show the delayed mutual information for small modulation amplitude and different modulation frequencies. Two peaks are obtained at values close to the maximum, τ_M, and minimum, τ_m, values of the time delay function. The fraction of the modulation period such that the time delay function is close to one value has a maximum for τ_M and τ_m (see figure 3.39). Then the DMI has also a maximum at these extreme values of $\tau(t)$. The location of the peaks at $\tau_M(\tau_m)$ decreases (increases) when the modulation frequency increases, in agreement with the results shown in figure 3.39. Since the time delay takes values between τ_m and τ_M the DMI also increases for the same range of values. The same behavior is also obtained at multiples of this interval. It is also found that the DMI decreases when the nonlinearity is increased (see figure 3.46).

The amplitude of the modulation of the DMI function increases when the modulation amplitude Δf increases. Then for large Δf the peaks located at τ_M and τ_m are nearly hidden by the DMI modulation (see 3.44 right).

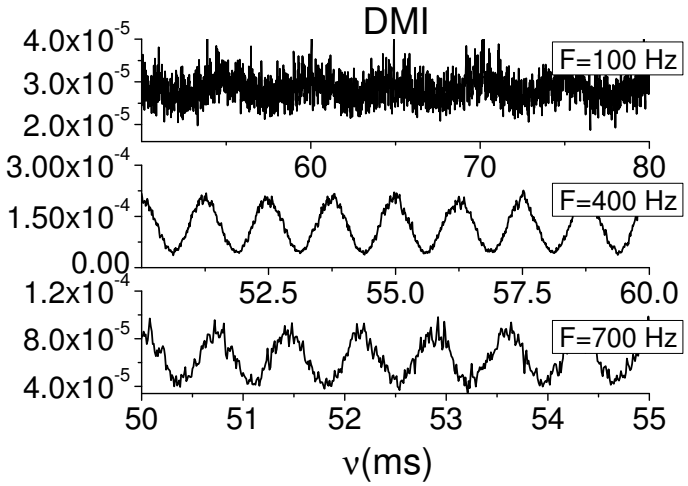

Figure 3.45: Delayed mutual information for low nonlinearity and sinusoidal modulation of the clock frequency around $f_0 = 2.25$ MHz for $\Delta f = 0.25$ MHz and different modulation frequencies: F = 100 (top), 400 (middle) and 700 (bottom) Hz.

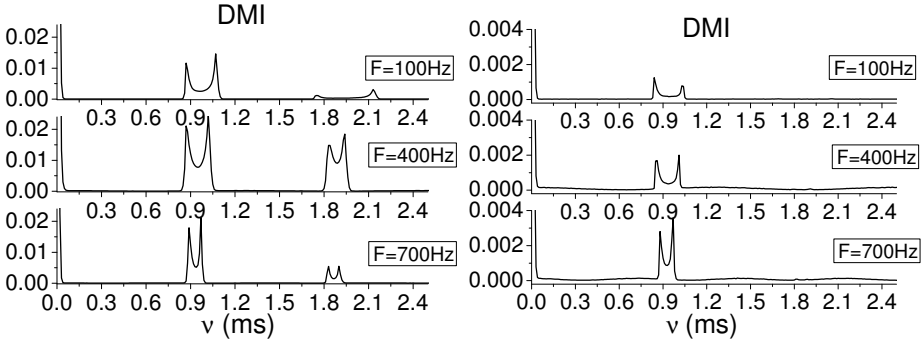

Figure 3.46: Delayed mutual information for sinusoidal modulation around $f_0 = 2.25$ MHz for $\Delta f = 0.25$ MHz and different modulation frequencies: F = 100 (top), 400 (middle) and 700 (bottom) Hz. Left: low nonlinearity. Right: high nonlinearity.

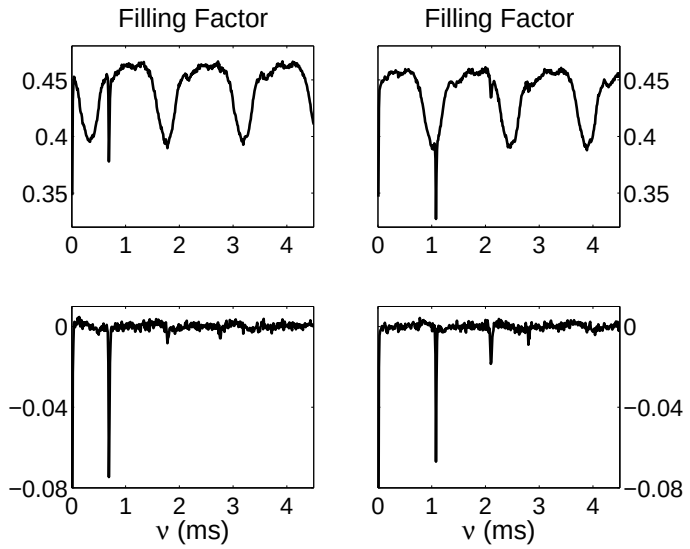

Figure 3.47: Top: Filling factor obtained from experimental data $x_n = (t_i + nT)$ for low nonlinearity and sinusoidal modulation of the clock frequency around $f_0 = 2.25$ MHz for $\Delta f = 1.25$ MHz and modulation frequency F = 700 Hz. Bottom: The same filling factor after removing the modulation. Two values of t_i are considered that yield two values of the time delay function: $\tau(t_1) = 0.7$ ms (left) and $\tau(t_2) = 1.1$ ms (right).

We have developed a modified filling factor method to recover the time delay function $\tau(t)$. The procedure is explained in the following lines. We take the experimental data sampled at each modulation period starting at a time t_i, $x_n(t_i) = \lambda(t_i + nT)$. Then the same time delay, $\tau(t_i)$, is associated with all the data $x_n(t_i)$. Therefore the filling factor method obtained from these data $x_n(t_i)$ exhibits a minimum at $\tau(t_i)$. We show in figure 3.47 the filling factor obtained for two different values of the initial time t_i. A minimum appears in the filling factor at $\tau(t_i)$. Moreover, it is found that the filling factor exhibits a modulation with a period T. When the modulation is removed (see figure 3.47 bottom), minima at multiples of the delay $\tau(t_i)$ can be also seen. The time delay function is obtained by sweeping the value of t_i over a period T.

The time delay functions retrieved from experimental data series are plotted in figures 3.48-3.50 for different modulation amplitudes and frequencies, and for low and high nonlinearity. A good agreement is obtained with the time delay function calculated by using the model. A systematic overestimation of around 20 μs is obtained. Similar results are obtained for low and high

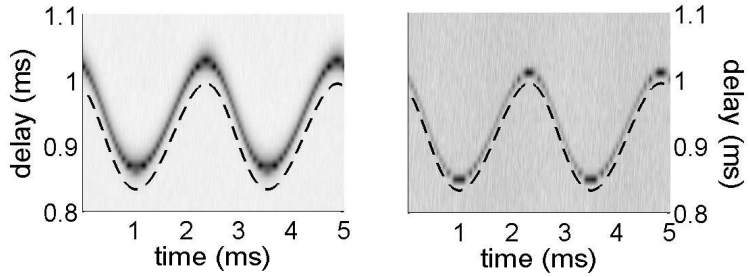

Figure 3.48: Periodic delay time obtained from experimental time series (solid) and model (dashed) for sinusoidal modulation of the clock frequency around $f_0 = 2.25$ MHz, $\Delta f = 0.25$ MHz and modulation frequency F = 400 Hz. Left: low nonlinearity. Right: high nonlinearity.

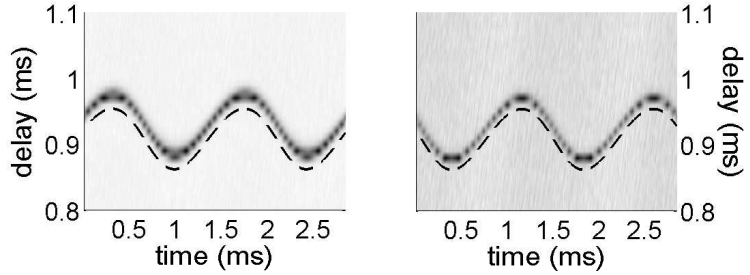

Figure 3.49: Periodic delay time obtained from experimental time series (solid) and model (dashed) for sinusoidal modulation of the clock frequency around $f_0 = 2.25$ MHz, $\Delta f = 0.25$ MHz and modulation frequency F = 700 Hz. Left: low nonlinearity. Right: high nonlinearity.

nonlinearity. For small modulation amplitude a quasi-sinusoidal modulation is obtained (see figures 3.48 and 3.49). When the modulation frequency is increased the minimum (maximum) value of the delay increases (decreases), and the range of the delay values is reduced, in agreement with the results shown in figure 3.39. When the modulation amplitude is increased the shape of $\tau(t)$ is distorted (see figure 3.50). The time delay function has an increasing slope that is smaller than the decreasing one, in agreement with the analysis previously performed for the delay module.

Summarizing, we have investigated the time-delay identification from the experimental time series generated by an optoelectronic feedback system with

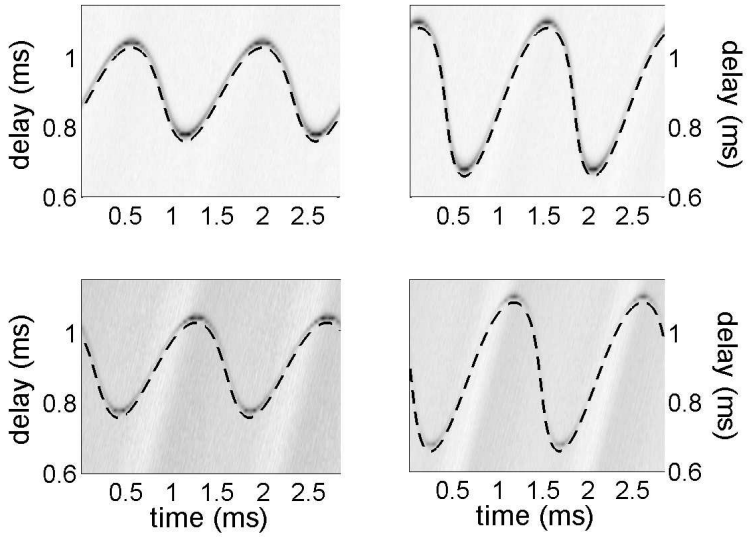

Figure 3.50: Periodic delay time obtained from experimental time series (solid) and model (dashed) for sinusoidal modulation of the clock frequency around $f_0 = 2.25$ MHz with modulation frequency F = 700 Hz and different modulation amplitudes: 0.75 (left) and 1.25 (right) MHz. Top: low nonlinearity. Bottom: high nonlinearity.

periodic time delay. First, we have shown that the modulation period T can be obtained from the mutual information for different modulation shapes, amplitudes and frequencies. This recovery becomes more difficult for small modulation amplitudes and low modulation frequencies. The range of the delay values can be also extracted from the mutual information. Next, a modified filling factor method has been used to obtain the time delay function for the case of sinusoidal modulation. A good agreement is obtained with the results given by the model developed for the delay module.

In a similar way that we will see for the case of two fixed time delays (see chapter 4, section 4.4), it can be expected that the retrieval of the time delay function will allow to reconstruct the nonlinear dynamics by working in a low-dimensional projection of the phase space. Then these optoelectronic feedback systems with periodic time delay are vulnerable. A way to enhance the security of these systems could be the use of a chaotic time delay [Kye et al. 2004], obtained as a function of the feedback system or generated by another chaotic system.

3.6 Conclusions

Along this chapter we have analyzed the time delay identification in semiconductor lasers subject to optical or optoelectronic feedback with different techniques. We have particulary focused on several cases proposed to difficult the time delay extraction: systems with variable time delay and multiples fixed time delays. We have also carefully analyzed the time delay identification in the all-optical case when low feedback rates are considered.

In the all optical feedback case, we have found that for large feedback rates, one and two fixed time delays can be easily extracted from numerical and experimental time series of the laser light output by standard identification methods. Similar results are obtained by the different standard techniques.

The most complicate time delay identification scenario for the all optical feedback system occurs for low feedback rates and a careful choice of the operational parameters, for which the laser relaxation-oscillation period is close to the delay. In this case, a simple ECSL with a single optical feedback can hide its time-delay when standard methods are employed. However, the range of parameters that conceals the time delay extraction is small and the complexity of the chaos (dimensions and entropy) generated in this case is not very suitable for the secure optical communications.

Regarding the optoelectronic case, we have found that the time delay of single optoelectronic feedback systems can be also retrieved from numerical and experimental time series using the standard techniques. Here, we have particulary studied the effect of the nonlinearity strength and the response time of the system on the time delay identification. We have found that an increment of the nonlinearity strength decreases the amplitude of the markers located at the time delay. On the other hand, the time delay of the system can be overestimated by some standard identification techniques due to the response time of the system. This effect is more noticeable for low nonlinearity strengths and time delays comparable with the response time. The forecasting error of a global model is the only technique that in a noisy system gives a accurate estimation of the time delay. In systems under moderate noise, the noise of the time series can be filtered so the filling factor and the statistical interval between extrema give estimated time delays that avoid the effect of the response time of the system.

In the optoelectronic system, we have also analyzed the two fixed delays case for two different configurations, serial and parallel. As happens with the all-optical systems the addition of a second delay does not avoid the time delay identification. In the parallel configuration it is possible to extract the delays using the same techniques that work for single delay systems. In the serial

configuration we have modified the filling factor method and the forecasting error of a model to identify multiples time delays. However, in this case the computational time required to identify the time delays increases exponentially with the number of delays.

In the two delay case, the time delay identification is only ambiguous when both delays are multiples or have close values. However, the relevance of both delays in the reconstruction of the nonlinear dynamics is a question that has to be addressed. The proximity or relationship of both delays can make possible the nonlinear reconstruction knowing only the approximate time delay given by the identification techniques. These results are valid for the optoelectronic and optical systems.

Actually, the most promising approach to avoid the time delay identification seems to be the variable time delay. However, we have developed customized techniques to extract the time delay function when the variable time delay is a periodic function. The procedure consists on extracting the period of the time delay from the delayed mutual information. Posteriorly, a modified filling factor method is used to obtain the time delay function. We have applied this technique to extract periodic time delays from experimental time series of an optoelectronic system.

Finally, let us mention that we have also analyzed the time delay identification from experimental time series of a optoelectronic system that presents chaos in intensity [Goedgebuer et al. 2002]. This system uses a Mach-Zehnder modulators to generated the nonlinearity of the system. Only low nonlinearities can be reached with this system and the response time of the system is low compared to the time delay. Therefore basic techniques as AF or DMI estimate the time delay with a good accuracy.

Chapter 4

Nonlinear dynamics reconstruction of time-delay systems

Modelling and predicting the dynamics of nonlinear chaotic systems is a challenging problem with important applications in many real-world problems. Most of the research done in nonlinear dynamics modelling from data is focused on low-dimensional dynamics. Different non-parametric and parametric techniques have been proposed for constructing approximate models from time series. The general approach consists in reconstructing the phase space from the observed data, most often by making use of the time delay embedding theorem [Sauer et al. 1991, Takens 1981]. Unfortunately, this approach suffers from severe limitations as soon as the dimension of the chaotic attractor becomes large.

Bünner et al. [1996a;b] has shown that it is possible to reconstruct the dynamics of time delayed chaotic systems with high dimensional attractors with much less variables than those required by the standard embedding theorems. They exploit the particular structure of time delay systems for the reconstruction. Following a similar approach, other investigators have reconstructed the dynamics of time delay chaotic systems [Bezruchko et al. 2001, Ellner et al. 1997, Ponomarenko and Prokhorov 2002, Prokhorov et al. 2005, Prokhorov and Ponomarenko 2008, Robilliard et al. 2006, Udaltsov et al. 2003, Voss and Kurths 1997; 1999, Zhou and Lai 1999]. These methods are only valid for scalar time delay systems, i.e. systems involving a single variable. Posteriorly,

Bünner et al. [1997] extended their technique to multi-variate delay systems, but a multi-variate measurement is required.

In the above mentioned cases, it is assumed that the structure of the delay differential equation that governs the chaotic generator is known. The method only estimates the functions and the parameters from the time series. A more general approach to the problem is to consider that the only information available about the chaotic generator is that we deal with a time-delay system. No more details about the particular structure of the delay differential equation are required. Under this assumption, Bünner et al. [2000a;b], Hegger et al. [1998] have demonstrated that it is possible to reconstruct the dynamics of time-delay systems with special "embedding" spaces which include both short-time and feedback-time delayed values of the variable. In this way, the dynamics is recovered in a space with a dimension smaller than the attractor's dimension, that can be high dimensional. They used this special "embedding" to reconstruct the nonlinear dynamics of time-delay systems with a local linear model [Bünner et al. 2000a;b, Hegger et al. 1998].

This special "embedding" can be applied to the same nonparametric models used to reconstruct low dimensional dynamics with standard embedding techniques. Among these nonparametric models, we want to highlight the neural networks (NNs). They can theoretically approximate any arbitrary function to any degree of accuracy and are robust versus moderate noise levels. Moreover, NNs are global models that overcome the problems associated to local models.

In this chapter we successfully apply modular and standard feedforward neural networks to recover the nonlinear dynamics of high dimensional time-delay systems, using the appropriate embedding techniques. The chapter is organized as follows. Section 4.1 is devoted to explain in detail the method to recover the nonlinear dynamics with multilayer feed-forward neural networks (FFNNs) and modular neural networks (MNNs) using the special embedding approach for high dimensional time-delay systems. In sections 4.2 and 4.3, we apply this technique to the Mackey-Glass and the Ikeda systems, respectively. For both systems numerical and experimental cases are considered. Next, in section 4.4, we reconstruct the nonlinear dynamics of a Ikeda system with two delays, extending the special like embedding to the double delay case. Finally, section 4.5 is devoted to the reconstruction of the nonlinear dynamics of an experimental optoelectronic feedback system. We summarize the main conclusions in section 4.6.

4.1 Nonlinear dynamics modelling of time-delay chaotic systems

The deterministic nature of chaotic systems allows modelling its functional structure from a time series using appropriate nonlinear techniques. In recent years, new approaches for nonlinear time series modelling have emerged (see [Kantz and Schreiber 1997] for a survey).

In the most general case, we deal with a measured time series, $x(t)$, sampled with a period δt, that lies on a D_F dimensional attractor of a Nth-order deterministic dynamical system. The starting point to model the nonlinear dynamics is to obtain an embedding space from the recorded data. A convenient, though not unique, embedding vector representation has the following form:

$$\mathbf{v}(t) = (x(t - \tau_e), ..., x(t - m\tau_e)) \tag{4.1}$$

where τ_e is the embedding time and m is the embedding dimension. According to the embedding theorems [Sauer et al. 1991, Takens 1981], if $m > 2D_F$ there will be a smooth map so:

$$x(t) = \tilde{\mathbf{F}}(\mathbf{v}(t)) \tag{4.2}$$

Taking this into account, one can build a model of a chaotic dynamical system. Clearly, a key issue in modelling nonlinear dynamics is the selection of an appropriate embedding space. As early emphasized, the direct reconstruction of attractors from scalar data through time delay embedding using Takens theorem is limited to low dimensional systems. The high dimension of typical time-delayed feedback systems usually prevents the implementation of the standard embedding techniques.

An optimal solution to such problem might require an embedding space in which the temporal distances from one coordinate to another are not necessarily the same. These embeddings are called irregular or nonuniform [Jones et al. 2002].

The reconstruction of the dynamics of high dimensional attractors with a nonuniform embedding space which include both short-time and feedback-time delayed values of the variable was carried out by Bünner et al. [2000a;b], Hegger et al. [1998]. The dynamics is recovered in a space with a dimension smaller than the attractor's dimension. They proved that it is possible to identify the underlying deterministic structure of systems ruled by delay differential equations (DDE) of the form:

$$\dot{x}(t) = F(x(t), x(t-\tau)) \tag{4.3}$$

when τ is the time delay. The time series $x(t)$ is sampled at equally spaced intervals δt. Note that here we only consider continuous time systems. However, a similar approach can be used in the case of the delayed maps (DM).

Bünner et al. [2000a;b] reconstruct the nonlinear dynamics in a state space whose dimension is independent of τ, in spite of the fact that D_F depends on the time delay. The dynamics in the state space is given by:

$$\hat{x}(t) = \tilde{F}(\mathbf{v}_\tau(t)), \tag{4.4}$$

where $\tilde{F}$ belongs to some class of parameterized functions, and

$$\begin{aligned} \mathbf{v}_\tau(t) &= (x(t-\tau_e), \ldots, x(t-m_1\tau_e), \\ &\quad x(t-\tau), x(t-\tau-\tau_e), \ldots, x(t-\tau-m_2\tau_e)) \end{aligned} \tag{4.5}$$

When the time delay τ is not a multiple of the sampling time, the closest sample is considered. Bünner et al. [2000a;b] demonstrated that the knowledge of these vectors is sufficient to determine the future dynamics. However, the sampling time has to be sufficiently short.

Bünner et al. [2000b] have applied this "special" or nonuniform embedding technique to recover the nonlinear dynamics of a CO_2 laser with a local linear model. Nonetheless there are different nonparametric models that can be used to reconstruct the nonlinear dynamics applying this special space method. To overcome the problems of the local linear models, such as the effort required to assemble the different local fits, one can use global models. In our case we will use neural networks (NNs) to model the dynamics of time-delay systems.

4.1.1 Standard and Modular Neural Networks

Artificial Neural Networks (NNs) have been successfully applied for nonlinear dynamics modelling of low dimensional chaotic systems [Genay and Liu 1997, Principe et al. 1992]. The NN models have been trained with input-output samples from the time series $x(t)$ according to the embedding theorem [Sauer et al. 1991, Takens 1981]. Moreover, it has been shown that the resulting approximate neural models reproduce the dynamical behavior and the nonlinear characteristics of the original model (similar unstable periodic orbits [Suykens and Vandewalle 1995], similar Lyapunov exponents or fractal dimension [Chen et al. 1997], etc.).

In fact, if the feedback time τ is short enough, the dynamics of time-delay chaotic systems can be approximated using the Takens embedding with an input vector $(x(t-\tau_e), ..., x(t-m\tau_e))$, where $m\tau_e > \tau$. For instance, Principe et al. [1992] approximates a Mackey-Glass model with $\tau = 17$ considering a input vector of the form $(x(t-6), x(t-12), \ldots, x(t-24))$. Nevertheless, when the feedback time is large, the above input vector may contain too many values leading to models with a large number of parameters. Therefore, for a successful recovery of high dimensional time-delay systems one has to apply the nonuniform embedding described in the previous section.

Among the different classes of NNs, it has been shown that feedforward neural networks (FFNNs) are an universal approximator for continuous (one hidden layer) or arbitrary (more than one hidden layer) functions [Cybenko 1989]. Hence, FFNNs are a powerful method to reconstruct the nonlinear dynamics of delayed or non-delayed nonlinear systems, independently of the particular details of the system. One of its main advantages is that no-priori knowledge of the system apart from the time delay (in the case of the time-delay chaotic systems) is necessary to construct the neural network model. The value given by the FFNN is $x_{nn}(t) = F_{nn}(\mathbf{v}(t))$, where $\mathbf{v}(t)$ is the embedding vector defined by equation (4.1) or (4.5) for non-delayed and delayed chaotic systems, respectively. The training process is carried out by considering input-output couples of the form $(\mathbf{v}(t), x(t))$.

Although the proposed standard FFNNs give faithful models that reconstruct the nonlinear dynamics, in recent years modular neural networks (MNNs) [Happel and Murre 1994] and functional networks [Castillo et al. 1999] have been introduced for obtaining flexible models using the idea of modularity. The concept of modularity is linked to the notion of local computation: each module is an independent system and interacts with others within a whole architecture in order to perform a given task. Thus, modularity tends to create some structure within the topology to specialize the performance of each module. In the case of MNNs these ideas lead to dispersed networks beyond the fully connected topology, thus requiring a smaller number of parameters. For instance, figure 4.1 shows a feedforward neural network and a more simple modular network dealing with the same problem.

The MNNs overcome some of the problems of fully connected FFNNs. However, in order to have meaningful and efficient models, each module has to perform an interpretable and relevant function according to the mathematical or physical properties of the system (domain knowledge). Thus, we need to adapt the structure of the modular network to the particular system.

Most of the scalar delay differential equations (DDE) can be expressed as the combination of two functions, f and g, each one depending only of the

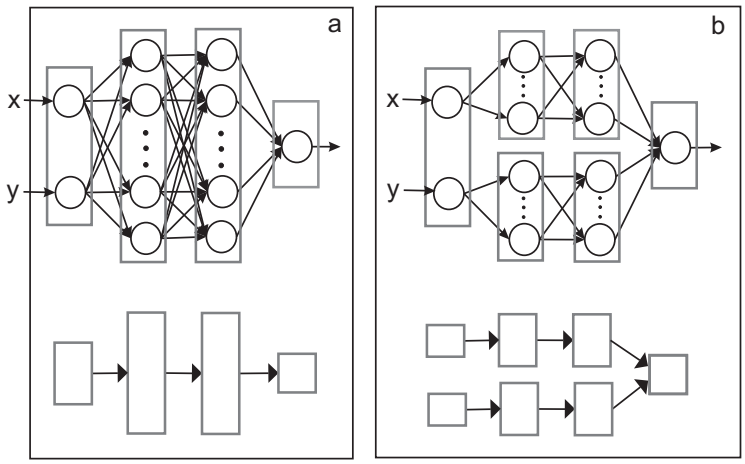

Figure 4.1: (a) A fully connected feedforward network; (b) a particular modular neural network

non-feedback and feedback part of the dynamics, respectively. In these cases, the equation (4.3) can be expressed as:

$$\dot{x}(t) = f(x(t)) + g(x(t-\tau)) \tag{4.6}$$

According to the structure of (4.6), we can use a MNN with two modules, one for the non-feedback part with input data delayed by the embedding time, τ_e, $\vec{x}_{nf} = (x(t-\tau_e), ..., x(t-m_1\tau_e))$ and a second one for the feedback part with input data delayed by the feedback time, τ, $\vec{x}_f = (x(t-\tau), ..., x(t-\tau-m_2\tau_e))$, where m_1 and m_2 are the numbers of non-feedback and feedback inputs, respectively. A feed-forward neural network is used for each of the modules. The value given by the MNN is $x_{nn}(t) = f_{nn}(\vec{x}_{nf}) + g_{nn}(\vec{x}_f)$, where f_{nn} and g_{nn} correspond to the functions inferred by the non-feedback and feedback modules, respectively (see figure 4.2).

Therefore, when the system can be expressed as the combination of two functions as in equation (4.6), instead of using a standard FFNN with an input vector given by (4.5), a MNN with two modules can be used. In both cases, the inputs are based on the nonuniform embedding approach used by Bünner et al. [2000a;b], but in the MNN case, the input vector is divided into its delayed and non-delayed part.

Once the type of model to reconstruct the nonlinear dynamics has been chosen, the following step to build the model is to determine the appropriate embedding space and finally to estimate whatever parameters the model may

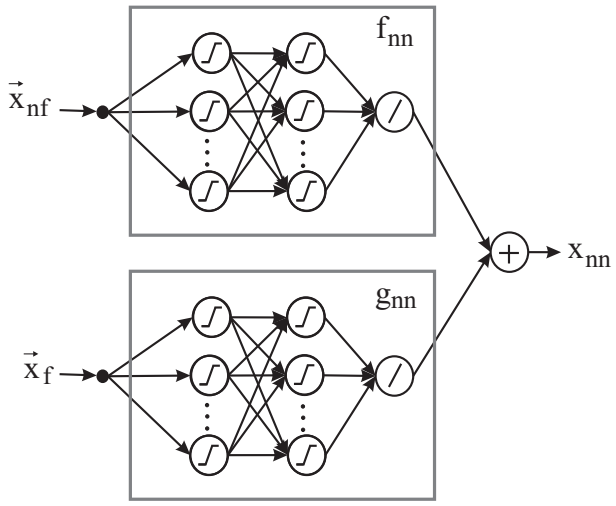

Figure 4.2: Topology of the MNN for a system described by equation (4.6). The input vectors are $\vec{x}_{nf}$ and $\vec{x}_f$ for the non-feedback and feedback modules, respectively. The output of the MNN is given by $x_{nn}(t) = f_{nn}(\vec{x}_{nf}) + g_{nn}(\vec{x}_f)$. Each module is formed by a feed-forward neural network.

have. The parameters are estimated by minimizing a cost function. In the case of the NNs, the most common cost function is the root mean squared error (RMSE) defined as:

$$RMSE = \sqrt{\frac{1}{N-1}\sum_{i=1}^{N}(x(t_i) - x_{nn}(t_i))^2} \tag{4.7}$$

where N is the number of test points, $x_{nn}(t)$ is the output of the NN and $x(t)$ is the desired output. Let us point out that to work with NNs, the original signal $x(t)$ is normalized to zero mean and standard deviation one. Thus, the errors given by the NN are normalized. Furthermore, as mentioned in the introduction (see 2.7), the RMSE depends on the initial conditions of the NN weights. In order to overcome this problem and avoid ill-posed initial conditions, the RMSEs presented through this thesis are calculated as the mean of the best five test errors obtained out of ten models trained starting at different initial weights.

A low RMSE is a necessary condition for the global reproduction of the observed dynamics, but does not guarantee the validity of the model when it is iterated in time. It has been proposed to use identical chaotic synchronization as a validation method [Aguirre et al. 2006, Brown et al. 1994]. The basic idea

behind this validation technique is that the identical synchronization is only possible when the model is very similar to the original system.

On the other hand, the number of parameters of the model that have to be estimated depends on the model structure. Hence, another key point is to choose a model structure that is as simple as possible, but also complex enough to capture the dynamics underlying the data. One way of addressing the structure selection problem is to define some measure of complexity for a given model. For instance, the maximum description length has been used in several papers [Small and Tse 2002]. However, in our particular case, to determine the optimal number of neurons we train the NN with different number of neurons. The optimal network can be easily obtained by visual inspection of the errors and the number of parameters.

4.2 The Mackey-Glass system

The Mackey-Glass [Mackey and Glass 1977] model is one of the most popular time-delay chaotic systems. It is a first order scalar differential equation with a force field that depends on a past value of the variable itself. The simplicity of the model and its easy implementation on electronic circuits, has converted the Mackey-Glass (MG) model in a paradigm of nonlinear dynamics reconstruction of time-delay chaotic systems.

One of the first attempts to use NNs to predict time-delay chaotic systems was made by Principe et al. [1992] with a MG system. Nevertheless, they used a Mackey-Glass with a short time delay, so the dimension of the system is not high and standard embedding techniques can be applied. In this section, we extend this pioneer work to Mackey-Glass systems with higher dimensions (longer time delays) by the use of the special embedding techniques that include the different (short and feedback) time scales present in the dynamics of the model.

The Mackey-Glass model is described in subsection 4.2.1. In subsection 4.2.2 we apply standard and modular feedforward NNs to recover the nonlinear dynamics of the MG from numerical time series. Next, in subsection 4.2.3, MNNs are used to reconstruct the dynamics of the MG from experimental time series. In all the cases we use the special like embedding described in the previous section.

4.2.1 The Mackey-Glass Model

The Mackey-Glass model [Mackey and Glass 1977] was suggested in a physiological context (regulations of the productions of red blood cells), where the

mechanism of time delayed feedback is rather common. It is described by a time-delay differential equation of the form:

$$\dot{x}(t) = f(x(t)) + g(x(t-\tau)) = -bx(t) + a\frac{x(t-\tau)}{1+x(t-\tau)^c} \tag{4.8}$$

where τ is the time delay and $a = 0.2$, $b = 0.1$ and $c = 10$ are the standard parameters. The system is chaotic for $\tau >$16.8. Its dimension is greater than 2.94 for $\tau > 30$. For long time delays, the dimension increases linearly with the delay, while the metric entropy remains constant [Farmer 1982]. This is due to the fact that all the Lyapunov exponents, both positive and negative, become smaller in absolute value as the delay is increased. Specifically, the positive exponents decrease as $1/\tau$.

We have carried out numerical simulations of the system to obtain data sets for values of the feedback delay time that correspond to short, τ=20, and long-delay systems, $\tau = 100$ and 300. The dimension of the chaotic attractor is given by 2.4 for $\tau = 20$, 10 for $\tau = 100$ and 30 for $\tau = 300$ [Farmer 1982]. Note that the linear response time of the system is 10. In our numerical simulations we have used the Adams-Moulton predictor-corrector scheme [Press et al. 1992] with a time integration step of 0.01. The time series corresponding to time delays of 20 and 300 are plotted in figure 4.3. Clearly, the time series show a more irregular behavior for $\tau = 300$ than for $\tau = 20$.

4.2.2 Nonlinear Modelling with Neural Networks

We are interested in approximating the functional model which characterizes the dynamics of the time series, $x(t)$, as a function of the past values of $x(t)$. The only available information is the observable time series, $x(t)$, obtained from equation (5.6) and sampled at equally spaced intervals with $\delta t = 0.1$.

To this aim we first consider standard feedforward neural networks (FFNNs) with sigmoidal $\sigma(y) = 1/(1+e^{-y})$ and linear activation functions for hidden and output layers, respectively. The FFNNs are trained with an input vector, $\mathbf{v}(t) = (x(t-\tau_e), \ldots, x(t-m_1\tau_e), x(t-\tau), \ldots, x(t-\tau-m_2\tau_e))$, where m_1 and m_2 are the number of input variables for short and feedback delay time components, respectively. The embedding time, τ_e, is in this case equal to the sampling time, δt. Note that the form of the input vector, $\mathbf{v}(t)$, fits the special embedding vector presented in the previous section for time-delay systems (see equation (4.5)). We use 21000 input-output patterns from the time series $x(t)$ of the form $(\mathbf{v}(t), x(t))$. This set is divided into two parts; the first one (1000 data) is used for training the NN using the Levenberg-Marquad algorithm [Hagan et al. 1996], whereas the second one (20000 data) is reserved

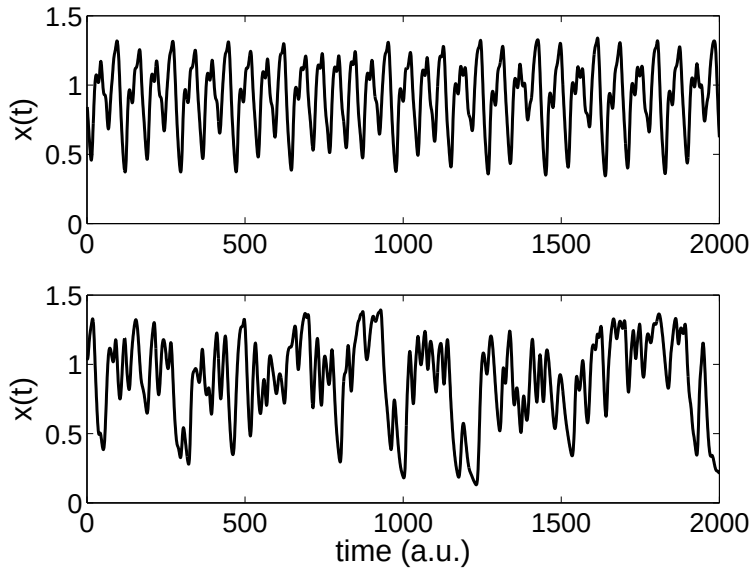

Figure 4.3: Numerical time series of the Mackey-glass system defined by equation (5.6) for $\tau = 20$ (top) and $\tau = 300$ (bottom).

for testing the resulting models. Note that the original time series, $x(t)$, is normalized with zero mean and standard deviation one before to use it as input of the FFNN.

At this point, let us point out that a successful extraction of the nonlinear dynamics of time-delay chaotic systems from a time series involves detecting the correct delay time. The time delay can be identified in a Mackey-Glass system with the same techniques that have been used in the previous chapter for the Ikeda system with low nonlinearity strength.

Table 4.1 shows the normalized test RMSE obtained after training the neural network with $m_1 = m_2 = 3$. We have considered different neural networks with increasing number of parameters (neurons) to fit the nonlinear dynamics of the Mackey-Glass time series with feedback times 20, 100, and 300. Note that as the number of parameters (neurons) increases, the normalized test RMSE decreases.

Hereafter, we use modular neural networks (MNNs) instead of the FFNNs to reconstruct the nonlinear dynamics of the MG. Modular neural networks can apport models with a lower number of parameters and more flexibility. The application of the MNN requires some prior knowledge of the problem that permits its decomposition into simpler tasks. In this particular case, we know

Model	FFNN(2:2)	FFNN(4:2)	FFNN(6:3)	MNN(2:2)	MNN(4:2)
Param.	20	38	63	14	26
τ=20	$5.1 \cdot 10^{-3}$	$3.3 \cdot 10^{-3}$	$2.8 \cdot 10^{-3}$	$2.9 \cdot 10^{-3}$	$2.7 \cdot 10^{-3}$
τ=100	$4.9 \cdot 10^{-3}$	$1.1 \cdot 10^{-3}$	$9.24 \cdot 10^{-4}$	$9.04 \cdot 10^{-4}$	$9.41 \cdot 10^{-4}$
τ=300	$6.5 \cdot 10^{-3}$	$2.7 \cdot 10^{-3}$	$2.7 \cdot 10^{-4}$	$2.6 \cdot 10^{-4}$	$2.3 \cdot 10^{-4}$

Table 4.1: Total number of parameters and test forecasting errors for different feedforward (FFNN) and Modular Neural Networks (MNN). FFNN(a:b) denotes a FFNN with two hidden layers with a and b neurons, respectively. MNN(a:b) denotes a modular network with a two layer a:b FF network for the nonlinear feedback component.

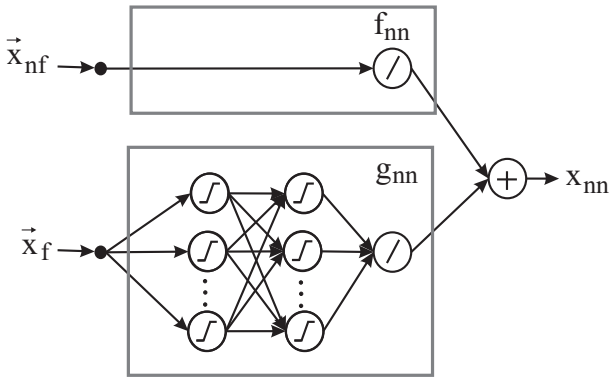

Figure 4.4: Topology of the MNN used in this work. The input vectors for the non-feedback and feedback modules are $\vec{x}_{nf}$ and $\vec{x}_f$, respectively. The output of the MNN is given by $x_{nn}(t) = f_{nn}(\vec{x}_{nf}) + g_{nn}(\vec{x}_f)$. The non-feedback module is formed by a linear neuron and the feedback module by a feedforward neural network.

that the original MG model can be divided into two functions (f and g), each one depending only on the feedback or non feedback part (see equation (5.6)). Based on this knowledge, we design a modular neural network with a linear component (neuron) for the short-time module and a FFNN for the feedback module (see figure 4.4). The normalized test RMSE are shown in table 4.1 when the MNN is trained with different number of neurons (parameters) in the feedforward module.

From table 4.1 we can obtain two main global conclusions. First, although the dimension of the attractor increases with the delay time, the neural network models can fit the dynamics with a similar degree of accuracy for the

different time delays. This conclusion is in agreement with similar results obtained with local models [Hegger et al. 1998] and with the fact that the metric entropy of the system remains almost the same for the different time delays [Farmer 1982]. Second, the MNNs obtain better results than the FFNNs with less number of parameters.

On the other hand, although the results shown in table 4.1 indicate a good accuracy in one-step ahead prediction using NNs, it does not mean that the obtained neural model can reproduce the dynamics of the MG system when iterated in time. A small forecast error of the constructed model is necessary but not sufficient condition to assure the model has captured the nonlinear dynamics of the system.

We use identical chaotic synchronization for comparing the dynamics of chaotic systems [Aguirre et al. 2006, Brown et al. 1994]. We consider diffusive coupling by adding a term $k\Delta^s(t) = k(x(t) - x^s_{nn}(t))$ to the approximate neural system in the short-term delayed component of the input vector. This means that the output of the synchronized MNN, x^s_{nn}, is given by:

$$\begin{aligned} x^s_{nn}(t) = \quad & F_{nn} \quad (x^s_{nn}(t-\tau_e) + k\Delta^s(t-\tau_e), \ldots, \\ & \qquad x^s_{nn}(t-m_1\tau_e) + k\Delta^s(t-m_1\tau_e), \\ & \qquad x^s_{nn}(t-\tau), \ldots, x^s_{nn}(t-\tau-m_2\tau_e)) \end{aligned} \tag{4.9}$$

where k is the coupling factor, x is the original signal and F_{nn} is the nonlinear function inferred by the NN.

The synchronization error η is defined as the RMSE between the original normalized signal and the output of the synchronized neural network x^s_{nn}. Figure 4.5 shows the synchronization error versus the coupling parameter k for the modular and FF neural networks. The synchronization between the original system and the model is achieved. In the range of k from 0.3 to 1.9, the synchronization error of the NN is of the order of the test error. Synchronization is unstable for large values of k. We will analyze this point in more detail in subsection 4.3.2. Although test errors are similar, the synchronization error is always greater for the FF neural networks than for the modular ones.

The agreement between the Lyapunov exponents of the original system and the model is also used as a tool to validate a model. In this case, we have calculated the largest Lyapunov exponent from the numerical time series generated by the iteration of the neural network model using the method developed by Wolf et al. [1985], obtained 0.0079 (0.0035) for $\tau = 20$ (100). These values are comparable with the largest Lyapunov exponent given by

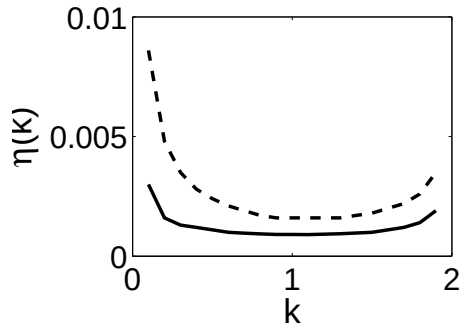

Figure 4.5: Synchronization error vs. the coupling parameter for the MG system with $\tau = 100$. The solid (dashed) line corresponds to MNN(2:2) (FFNN(4:2)).

the linearized original equation, 0.0077 (0.0035) for $\tau = 20$ (100). These results are consistent with the previous validation of the model using identical synchronization method.

Finally, we conclude that the MNNs are a more suitable option than standard NNs to extract the nonlinear dynamics of the MG model. We have demonstrated that the MNNs offer models with better test RMSE for the same number of parameters than the FFNNs. Moreover, smaller synchronization errors are obtained with the modular than for FF neural networks when the synchronization between the data and the model with diffusive coupling is used to test the similarity of the system and the NN model.

In addition to NN, new approaches as support vector machines [Müller et al. 1997, Quiñonero Candela and Hansen 2002] or recurrent neural networks [Ma et al. 2007] have been used to predict the time series of a MG model. In these studies, short time delays ($\tau = 17$) with standard embedding techniques have been considered. The results for the short time delays obtained using NNs are similar to the results presented in the above mentioned references.

4.2.3 Experiments

We have implemented the Mackey-Glass system in an electronic circuit. The circuit was built using a bucket brigade delay line for the feedback term. The feedback delay time can be varied from 2.5 ms to 27 ms. The linear response time is around 2 ms. The layout of the circuit is shown in figure 4.6. The signals were acquired using a 2GS/s oscilloscope with a resolution of 12 bits. The sampling period was 0.04 ms and the total acquisition time 2 s, i.e., 50000 data points. A sample of the recorded time series for long and short

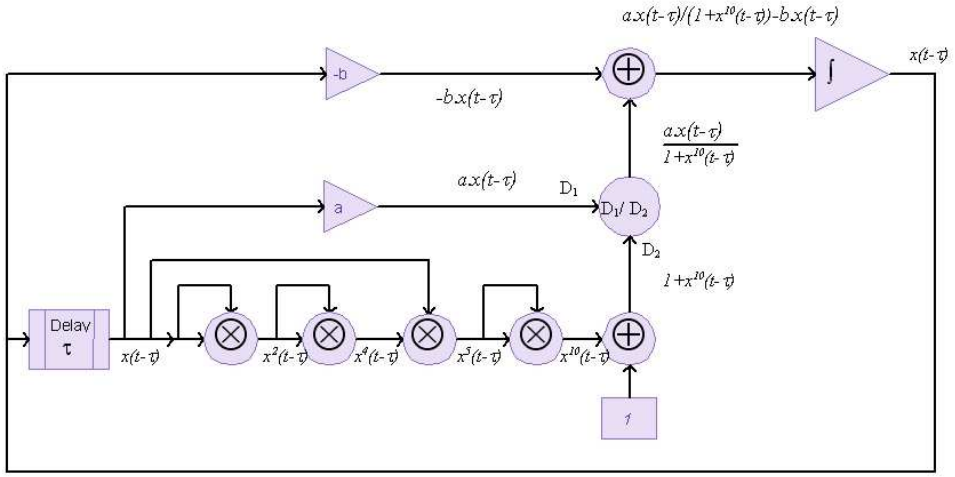

Figure 4.6: Scheme of the experimental Mackey Glass circuit.

feedback delay times is plotted in figure 4.7. The short time delay series looks more regular than the large time delay series, as happened with the numerical simulations (see figure 4.3).

In this subsection we apply MNNs to the experimental time series recorded from the above mentioned circuit for a short ($\tau = 5.26$ ms) and a long value ($\tau = 20.6$ ms) of the feedback delay time.

As we have early emphasized, a successful extraction of the nonlinear dynamics from the time series involves detecting the correct delay time. As mentioned in chapter 3, a simple way for estimating the delay time is considering the first dip that appears in the autocorrelation function (AF). However, this method leads to an overestimation of the delay time, due to the finite reaction of the system [Bünner et al. 2000a]. To overcome this problem and considering that the experimental data are almost free noise, we can use the filling factor method (FF) taking into account only the extrema of the time series. The estimated time delay, $\hat{\tau}$, with both methods is presented in table 4.2. The overestimation with the AF is approximately $T/2$, where T is the response time. Therefore, the AF is not a suitable method to recover the time delay in this particular case. This results are in total agreement with the conclusions reached in chapter 3 about the time delay identification in chaotic systems.

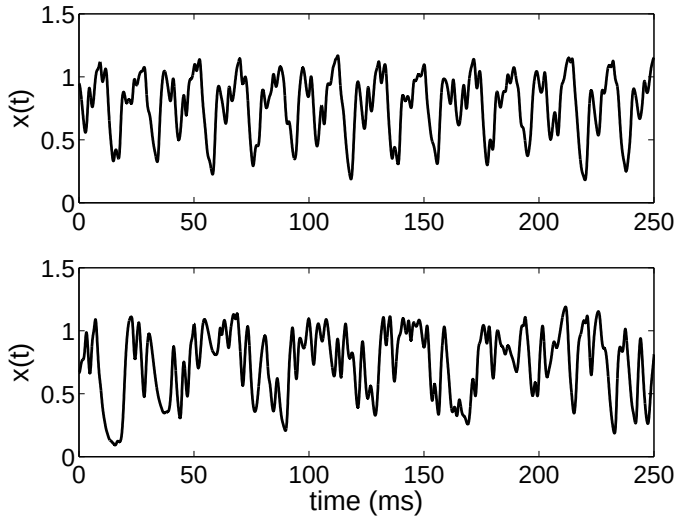

Figure 4.7: Experimental time series of the Mackey Glass system. Top: $\tau = 5.26$ ms. Bottom: $\tau = 20.6$ ms.

	$\hat{\tau}$ (ms)	
	short τ	long τ
AF	6.12	21.4
FF	5.24	20.6

Table 4.2: Estimated time delay ($\hat{\tau}$) from experimental MG data with the Autocorrelation function (AF) and the filling factor method (FF). The experimentally measured time delay is 5.26 ms and 20.6 ms respectively.

Regarding the nonlinear dynamics reconstruction, two MNN(2:2) have been trained for the data corresponding to 5.26 and 20.6 ms feedback time delays. The procedure is identical to the one followed with the numerical data. The test RMSE obtained are $3.9 \cdot 10^{-3}$ and $4.1 \cdot 10^{-3}$, respectively. To test the similarity of the MNN model with the electronic circuit dynamics a diffusive coupling is used with the experimental data as the driving signal. Figure 4.8 shows that when the coupling constant ranges from 0.5 to 1.4 synchronization errors are similar to test errors. Moreover, the phase portrait of both models are found to be indistinguishable from the original ones (see figure 4.9). Finally, we have also calculated from the experimental time series the largest

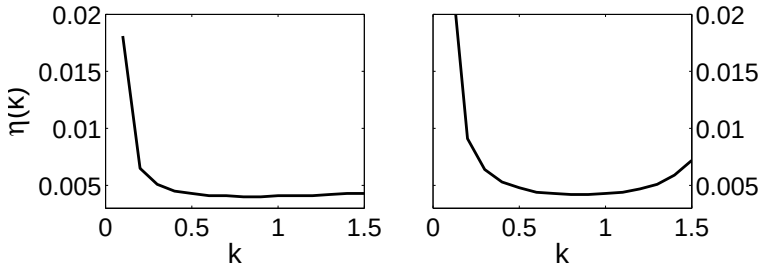

Figure 4.8: Synchronization error of the experimental MG data with a MNN(2:2). Left: $\tau = 5.16$ ms. Right: $\tau = 20.6$ ms

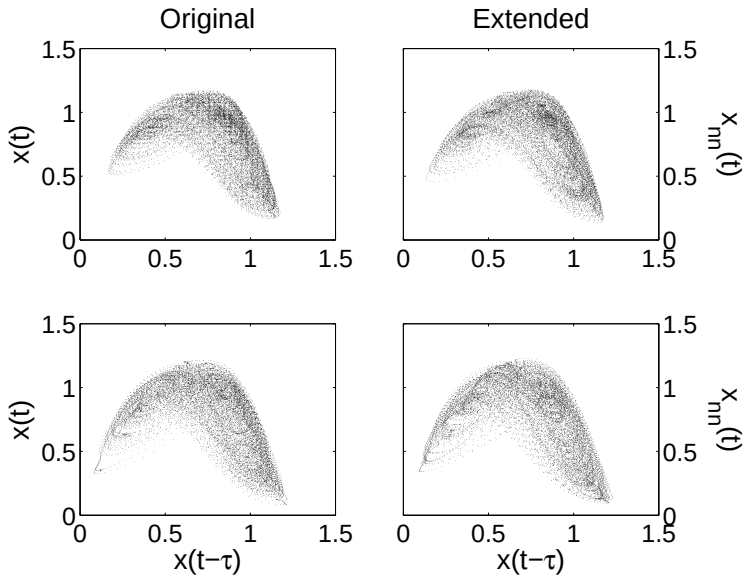

Figure 4.9: Phase Portrait of the original experimental time series (left) and the extended time series with the MNN(2:2) model (right). Top: $\tau = 5.16$ ms. Bottom: $\tau = 20.6$ ms

Lyapunov exponent, obtained 0.04 ms^{-1} (0.02 ms^{-1}) for $\tau = 5.26$ ms (20.6 ms).

Therefore, it has been shown that the nonlinear dynamics of the electronic circuit can be reconstructed with a simple MNN(2:2) for different values of the feedback delay time. Moreover, as in the numerical simulations, we have found that the complexity of the neural network model required to reconstruct the nonlinear dynamics with a small training error (of order 10^{-3}) does not

increase with the delay time. This seems to indicate, that when the special like "embedding" is used, the difficulty to recover the nonlinear dynamics depends on the entropy of the system and not on its dimension.

Through this section, we have used a Mackey-Glass system as an initial approach to the nonlinear dynamics reconstruction with neural networks. In successive sections we will present more optimized NN models to recover the nonlinear dynamics of time delay chaotic systems, particularly the Ikeda system.

4.3 The Ikeda system

The Ikeda system has turned out to be a paradigm for the dynamical behavior of delayed-feedback systems under the variation of control parameters. Together with the Mackey-Glass is one of the most well-known scalar chaotic system.

The Ikeda scalar delay differential equation was proposed to model a passive optical bistable resonator system [Ikeda 1979, Ikeda and Matsumoto 1987] and is given by:

$$T\dot{x}(t) = f(x(t)) + g(x(t-\tau)) = -x(t) + \beta(\sin^2(t-\tau) - \phi) \tag{4.10}$$

where τ is the feedback time, T is the response time of the system and ϕ is the phase. The parameter β determines the strength of the feedback as well as the strength of the nonlinearity. The complexity of the system, related to the number of extreme values of the $\sin^2$ nonlinear function increases with β (see chapter 2, subsection 2.4.2). The Ikeda system permits the study of the nonlinear modelling as function of the nonlinearity of the system, whereas the MG system has always a nonlinear function with only one extreme that corresponds to low nonlinearity strength.

In addition to the above mentioned features, one of the main reason to consider the Ikeda system is that the dynamics of some generators in optical chaotic communication systems [Goedgebuer et al. 1998a;b, Larger et al. 1998a;b] can be described by the Ikeda equation (see 2.4.2). The extraction of the Ikeda nonlinear dynamics from time series compromises the security of these systems, allowing the extraction of the transmitted message as we shall see in chapter 6.

In this section we extract the Ikeda nonlinear dynamics from time series applying MNNs with the nonuniform embedding. We can also use the standard FFNN to recover the nonlinear dynamics. However, we have demonstrated

that MNNs present serious advantages over the standard ones for the MG (see section 4.2) and the Ikeda system [Ortín et al. 2005; 2007]. From now on, we only apply the MNNs.

The section is organized as follows. In subsection 4.3.1 we reconstruct the nonlinear dynamics of the Ikeda system from numerical time series with MNNs using the especial embedding described in section 4.1. Section 4.3.2 is dedicated to the validation of the MNN model. Finally, in subsections 4.3.3 and 4.3.4 we study the effect of the time delay mismatch and the presence of noise on the obtained MNN model.

4.3.1 Nonlinear modelling with Modular Neural Networks

Following the same approach as in the case of the Mackey Glass model, we reconstruct the nonlinear dynamics of the Ikeda system with a MNN. The MNN is trained from time series obtained by the simulation of equation (4.10) with a Adams-Bashforth-Moulton fourth order predictor-corrector method [Press et al. 1992] and an integration step of 0.01. To ensure the time series reproduce faithfully the characteristics of the continuous-time system even for $\beta = 50$, the sampling period is $\delta t = T/100$, where $T = 1$ is the linear response time.

Regarding the structure of the MNN, it has two modules, one for the non-feedback part with input data delayed by the embedding time (τ_e):

$$\vec{x}_{nf} = (x(t - \tau_e), ..., x(t - m_1\tau_e)) \tag{4.11}$$

and a second one for the feedback part with input data delayed by the feedback time (τ),

$$\vec{x}_f = (x(t - \tau - m_2\tau_e), ..., x(t - \tau), ..., x(t - \tau + m_2\tau_e)) \tag{4.12}$$

where m_1 and $2m_2 + 1$ are the numbers of non-feedback and feedback inputs, respectively. The value given by the MNN is $x_{nn}(t) = f_{nn}(\vec{x}_{nf}) + g_{nn}(\vec{x}_f)$, where f_{nn} and g_{nn} correspond to the functions inferred by the non-feedback and feedback modules, respectively. As in the case of the MG system, the feedback module is a feedforward neural network and the non-feedback module is a single linear neuron (see figure 4.4). We have checked that one non-linear neuron also yields a linear function for the non-feedback module. A non-feedback module with more layers and neurons only increases the parameters of the MNN model but not its accuracy. Clearly, a more complicated $f(x(t))$ would require a feedforward neural network in the non-feedback module.

Once the structure of the MNN has been chosen, we have to decide the number of inputs for the non-feedback and feedback modules (m_1 and $2m_2+1$).

The question is solved by trial and error. In free noise systems with small sampling periods, as a general rule we have found that $m_1 = 1$ and $m_2 = 1$ (i.e. three delayed input) are a good option. In fact, when the sampling period leads to time series with strong linear correlations between neighboring samples, the NN is able to minimize the forecast error only taking into account the linear dynamics if $m_1 > 1$. This yields no suitable models with lower forecasting error that fail in the reproduction of the nonlinear dynamics. Regarding the delayed inputs, $m_2 = 1$ is the minimum value to assure that the model can capture the dynamics. Not significant better models are obtained for larger values of m_2.

To determine the optimal number of neurons we train the MNN with different number of parameters (the number of neurons of the feedback module). A more precise way to obtain the optimal model is using some model selection algorithm (such as the Minimum Description Length Principle [Small and Tse 2002]). However, in this case, the optimal network can be easily obtained by visual inspection of the errors and the number of parameters.

Two main points have been improved respect to the procedure followed in the MG case to reconstruct the nonlinear dynamics with the MNN. The first is related to the composition of $\vec{x}_f$. In the special like embedding vector presented in (4.5) and used with the Mackey Glass system, the components delayed by the time delay are always consecutive to $x(t-\tau)$. Now, the delayed components are equally distributed around $x(t-\tau)$. For instance, if there are three delayed inputs, the input vector was $\vec{x}_f = (x(t-\tau)$,$x(t-\tau-\tau_e)$,$x(t-\tau-2\tau_e))$ for the MG case whereas now we have $\vec{x}_f = (x(t-\tau-\tau_e), x(t-\tau), x(t-\tau+\tau_e))$. Through trial and error, we have observed that slightly better models are obtained in the second case. Thus, the feedback inputs minimize the distance to the feedback coordinate, $x(t-\tau)$, that is the one that carries the information.

The second improvement concerns the training process, more specifically the way the training points are chosen. The time series is divided into two sets, one for the training and other for the test (see chapter 2, section 2.7). To capture faithfully the dynamics of the attractor with our model, the training set must cover the whole attractor. For the sake of clarity, let us suppose that the training set has the minimum size to cover the whole attractor. If we choose the training points consecutively from the training set (as in the MG case), we have to take all the set to assure a good capture of the attractor dynamics with the model. To reduce the number of training points, we can choose them randomly over the training set. However, with this approach, the proportion of training points corresponding to the less visited parts of the attractor can be negligible. To overcome this problem, we choose the

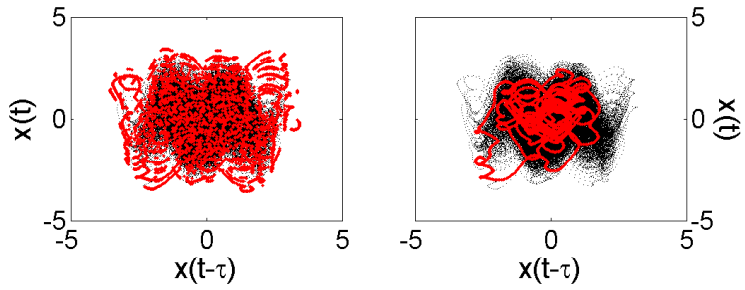

Figure 4.10: Black points correspond to $x(t-\tau)$ versus $x(t)$ for a Ikeda system with $\beta = 15$ and $\tau = 100$. The red points indicate the position of 3000 training points chosen consecutive (right) or to cover uniformly the attractor (left).

training points from the training ensemble so they are uniformly distributed over the attractor. In scalar time-delay chaotic systems, we achieve this by taking points randomly from the training ensemble until they cover uniformly the area $(x(t), x(t-\tau))$. To this aim, when β is high, the training set must cover a large time interval. This increases the minimum length of the time series used to train the NN, although the number of training points can be low. Figure 4.10 shows the position of the training points in the space $(x(t), x(t-\tau))$ for the Ikeda system with $\beta = 15$ when they are chosen to cover uniformly the attractor (figure 4.10 left) or consecutively (figure 4.10 right). It is clear that with the same number of training points, if they are chosen consecutively part of the dynamics is not trained. For the Ikeda system, we use 3000 training points uniformly distributed over the attractor when the system is noise-free.

Taking the previous points into account, in figure 4.11 we plot the RMSE of the MNN model, calculated over 100000 test points, for different values of β, τ (short $\tau = 10$ and long $\tau = 100$) and number of parameters of the MNN (neurons of the feedback module). The phase and the response time of the system are $\phi = 0.26\pi$ and $T = 1$. The results hold for different values of ϕ and T. Note that the embedding time is $\tau_e = 0.01$. The figure 4.11 shows that the MNN RMSE increases with the feedback strength of the system, β, but not with the time delay, τ. These results are related to the fact that the dimension of the system increases with τ but the entropy only increases with β. The case of β =25 corresponds to the limit value of β that has been performed experimentally [Goedgebuer et al. 1998a]. For a fixed β, the MNN error decreases as the number of parameters of the model increases. However, for MNN with sufficiently large number of parameters, the addition of more parameters does not lead to any further significant decrease of the MNN error.

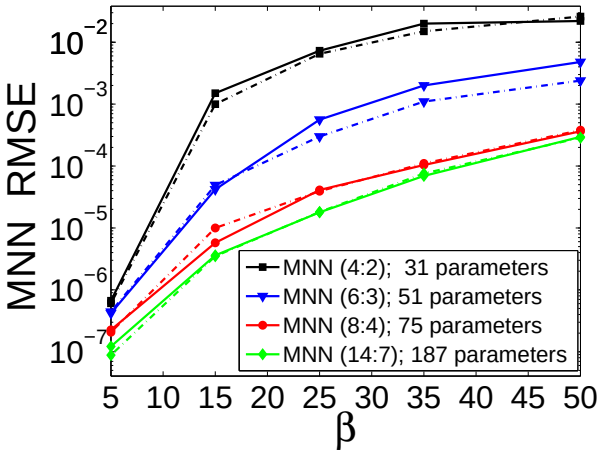

Figure 4.11: MNN RMS test error vs. β. The solid (dashed) lines correspond to $\tau = 100$ (10). The RMSE is presented for different MNN parameters. MNN(a:b) denotes a modular network with a two layer a:b FF network for the nonlinear feedback component.

Once the MNN has been trained, thanks to the modularity of the model, it is possible to represent the feedback and non-feedback functions given by the MNN model. Figure 4.12 shows the functions of non-feedback and feedback modules, f_{nn} and g_{nn}, for three different values of the feedback strength β, 5, 25 and 50, that yield nonlinear feedback functions with 3, 8 and 14 extrema respectively. Note that the MNN optimizes the total output of the model instead of the non-feedback and feedback modules independently. The functions extracted by the MNN approximately correspond to the linear and nonlinear terms of a discrete-time version of equation (4.10), given by:

$$x(t+\delta t) = x(t)(1-\delta t) + \delta t \beta \sin^2(x(t-\tau) - \phi) \tag{4.13}$$

From figure 4.12 it seems that $f_{nn} \approx x(t)(1-\delta t)$ and $g_{nn} \approx \delta t \beta \sin^2(x(t-\tau) - \phi)$. However, note that the functions f_{nn} and g_{nn} used in the neural network depend on the vectors $\vec{x}_{nf}$ and $\vec{x}_f$ respectively and not only on $x(t)$ and $x(t-\tau)$.

4.3.2 Validation of the model

The one-step-ahead forecasting error is a local measure of the validity of a given model. Therefore, a low RMSE is a necessary condition for a global reproduction of the observed dynamics, but it is not at all sufficient. As we already mentioned in the previous section, identical chaotic synchronization

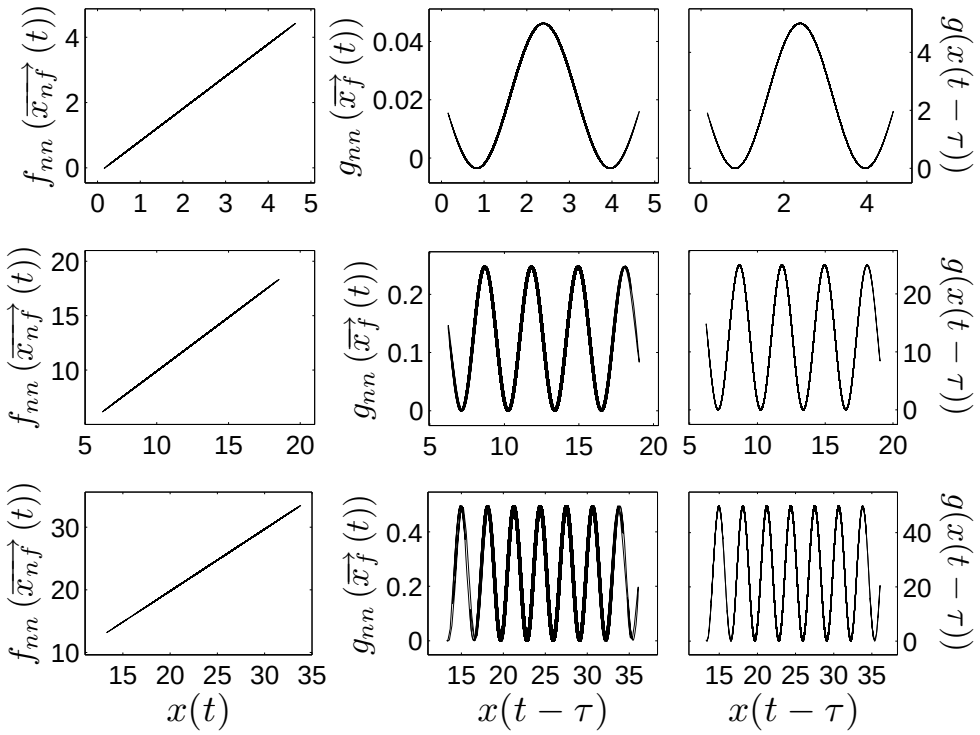

Figure 4.12: Comparison between the original nonlinear function (right) and MNN Functions for the non-feedback (left, vs. $x(t)$) and feedback (center, vs. $x(t-\tau)$) modules of the neural network. From top to bottom, the Ikeda system has $\beta = 5$, 25 and 50. In all the cases $\tau = 100$.

can be used as a technique for comparing the dynamics of chaotic systems [Aguirre et al. 2006, Brown et al. 1994]. We consider identical chaotic synchronization between the system and the MNN model with diffusive coupling. A term $k(x - x^s_{nn})$ is added to the approximate synchronized neural system x^s_{nn} in the input of the non-feedback module. The normalized RMSE synchronization error, η, divided by the MNN RMSE as function of the coupling parameter, k, is depicted in figure 4.13 for different values of β and $\tau = 10$. Similar results are obtained for $\tau = 100$. Moreover, the ratio between η and the RMSE is almost independent of the β parameter (see figure 4.13). In the range $0.3 < k < 1.9$ the synchronization between the original data and the MNN model is achieved and η is of the order of the MNN RMSE. For $k > 1.9$ the synchronization is unstable. Let us examine in detail this last point. If we consider two identical time continuous systems of the form:

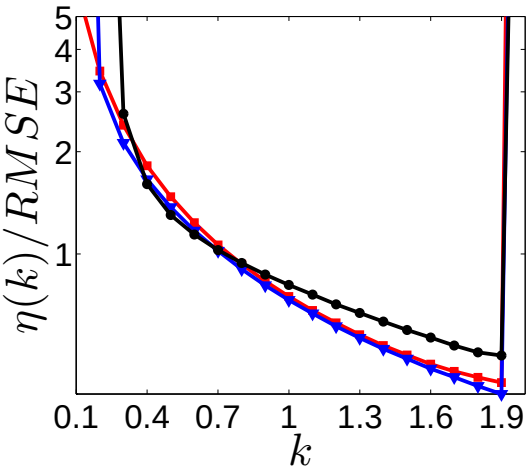

Figure 4.13: Synchronization error, η, divided by the MNN RMSE versus k for a Ikeda system with β =5 (black-circles), 25 (red-squares) and 50 (blue-triangles). The MNN has 31 parameters for $\beta = 5$, 51 for $\beta = 25$ and 75 for $\beta = 50$. In all the cases $\tau = 10$, $T = 1$ and $\phi = 0.26\pi$.

$$\begin{aligned} \dot{x} &= -x + \beta f(x(t-\tau)) \\ \dot{y} &= -y + \beta f(y(t-\tau)) - k_c(y-x) \end{aligned} \tag{4.14}$$

where $k_c > 0$ is the coupling parameter, x is the master and y is the slave, the synchronization error is defined as:

$$\epsilon = x - y \tag{4.15}$$

Taking into account the equation system (4.14), the derivative of the synchronization error is given by:

$$\dot{\epsilon} = -(1+k_c)\epsilon + \beta(f(x(t-\tau)) - f(y(t-\tau))) \tag{4.16}$$

If $\epsilon << 1$, which is true for sufficient large k_c:

$$\dot{\epsilon} \simeq -(1 + k_c - \beta \dot{f}(x(t-\tau)))\epsilon \tag{4.17}$$

Solving equation (4.17) we have:

$$\epsilon^2(t) \approx \epsilon^2(t_0) \cdot e^{-2(1+k_c)(t-t_0)+2\beta \int_{t_0}^{t} \dot{f}(x(s-\tau))ds} \tag{4.18}$$

In the Ikeda system, $f(x) = \sin^2 x$, and for sufficient large t, $\int_{t_0}^{t} \dot{f}(x(s - \tau)ds \approx 0$. Therefore, in the continuous case, the synchronization error decreases for increasing k_c. Nonetheless, if we consider now the discrete version of (4.14) this is no longer true. In the discrete version we have:

$$\begin{aligned} x(t+\delta t) &= (1-\delta t)x(t) + \delta t\ \beta f(x(t-\tau)) \\ y(t+\delta t) &= (1-\delta t)y(t) + \delta t\ \beta f(y(t-\tau)) - \delta t\ k_c(y(t)-x(t)) \end{aligned} \tag{4.19}$$

The synchronization error is also defined by (4.15) and considering that $\epsilon << 1$,

$$\epsilon(t+\delta t) \approx -(k_c\delta t + \delta t - 1)(1 - \frac{\delta t\ \beta \dot{f}(x(t-\tau))}{k_c\delta t + \delta t - 1})\epsilon(t) \tag{4.20}$$

Now, iterating n times the previous equation to obtain $\epsilon(t + n\delta t)$ and taking absolute values, we have:

$$|\epsilon(t+n\delta t)| \approx |k_c\delta t + \delta t - 1|^n \prod_{i=0}^{n-1} |1 - \frac{\delta t\beta \dot{f}(x(t-\tau-i\delta t))}{k_c\delta t + \delta t - 1}||\epsilon(t)| \tag{4.21}$$

The term depending on $x(t - \tau - i\delta t)$ can be considered as a noise whose contribution is negligible (around 0.07 for $\beta = 50$ with our parameters) and we obtain:

$$|\frac{\epsilon(t+n\delta t)}{\epsilon(t)}| \approx e^{n|k_c\delta t+\delta t-1|} \tag{4.22}$$

To avoid that the error increases towards infinite, we need that $|k_c\delta t + \delta t - 1| < 1$. Obviously the system is unstable for $k_c\delta t > 2 - \delta t$. In our case $k_c\delta t \equiv k$, so we have that if $k > 2 - \delta t$, the synchronization error increases towards infinite. This conclusion is in agreement with the numerical results shown in figure 4.13 for the Ikeda system where the synchronization error increases for $k > 1.9$. The same happens in the MG case (see figures 4.5 and 4.8 for numerical and experimental results respectively).

To conclude, we have demonstrated that the dynamics of the system governed by (4.10) is reconstructed with MNNs. The synchronization between the original data and the MNN model has been used to validate the model. Nonetheless, apart from the synchronization, other techniques are commonly used to model validation [see Gouesbet et al. 2003, for a survey]. Most of them are based on the comparison between some features of the original time series

and an artificial time series obtained by iteration of the model. Among such features, the Lyapunov exponents are frequently used. In the reconstructed phase space, one can obtain an estimation of the maximal Lyapunov exponent by following the divergence of nearby segments of the trajectory from the time series. We have estimated the maximal Lyapunov exponent of the iterated time series given by the MNN by the method proposed by [Wolf et al. 1985]. The maximal estimated Lyapunov exponents for $\tau = 10$ and $\beta = 5, 25$ and 50 are 0.48, 1.44 and 1.63, respectively. We compare these results with the maximal estimated Lyapunov exponents of the corresponding original time series obtaining similar results: 0.47, 1.46 and 1.64 for $\beta = 5, 25$ and 50, respectively. The values for the maximal Lyapunov exponents obtained for $\beta = 5$ and 25 are close to the ones calculated from the linearized equation in [Vicente et al. 2005].

Taking all this together we can conclude that the MNN model correctly reconstructs the dynamics of the system governed by equation (4.10) in spite of the very high dimension of the chaotic attractor. In fact, an estimate of the dimension of the chaotic attractor is given by $0.4\beta\tau/T$ [Vicente et al. 2005] and leads to dimensions as large as 2000 for $\beta = 50$ and $\tau = 100$.

4.3.3 Time delay mismatch

As it has been emphasized throughout the thesis, to reconstruct the nonlinear dynamics of time-delay chaotic systems with neural networks, the time delay of the system is the only parameter that has to be known in advance. In the previous subsections, we suppose no error in the estimation of the time delay. However, it has been shown in chapter 3 that this is not always a valid premise. Let us suppose that the estimated time delay is $\hat{\tau} = \tau \pm \Delta\tau$. Clearly, the MNN RMSE increases with $\Delta\tau$. The increment of the RMSE respects to $\Delta\tau$ follows a power law whose exponent depends on β and the number of inputs of the feedback module, together with other factors (see figure 4.14). The RMSE increases when higher values of β are considered for the same values of $\Delta\tau$ because the dynamics is faster. Hence, the difference between $x(t-\tau)$ and $x(t-\tau \pm \Delta\tau)$ increases with β. Evidently, small errors in the time delay estimation can be counteracted by the increment of the number of delayed inputs, so the vector $\vec{x}_f$ includes the correct time delay.

To summarize, a good estimation of the time delay is critical to recover the nonlinear dynamics of a chaotic time-delay system, specially for high nonlinearities. The degradation of the RMSE with the deviation in the estimation of the time delay follows a power law. As a result, a bad time delay identi-

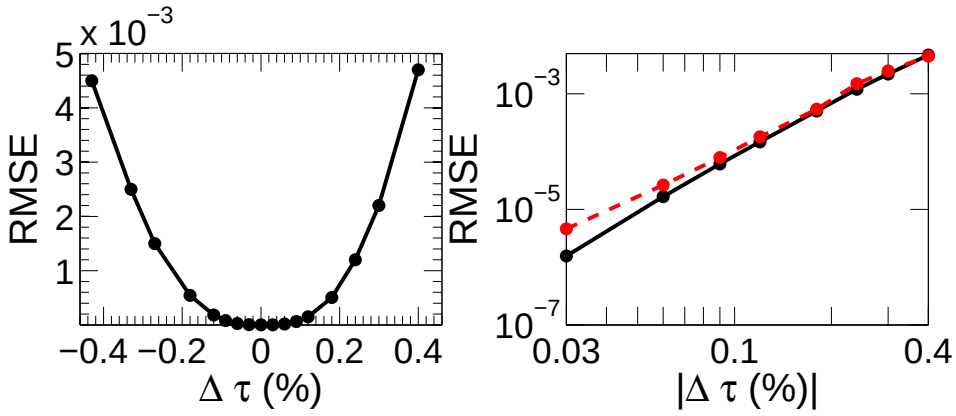

Figure 4.14: RMSE vs. $\Delta\tau = \tau - \hat{\tau}$ as percentage of τ. The Ikeda system has been carried out with $\beta = 5$ and $\tau = 100$. A MNN(8:4) is used. Left (right): axis in linear (logarithmic) mode. In the right panel, the black (red) line corresponds to RMSE for $\Delta\tau(\%) > (< 0)$.

fication can deteriorate the reconstruction of the nonlinear dynamics of the chaotic time-delay system.

4.3.4 The effect of noise

One of the multiples applications of nonlinear dynamics reconstruction is the nonlinear filtering of the original data [Kantz and Schreiber 1997]. A good nonlinear reconstruction from noisy data can yield models that are able to act as nonlinear filters of the original data. Moreover, it is worth to know the behavior of the model in the presence of noise since experimental data are usually affected by it.

To investigate the robustness of the extraction of the nonlinear dynamics using MNNs to additional noise, we add a zero mean Gaussian noise to the original variable $x(t)$. Obviously, the presence of noise in time series decreases the quality of the MNN model obtained. Nonetheless, one of the advantages of the NN models is their capacity to filter the noise data and to recover the underlying nonlinear dynamics. Thus, we expect that the recovered data are less noisy than the original ones.

To measure the level noise added to the system we use the CNR (Chaotic carrier to Noise Ratio), defined as the ratio between the standard deviations of the chaotic carrier $x(t)$ and the noise $n(t)$ in dB:

$$CNR = 20 \log \frac{\sigma_x}{\sigma_n} \tag{4.23}$$

where $\sigma_y = \langle (y(t) - \langle y(t) \rangle)^2 \rangle^{1/2}$ and $\langle\rangle$ implies averaging over time.

Now, we reconstruct the nonlinear dynamics of the system governed by equation (4.10) by using MNNs trained from $x(t) + n(t)$. We have considered CNR from 40 dB (1%) to 20 dB (10%). The structure of the MNN is the same as the one used for the free noise case, but the number of inputs has been increased so the MNN can average the effect of noise. In this particular case, we have used $m_1 = 10$ and $2m_2 + 1 = 5$. The non-feedback inputs, $\vec{x}_{nf}$, are chosen over the range where the autocorrelation has decreased a 10% instead of taking the successive $x(t - m\tau_e)$ with $m = 1, ..., m_1$. The normalized RMSE is obtained by comparing the output of the MNN, $x_{nn}(t)$, with the free-noise data, $x(t)$, and not with the input of the MNN, $x(t) + n(t)$. In this way we check if the MNN model is able to filter the noise and to recover the underlying nonlinear dynamics.

The MNN RMS test error is shown in figure 4.15 as a function of β for different levels of noise. As expected, the RMSE increases with the noise level and with β. However, for high noise levels the RMSE MNN increases only slightly with β. In these cases the main contribution to the RMSE is due to the input noise, that overcomes the model error that increases with β. On the other hand, the number of inputs, training points and neurons of the feedback module of the MNN have been increased respect to the free noise case. This permits to obtain more flexible models capable of adapting to noisy systems. Nonetheless, the improvement in the RMSE due to the increase in the number of the training points and parameters of the MNN has a limit. Similar RMSE are obtained for a MNN(10:5) training with 8000 points (more than the double of the noise free case) (solid line in figure 4.15) than for a MNN(20:10) training with 14000 points (dashed line in figure 4.15). Likewise, the number of inputs can be also increased, but above a certain value the new inputs have not any relationship with the variable that we want to predict.

As previously mentioned, the RMS test error shown in figure 4.15 is calculated by using the free noise data $x(t)$. When the free noise data are not available, like in an experimental setup, the RMSE has to be calculated versus the noisy input of the MNN. In this case, assuming a noise with zero mean and a perfectly matched model, the RMSE would be the standard deviation of the noise. Hence, the good accuracy in the one step ahead prediction of the MNN should be determined by other methods as far as the MNN error is governed by the noise. The recovering of the nonlinear function (see figure 4.16) can give an approximate idea to select the best MNN model, but it is not

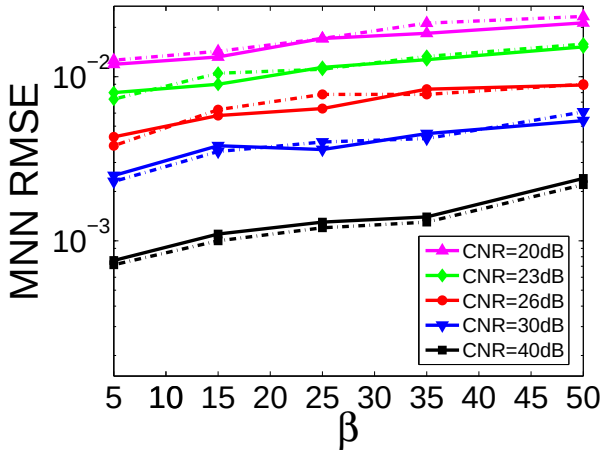

Figure 4.15: MNN RMSE vs. β for different CNR (Chaos to Noise Ratio). The solid lines correspond to a MNN(10:5) -131 parameters- training with 8000 points. The dashed lines correspond to a MNN(20:10) -351 parameters- training with 14000 points. The MNN RMSE is evaluated over 100000 test points. In all the cases $\tau = 100$.

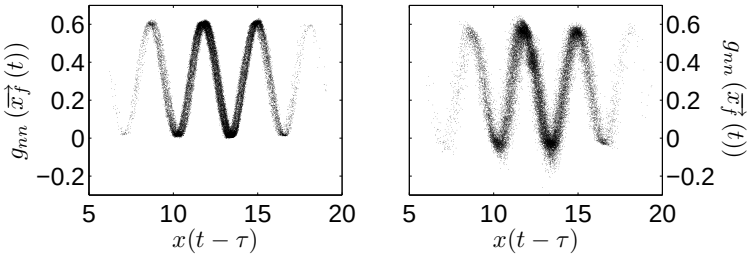

Figure 4.16: Nonlinear functions extracted by the feedback module of the MNN. In both cases the Ikeda system has $\beta = 25$ and $\tau = 100$. Right: CNR = 20 dB. Left: CNR = 30 dB.

a sufficient condition. By contrast, the synchronization is still a very useful tool to validate the model. We have achieved synchronization between the MNN and the time series in all the cases presented in this subsection. The synchronization error between x^s_{nn} and the noise time series, $x(t) + n(t)$, is determined by the noise of the system. This error decreases with the coupling parameter, k, as in the free noise case.

Finally, we check if the MNN is able to filter the input noise to some extent. For this purpose we calculate the difference between the CNR at the

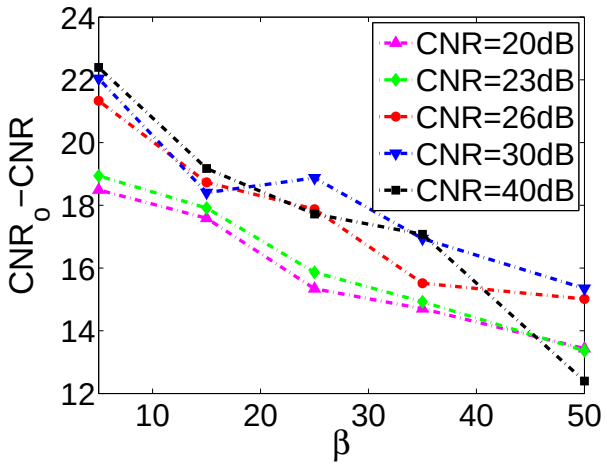

Figure 4.17: $CNR_o - CNR$ versus β. In all the cases $\tau = 100$ and a MNN(10:5) -131 parameters- is used.

output (CNR_o) and the CNR at the input of the MNN (CNR). The CNR_o is defined as $20\log(\sigma_x/(\sigma_{x-x_{nn}}))$, i.e. $CNR_o - CNR = 20\log(\sigma_n/RMSE)$. The results are plotted in figure 4.17. The capacity of the MNN to filter the input noise decreases for higher βs. However, even in the worst studied case, the $CNR_o - CNR$ is at least 12 dB.

4.4 The Ikeda system with two delays

Chaotic systems with multiple feedbacks have been proposed to improve the privacy of chaotic communication systems [Lee et al. 2004; 2005, Udaltsov et al. 2005]. It was expected that the inclusion of additional delays could difficult or avoid the time delay identification. However, we have demonstrated in chapter 3 that it is always possible to identify the time delays of the system, although the extraction can be more complicated depending on the system topology.

Once the time delays of the system have been identified, the objective of this section is to analyze if the additional delays can complicate the extraction of the nonlinear dynamics. One expects that the nonlinear dynamics reconstruction can require more resources, provided that multiple time delay systems have a more complex dynamics than single delay systems [Lee et al. 2004]. The extraction of the nonlinear dynamics of chaotic systems with two time delays have been only studied in the literature with a MG system when

the structure of the DDE that rules the system is perfectly known [Bünner et al. 1998, Prokhorov et al. 2005].

In this section, we study the nonlinear dynamics reconstruction of a semiconductor laser with two electro-optical feedback loops by using MNNs. The dynamics of the system is ruled by the Ikeda DDE with two delays. The section is structured as follows. In section 4.4.1 we reconstruct the nonlinear dynamics with the MNN following the same procedure as in the one delay case but taking into account the two time delays of the system. Two different configurations, serial and parallel, are examined to determine the more secure scheme. In section 4.4.2 we adapt the MNN to the two delays case in order to improve the obtained nonlinear models. Finally, sections 4.4.3 and 4.4.4 are dedicated to analyze the effect of system parameters and noise on the nonlinear dynamics reconstruction with two delays.

4.4.1 Nonlinear Modelling with Modular Neural Networks

We have shown in previous sections (see 4.2 and 4.3) that the nonlinear dynamics of chaotic feedback system with one delay can be reconstructed by modular neural networks (MNN) with two modules, one for the non-feedback part with inputs delayed by the embedding time and another one for the feedback part with inputs delayed by the feedback time.

Now, we apply the modular neural networks method to reconstruct the nonlinear dynamics of feedback systems with two delays. The equation of the Ikeda system with two delays has been presented in chapter 3, section 3.3.3. It is basically defined by the following delay differential equation with two time delays τ_1 and τ_2,

$$x(t) + T\frac{dx(t)}{dt} = G(x(t-\tau_1), x(t-\tau_2)), \tag{4.24}$$

where $x(t)$ is the dynamical variable, G is a nonlinear function and T is the response time of a low pass filter which limits the dynamics of the system. Two different configurations, serial and parallel, related to the way the feedback terms are included in the nonlinear function are considered. The parallel configuration has a nonlinear function defined by:

$$G_p[x(t-\tau_1), x(t-\tau_2)] = \beta_1 \sin^2\left(x(t-\tau_1) - \phi_1\right) + \beta_2 \sin^2\left(x(t-\tau_2) - \phi_2\right), \tag{4.25}$$

and the serial configuration has a nonlinear function given by,

$$G_s[x(t-\tau_1), x(t-\tau_2)] = \beta \sin^2\left(x(t-\tau_1) + x(t-\tau_2) - \phi\right), \qquad (4.26)$$

where β_1, β_2, β are the nonlinear strengths and ϕ_1, ϕ_2, ϕ are phase shifts. The numerical simulations of the system described by equation (4.24) are carried out using the Adams-Bashforth-Moulton predictor-corrector scheme [Press et al. 1992] with a time integration step of 0.01 for both configurations.

Given these time series, the first step to extract the nonlinear dynamics of the Ikeda system with double delay is the estimation of the time delays as in the single delay case. In chapter 3, section 3.3.3, we have shown that it is possible to extract both time delays although in the serial configuration case is necessary to apply adapted techniques that involve longer computational times. Hereafter, we consider that the values of the time delays are known in order to extract the nonlinear dynamics.

To reconstruct the nonlinear dynamics, we follow the same procedure as in the one delay case, but taking into account that the second delay of the system implies the modification of the state space of the system. Now, it is defined by data delayed by both time delays, τ_1 and τ_2.

In our first approximation to the problem, we use the same MNN structure as in the single delay case (see figure 4.4). Hence, the MNN has two modules, one for the non-feedback part with input data delayed by the embedding time (τ_e), $\vec{x}_{nf} = (x(t-\tau_e), ..., x(t-m_1\tau_e))$, and a second one for the feedback part. To take into account the two delays of the system, the feedback module has input data delayed by both feedback times, $\vec{x}_f = (x(t-\tau_1+m_2\tau_e), \ldots, x(t-\tau_1), \ldots, x(t-\tau_1-m_2\tau_e), x(t-\tau_2+m_2\tau_e), \ldots, x(t-\tau_2), \ldots, x(t-\tau_2-m_2\tau_e))$. The number of non-feedback and feedback inputs are m_1 and $2(2m_2+1)$, respectively.

We have carried out numerical simulations of equation (4.24) for $\beta = \beta_1 = \beta_2 = 15$ with an integration step of 0.01. The response time is $T = 1$ and the delay times are $\tau_1 = 100$ and $\tau_2 = 215$. The feedback phase is $\phi = \phi_1 = \phi_2 = 0.26\pi$. This case corresponds to a highly nonlinear system with a $\sin^2$ nonlinear function with 12 extrema. A similar number of extrema is obtained in the single delay case for a value of the normalized feedback strength greater than 25 (see figure 4.12). Keep in mind that in the two delays system the upper bound of the effective feedback strength is approximately 2β when $\beta_1 = \beta_2 = \beta$ (see 3.3.3). In the following we compare the two-delay system with $\beta = \beta_1 = \beta_2 = 15$ to the single-delay system with a feedback strength of 30.

Next, the MNN model is trained with different number of parameters (number of neurons of the FFNN of the feedback module) with $m_1 = 1$ and

	MNN RMS error		
NN feedback	one delay	two delays parallel	two delays serial
6 : 3	$2.33 \cdot 10^{-3}$	0.015 (0.017)	$2 \cdot 10^{-3}$ $(2 \cdot 10^{-4})$
8 : 4	$6.62 \cdot 10^{-5}$	$9.7 \cdot 10^{-3}$ $(8.4 \cdot 10^{-3})$	$3.63 \cdot 10^{-5}$ $(3.11 \cdot 10^{-5})$
10 : 5	$6.12 \cdot 10^{-5}$	$4.7 \cdot 10^{-3}$ $(8.4 \cdot 10^{-3})$	$3.57 \cdot 10^{-5}$ $(2.93 \cdot 10^{-5})$
12 : 6	$4.03 \cdot 10^{-5}$	$2.4 \cdot 10^{-3}$ $(1.2 \cdot 10^{-3})$	$3.21 \cdot 10^{-5}$ $(2.81 \cdot 10^{-5})$
14 : 7	$4.03 \cdot 10^{-5}$	$1 \cdot 10^{-3}$ $(8 \cdot 10^{-4})$	$1.74 \cdot 10^{-5}$ $(2.27 \cdot 10^{-5})$

Table 4.3: RMS test error of the MNN model. The system parameters for the one delay system are $\tau = 215$ and a nonlinearity strength of 30. In the two delays case the parameters are $\beta = \beta_1 = \beta_2 = 15$, $\tau_1 = 100$ and $\tau_2 = 215$. The MNN for the two-delay system has been trained with 3000 and 8000 points (RMSE corresponding to 8000 points is between parenthesis).

$m_2 = 3$. Note that the embedding time is $\tau_e = 0.01$. The RMS normalized errors of the MNN model tested over 100000 points are shown in table 4.3. The NN feedback column, $a : b$, makes reference to the number of neurons of the first (a) and second (b) layer of the feedback module. The MNN RMSE is similar for the two delays serial configuration and the single delay case. Comparing the double delay configurations, the parallel configuration gives MNN RMSE two orders of magnitude higher than the serial configuration.

The MNN has been trained with 3000 and 8000 points chosen to cover uniformly the chaotic attractor. One can observe that the increment of training points yields similar MNN RMSE. It is also interesting to point out that as in the one delay case, the MNN error decreases for MNN models with increasing number of parameters (neurons) but a limit value is reached. To decrease the error below its limit value, lower embedding times have to be considered.

Taking all this into account, we can conclude that once the time delays of the system are known, it is possible to reconstruct the nonlinear dynamics of chaotic system with multiples delays using MNNs. However, the nonlinear dynamics reconstruction is worse for the parallel than for the serial configuration. By contrast, the time delays can be identified in the parallel configuration with the techniques used in the single delay case (see chapter 3, section 3.3.3). On the other hand, the inclusion of multiples delays can be used as a practical method to increment the effective nonlinearity of the system.

We can now show the shape of the nonlinear function obtained from the model. In figures 4.18 and 4.19 the original and MNN recovered nonlinear

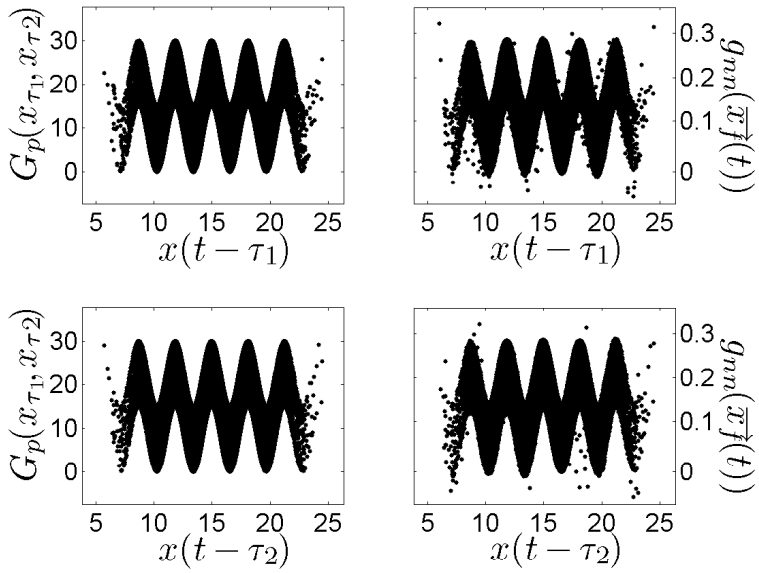

Figure 4.18: Comparison between the original nonlinear function (left) and nonlinear functions recovered by the feedback module of the MNN (right). The two-delay Ikeda system parameters are $\beta_1 = \beta_2 = 15$, $\tau_1 = 100$ and $\tau_2 = 215$ for the parallel configuration. The MNN has a feedback module with $14:7$ neurons.

functions are plotted for the parallel and serial configurations, respectively. In both cases we use a MNN(14:7). For the sake of clarity, the projection of the 3D figure over the $x(t-\tau_1) = 0$ and $x(t-\tau_2) = 0$ planes is plotted for the parallel case. The shape of the recovered nonlinear function g_{nn} is similar to G_s and G_p for the serial and parallel configurations, respectively. In fact, as in the one delay case, the MNN feedback functions are similar to the nonlinear terms of a discrete-time version of equation (4.24). However, the original and recovered nonlinear functions match better for the serial case thanks to the lower MNN RMSE. Note that the nonlinear recovered function $g_{nn}(\vec{x}_f)$ depends on the input vector of the feedback module $\vec{x}_f$ and not only on $x(t-\tau_1)$ and $x(t-\tau_2)$.

Finally, we test that the obtained MNN model can also reproduce the nonlinear dynamics of the system when iterated in time using the chaotic synchronization [Aguirre et al. 2006, Brown et al. 1994]. We synchronize with diffusive coupling the MNN model with the original system. The synchronization manifold, ($x^s_{nn}(t)$ vs $x(t)$), is plotted in figure 4.20 for a coupling parameter $k = 0.4$. The RMS synchronization errors are of the order of

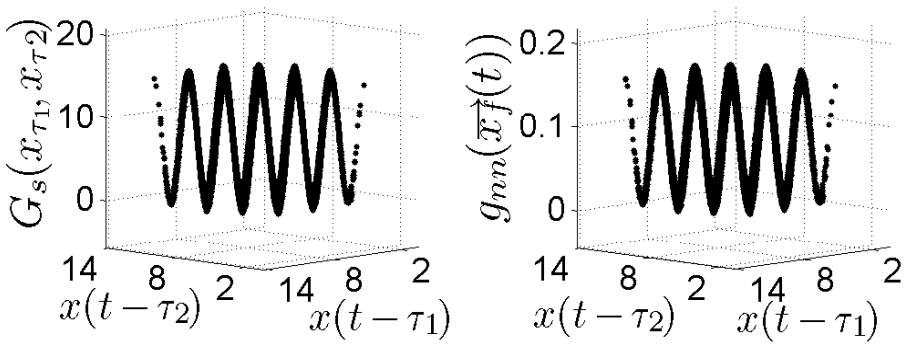

Figure 4.19: Comparison between the original nonlinear function (left) and nonlinear functions recovered by the feedback module of the MNN (right). The two-delay Ikeda system parameters are $\beta = 15$, $\tau_1 = 100$ and $\tau_2 = 215$ for the serial configuration. The MNN has a feedback module with $14:7$ neurons.

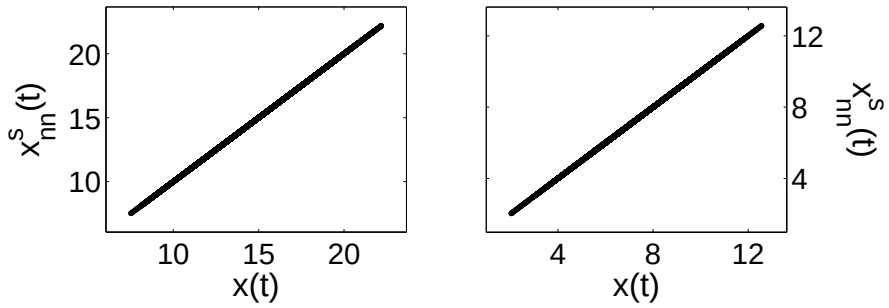

Figure 4.20: The synchronization manifold with a coupling parameter $k = 0.4$ for the two delays parallel (left) and serial (right) configurations. The parameters of the system are $\beta_1 = \beta_2 = \beta = 15$, $\tau_1 = 100$ and $\tau_2 = 215$. We use a MNN(14:7).

the RMS MNN errors. For this particular case, the synchronization error is $3.5 \cdot 10^{-3}$ and $2.28 \cdot 10^{-5}$ for the parallel and serial configurations, respectively. The synchronization errors have the same behavior with k as in the one delay case. We can conclude that the dynamics of the Ikeda system with two delays (ruled by equation (4.24)) is extracted by the MNN model.

4.4.2 Nonlinear Modelling with Adapted MNN

We can adapt the MNN model for exploiting better the characteristics of the two delays systems. This is specially interesting in the two delays parallel configuration where worse RMSE are obtained. In the following, we study

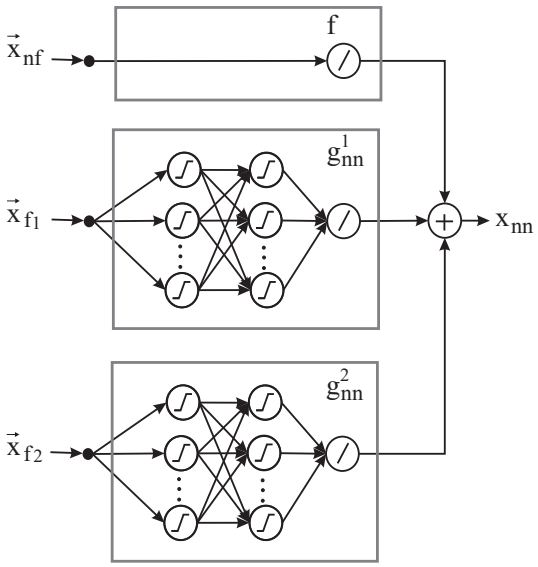

Figure 4.21: Topology of the adapted MNN for the two delays parallel case. The output of the MNN is given by $x_{nn}(t) = f_{nn}(\vec{x}_{nf}) + g^1_{nn}(\vec{x}_{f1}) + g^2_{nn}(\vec{x}_{f2})$. $\vec{x}_{nf}$, $\vec{x}_{f1}$ and $\vec{x}_{f2}$ are the input vectors for the non-feedback, first and second feedback module, respectively. Each feedback module is formed by a feed-forward neural network.

the drawbacks and advantages of the adapted MNN models over the standard ones.

In the two delays parallel configuration, we implement an adapted MNN model with two feedback modules, each one for the nonlinear functions with arguments $x(t-\tau_1)$ and $x(t-\tau_2)$. In this way the structure of the MNN model resembles more the original nonlinear function G_p. The non-feedback module is not modified. The inputs for each feedback module are only delayed by the corresponding τ_i, $\vec{x}_{fi} = (x(t-\tau_i+m_2\tau_e),\ldots,x(t-\tau_i),\ldots,x(t-\tau_i-m_2\tau_e))$, where $i=1,2$. In this case, the output of the MNN is given by $x_{nn}(t) = f_{nn}(\vec{x}_{nf}) + g^1_{nn}(\vec{x}_{f1}) + g^2_{nn}(\vec{x}_{f2})$, where f_{nn}, g^1_{nn} and g^2_{nn} correspond to the functions of the non-feedback, first and second feedback modules, respectively (see figure 4.21).

In the two delays serial configuration, the structure of the MNN remains the same, but we change the inputs of the model. Instead of taking each delayed term separately, the inputs of the feedback module are directly the argument of the nonlinear function (in our case the sum of the delayed variables, $x(t-\tau_1)+x(t-\tau_2)$). Hence, $\vec{x}_f = (x(t-\tau_1+m_2\tau_e)+x(t-\tau_2+m_2\tau_e),\ldots,x(t-\tau_1)+x(t-\tau_2),\ldots,x(t-\tau_1-m_2\tau_e)+x(t-\tau_2-m_2\tau_e))$.

	MNN error	
NN feedback	two delays parallel	two delays serial
6:3	$1.7 \cdot 10^{-3}$	$2 \cdot 10^{-4}$
8:4	$4.11 \cdot 10^{-5}$	$6.01 \cdot 10^{-5}$
10:5	$2.53 \cdot 10^{-5}$	$3.27 \cdot 10^{-5}$
12:6	$2.39 \cdot 10^{-5}$	$1.81 \cdot 10^{-5}$
14:7	$1.62 \cdot 10^{-5}$	$1.79 \cdot 10^{-5}$

Table 4.4: Test RMSE of the adapted MNN model trained with 3000 points. The feedback modules has 14:7 neurons. The parameters of the system are $\beta = \beta_1 = \beta_2 = 15$, $\tau_1 = 100$ and $\tau_2 = 215$.

The RMS normalized errors for the adapted MNN models are shown in table 4.4. Let us compare with the non-adapted MNN RMSE presented in table 4.3. Regarding the serial configuration, no advantage over the standard MNN is observed. In this case, the only modification over the standard case is the way the feedback inputs are injected into the model. Clearly, the MNN is able to find the relationship of the inputs with the nonlinear function without extra information. By contrast, in the parallel case, the adapted MNN yields RMSE two orders of magnitude lower than the non adapted MNN. Hence, the adapted MNN models permit to obtain MNN RMSE comparable with the two delays serial configuration.

Now, we focus on the number of parameters of the model (shown in table 4.5). Clearly, the additional inputs due to the second delay of the system increment the parameters of the MNN respect to the one delay case. In the serial configuration, the only advantage of the adapted MNN versus the non-adapted one is the reduction of the MNN parameters. However, this slight reduction of parameters implies a total knowledge of the nonlinear function argument. This constrains the universality of the model and does not apport any improvement to the error. For instance, the non-adapted MNN is valid when the argument of the nonlinear function is $(x(t-\tau_1) - x(t-\tau_2))$ instead of $(x(t-\tau_1) + x(t-\tau_2))$. Therefore, the standard MNN is the better option for the serial configuration.

In the parallel configuration the inclusion of a second feedback module leads to adapted MNNs that almost double the parameters of the standard MNN model. In spite of the increment in the number of parameters, the

	Number of MNN parameters				
	One delay	2 delays parallel		2 delays serial	
NN feedback		Non adapt	adapt	Non adapt	adapt
6 : 3	51	69	100	69	51
8 : 4	75	99	148	99	75
10 : 5	103	133	204	133	103
12 : 6	135	171	268	171	135
14 : 7	187	229	372	229	187

Table 4.5: Number of parameters of the adapted and non adapted MNN models. The two-delay Ikeda system has $\beta = \beta_1 = \beta_2 = 15$, $\tau_1 = 100$ and $\tau_2 = 215$. The one delay Ikeda system has a nonlinearity strength of 30 and a time delay of 100.

improvement in the RMSE implies that the adapted MNN model is more adequate to extract the nonlinear dynamics in this case.

Finally, the original and MNN recovered nonlinear functions using the adapted MNN for parallel and serial configuration are depicted in figures 4.22 and 4.23, respectively. Good agrement between the original and recovered functions are found for both cases. Note that in the parallel case, each MNN nonlinear function only depends on one delayed term, whereas the original nonlinear function depends on both delayed terms. Therefore, the functions extracted by the MNN model are sharper than the original ones.

4.4.3 Influence of the system parameters

We have demonstrated through this chapter that the RMSE of the MNN model increases with the feedback strength of the system, β, but not with the time delay, τ. These results are in agreement with the fact the entropy of the system increases with β but not with τ. These results are also valid for the multiple delays case. In the two delays case we can also analyze the effect of the ratio between both delays. Furthermore, in the parallel configuration, we can study the influence of different βs and phase shift values in the nonlinear dynamics reconstruction with MNN.

Regarding the time delays, three different situations are studied in this subsection. Both delays are multiples ($\tau_1 = 100$ and $\tau_2 = 200$), take close values ($\tau_1 = 100$ and $\tau_2 = 101$) or do not have an integer ratio ($\tau_1 = 100$ and $\tau_2 = 215$). In all the cases $\beta = \beta_1 = \beta_2 = 15$, $\phi_1 = \phi_2 = \phi = 0.26\pi$ and

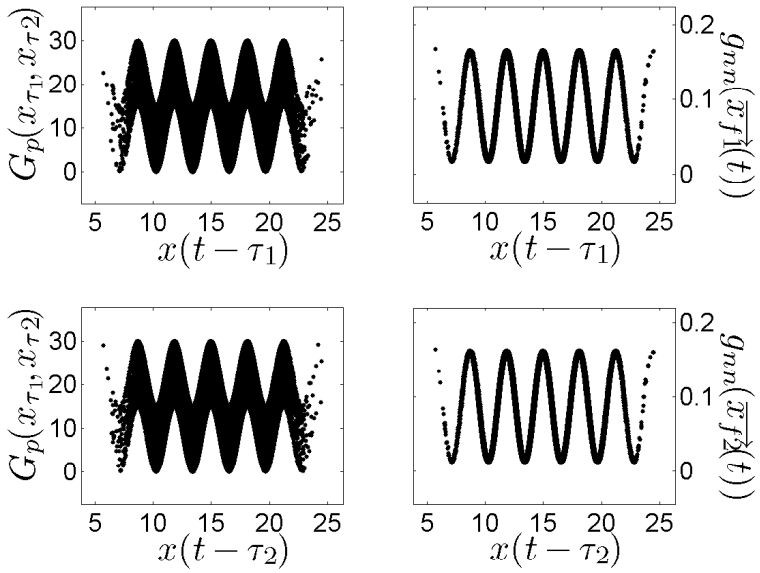

Figure 4.22: Comparison between original non-linear functions (left) and MNN functions for the first and second feedback module (right upon and bottom). The system parameters for the parallel configuration are $\beta_1 = \beta_2 = 15$, $\tau_1 = 100$ and $\tau_2 = 215$. The adapted MNN has two feedback modules each one with $14:7$ neurons.

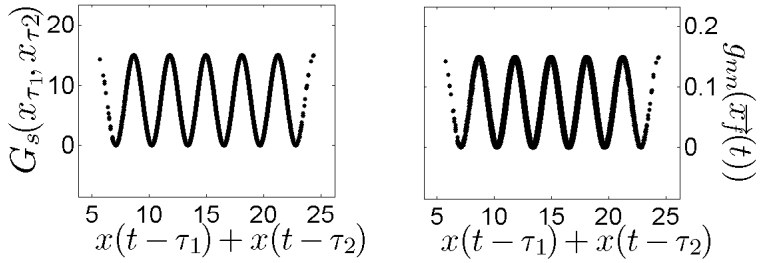

Figure 4.23: Comparison between original non-linear function (left) and MNN function (right) in the serial configuration with adapted MNN. The MNN has a feedback module with $14:7$ neurons. The system parameters are $\beta = 15$, $\tau_1 = 100$ and $\tau_2 = 215$.

		MNN error			
		2 delays parallel		2 delays serial	
τ_1	τ_2	Non Adapt	Adapt	Non Adapt	Adapt
100	215	$1 \cdot 10^{-3}$	$1.62 \cdot 10^{-5}$	$1.74 \cdot 10^{-5}$	$1.81 \cdot 10^{-5}$
100	200	$4 \cdot 10^{-4}$	$1.44 \cdot 10^{-5}$	$2.42 \cdot 10^{-5}$	$2.16 \cdot 10^{-5}$
100	101	$1.9 \cdot 10^{-3}$	$1.51 \cdot 10^{-5}$	$2.71 \cdot 10^{-5}$	$1.32 \cdot 10^{-5}$

Table 4.6: Test RMSE of the MNN model for different time delay ratios. The parameters of the two-delay Ikeda system are $\beta = \beta_1 = \beta_2 = 15$, $T = 1$ and $\phi_1 = \phi_2 = \phi = 0.26\pi$. The MNN has been trained with 3000 points. The feedback modules have 14 : 7 neurons

an adapted MNN with feedback modules of 14 : 7 is considered. The RMS test error of the MNN for each case is presented in table 4.6. Clearly, the RMSE of the MNN is independent of the ratio between delays for the serial configuration. The same conclusion is obtained for the parallel configuration when an adapted MNN is used. The latter conclusion is evident because each time delay has associated its own feedback module in the adapted MNN. However, if the time delays are multiples and a standard MNN is used, the RMSE decreases for the parallel configuration. Similar results are obtained in the case of a standard FFNN.

Next, focusing only on the parallel configuration, we can analyze the effect of the relative phase shift $(\phi_1 - \phi_2)$ and $\beta_1 \neq \beta_2$. As it is illustrated in table 4.7, the effect of different relative phase shifts over the RMSE MNN is negligible. Although it has been demonstrated with numerical simulations that the entropy of the system is slightly higher for $\phi_1 - \phi_2 = \pi/4$ [Pazó 2009], this increment is not enough to affect the nonlinear dynamics reconstruction. With respect to the nonlinear modelling with MNN in the two delays parallel configuration with $\beta_1 \neq \beta_2$, table 4.8 shows that the MNN RMSE increases with β in agreement with the results obtained for the one delay case (if we consider the upper bound for the effective nonlinearity when $x(t - \tau_1) \approx x(t - \tau_2)$, then the results of table 4.8 can be compared to the single delay case for $\beta = 20$, 30 and 40).

To sum up this subsection, the most important parameter in the design of a two-delay Ikeda system to complicate the nonlinear dynamics extraction with a MNN is the nonlinear strength. In the parallel configuration, higher βs values have to be used in both terms of the nonlinear function in order to increment the privacy of the system. Moreover, an integer ratio between both

	MNN error: two delays parallel	
$\phi_1 - \phi_2$	No Adapt	Adapt
0	$1 \cdot 10^{-3}$	$1.62 \cdot 10^{-5}$
$\pi/2$	$1.78 \cdot 10^{-3}$	$1.34 \cdot 10^{-5}$
$\pi/4$	$2.1 \cdot 10^{-3}$	$1.22 \cdot 10^{-5}$

Table 4.7: Test RMSE of the MNN model for different $\phi_1 - \phi_2$. The parameters of the two-delay Ikeda system using the parallel configuration are $\beta_1 = \beta_2 = 15$, $T = 1$, $\tau_1 = 100$ and $\tau_2 = 215$. The MNN has been trained with 3000 points. The feedback modules have $14:7$ neurons

		MNN error: two delays parallel	
β_1	β_2	Non Adapt	Adapt
15	5	$4.31 \cdot 10^{-5}$	$8.41 \cdot 10^{-6}$
15	15	$1 \cdot 10^{-3}$	$1.62 \cdot 10^{-5}$
15	25	$6.47 \cdot 10^{-3}$	$4.18 \cdot 10^{-5}$

Table 4.8: Test RMSE of the MNN model for different β_2 values. The parameters of the two-delay Ikeda system using the parallel configuration are $T = 1$, $\phi_1 = \phi_2 = 0.26\pi$, $\tau_1 = 100$ and $\tau_2 = 215$. The MNN has been trained with 3000 points. The feedback modules have $14:7$ neurons

delays should be avoided in the parallel configuration. By contrast, the phase shifts of the system can take any value provided the system is working in the chaotic regime.

4.4.4 The effect of noise

In this subsection we investigate the robustness of the nonlinear dynamics reconstruction of a two-delay Ikeda system in presence of noise using MNN. Following the same approach as in the single delay case, a zero-mean Gaussian noise is added to the output of the double delay Ikeda system defined by equation (4.24). We study the nonlinear dynamics reconstruction for different Chaos to Noise Ratio (CNR).

Taking into account the conclusions of the previous subsections, we use an adapted MNN for the parallel configuration and a non-adapted MNN for the serial topology. In accordance with the procedure followed in the single delay case, the MNN structure is the same as in the absence of noise. We

	MNN error	
CNR (dB)	two delays parallel	two delays serial
40	$1.6 \cdot 10^{-3}$	$1.9 \cdot 10^{-3}$
30	$4.83 \cdot 10^{-3}$	$9.1 \cdot 10^{-3}$
25	0.011	0.015
20	0.023	0.031

Table 4.9: Test RMSE of the MNN model for different CNR. The two-delay Ikeda system parameters are $\beta = \beta_1 = \beta_2 = 15$, $\tau_1 = 100$ and $\tau_2 = 215$. The MNN has been trained with 8000 points and the feedback modules have 14:7. A non-adapted (adapted) MNN is used for the serial (parallel) configuration.

only increase the number of inputs and training points respect to the free noise case to obtain more flexible models capable of being adapted to noisy systems. Hence, the MNN is trained with 8000 points, $m_1 = 10$ and $m_2 = 5$. The non-feedback inputs, $\vec{x}_{nf}$, are chosen over the range where the linear autocorrelation value has decreased a 10%.

The RMSE obtained for different CNR is presented in table 4.9. As in the one delay case, the RMSE is calculated with respect to the system without noise. As expected, the MNN error increases with the noise level. However, the noise affects more to the serial configuration. Similar results are obtained when the number of training points is increased to 15000 and a MNN with feedback modules $(20 : 10)$ is used. In all the cases, the MNN model synchronizes with the original system. The behavior of the synchronization error with the model error and the coupling parameter is the same as in the one delay case.

It is worth pointing out that the MNN model has filtered the noise to some extends as it happens in the one delay case. We present in table 4.10 the CNR at the input and at the output of the MNN model. The capacity of the MNN to filter the noise decreases with the input noise level. The noise filtering is less efficient in the serial configuration, in agreement with the worse test RMSE MNN obtained for this configuration.

Finally, we show the recovered nonlinear functions for the parallel and serial topologies when $CNR = 20$ dB in figures 4.24 and 4.25. The recovered nonlinear functions are affected by the noise, but they still resemble the original ones. However, due to the effect of the noise, they do not correspond to the nonlinear discrete-terms of the original DDE, as happened in the absence of noise.

	CNR (output) (dB)	
CNR (input) (dB)	two delays parallel	two delays serial
40	56	54
30	46	41
25	39	36
20	33	30

Table 4.10: CNR in dB at the input and the output of the MNN model. The two-delay Ikeda system parameters are $\beta = \beta_1 = \beta_2 = 15$, $\tau_1 = 100$ and $\tau_2 = 215$. The MNN has been trained with 8000 points and the feedback modules have 14:7. A non-adapted (adapted) MNN is used for the serial (parallel) configuration.

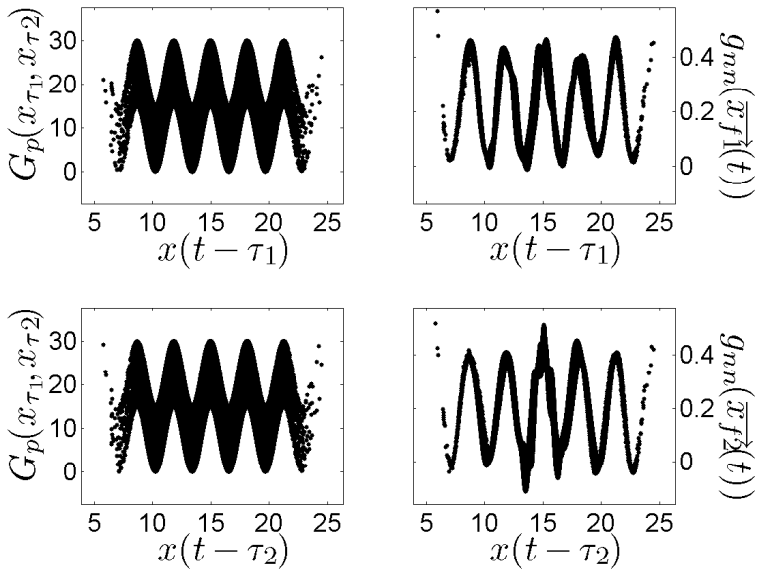

Figure 4.24: Comparison between original non-linear function (left) and MNN functions for the first and second feedback module (right upon and bottom). The CNR = 20 dB. The system parameters for the parallel configuration are $\beta_1 = \beta_2 = 15$, $\tau_1 = 100$ and $\tau_2 = 215$. The adapted MNN has two feedback modules each one with $14:7$ neurons.

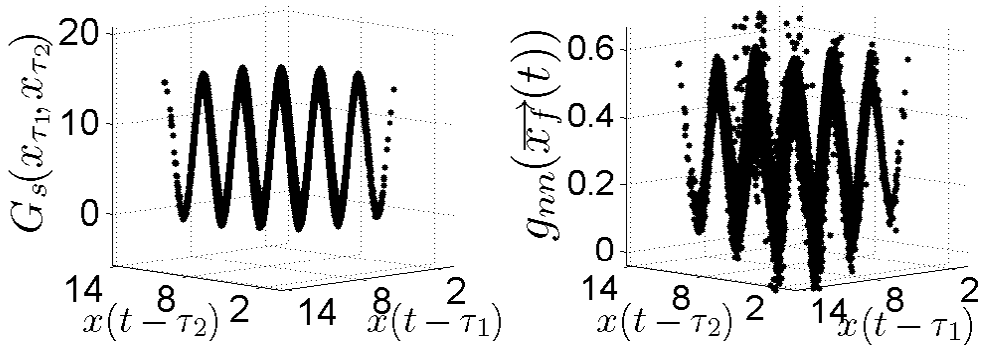

Figure 4.25: Comparison between original non-linear function (left) and MNN function (right) in the serial configuration with non-adapted MNN(14:7). The CNR = 20 dB. The system parameters are $\beta = 15$, $\tau_1 = 100$ and $\tau_2 = 215$.

4.5 Optoelectronic feedback systems: Experiments

In this section we reconstruct the nonlinear dynamics from experimental time series with MNNs following the same approach used with numerical simulations.

The experimental setup is explained in detail in chapter 3, subsection 3.4.1. Basically, the experimental generator of the chaotic wavelength beam consists of an electrically tunable DBR multielectrode laser diode with a feedback loop formed by a delay line and an optically birefringent plate whose peculiarity is to exhibit a nonlinearity in wavelength. The wavelength of the chaotic carrier can be described by a time-delay differential equation given by:

$$T\frac{d\lambda(t)}{dt} = -\lambda(t) + \beta_\lambda \sin^2(\frac{\pi D}{\Lambda_0^2}\lambda(t-\tau) - \phi) \tag{4.27}$$

where λ is the wavelength deviation from the center wavelength Λ_0, D is the optical path difference of the birefringent plate which constitutes the nonlinearity, ϕ is the feedback phase, τ is the time delay, T is the response time of the feedback loop, implemented by a first-order low-pass filter and β_λ is the feedback strength.

The system parameters are set to operate in the chaotic regime. The maximum number of extrema of the nonlinear function reached with the present set-up when the loop is closed is around 6. The number of extreme values increases with the nonlinearity of the system that can be adjusted through the

gain of the amplifier. The equation (4.27) can be normalized to the well-known Ikeda equation (4.10).

The experimental time series have been recorded with a high end digital storage oscilloscope with 8 bits for the analog-digital conversion. However, it was found that for low sampling rates the recorded time series present an important quantification noise. To overcome this problem the time series has been also recorded with a digital storage oscilloscope with 12 bits of resolution. This latter oscilloscope has a small bandwidth of 200 MHz, but it covers without problems the bandwidth of the recorded time series that is constrained by the low pass filter. Let us point out that the stored time series, $\lambda(t)$, is measured in volts that is proportional to the value of the wavelength deviation.

To reconstruct the nonlinear dynamics from a time series the first step is the identification of the time delay. In chapter 3, section 3.4, we have analyzed the time delay identification in this experimental setup, finding that the time delay can be identified through different techniques.

Hereafter, we reconstruct the nonlinear dynamics from the experimental time series for two different cut-off frequencies of the low-pass filter, 20 KHz and 200 Hz. This leads to short (8 μs) and long response times (800 μs), respectively.

4.5.1 Long response time

In this case, we reconstruct the nonlinear dynamics from experimental time series when the low pass filter has a cut off frequency of 200 Hz yielding a response time of the system, $T = 800$ μs. To this aim, we use experimental time series sampled each 10 μs (around 100 times lower than the response of the system) during 1 second, i.e., 10^5 points. The time series are recorded with a high end digital oscilloscope of 8 bits. Here we only consider the case of a nonlinear function with 5 extrema that is close to the maximum nonlinear strength reached with the present experimental set-up and a time delay, $\tau = 2.08$ ms. The results are similar for different time delays and better dynamics reconstruction is possible for lower nonlinearity strengths.

As previously explained (see chapter 3, subsection 3.4.2), a rough estimation of the noise of the time series can be made by subtracting the original time series (normalized to mean zero and variance unity) and an average version of it. This method yields an estimated noise with a standard deviation of 0.028, i.e., a CNR=31 dB. The noise level is normalized to the standard deviation of the chaotic carrier.

Following the same approach as in the numerical simulations with noise, we reconstruct the nonlinear dynamics from the experimental time series using

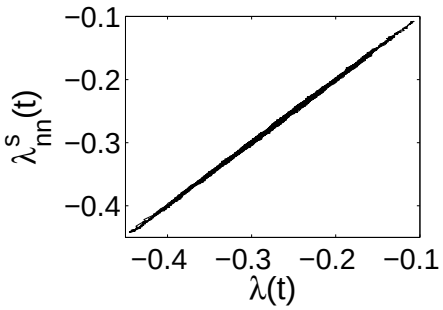

Figure 4.26: Synchronization manifold between the original experimental signal and the MNN synchronized output with a diffusive coupling of $k = 0.4$. The time series has been generated by a chaotic generator with $\tau = 2080$ μs, $T = 800$ μs and a nonlinear function with 5 extrema. The sampling period is 10 μs. $\lambda(t)$ is measured in volts.

a MNN(10:5). This means that the MNN has a feedback module with $10:5$ neurons and a non-feedback module with one linear neuron. The non-delayed inputs of the MNN are chosen over the interval where the autocorrelation function of the time series has decayed a ten percent, leading to eight non-delayed inputs ($m_1 = 8$). Nonetheless, we have found by trial and error that the number of non delayed inputs can be reduced to $m_1 = 4$ giving similar results. Respect to the delayed inputs, we take five values around the delay time ($m_2 = 2$). The number of training points are around ten thousand and the MNN model is tested over 100000 points. The MNN RMSE is 0.029, similar to the estimated noise of the system. Similar RMSE are obtained for higher number of neurons of the feedback module and training points.

Due to the presence of noise in the time series, the RMSE can not be used to validate our model. Therefore, to test the validity of the model we synchronize the MNN with the original time series through a diffusive coupling as in the numerical simulations. The synchronization manifold when the coupling parameter, k, is 0.4, is plotted in figure 4.26. The synchronization error for $k = 0.4$ is 0.0224.

Finally, we plot in figure 4.27 the functions f_{nn} and g_{nn} extracted by the MNN model that correspond to the non-feedback and feedback modules, respectively. The original non-linear function can be estimated from the averaged experimental time series by plotting $\lambda(t)$ versus $\lambda(t-\tau)$ only for the extrema points (see figure 4.27 (rigth)). It can be seen that the MNN model recovers the shape of the $\sin^2$ original nonlinear function.

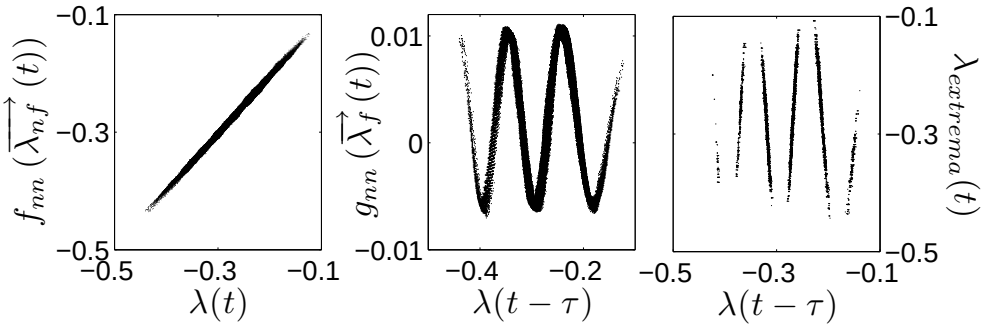

Figure 4.27: Left (middle): non-feedback (feedback) module function of the MNN(10:5) model. Right: Estimation of the original nonlinear function given by the plot of $\lambda(t)$ versus $\lambda(t-\tau)$ only for the extrema points of $\lambda(t)$. The time series has been generated by a chaotic generator with $\tau = 2080\ \mu s$, $T = 800\ \mu s$ and a nonlinear function with 5 extrema. The sampling period is 10 μs. $\lambda(t)$ is measured in volts.

The case analyzed in this subsection corresponds to a situation where the time delay of the system is around 2.6 times the response time of the system. Therefore, the dimension of the chaotic attractor does not scale with the time delay of the system [Vicente et al. 2005]. In the next subsection we analyze the system for $T = 8\ \mu s$, where the dimension of the attractor scales with the time delay of the system.

4.5.2 Short response time

In this case, we reconstruct the nonlinear dynamics from experimental time series when the low pass filter has a cut off frequency of 20 Khz yielding a response time of the system, $T = 8\ \mu s$. The experimental time series are sampled each 1 μs (around 10 times lower than the response of the system) and the time delay of the system is 0.476 ms. The time series are recorded with a high end digital oscilloscope of 8 bits of resolution.

We analyze three different scenarios that correspond to nonlinear functions with 2 (low nonlinearity strength), 5 and 6 extrema (moderate nonlinearity strength). The last case corresponds to the maximum number of extrema that can be reached for the present experimental setup. In this case the chaotic carrier has Gaussian probability density and the normalized standard deviation is 0.23. The standard deviation normalized to the mean value decreases when β is increased. The value of the parameter β can be estimated by comparing the normalized standard deviation and the number of extrema of the nonlin-

ear function of the numerical simulations with the experiment. The maximum feedback strength reached (nonlinear function with 6 extrema) corresponds to a value of the normalized parameter β around 15.

Following the same approach as in the case of $T = 800\mu s$, we roughly estimate the noise of the time series. In this case, the estimated noise has a standard deviation of 0.0239, i.e. a CNR = 32 dB. The level noise is similar to the case of $T = 800\mu s$.

To reconstruct the nonlinear dynamics we use a MNN with two modules: a non-feedback one formed by one linear neuron and a feedback one formed by a feedforward NN. The input vector of the non-feedback module, $\vec{\lambda}_{nf} = [\lambda(t-\tau_e), \lambda(t-2\tau_e), \lambda(t-3\tau_e), \lambda(t-4\tau_e)]$, has four components ($m_1 = 4$) delayed by the embedding time, $\tau_e = 1\ \mu s$. The input vector of the feedback module, $\vec{\lambda}_f = [\lambda(t-\tau+2\tau_e), \lambda(t-\tau+\tau_e), \lambda(t-\tau), \lambda(t-\tau-\tau_e), \lambda(t-\tau-2\tau_e)]$, has five components ($m_2 = 2$) delayed by the feedback time, τ. We use around 25000 training points distributed to cover uniformly the attractor. The feedback module has two layers with $4:2$ neurons for the low nonlinearity (2 extrema) and $6:3$ neurons for the moderate nonlinearities (5 and 6 extrema).

The MNN RMSE obtained is around 0.033, 0.06 and 0.08 for the nonlinear functions with 2, 5 and 6 extrema, respectively. Hence, the RMSE increases with the nonlinearity of the system and it is always higher than the estimated noise of the time series (0.024). As previously emphasized, the RMSE is affected by the noise of the system. Therefore, other methods should be used to select the best MNN. The nonlinear function inferred by the MNN model can give an approximate idea. The linear and nonlinear MNN functions, f_{nn} and g_{nn}, are plotted in figure 4.28 for the nonlinear functions with 2, 5 and 6 extrema. Good agrement between the shape of the MNN functions and its estimation from the time series are found.

To validate the obtained MNN models, we synchronize the MNN with the experimental time series using a diffusive coupling. The synchronization error divided by the MNN RMSE is depicted in figure 4.29. The range of k where the synchronization is achieved decreases for increasing nonlinearity. However, in all the cases exits a range of k where the synchronization errors are of the order of the test RMSE. Similar behavior has been found with the numerical simulations of the Ikeda system (see figure 4.13) and with the MG simulations and experiments (see figures 4.5 and 4.8).

The MNN models can not be improved by increasing the training points, the number of neurons or inputs of the MNN. In fact, the number of non-delayed inputs used ($m_1 = 4$) is the minimum to reconstruct the nonlinear dynamics from the experimental time series with a sampling period of $1\mu s$.

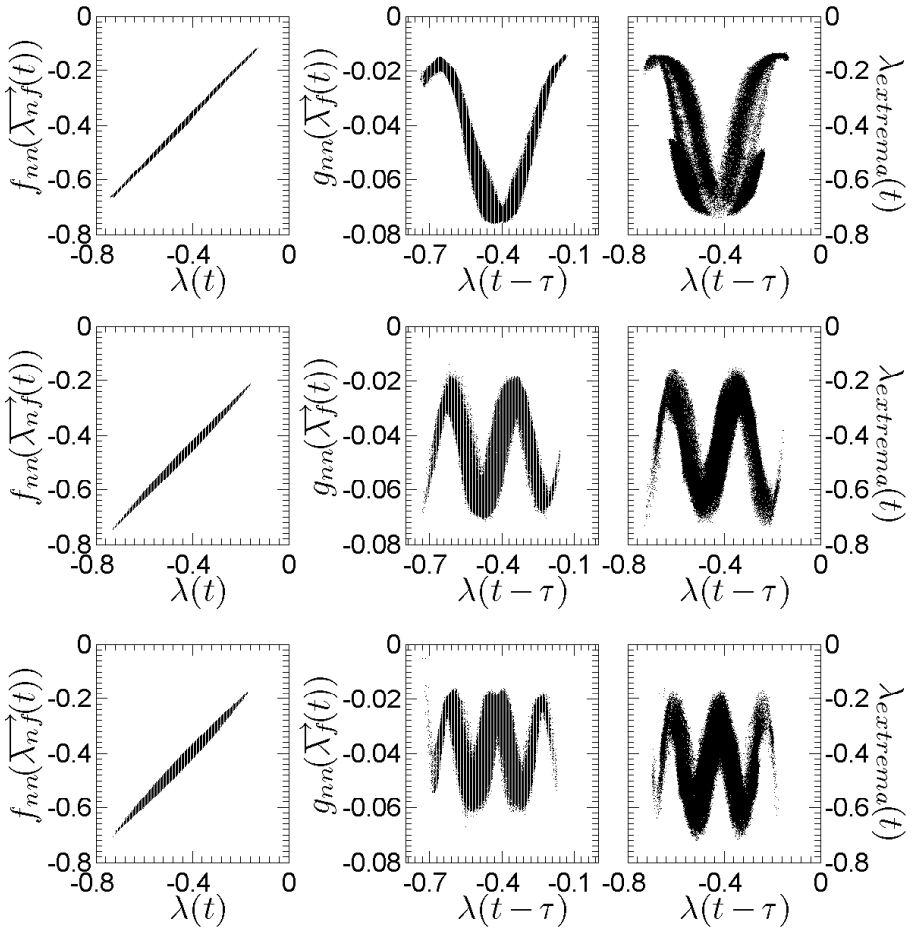

Figure 4.28: Left (middle): non-feedback (feedback) module function of the MNN model. Right: Estimation of the original nonlinear function given by the plot of $\lambda(t)$ versus $\lambda(t-\tau)$ only for the extrema points of $\lambda(t)$. From top to bottom the nonlinear function has 2, 5 and 6 extrema. A MNN(4:2) (MNN(6:3)) is used when the nonlinear function has 2 (5 and 6) extrema. The time series has been generated by a chaotic generator with $\tau = 0.476$ ms and $T = 8$ μs. The sampling period is 1 μs. $\lambda(t)$ is measured in volts.

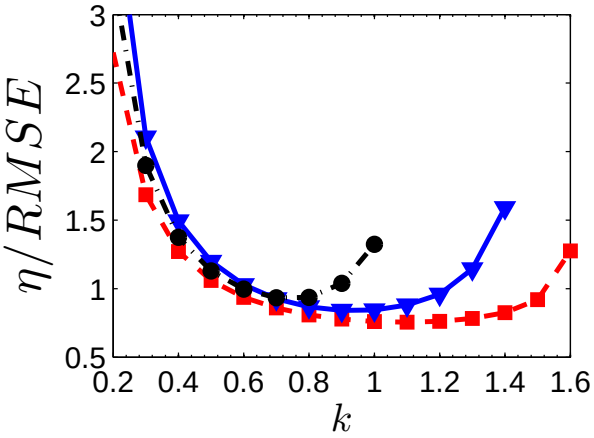

Figure 4.29: The synchronization error, η, divided by the MNN RMSE error versus the coupling parameter, k. The red (squares), blue (triangles) and black (circles) lines correspond to a chaotic generator whose nonlinear function has 2, 5 and 6 extrema, respectively. In all the cases $T = 8$ μs and $\tau = 0.476$ ms. The sampling period is 1 μs.

In order to obtain better models, we can try to extract the nonlinear dynamics from time series with lower sampling period, $\delta t = 0.1$ μs (around 100 times smaller than the response time of the system). In this case the data are recorded with a 12 bits oscilloscope to avoid the quantification noise that appears in the data recorded with the 8 bits oscilloscope for this sampling period.

One possible way to improve the nonlinear dynamics reconstruction could be to filter part of the noise of the experimental time series. Nonetheless, the relevant frequencies of the system are larger than inverse of the response time of the system [Bavard et al. 2007]. In our case, the maximum average time when $T = 8$ μs is around 0.3 μs. Thus, the filtered time series that lead to valid MNN models (able to synchronize with the time series by the diffusive coupling) do not increase significantly the model quality.

In the case of $\delta t = 0.1$ μs, to reconstruct the nonlinear dynamics the only modification with respect to the case of $\delta t = 1$ μs is the number of non-delayed inputs. We take $m_1 = 1$, yielding a non-delayed input vector, $\lambda_{nf} = [\lambda(t-\tau_e)]$. More non-delayed inputs leads to MNN models that are not able to describe the global dynamics when they are iterated in time.

The linear and nonlinear MNN functions when $\delta t = 0.1$ μs are plotted in figure 4.30. The feedback module of the MNN has $4:2$, $8:4$ and $10:5$ for the

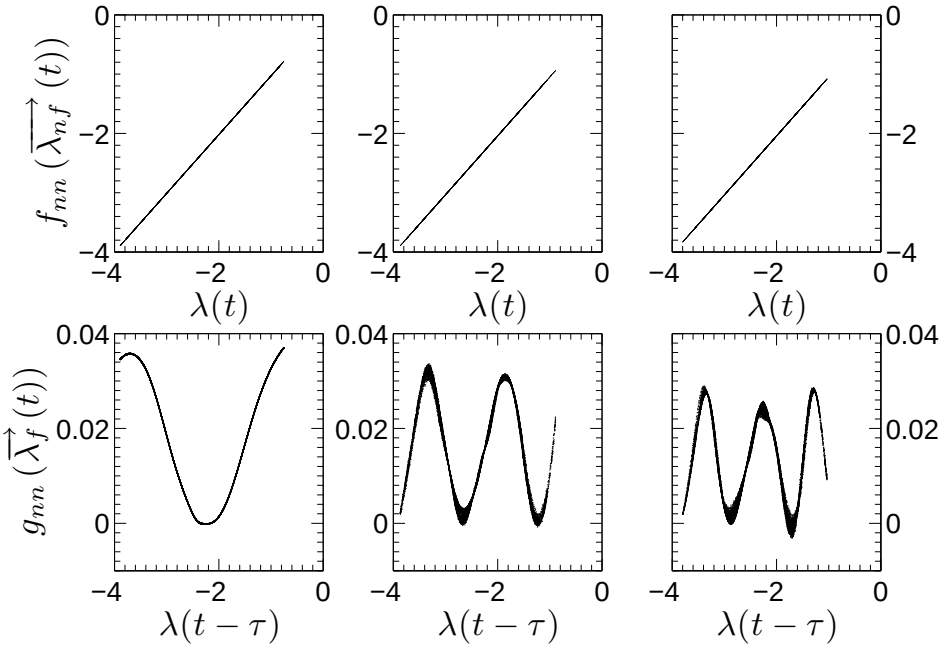

Figure 4.30: Top (Bottom): The recovered functions of the non-feedback (feedback) modules of the MNN. The time series has been generated by a chaotic generator with a nonlinear function with 2 (left), 5 (middle) and 6 (right) extrema, $\tau = 0.476$ ms and $T = 8\ \mu s$. The sampling period is 0.1 μs. $\lambda(t)$ is measured in volts.

nonlinear functions with 2, 5 and 6 extrema, respectively. The MNN functions are sharper in this case due to the lower sampling period. The RMSE are in all the cases around the level noise (0.013 for $\delta t = 0.1\ \mu s$ and the data recorded with the 12 bits oscilloscope). The validation of the models have been made by the synchronization with the experimental time series.

We want to point out that although the above results have been obtained with a time delay of $\tau = 0.476$ ms, similar results have been reached for others time delays, such as 2.05 and 1.23 ms. Therefore, the difficulty to reconstruct the experimental nonlinear dynamics is comparable for different time delays of the system. The same conclusion has been obtained from the numerical simulations.

We conclude that the MNN model correctly reconstructs the dynamics of the experimental system in spite of the very high dimension of the chaotic attractor, that can be estimated to be greater than 200 in all the cases. An estimate of the dimension of the chaotic attractor given by $0.4\beta\tau/T$ [Vicente et al.

2005] leads to dimensions from 280 for $\tau = 0.476$ ms to 1200 for $\tau = 2.05$ ms. Note that we have used for this estimation $\beta = 12$. As previously mentioned, the feedback strength corresponds to a value of the normalized parameter β around 15 when the experimental nonlinear function has 5-6 extrema.

4.6 Conclusions

We have reconstructed the nonlinear dynamics from numerical and experimental time series of time-delay chaotic systems using neural networks. The MG system and systems based on optoelectronic feedback have been used for this analysis. The neural networks are trained with data delayed by the embedding time and by the feedback time of the system. Therefore, to model the nonlinear dynamics of time-delay system with neural networks, it is only necessary to know the feedback time of the system. The feedback time of the system can be extracted from the time series (see chapter 3) and its accuracy estimation is critical to model the system. No a-priori knowledge is necessary about the structure of the scalar equation that rules the chaotic dynamics.

However, we have demonstrated that a new type of Modular Neural Network gives better models with less parameters than the standard feedforward neural networks. The MNN is constructed according with the structure of the time-delay systems and has two modules: one for non-feedback part with input data delayed by the embedding time, and a second one for the feedback part with input data delayed by the feedback time. We have used the chaotic identical synchronization to validate the neural network models.

Nonlinear dynamics attractors with dimensions greater than 200 have been reconstructed from experimental and numerical time series of optoelectronic feedback systems with one delay. We have also reconstructed the nonlinear dynamics of optoelectronic systems with two feedbacks from numerical time series. Two different feedback configurations, serial and parallel, have been considered. The parallel configuration requires adapted MNN (each nonlinear function is modelled by a module) to give model errors similar to the serial configuration.

We have found that the number of parameters of the models necessary to obtain accurate models increases with the feedback strength of the system. However, the complexity of the neural network required to achieve a low model error does not increase with the time delay of the system, in spice of the very high dimension of the chaotic attractor. These results are in agreement with the fact that the entropy of the system increases with the feedback strength but not with the time delay.

Finally, we have also demonstrated that the neural networks can reconstruct the nonlinear dynamics of the system under moderate noise levels. They are even able to filter part of the original noise of the time series.

The main conclusion of this chapter is that chaotic carriers based on time-delay systems with several fixed time delays are vulnerable. It is possible to use the NN models to extract a transmitted message encoded by these type of chaotic carries as we shall see in chapter 6 or to predict the nonlinear dynamics of the system (see chapter 5).

Chapter 5

Prediction of time-delay nonlinear systems

One of the main motivations to reconstruct the nonlinear dynamics of chaotic systems from time series is the prediction of the original chaotic system. Once we have a model of the system, the standard prediction method consists in the forward iteration of the model from the initial state. In this method synchronization between the model and the system has been used to achieve data assimilation and drive the two systems to initially close starting points, from which future predictions can be made [Cohen et al. 2008]. Another alternative technique for predicting the dynamics of chaotic systems that has been recently proposed is the anticipated synchronization [Voss 2000]. In this scenario the driving signal is provided by the original data and the model is the slave in the anticipated synchronization scheme. A cascade of anticipated synchronized models can be used to increase the anticipation time [Voss 2001a]. However, it has been recently shown that a chain of anticipated synchronized exact replicas (slaves) of the original system is unstable to propagating perturbations. The spatiotemporal character of the coupled chain introduces a convective like instability into the synchronization manifold [Mendoza et al. 2004].

In this chapter, we study the above presented issues in the case of time-delay systems. Section 5.1 describes the mechanism of the anticipated synchronization. In section 5.2 we analyze the attainable forecast horizon of a Mackey-Glass system modelled by Modular Neural Networks obtained from the standard prediction and the anticipated synchronization. Experimental and simulations results are presented. Next, in section 5.3 we study the

prediction of the Mackey-Glass system by anticipated synchronization using identical replicas of the original system. Finally, in section 5.4 we analyze the stability of the synchronization manifold of a cascade of time-delay system with non-anticipated synchronization. In this scheme, a convective instability also appears and we characterize it as function of several parameters of the system. Section 5.5 is devoted to summarize and conclude the main results of this chapter.

5.1 Anticipated synchronization

Since the discovery of the chaotic synchronization by Pecora and Carroll [1990], several schemes have been proposed to achieve synchronization. Given two identical autonomous chaotic systems, a master ($\dot{\mathbf{u}}_0 = \mathbf{f}(\mathbf{u}_0)$) and a slave ($\dot{\mathbf{u}}_1 = \mathbf{f}(\mathbf{u}_1)$), one of the simplest synchronization schemes uses a dissipative coupling [Pyragas 1993]:

$$\begin{aligned} \dot{\mathbf{u}}_0(t) &= \mathbf{f}(\mathbf{u}_0(t)) && (5.1) \\ \dot{\mathbf{u}}_1(t) &= \mathbf{f}(\mathbf{u}_1(t)) + \mathbf{K}(\mathbf{u}_0(t) - \mathbf{u}_1(t)) && (5.2) \end{aligned}$$

For particular values of the coupling matrix parameters $\mathbf{K}$ and after some transient time, the dynamics of both systems will be restricted to the synchronization manifold of the unidirectionally coupled system, $\mathbf{u}_0(t) = \mathbf{u}_1(t)$.

The above presented synchronization scheme, where the master and slave system exhibit identical dynamical behavior, is called complete or identical synchronization (see 2, section 2.2). Another interesting type of synchronization in unidirectionally coupled systems is the anticipated synchronization presented recently by Voss [2000]. He has shown that dissipative chaotic systems can drive near-identical system in such a way that the slave anticipates the master by synchronizing with futures states. Amongst the different possibilities to achieve the anticipated synchronization, we restrict ourselves in this thesis to the anticipated synchronization scheme of the form:

$$\begin{aligned} \dot{\mathbf{u}}_0(t) &= \mathbf{f}(\mathbf{u}_0(t)) && (5.3) \\ \dot{\mathbf{u}}_1(t) &= \mathbf{f}(\mathbf{u}_1(t)) + \mathbf{K}(\mathbf{u}_0(t) - \mathbf{u}_1(t - \tau_a)) && (5.4) \end{aligned}$$

The inclusion of the anticipated delay time τ_a in the equation of the slave yields a synchronization manifold, $\mathbf{u}_1(t) = \mathbf{u}_0(t + \tau_a)$. Thus the dynamics of the slave system anticipates by a time τ_a the dynamics of the master for some

bounded region of the coupling parameters $\mathbf{K}$ and the anticipated delay times τ_a.

The anticipated synchronization is globally stable, robust and constitutes a rather universal phenomenon of nonlinear dynamics. After its discovery, the anticipated synchronization have been found in many classes of systems [Hernández-García et al. 2002, Voss 2001a] and it has been demonstrated experimentally in electronic circuits [Voss 2001b] as well as in semiconductor lasers [Liu et al. 2002].

As early emphasized, the anticipated synchronization has attracted a lot of attention because of its potential applications for predicting the dynamics of chaotic systems. Voss [2001a] have proposed to use a chain of anticipated synchronized exact replicas (slaves) of the original system to obtain an arbitrary large forecast horizon. A chain of identical $N+1$ unidirectionally coupled systems is defined in the following way:

$$\begin{aligned} \dot{\mathbf{u}}_0(t) &= \mathbf{f}(\mathbf{u}_0(t)) \\ \dot{\mathbf{u}}_1(t) &= \mathbf{f}(\mathbf{u}_1(t)) + \mathbf{k}(\mathbf{u}_0(t) - \mathbf{u}_1(t-\tau_a)) \\ &\cdots \\ \dot{\mathbf{u}}_N(t) &= \mathbf{f}(\mathbf{u}_N(t)) + \mathbf{k}(\mathbf{u}_{N-1}(t) - \mathbf{u}_N(t-\tau_a)) \end{aligned} \tag{5.5}$$

where subsystem $\mathbf{u}_0(t)$ is the master and subsystems $\mathbf{u}_i(t)$ with $i = 1, \ldots, N$ are slaves. In theory the total prediction time (the anticipation time of the Nth slave as compared to the master), $N\tau_a$, is much larger than that of the single slave scheme. However, in this scheme convective-like instabilities introduced by the spatiotemporal character of the chain appear. They reduce the maximum anticipated time attainable [Mendoza et al. 2004].

5.2 Prediction using non-identical replicas

In most practical cases, the original system is unknown and approximate models fitted to the available data are used to model and forecast its nonlinear dynamics. The forecast horizon in these cases depend not only on the dynamics of the original system, but also on the error of the approximate model.

In this section, we analyze the forecasting of time-delay chaotic systems using the standard prediction and the anticipated synchronization with non-identical replicas. To this aim, we use the Mackey-Glass (MG) system. The MG is described by a time-delay differential equation of the form:

$$\dot{x}(t) = f(x(t)) + g(x(t-\tau)) = -bx(t) + a\frac{x(t-\tau)}{1+x(t-\tau)^c} \tag{5.6}$$

where τ is the time delay and $a = 0.2$, $b = 0.1$ and $c = 10$ are the standard parameters. We have carried out numerical simulations of the system (5.6) by the Adams-Moulton predictor-corrector scheme [Press et al. 1992] with a time integration step of 0.01. In chapter 4, section 4.2, we have reconstructed the nonlinear dynamics of the MG system from experimental and numerical time series by standard and modular neural networks for feedback delay times that correspond to short and long-delay systems.

Now, we use these modular neural network models to predict the future behavior of the MG system. Similar results are expected using the standard neural networks provided the model errors are similar. In this section we use the MNN(2:2) model obtained from the numerical time series with a RMSE around to $2.9 \cdot 10^{-3}$ ($9.04 \cdot 10^{-4}$) for $\tau = 20$ ($\tau = 100$). Regarding the experimental data we use a MNN(2:2) with a RMSE of $3.9 \cdot 10^{-3}$ ($4.1 \cdot 10^{-3}$) for $\tau = 5.26$ ms ($\tau = 20.6$ ms). The largest Lyapunov exponent is extracted from the numerical and experimental time series [Wolf et al. 1985]. In the numerical case we have obtained a largest Lyapunov exponent of 0.0079 (0.0035) for $\tau = 20$ (100). From the experimental time series we obtain that the largest Lyapunov exponent is 0.04 ms^{-1} (0.02 ms^{-1}) for $\tau = 5.26$ ms (20.6 ms).

5.2.1 Standard prediction with Neural Networks

The standard prediction technique consists on iterating forward in time the approximate model from an initial condition (the present point). The attainable forecast horizon depends on the precise location of the initial condition within the attractor. Thus, the forecast horizon can be only considered in an averaged sense. Lower horizon values correspond to initial conditions chosen in the unstable regions of the attractor where transitions are more likely to occur.

In order to obtain an averaged forecast horizon we iterate the MNN model from 500 different initial conditions distributed over the attractor. We compute the forecast horizon t_p as the time where the distance between the neural and real orbits is larger than 5% of the system's amplitude. The histogram of the horizon time is shown in figure 5.1 for numerical simulations and experiments. In the numerical simulations, the average of the forecast horizon is 375 (1129) for $\tau = 20$ ($\tau = 100$). Moreover, the prediction error is smaller than 0.05 for a prediction time $t_p = 180$ ($t_p = 500$) for $\tau = 20$ ($\tau = 100$) (see figure 5.1(a)).

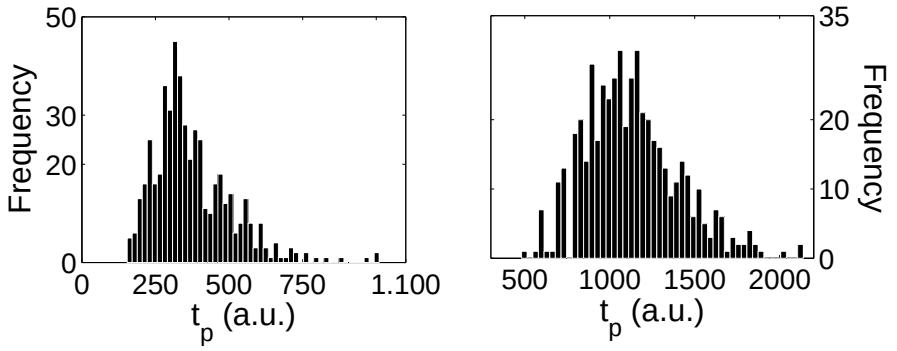

(a) $\tau = 20$ (left) and $\tau = 100$ (right)

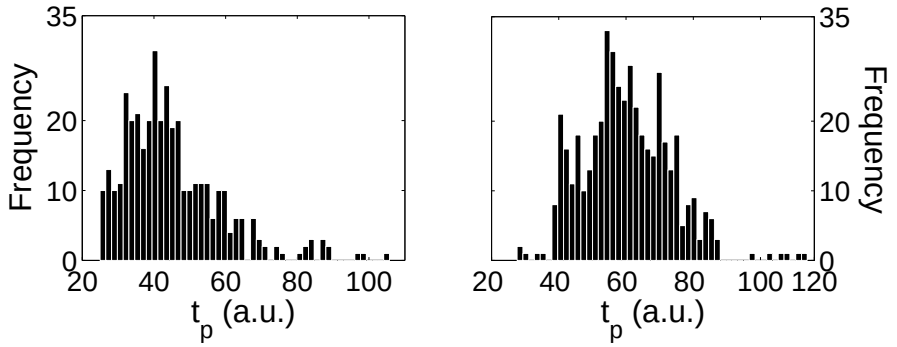

(b) $\tau = 5.26$ ms (left) and $\tau = 20.6$ ms (right)

Figure 5.1: Histogram of the prediction horizon for numerical simulations (a) and experiments (b) of a Mackey-Glass system.

In the experimental case, the average of the forecast horizon is 45 ms (96 ms) when the feedback time is 5.26 ms (20.6 ms). The mean prediction error is smaller than 0.05 for a prediction time $t_p < 20$ ms ($t_p < 45$ ms) when $\tau = 5.26$ ms ($\tau = 20.6$ ms) according to figure 5.1(b). We can also plot the mean prediction error as a function of the forecast time (see figure 5.2 for the experimental case for $\tau = 5.26$ ms and 20.6 ms). We have found that for small errors the error is nearly constant for intervals of the prediction time of the order of the feedback delay time. Then prediction errors increase according to the time scale given by τ and not to the linear response time. Similar results are obtained from the numerical simulations.

The differences between the original time series and the neural network prediction are negligible when the mean error is low. For instance the time

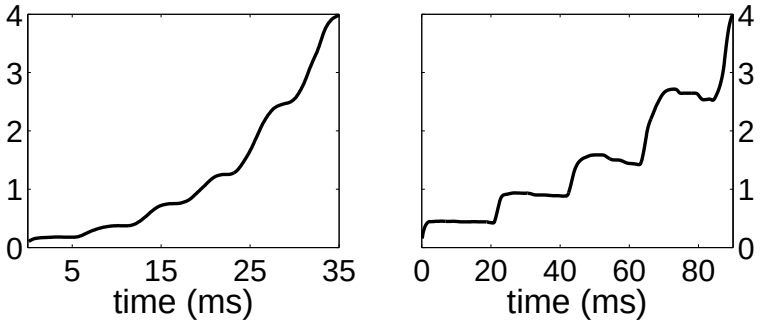

Figure 5.2: Mean prediction error (in %) vs. forecast time. Left (Right): $\tau = 5.26$ ms ($\tau = 20.6$ ms).

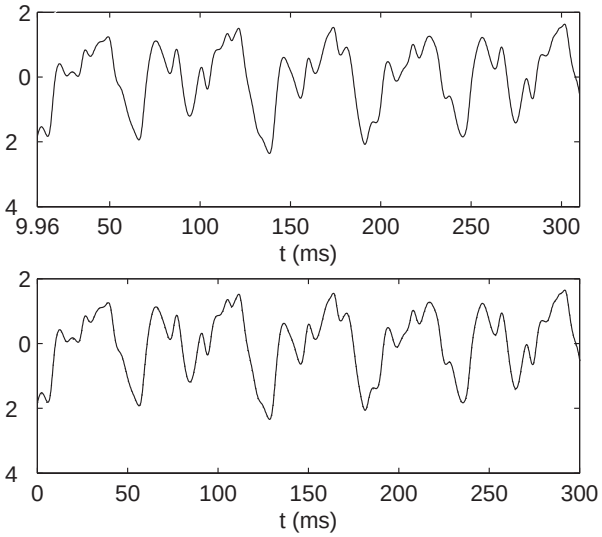

Figure 5.3: Time series in normalized units of experimental data (top) and neural network prediction (bottom) (prediction time $t_p = 10$) ms for $\tau = 5.26$ ms.

series of the experimental data and the MNN prediction (prediction time $t_p =$ 10 ms) for $\tau = 5.26$ ms is shown in figure. 5.3. In this case the mean error is smaller than 0.5%.

The main conclusion of this subsection is that the standard prediction using non-identical replicas of the original system leads to prediction times of the order of the inverse of Lyapunov exponents for experiments and numeri-

cal simulations. Then the maximum prediction time scales with the feedback delay time. Moreover, the prediction horizon can be only given in the probabilistic terms.

5.2.2 Anticipated synchronization with Neural Networks

In this subsection, we use the anticipated synchronization to predict the dynamics of the time-delay chaotic system. We consider an anticipated synchronization scheme where the master system is the original chaotic system, and the slave system is replaced by the modular neural network approximation obtained in chapter 4, section 4.2. A cascade of slave systems is also used to try to increase the anticipation time [Voss 2001a].

Figures 5.4 and 5.5 show the stability regions K vs t_a obtained when coupling the Mackey-Glass system to the MNN(2:2) for the numerical simulations and experiments, respectively. In both cases, we analyze the results for short and large time delays. We consider that synchronization is obtained when the correlation is greater than 0.95. The correlation between two time series $x(t)$ and $y(t)$ is defined as:

$$C = \frac{1}{\sigma_x \sigma_y} \langle (x(t) - \langle x(t) \rangle)(y(t) - \langle y(t) \rangle) \rangle \tag{5.7}$$

where $\sigma_x = \langle (x(t) - \langle x(t) \rangle)^2 \rangle^{1/2}$.

We have found that the results are similar for different feedback delay times ($\tau = 20$ and 100 for the numerical simulations and $\tau = 5.26$ ms and $\tau = 20.6$ ms for the experiments). A reduction of the stability region is obtained when the number of slaves increases. Since the systems are not identical, the errors introduced in each of the slave systems propagate through the cascade. The maximum anticipation time (that corresponds to a correlation greater than 0.95) is around $t_a = 5$ for the simulations and $t_a = 0.8$ ms for the experiments. In both cases, this time is not increased in a significant way by using a cascade of two or more slaves. We can then conclude that the maximum anticipation times are similar for different feedback delay times, and the limit seems to be given by the linear response time (that is 10 for the numerical simulations and around 2 ms for the experiments).

In order to test this conclusion, we calculate the mean synchronization errors in the parameter space K and t_a. In figure 5.6 it is shown for the experimental case that a maximum prediction time of around 1.8 ms with a mean error smaller than 1% is obtained for both feedback delay times. This anticipation time can not be increased by using a cascade of more than three slaves. Moreover, the time series of experimental data (solid line) and

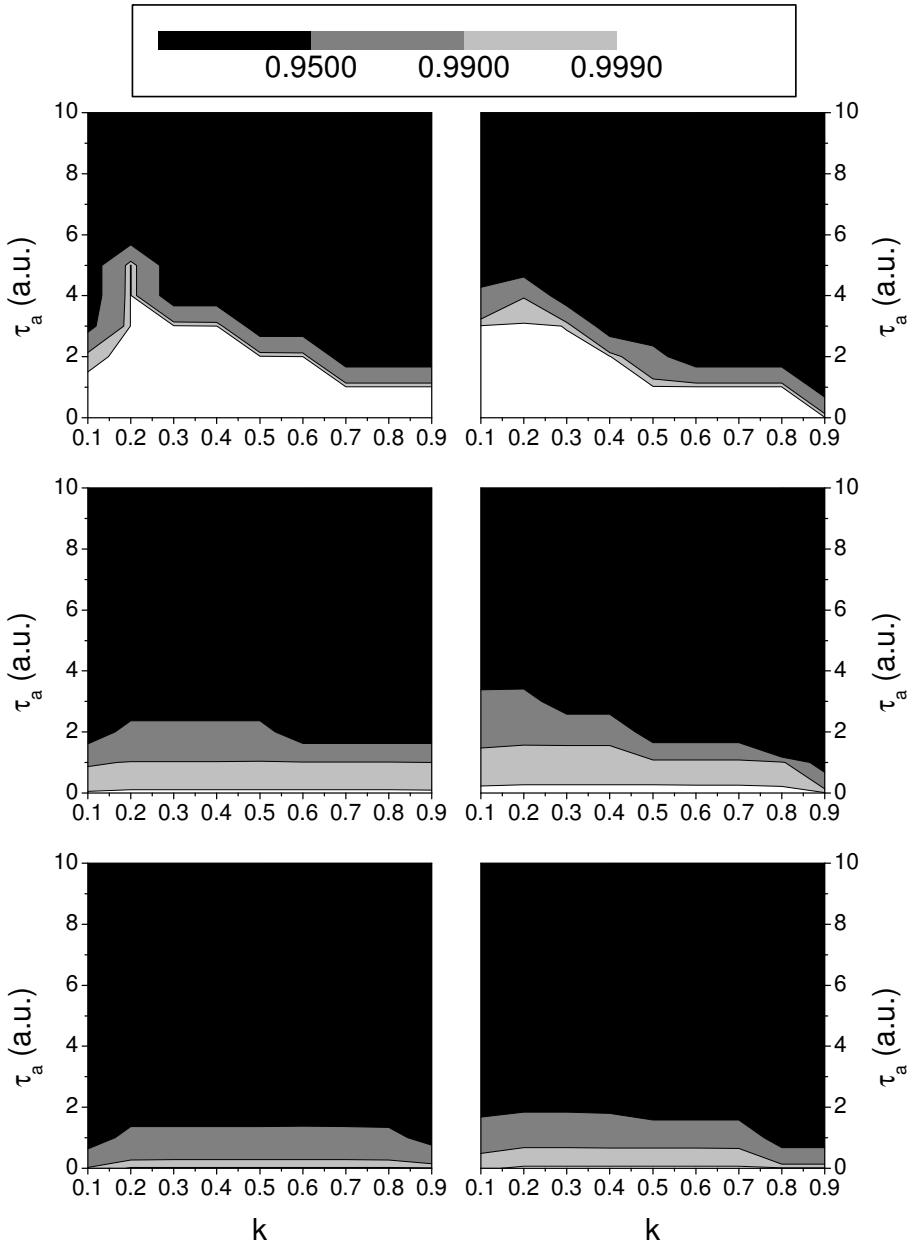

Figure 5.4: Stability region in the parameter space K and t_a for anticipated synchronization of the numerical simulations of the Mackey-Glass system (right: $\tau = 20$; left: $\tau = 100$) with one, two and three slave MNN(2:2) (from top to bottom).

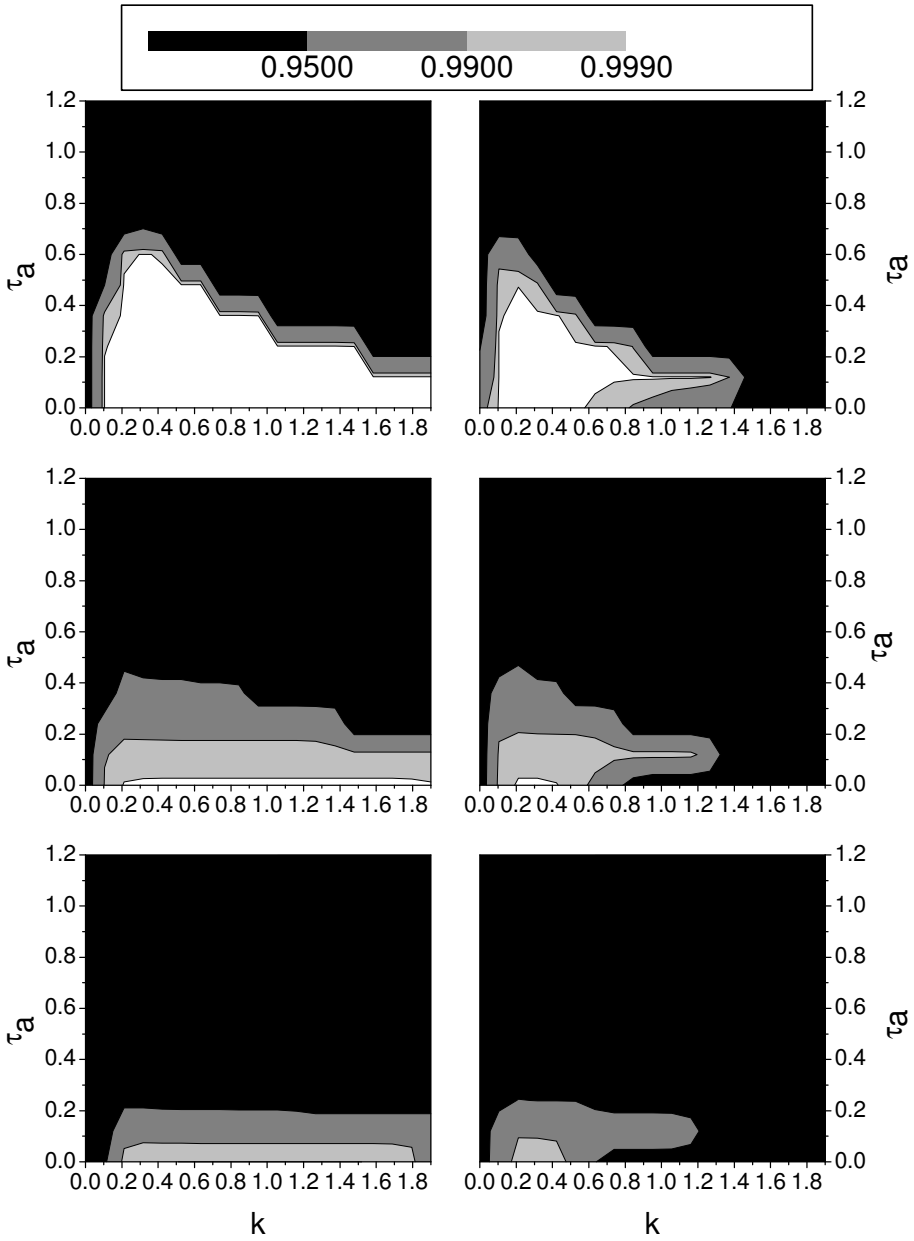

Figure 5.5: Stability region in the parameter space K and t_a for anticipated synchronization of the experimental data of the Mackey-Glass system (right: $\tau = 5.26$ ms; left: $\tau = 20.6$ ms) with one, two and three slave MNN(2:2) (from top to bottom). τ_a is in ms.

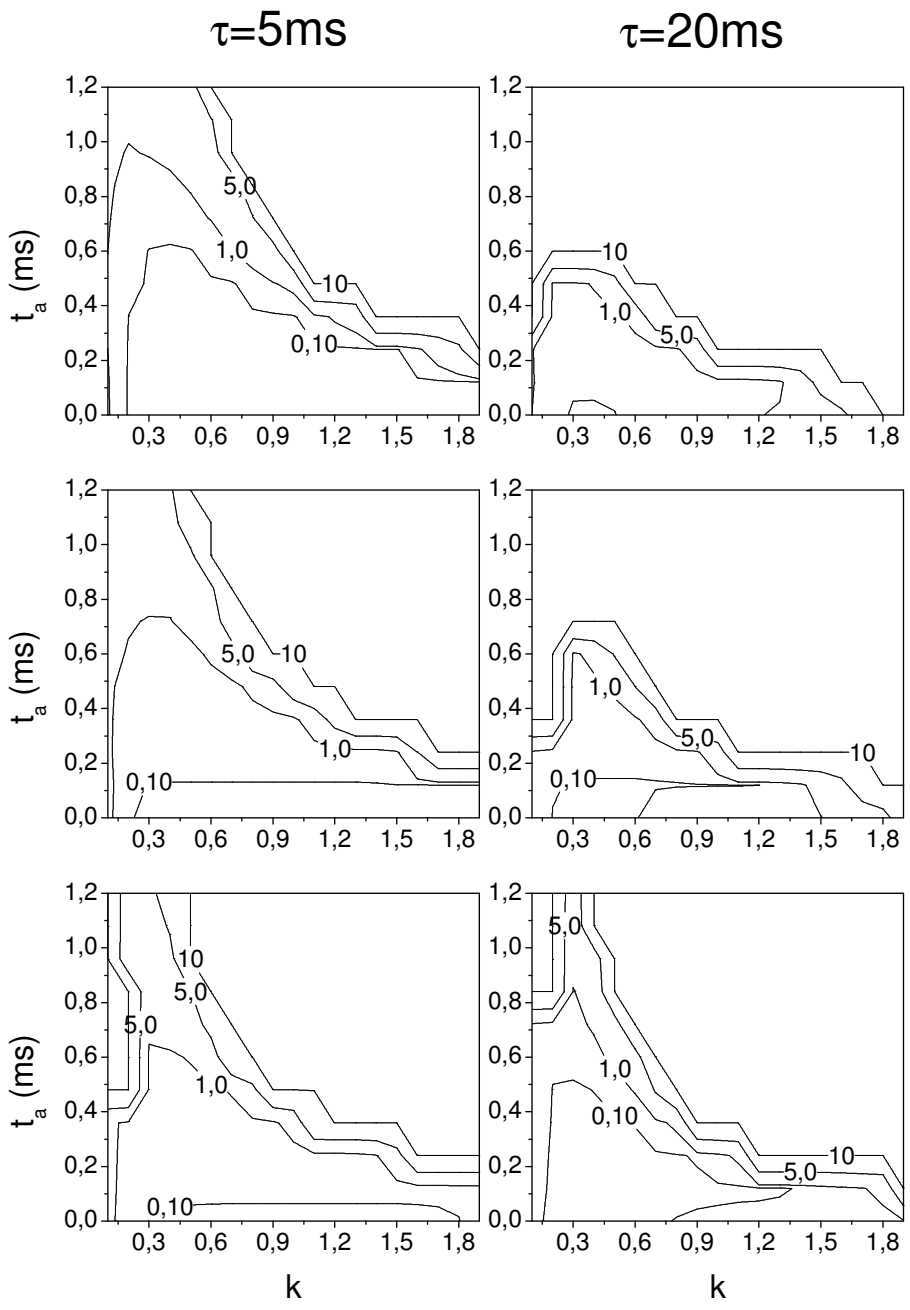

Figure 5.6: Mean synchronization error levels (in %) in the parameter space K and t_a for anticipated synchronization of the experimental data (right: $\tau = 5.26$ ms; left: $\tau = 20.6$ ms) with one, two and three slave MNN(2:2) (from top to bottom).

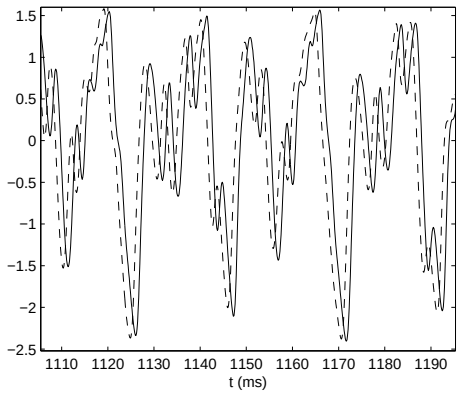

Figure 5.7: Time series of experimental data (solid line) and anticipated slave MNN(2:2) ($t_a = 1$ ms) (dashed line) in normalized units for $\tau = 5.26$ ms.

anticipated slave neural network ($t_a = 1$ ms) for $\tau = 5.26$ ms is shown in figure 5.7.

5.2.3 Conclusions

Two alternative practical techniques have been considered to anticipate the dynamics of the chaotic time-delay systems. On the one hand, the neural network trained to the available data is used to predict the dynamics by the standard technique of iterating the model from an initial condition forward in time. One shortcoming of this method is that the prediction horizon can be only given in the probabilistic terms. Our results for both numerical and experimental data show that the forecast horizon is limited in this technique by the inverse of the largest Lyapunov exponent. Then the maximum prediction time scales with the feedback delay time.

The second technique that we have considered is anticipated synchronization with diffusive coupling between the neural network and the chaotic system. In this scheme the driving signal is provided by the available data. A cascade of slave model systems have been used to increase the anticipation time. Reversely to the previous case, here the horizon anticipation time is a fixed value. We have found for both numerical and experimental data that the maximum prediction times are similar for different feedback delay times. The forecast horizon with a single slave is limited by the linear response time. Prediction times are not increased in a significant way by using a cascade of slave model systems.

These conclusions are in agreement with the numerical results obtained for low dimensional and non-delayed chaotic system (Lorentz and Rössler) [Ciszak et al. 2005].

5.3 Prediction using identical replicas

In the previous section we have shown that the anticipated synchronization scheme using a single non-identical replica as slave does not reach anticipated times larger than the linear response time of the system.

The limit imposed by the response time of the system to the maximum attainable anticipated time can be explained analyzing the anticipated synchronization with identical copies of the original system.

The first approximation to the forecasting of a dynamical system with the anticipated synchronization is to take two identical chaotic systems and determine the maximum anticipated time delay without destabilizing the system.

The anticipated synchronization by a diffusive coupling in scalar time-delay chaotic system is given by:

$$\begin{aligned} \dot{u_0}(t) &= f(u_0(t)) + g(u_0(t-\tau)) \\ \dot{u_1}(t) &= f(u_1) + g(u_1(t-\tau)) + K(u_0(t) - u_1(t-t_a)) \end{aligned} \tag{5.8}$$

We first consider a couple of identical master-slave Mackey-Glass models with $\tau = 30$, $a = 0.2$, $b = 0.1$ and $c = 10$. The correlation between the master $u_0(t)$ and the slave $u_1(t-t_a)$ is shown in figure 5.8. Similar results are obtained for $\tau = 100$. If we consider that synchronization is obtained when the correlation is greater than 0.95, the maximum anticipation time is around $t_a = 5$. This time is smaller than the linear response time $T = 10$.

This suggests that the anticipated synchronization mechanism is limited to a neighborhood of t, where $u_1(t-\tau_a)$ can be linearly approximated in terms of $u_1(t)$. Substituting the linear approximation $u_1(t-t_a) = u_1(t) - t_a\dot{u}_1(t)$ into the equation (5.8), we get the following expression:

$$R\dot{u_1}(t) = f(u_1(t)) + g(u_1(t-\tau)) + K(u_0(t) - u_1(t)) \tag{5.9}$$

where $R = 1 - K\,t_a$. Thus, using a first-order approximation, the anticipated synchronization scheme can be reduced to a non-anticipated synchronization scheme with a different time scale ($t' = t/(1-K\tau_a)$). Anticipation requires (in the first-order approximation framework) $0 < 1-K\tau_a < 1$, giving the following two constrains for anticipated synchronization $K\tau_a > 0$ and $K\tau_a < 1$.

This simple prediction has been compared with the numerical anticipated synchronization diagram of the MG system. Figure 5.8 (left) shows that the

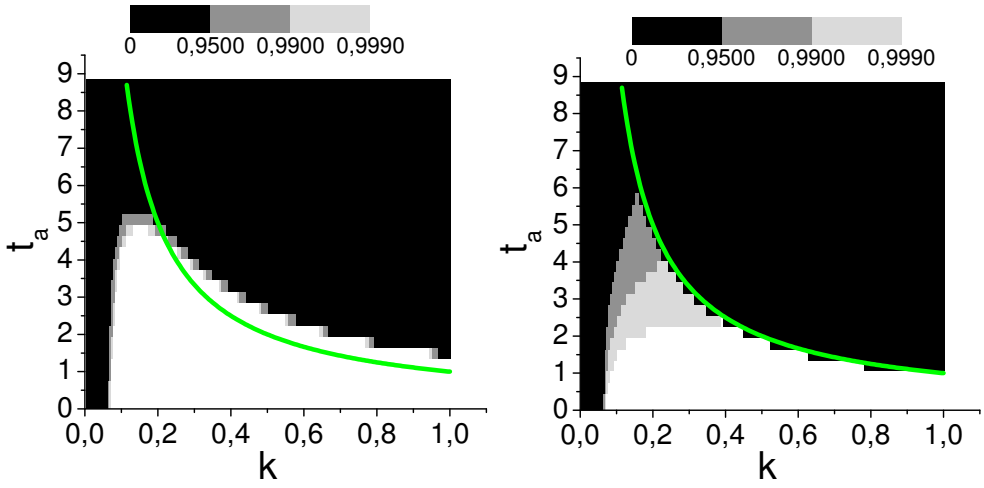

Figure 5.8: Stability region in the parameter space K and t_a of the Mackey-Glass system ($\tau = 30$) with one identical copy for anticipated synchronization scheme (left) and the first-order approximation scheme (right). The green line corresponds to the curve $K\,t_a = 1$

curve $K\,\tau_a = 1$ gives a bound in qualitative agreement with numerical results. For comparison, we have also included in figure 5.8 (right) the synchronization diagram coming directly from the approximation scheme given by equation (5.9). The similarity between the two figures (5.8 right and left) confirms the validity of our simple approximation. This approximation is also valid for non-delayed chaotic systems [Ciszak et al. 2005].

The bound of $K > 0$ is only a necessary condition for the anticipated synchronization, but it turns out that a minimum coupling value is required in order to achieve synchronization.

We can then conclude that anticipated synchronization is limited to anticipation times of the order of the linear response time, thus strongly limiting its practical application. To obtain longer anticipation times it is necessary to consider a chain of slave systems.

It has been demonstrated that chains of anticipated synchronized identical slaves chaotic systems can reach a total anticipation time much larger than the the inverse of the largest Lyapunov exponent [Ciszak et al. 2005, Voss 2001a]. Although the maximum anticipation time attainable with the chain of the coupled system decreases with N, the total prediction time, $N\tau_a$, can be much larger than that of the single slave scheme. However, recently it has been shown that convective-like instabilities introduced by the spatiotemporal

character of the chain reduce the maximum anticipation time τ_a in each unit as compared to the case of a single slave [Mendoza et al. 2004]. Although the anticipating synchronization manifold of the chain is absolute stable, the convective instability undermines the stability of the synchronous regime in long chains.

5.4 Convective instability

Convective instabilities are typical of spatially extended systems. A convective instability is one in which a small localized perturbation moves spatially such that the perturbation grows only in a moving frame of reference [Briggs 1964, Deissler 1987].

Time-delay systems have been also interpreted as a spatially extended system by decomposing the time variable in intervals of the time delay of the system. Under this assumption, convective instabilities have been also found in a CO_2 laser with delayed feedback [Giacomelli et al. 2000]. Convective instability also appears in systems with nonlocal coupling that is the spatial analogous of temporal delay [Papoff and Zambrini 2005].

On the other hand, an open chain of unidirectionally coupled chaotic slaves (oscillators) can be also interpreted as a spatially extended system by considering the integer i labelling the slaves (oscillators) as a space variable. Therefore, the absolute stability of the synchronization manifold is only a necessary condition for the robustness of synchronization properties in chains of unidirectionally coupled systems. In this systems, it is also necessary to assure the stability versus the convective growth of perturbations in suitable moving frames

Regarding the latter point, Mendoza et al. [2004] have recently demonstrated that the synchronization manifold of anticipating synchronization in an open chain of unidirectionally coupled identical chaotic oscillators is unstable to propagating perturbations. In this scheme, the oscillators or slaves are non-delayed chaotic systems (Rössler). The convective instabilities are favored in this case by the feedback time, τ_a, provided by the anticipated synchronization.

Now, we focus on the study of an open chain of unidirectionally coupled identical time-delay chaotic oscillators. We first study the case of the identical synchronization without anticipation, i.e. $\tau_a = 0$. In order to address such a problem, let us consider an open chain of N unidirectionally coupled identical Mackey-Glass oscillators (slaves), given by:

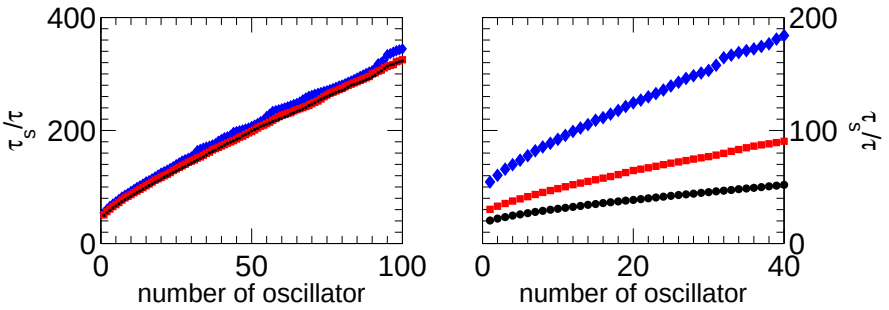

Figure 5.9: Time to reach the synchronization state, τ_s (defined as the time where the synchronization error is lower that 10^{-15}). Data are obtained from an ensemble average of 1000 perturbations. Left: The blue diamonds, red squares and black circles correspond to $K = 0.3$, $\tau = 30, 60$ and 90, respectively. Right: The blue diamonds, red squares and black circles correspond to $\tau = 30$, $K = 0.3, 0.6$ and 1.2, respectively.

$$\dot{u}_i(t) = f(u_i(t)) + g(u_i(t-\tau)) + K(u_{i-1}(t) - u_i(t)) \tag{5.10}$$

where $u_i(t)$ determines the dynamic of the ith driven oscillator ($i = 1, \ldots, N$), K is the coupling parameter, τ is the time delay, $f(u_i(t)) = -au_i(t)$, $g(u_i(t-\tau)) = bx(t-\tau)/(1+x(t-\tau^c))$ and the parameters of the Mackey-Glass system are the standard $a = 0.1$, $b = 0.2$, $c = 10$. Farmer demonstrated that the Mackey-Glass system is chaotic for $\tau > 16.8$ and that the synchronization is possible for large enough values of K [Farmer 1982].

Following a similar approach as presented in [Mendoza et al. 2004], we now study the evolution of a perturbation once the system (5.10) has reached the synchronization manifold. To this aim, system (5.10) is evolved from a random initial condition for $N = 100$, up to the time at which an absolutely stable synchronization manifold (SM) is reached. Stability remains independent of the chain length, but the time necessary to reach the stable synchronization manifold has a linear dependence with the number of oscillator of the chain and scales with the feedback time of the system (see figure 5.9 (left)). Moreover, the time necessary to reach the stable synchronization manifold is inversely proportional to the coupling parameter K (see figure 5.9 (right)).

At this point, we investigate the response of the system to a delta-like perturbation. More precisely, we have let the system (5.10) evolve from a random initial condition at $t = 0$ until it reaches (within numerical accuracy) the synchronization manifold. Then, the evolution is restarted after perturbing u_1 by a small amount $\delta = 10^{-12}$, while all other variables are left unchanged.

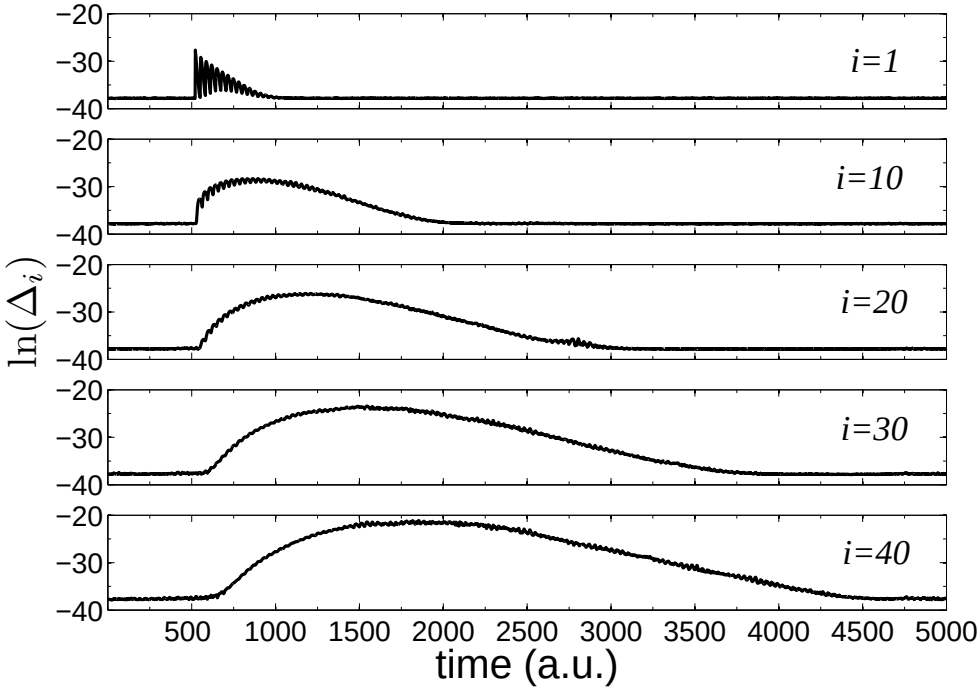

Figure 5.10: Time evolution of the ensemble averaged differences $\Delta(i,t)$. Data is obtained from an ensemble average of 1000 perturbations, for $\tau = 30$, $K = 0.3$ and $\delta = 10^{-12}$.

The perturbations or deviations from the stable SM are studied by monitoring $\Delta(i,t) = |u_i(t) - u_0(t)|$. The $\ln(\Delta(i,t))$ corresponding to different oscillators are plotted in figures 5.10 and 5.11 for $\tau = 30$, $K = 0.3$ and $K = 0.6$, respectively. We observe for each oscillator that the deviation from the SM initially grows but finally converges to zero thus confirming its absolute stability. In spite of this, the maximum of $\ln(\Delta(i,t))$ increases for oscillators labelled by larger i. This behavior is analogous to that of convective unstable coupled spatially extended systems where a small localized perturbation dies if observed where it has been generated while it appears to grow in suitably moving frames [Briggs 1964, Deissler 1987].

The perturbation not only increases its amplitude whereas propagates through the chain of oscillators. The perturbation width grows linearly with the number of the oscillator (see figure 5.12). Moreover, the width of the perturbation decreases for larger coupling parameters. At larger K, the slave system synchronizes faster with the master, so the slaves can get back faster to

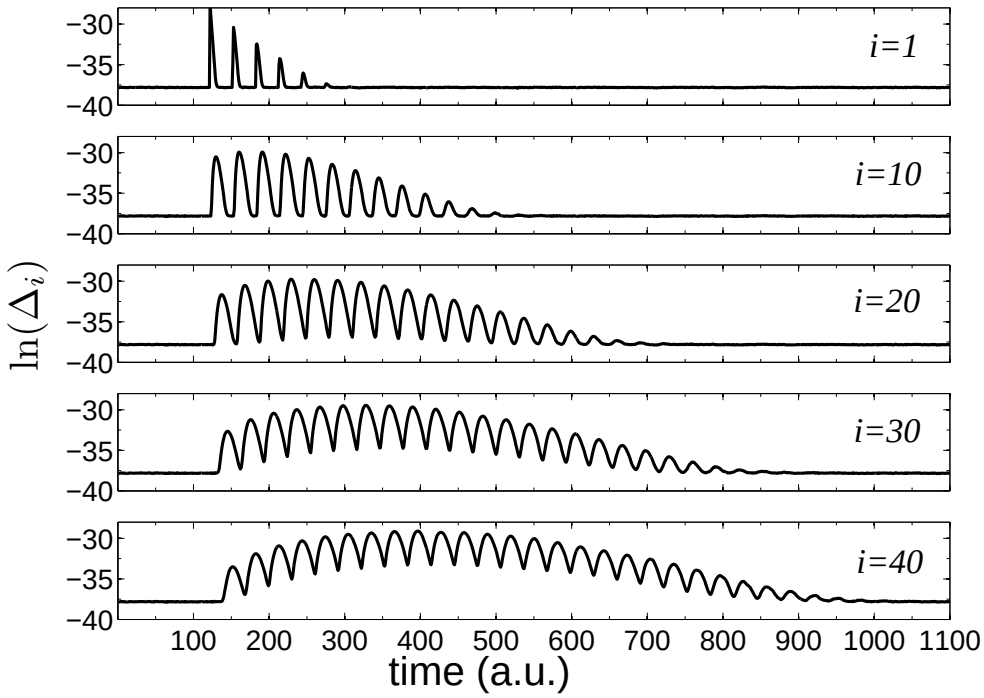

Figure 5.11: Time evolution of the ensemble averaged differences $\Delta(i,t)$. Data is obtained from an ensemble average of 1000 perturbations, for $\tau = 30$, $K = 0.6$ and $\delta = 10^{-12}$.

the stable synchronization manifold after a perturbation. We have also found that for the MG system, the perturbation fulfills the following relation:

$$\frac{\Delta(i,t)}{\Delta(i,t-\tau)} = \frac{\Delta(i-1,t)}{\Delta(i-1,t-\tau)} \tag{5.11}$$

where i indicate the number of oscillator (space) and t is the time.

The origin of the convective-like growth in synchronized chains of chaotic systems is a question that has to be addressed. In time-delay systems, the perturbation at oscillator i consists of the response to the perturbation from the previous oscillator $i-1$ and the replicas generated by the oscillator i approximately at multiples of the time-delay due to its own feedback. This effect can be better appreciated in chains with large K where the response to the original perturbation has decayed before the replicas due to the time-delay of the system appear (see figure 5.11). If K is not strong enough the effect of the perturbation and its replicas overlap (see figure 5.10). A possible

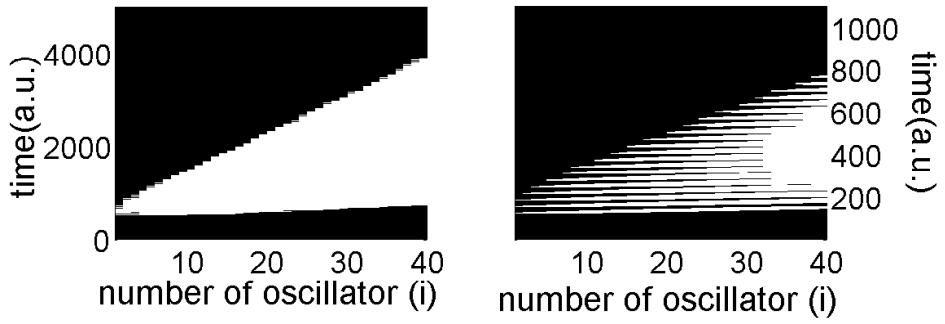

Figure 5.12: Synchronized (black) and desynchronized (white) areas. The system is considered synchronized when $\Delta(i,t) < 10^{-17}$. The right (left) panel corresponds to $K = 0.3$ ($K = 1.2$).

mechanism for the growth of the perturbation in a moving frame of reference is the enhancement of the perturbation by the replicas.

Now, we want to characterize the convective instability propagation and amplification as a function of the time delay and the coupling parameter. In the context of one-dimensional lattices, the convective Lyapunov exponent is defined as [Deissler and Kaneko 1987]:

$$\Lambda(v) = \lim_{t\to\infty} \frac{1}{t} \ln \frac{|\Delta(i = vt, t)|}{|\Delta(0,0)|}, \tag{5.12}$$

where $\Delta(i,t)$ denotes the perturbation amplitude in oscillator i at time t and is initially localized in a finite region around the origin. The convective Lyapunov exponent expresses the growth rate of a localized perturbation, when observed in a frame moving with velocity v. This is equivalent to stating that the asymptotic perturbation amplitude on oscillator i and a time t grows like:

$$\Delta(i,t) \simeq \exp(\Lambda(v)t) = \exp(\frac{\Lambda(v)}{v} i) \tag{5.13}$$

when both $|i|$ and t are large enough.

From a numerical point of view, $\Lambda(v)$ can be accurately estimated by comparing the perturbation amplitude at two different space-time positions $P_1 = (i_1, t_1)$, $P_2 = (i_2, t_2)$,

$$\Lambda(v) = \frac{v}{i_2 - i_1} \ln \frac{\Delta(i_2, t_2)}{\Delta(i_1, t_1)}, \tag{5.14}$$

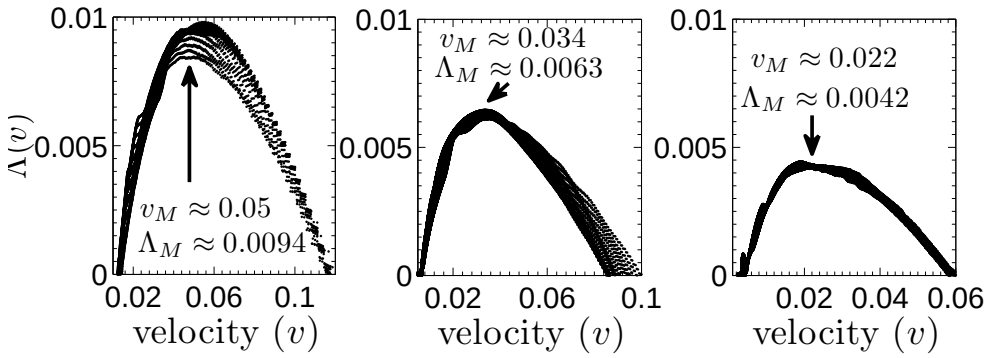

Figure 5.13: Convective Lyapunov exponent versus the propagation velocity, computed according to equation (5.14) for different pairs of oscillators so $(i_2 - i_1) = 4$. In all the cases $K = 0.3$ and from left to right $\tau = 30$, 60 and 90, respectively.

where $v = i_1/t_1 = i_2/t_2$. The typical behavior of $\Lambda(v)$ in convective unstable system is: as v is increased from zero, the convective Lyapunov exponent will increase until it reaches a positive maximum, Λ_M, at a velocity v_M, and then it decreases until it again becomes negative.

Now, we calculate $\Lambda(v)$ for different time delays (see figure 5.13 and 5.14). We can see that $\Lambda(v)$ follows the typical behavior of convective unstable system. The existence of a positive maximum of $\Lambda(v)$ implies that perturbations travelling with a velocity $v = i/t$ between the two zeros of $\Lambda(v)$ are amplified.

We have found that for $\tau = 30, 60$ and 90 (chaotic regime), $\Lambda_M/v_M = 0.19$ when $K = 0.3$. Therefore, for long values of the time delay, the amplification of the perturbation with i is independent of τ. However, this behavior of Λ_M/v_M with respect to τ is not observed for short values of the time delay (non-chaotic regime). In these cases, the amplification of the perturbation with i depends on τ, although the amplification rate is always lower than for the chaotic regime. For instance, when $K = 0.6$, for $\tau = 30, 7$ and 3.5, $\Lambda_M/v_M = 0.08, 0.069$ and 0.056, respectively.

We can also analyze the behavior of the convective Lyapunov exponent with the coupling parameter K (see figure 5.15). Here, Λ_M slightly decreases with the coupling strength whereas v_M is proportional to K. Thus, the amplification of the perturbation, $\Delta(i, v/i)$, is almost inversely proportional to K (see figure 5.16). Therefore, large coupling parameters decrease the amplifica-

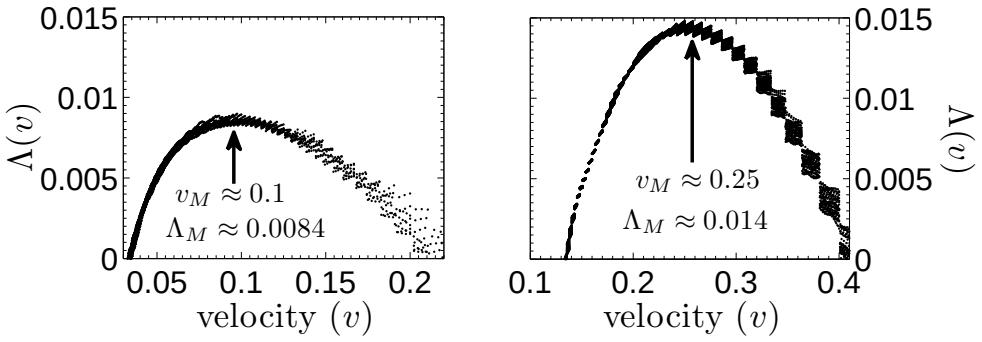

Figure 5.14: Convective Lyapunov exponent versus the propagation velocity, computed according to equation (5.14) for different pairs of oscillators so $(i_2 - i_1) = 4$. In all the cases $K = 0.6$ and in the left (right) panel $\tau = 30$ ($\tau = 7$).

tion of the perturbation. This result agrees with the fact that large coupling parameter forces more the slave system to follow the dynamics of the master.

The value of the maximum convective exponent, Λ_M, can be independently checked by monitoring the maximum value of the perturbation, Δ_M, for each oscillator i (see figures 5.17 and 5.18). From figure 5.17 (left) it is clearly appreciated that the growth of the convective instability is independent of τ. Moreover, the slope of $\ln(\Delta_M(i))$ is 0.2, in good agreement with the value of $\Lambda_M/v_M = 0.19$ obtained previously. However, for short values of the time delay (non-chaotic regime) the amplification of the perturbation with i depends on τ (see figure 5.17 right). In this case the amplification rate is always lower than for the chaotic regime. Likewise, figure 5.18 shows how the amplitude of the perturbation decreases as K is increasing. The fit of figure 5.18 also agrees with the result showed in figure 5.16.

However, let us point out that the scaling growth behavior of the perturbation starts only above a certain oscillator i (see figures 5.18 and 5.17). Our results show that the length of the chain necessary for the perturbation to grow depends basically on K. As we can see from figure 5.18, the larger the coupling parameter, the larger the oscillator at which the convective instability starts to grow. In fact, we have found that for $K = 1.2$, the chain length should be larger than 40 oscillators.

This opens a door to use chains of anticipated synchronized identical time-delay chaotic systems oscillators as a forecasting method. However, preliminary results obtained in anticipated synchronized chains of unidirectionally

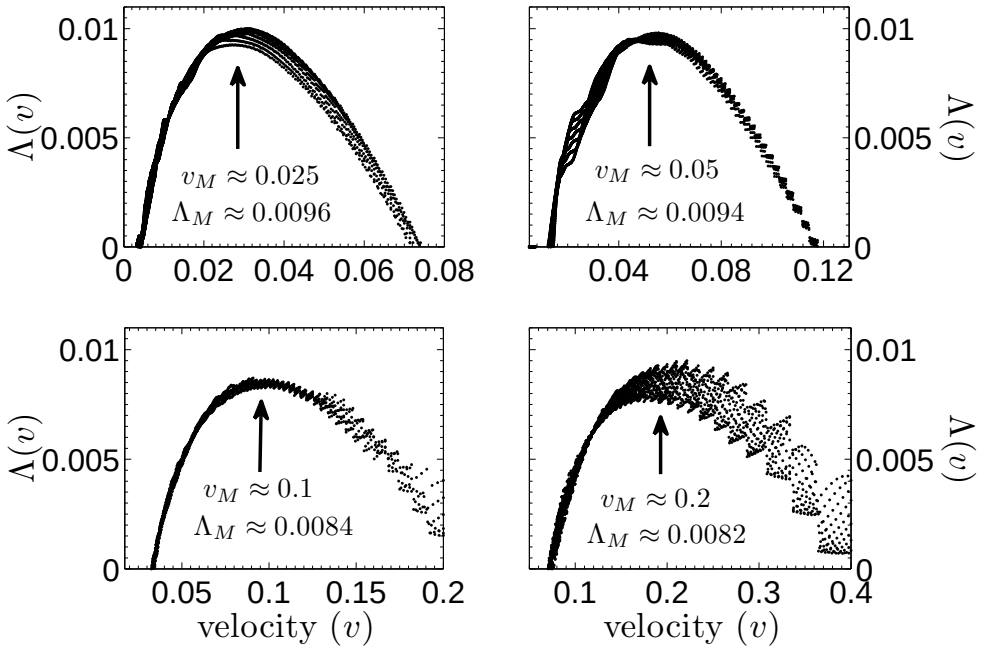

Figure 5.15: Convective Lyapunov exponent versus the propagation velocity, computed according to equation (5.14) for different pairs of oscillators so $(i_2 - i_1) = 4$. In all the cases $\tau = 30$ and $K = 0.15$, 0.3, 0.6, 0.12 from left to right.

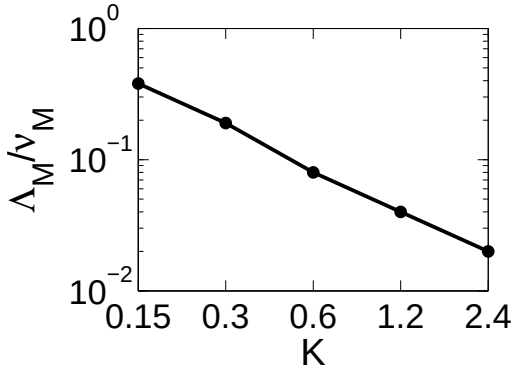

Figure 5.16: Λ_M/v_M versus K for a unidirectionally chain of identical synchronized MG when $\tau = 30$.

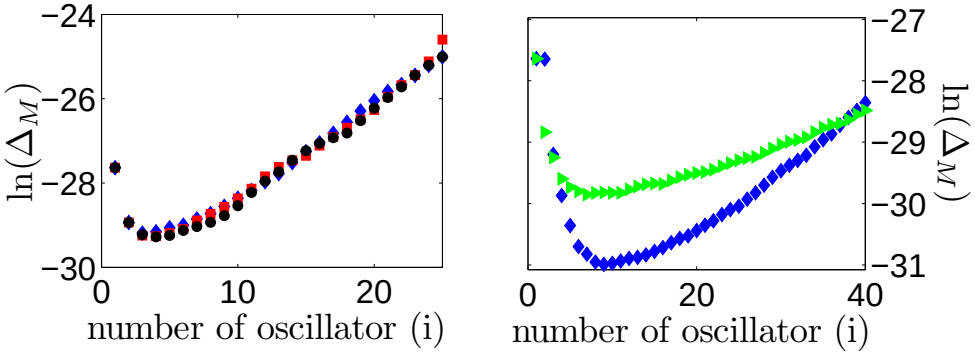

Figure 5.17: The maxima of $\Delta(i,t)$, Δ_M, versus the oscillator number. The blue diamonds, red squares, black circles, and green triangles correspond to $\tau = 30$, 60, 90 and 7, respectively. Left (Right): $K = 0.3$ ($K = 0.6$).

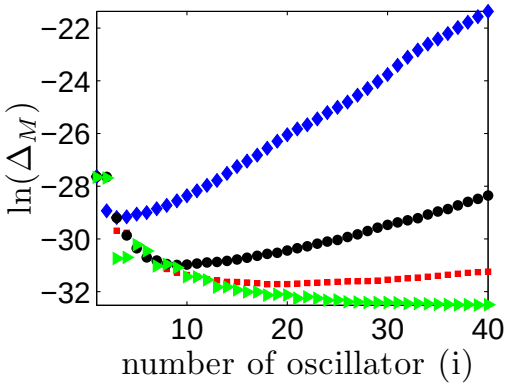

Figure 5.18: The maxima of $\Delta(i,t)$, Δ_M, versus the oscillator number. The blue diamonds, red squares, black circles, and green triangles correspond to $K = 0.15$, 0.3, 0.6 and 1.2, respectively. In all the cases $\tau = 30$.

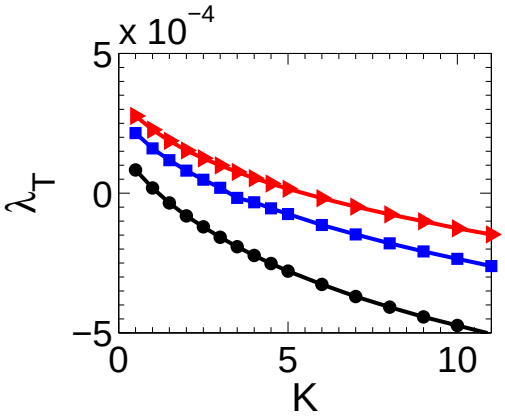

Figure 5.19: The transverse Lyapunov exponent versus the coupling parameter K for the Ikeda system when $\tau = 10$. The red triangles, blue squares and black circles correspond to $\beta = 15, 10$ and 5, respectively.

coupled identical time-delayed chaotic oscillators show that the amplitude of the perturbation starts to grow earlier and grows faster than for $\tau_a = 0$. Moreover, we have previously shown that the large coupling parameter, the shorter the anticipation time of the system, so $K\tau_a \sim cte$ (see section 5.3). Therefore, use of chains of anticipated synchronized identical time-delay chaotic systems oscillators as a forecasting method seems to be an unpractical method.

Finally, we present the preliminary results obtained from a chain of unidirectionally Ikeda identical coupled systems. This scheme is interesting because permit us to study the behavior of the convective instability as function of the nonlinearity strength (related to the entropy) of the system. All reported simulations of the Ikeda system have been performed by implementing an Adams Moulton predictor corrector scheme [Press et al. 1992].

The transverse Lyapunov exponent, describing the convergence rate of the orbits along the synchronization manifold, should be negative for an achievement of stable synchronization in the coupled systems. For the Ikeda system, the coupling parameter necessary to have a negative transverse Lyapunov exponent increases with the nonlinearity strength, β (see figure 5.19).

Once the chain of unidirectionally Ikeda identical synchronized systems has reached the stable manifold (the time to reach the synchronization state increase with β), we introduce an initial perturbation $\delta = 10^{-12}$ into the first slave. In this case, the maximum convective Lyapunov exponent Λ_M increases with β whereas v_M is constant. In figure 5.20, we plot the maximum

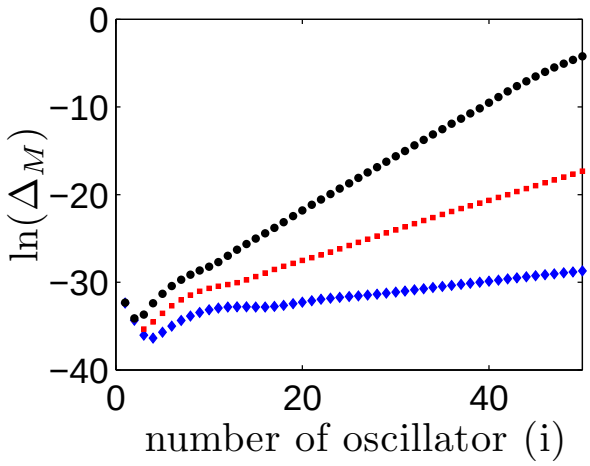

Figure 5.20: Left (Right): The maxima of $\Delta(i,t)$, (Δ_M), of each i versus their occurrence time. The blue diamonds, red squares, and black circles,correspond to $\beta = 5$, 10, and 15, respectively. In all the cases $\tau = 10$ and $K = 12$.

of the perturbation, Δ_M for different βs. Clearly, the amplification of the perturbation increases with β. Moreover, the estimation of Λ_M/v_M from figure 5.20 gives 0.1 ($\beta = 15$), 0.63 ($\beta = 10$) and 0.35 ($\beta = 5$).

To conclude, we have demonstrated that convective instabilities appear in chains of unidirectionally synchronized identical time-delay chaotic oscillators, when even a small amount of noise is present. Moreover, we have shown that in the chaotic regime, the growth of the convective instabilities is independent of the time delay and increases for weak coupling parameters. Preliminary results obtained from the Ikeda system also show that the amplification of the perturbation increases with the nonlinearity strength of the system.

5.5 Conclusions

We have studied the predictability of time-delay chaotic system using the standard prediction and the anticipated synchronization.

In most practical cases, the original system is unknown and approximate models fitted to the available data are used to model and forecast its nonlinear dynamics. The forecast horizon in these cases depend not only on the dynamics of the original system, but also on the error of the approximate model.

When non-identical replicas are used, we have found for both numerical and experimental data that the forecast horizon obtained with the standard prediction is of the order of the inverse of the largest Lyapunov exponent.

Regarding the anticipated synchronization with diffusive coupling between the neural network and the chaotic system, we have demonstrated for both numerical and experimental data that the maximum prediction times are similar for different feedback delay times. The forecast horizon with a single slave is limited by the linear response time. Prediction times are not increased in a significant way by using a cascade of slave model systems.

Therefore, the anticipated synchronization scheme discussed here cannot forecast longer that the linear prediction time and much less than the inverse of the largest Lyapunov exponent.

We have also shown that chains of anticipated non-identical replicas do not increase significantly the prediction time of the system. Using identical replicas the prediction time of the system is longer than the characteristic ones. However, the anticipation time leads to the apparition of convective instabilities.

We have used the original system as master and N identical synchronized models as chain of slaves. In our case, the intrinsic time delay of the system yields to the appearance of convective instabilities when the identical or complete synchronization are considered. In this case the feedback time of the system plays the role of the anticipated time. We have characterized these convective instabilities by the convective Lyapunov exponent. We have found that for long values of the time delay the amplification of the perturbation at each oscillator is independent of τ and decreases almost inversely proportional with the coupling parameter K. Moreover, the growth of perturbation is faster than in chains of unidirectionally coupled non-delayed systems (Rössler) synchronized anticipated, where $\Lambda_M/\nu_M = 0.0034$.

Chapter 6

Unmasking messages encoded by time-delay chaotic systems

Chaotic communications applying chaos synchronization have attracted a great deal of attention due to their multiples applications. Specially interesting is the possibility of using chaotic communications to improve the security of communication systems. However, the security of chaotic communication systems remains the key to be addressed.

Privacy in chaotic communication systems is based on the fact that the emitter and receiver must posses the same configuration and parameter settings. Important aspects of receiver design are the number of parameters that have to be matched for information recovery and the precision required for parameter matching. The decoding of the message is possible only when the emitter and receiver systems are almost perfectly identical.

The security of chaotic communication systems has been extensively researched but most of the research is focused on low-dimensional dynamics. Many chaos-based encryption schemes with low dimensional chaos have been proposed and many of those schemes have been broken later. [Pérez and Cerdeira 1995, Rulkov et al. 1995, Short 1994; 1996, Short and Parker 1998, Yang et al. 1998a;b;c]. Lately, the interest has turned to develop chaotic communications systems that can generate high dimensional hyperchaos, because it is expected that these systems will improve the confidentiality of the transmitted messages.

Nonlinear systems with delayed feedback can have many positive Lyapunov exponents and chaotic attractors whose dimension increases with the delay time reaching very high values [Farmer 1982]. Nonetheless, high-dimensional

chaotic communication systems based on delayed feedback systems have been also unmasked by nonlinear time series analysis that exploits the particular structure of time-delay systems [Ponomarenko and Prokhorov 2002, Prokhorov and Ponomarenko 2008, Robilliard et al. 2006, Udaltsov et al. 2003, Zhou and Lai 1999]. In these cases, to unmask the chaotic communication system, it is assumed that the structure of the equations that govern the delay time systems is known.

When the structure of the equations is unknown, we have demonstrated in chapter 4 that a method based on neural networks can reconstruct the nonlinear dynamics of the chaotic time-delay carriers. These neural network models can be used to decode the message.

In this chapter we study the security of optical chaotic communication systems based on chaotic carriers generated by laser diodes subject to delayed optoelectronic feedback. Diode lasers subject to delayed feedback provide simple ways of generating very high-dimensional and high information entropy chaotic carriers [Vicente et al. 2005]. Furthermore, it has been proved that these systems can reach high transmission rates and can be compatible with existing telecommunication infrastructures [Argyris et al. 2005].

The chapter is structured as follows. Section 6.1 describes the different ways to inject the message into the chaotic carrier inside the nonlinear feedback loop. Section 6.2 presents the optical communication system based on semiconductor laser subject to optoelectronic feedback. In section 6.3, we detail the way of working of the modular neural network as an unauthorized receiver. Sections 6.4 and 6.5 are devoted to message extraction from numerical simulations when the chaotic carrier has one and two delays, respectively. Section 6.6 analyzes the recovery of the message from experimental time series for different parameters values. Finally, we summarize our main conclusions in section 6.7.

6.1 Chaos modulation scheme in time-delay systems

A large variety of modulation and demodulation schemes have been proposed for chaotic communication systems. Particulary interesting is the chaos modulation scheme (CMO), where the information signal is embedded into the dynamics of the chaotic carrier (see chapter 2, section 2.3). When the dynamical state of the chaotic time-delay generator can be described by a delayed differential equation, there are different ways to implement the CMO scheme [Prokhorov and Ponomarenko 2008, Udaltsov et al. 2001]. Let us consider a

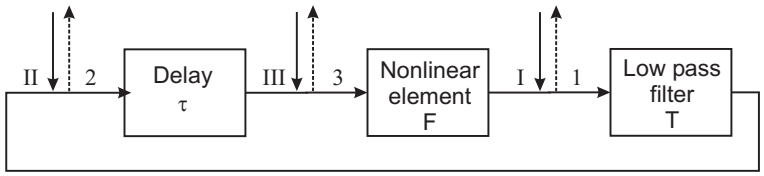

Figure 6.1: Block diagram of a delayed nonlinear feedback system generating a chaotic signal. The numerals I-III indicate points where an information signal can be injected into the system. The numerals 1-3 indicated the output points of the transmitter.

chaotic carrier governed in absence of information signal by a delayed differential equation of the form:

$$T\dot{x}(t) = -x(t) + F(x(t-\tau)) \tag{6.1}$$

where $x(t)$ is the system state at time t, F is the nonlinear function, τ is the time delay and T characterizes the response time of the system. This DDE can be represented by a simple ring system composed of delay, nonlinear and a low-frequency first-order filter that provides the response time of the system (see the block diagram plotted in figure 6.1).

According to the analysis presented in [Prokhorov and Ponomarenko 2008, Udaltsov et al. 2001], the information signal, s(t), can be injected into the feedback loop at different points denoted in figure 6.1 by the romans numerals I-III. Likewise, the signal transmitted into the communication channel, $x_r(t)$, can be taken from different points of the ring system indicated in figure 6.1 by the arabic numerals 1-3. Thus, given a chaotic carrier defined by equation (6.1), there are several ways to build the transmitter.

Depending on the point at which the message signal is injected into the feedback circuit of the transmitter, the system dynamics is governed by a different DDE (see table 6.1). In all the cases, the information signal is directly involved in the formation of the dynamics of the chaotic carrier. Hence, the transmitted signal, $x_r(t)$, represents more than the simple superposition of the chaotic signal and the information signal.

The authorized receiver is composed of the same elements as the transmitter, with the same parameters. Nevertheless, the receiver presents an open loop configuration, i.e., the feedback loop in the receiver is broken by the transmitted signal. It is critical to inject the signal from the transmitter at the receiver layout in the same point where is collected in the transmitter.

Now, we define $\Delta(t)$ as the difference between the output receiver and the transmitted signal. Not all the possible combinations of injected/collected

Injected point	Transmitter DDE
I	$T\dot{x}(t) = -x(t) + F[x(t-\tau)] + s(t)$
II	$T\dot{x}(t) = -x(t) + F[x(t-\tau) + s(t-\tau)]$
III	$T\dot{x}(t) = -x(t) + F[x(t-\tau) + s(t)]$

Table 6.1: Delay differential equation for the transmitter plotted in figure 6.1 depending on the injected point of the information signal s(t)

Input point	Output point		
	1	2	3
I	$s(t)$	$T\dot{\Delta}(t) + \Delta(t) = s(t)$	$T\dot{\Delta}(t) + \Delta(t) = s(t-\tau)$
II	processing	$s(t)$	$s(t-\tau)$
III	processing	processing	$s(t)$

Table 6.2: The difference signal $\Delta(t)$ for different injection points of the information signal into the feedback loop of the transmitter (I-III) and different output points of the transmitted signal $x_r(t)$ (1-3).

points lead to a direct message extraction from $\Delta(t)$. As shown in table 6.2, processing of the signal $\Delta(t)$ is necessary to recover the message in several cases. Evidently, these cases are not attractive for communication purposes. The state-of-the-art of the experimental systems is based on the combinations that lead to a direct recovering of the information signal from $\Delta(t)$. In the following section, we explain in detail the configurations I/2 and II/2. Both have been experimentally implemented in an optical chaos based communication system where the chaotic generator is a semiconductor laser subject to optoelectronic feedback [Bavard et al. 2007, Larger et al. 1998a].

6.2 The optical chaotic communication system

One of the first chaos based communication system based on semiconductor lasers subject to optoelectronic feedback was experimentally realized by Goedgebuer et al. [1998a], Larger et al. [1998a] (see chapter 3, section 3.4 for more details about the experimental setup). The system shows chaos in wavelength and a CMO modulation scheme is used. The schematic diagram of the chaotic communication system is presented in figure 6.2. The chaotic

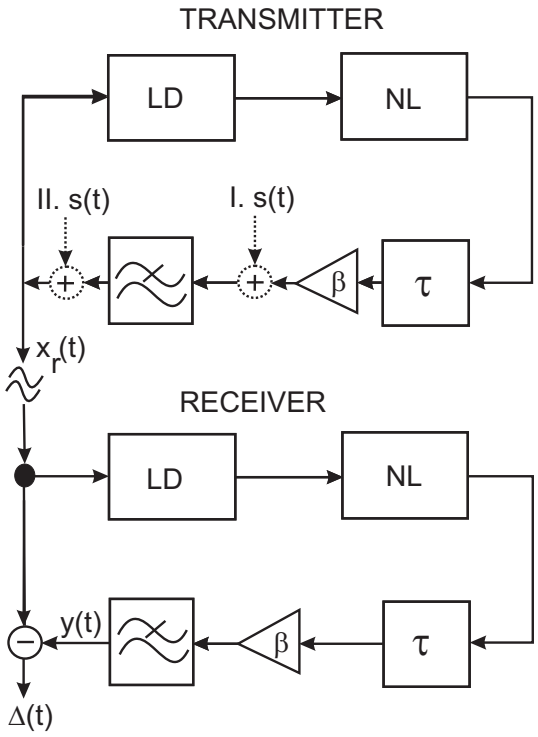

Figure 6.2: Schematic diagram of the chaotic communication system. The elements of the chaotic communication system are the Laser Diode [LD], the nonlinear element [NL], the delay line [τ], the amplifier [β] and the low pass filter. Points I and II represent the two possible injection points of the message into the transmitter

dynamics of the transmitter without information signal can be described by the equation:

$$T\frac{dx(t)}{dt} = -x(t) + \beta \sin^2\left(x(t-\tau) - \phi\right) \tag{6.2}$$

where T is the response time of the system, β is the nonlinearity strength, τ is the delay of the feedback loop and ϕ is the phase.

In the transmitter, the information signal, $s(t)$, is injected inside the loop of the chaotic generator. Two different injection points, both performed experimentally [Bavard et al. 2007, Larger et al. 1998a], are considered in this section. In the first case, $s(t)$ is injected after the low pass filter (point II in figure 6.2) [Larger et al. 1998a]. This transmitter configuration corresponds to

the II/2 scheme presented in the previous section, and the transmitted signal is given by:

$$x_r(t) = x_c(t) + s(t) \tag{6.3}$$

where the chaotic part of the transmitter signal, $x_c(t)$, obeys the following equation:

$$T\frac{dx_c(t)}{dt} = -x_c(t) + \beta \sin^2\left(x_c(t-\tau) - \phi + s(t-\tau)\right) \tag{6.4}$$

The second case consists on the injection of $s(t)$ before the low pass filter (point I in figure 6.2) [Bavard et al. 2007]. Thus, the transmitter configuration corresponds to the I/2 scheme described in the previous section. The transmitted signal is defined by:

$$T\frac{dx_r(t)}{dt} = -x_r(t) + \beta \sin^2\left(x_r(t-\tau) - \phi\right) + s(t) \tag{6.5}$$

Both configurations use the same authorized receiver, $y(t)$, to recover the message, described by the equation:

$$T\frac{dy(t)}{dt} = -y(t) + \beta \sin^2\left(x_r(t-\tau) - \phi\right) \tag{6.6}$$

The transmitter and receiver are identical, i.e. they have the same components with the same parameters. The message is recovered by subtracting $y(t)$ from the transmitted signal, $x_r(t)$, once the receiver synchronizes with the transmitter. The receiver architecture can be viewed as performing a nonlinear filtering process, intended to generate locally a message-free chaotic signal, which is subtracted from the transmitted signal to extract the message. When $x_r(t)$ follows equation (6.3) (the message is embedded into point II), $\Delta(t) = x_r(t) - y(t)$ yields directly the message $s(t)$. However, when $x_r(t)$ is given by equation (6.5) (the message is embedded into point I), $\Delta(t)$ is described by a first order non-autonomous differential equation:

$$T\frac{d\Delta(t)}{dt} + \Delta(t) = s(t) \tag{6.7}$$

6.3 The unauthorized receiver

To recover the information signal, an eavesdropper can construct a model that reproduces the nonlinear dynamics of the chaotic carrier from the transmitted signal. The more accurate is the extraction of the nonlinear dynamics,

the higher is the quality of the synchronous chaotic response of the unauthorized receiver and, as a consequence, the higher is the quality of the message extraction.

We have demonstrated in chapter 4 that MNNs can reproduce the nonlinear dynamics of time-delay systems described by equation (6.2) under different parameters values. Moreover, we have shown that the obtained MNN model is able to synchronize with the original chaotic data. Thus, we can use the MNN to recover the encoded information signal in the chaos communication system presented in the previous section.

We can divide the procedure to extract the message into two phases. The first one is to obtain the model that reconstructs the nonlinear dynamics of the chaotic generator. To achieve this, we train a MNN from the transmitted signal, $x_r(t)$. As described in chapter 4, the output of the MNN is given by:

$$x_{nn}(t) = f_{nn}(\vec{x}_r^{\,nf}(t)) + g_{nn}(\vec{x}_r^{\,f}(t)) \tag{6.8}$$

where f_{nn} and g_{nn} resemble the original linear and nonlinear functions of the chaotic carrier governed by equation (6.2). The vectors $\vec{x}_r^{\,nf}(t)$ and $\vec{x}_r^{\,f}(t)$ are given by:

$$\vec{x}_r^{\,nf}(t) = (x_r(t-\tau_e), ..., x_r(t-m_1\tau_e)) \tag{6.9a}$$

$$\vec{x}_r^{\,f}(t) = (x_r(t-\tau-m_2\tau_e), ..., x_r(t-\tau), ..., x_r(t-\tau+m_2\tau_e)) \tag{6.9b}$$

where τ_e is the embedding time, and m_1 and $2m_2+1$ are the numbers of non-feedback and feedback inputs, respectively.

The second phase is the construction of the unauthorized receiver using the model, in our case a MNN. The output of the unauthorized receiver is given by:

$$y_{nn}(t) = f_{nn}(\vec{y}_{nn}^{\,nf}(t)) + g_{nn}(\vec{x}_r^{\,f}(t)), \tag{6.10}$$

where $\vec{y}_{nn}^{\,nf}(t) = (y_{nn}(t-\tau_e), ..., y_{nn}(t-m_1\tau_e))$. Providing the MNN model reproduces the nonlinear dynamics of the chaotic carrier, the output of the MNN receiver, y_{nn}, should be similar to the output of the authorized receiver, y, ruled by equation (6.6). Thus, following the same approach as the original receiver, the information signal is retrieved by the substraction of the input and output of the MNN receiver, $\Delta_{nn}(t) = x_r(t) - y_{nn}(t)$. The schematic of the chaotic communication system with the unauthorized MNN receiver is presented in figure 6.3.

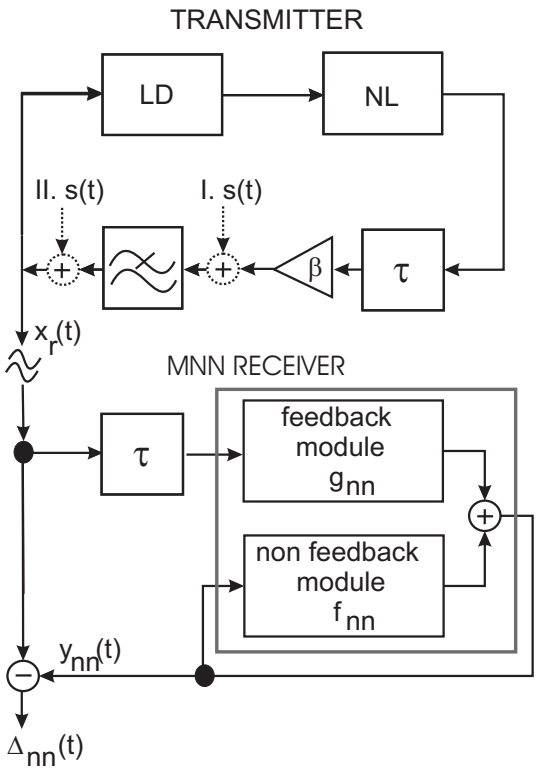

Figure 6.3: Schematic diagram of the chaotic transmitter and the MNN unauthorized receiver. The elements of system are the Laser Diode [LD], the nonlinear element [NL], the delay line [τ], the amplifier [β] and the low pass filter. Points I and II represent the two possible injection points of the message into the transmitter.

It is worth highlight that depending on the way the message is injected into the chaotic carrier other approaches exist to recover the information signal. For instance, one can try to extract the information signal by evaluating $x_{nn}(t) - x_r(t)$, where x_{nn} is the simple MNN prediction (see equation 6.8). The latter scenario only works when the message is placed in the DDE outside the nonlinear function, e.g. point I. In other cases, such as messages injected into point II, the information signal can not be retrieved by the evaluation of $x_{nn}(t) - x_r(t)$. Hence, the encoding scheme also plays a role in the privacy of the chaotic communication system.

The signal to noise ratio (SNR) of the recovered message directly depends on the mismatch between the transmitter and receiver. When the transmitter and receiver are perfectly matched and no message is transmitted, the

recovery signal, $\Delta(t)$, is equal to zero. However, when not perfectly matched transmitter and receiver are considered, $\Delta(t)$ is altered by a decoding error, ϵ. We define the decoding error, ϵ, as the RMS amplitude of $\Delta(t)$ when no information signal is injected. Therefore, $\epsilon = \sqrt{\langle \Delta(t)^2 \rangle} \Big|_{s(t)=0}$, where $\langle\rangle$ implies averaging over time. This error is normalized to the standard deviation of the chaotic carrier. For the particular case of the unauthorized MNN receiver, we define the decoding error as $\epsilon_{nn} = \sqrt{\langle \Delta_{nn}(t)^2 \rangle} \Big|_{s(t)=0}$. The decoding error determines the minimum amplitude of $s(t)$ that can be decoded by the receiver. In the case of the MNN unauthorized receiver, ϵ_{nn} is always greater than the RMSE. Furthermore, ϵ_{nn} increases with the RMSE in a nonlinear way, i.e. small increments in the RMSE can lead to high increments of ϵ_{nn}.

6.4 One delay systems: Message extraction from simulations

In chaos based communication systems, the message is hidden into the noisy appearance of the chaotic carrier. The amplitude and frequency of the information signal should be chosen to avoid the detection of the message from the power spectrum or from the time series of the transmitted signal.

In the chaotic communication system presented in section 6.2, the chaotic carrier has a power spectrum limited by the first-order filter of cut-off frequency $1/(2\pi T)$ (see figure 6.4). To avoid the detection of the message from the power spectrum or from the time series of $x_r(t)$, the transmission rates are limited by T and the amplitude of the message must be smaller than the amplitude of the chaotic carrier.

To illustrate the message recovery with the MNN, we use the chaotic communication system presented in section 6.2 to transmit a information signal with frequency 0.04, in the middle of the plain zone of the spectrum of the chaotic carrier (see figure 6.4). This frequency assures the concealment of the message in the power spectrum of the transmitted signal, regardless of its shape (sinusoidal or square functions).

Regarding the amplitude of the message, we define the message to chaos ratio (MCR), as the ratio between the standard deviation of $s(t)$ and that of the chaotic carrier without message, $x(t)$, in dB:

$$MCR = 20 \log \frac{\sigma_s}{\sigma_x} \tag{6.11}$$

where $\sigma_z = \langle (z(t) - \langle z(t) \rangle)^2 \rangle^{1/2}$ and $\langle\rangle$ implies averaging over time.

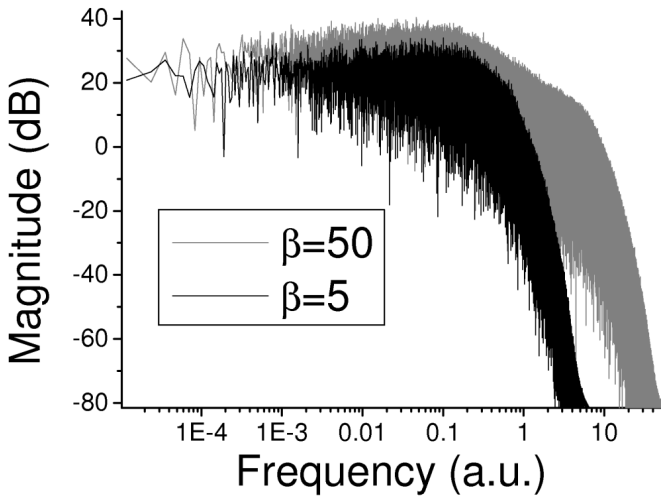

Figure 6.4: Power spectrum of the chaotic signal $x(t)$ ruled by the equation (6.2) for $\tau = 100$, $\phi = 0.26\pi$ and $T = 1$.

Following the same approach used in the experimental setup [Bavard et al. 2007, Larger et al. 1998a], the MCR is chosen as the highest one that avoids the detection of the message in the spectrum of the transmitted signal. Thus, the SNR at the output of the receiver is maximal.

Nonetheless, a perfectly hidden message in frequency and time is a necessary but not sufficient condition to guarantee the confidentiality of the transmitted signal. An eavesdropper can extract the message from $x_r(t)$ by a model that reproduces the nonlinear dynamics of the transmitter. In our case we use a MNN to extract the nonlinear dynamics of the chaotic carrier and the information signal. We consider two different situations:

- The MNN is trained from the transmitted signal without message
- The MNN is trained from the transmitted signal with message

Respect to the chaotic generator governed by equation (6.2), we focus on the most difficult case for an eavesdropper. The chaotic carrier has $\beta = 50$ and $\tau = 100$. As we have shown in chapter 4, the difficulty to reconstruct the nonlinear dynamics increases with β but not with the time delay τ. Higher βs imply higher RMSE and therefore worse message recovery.

6.4.1 Training without message

In this subsection, we train the MNN from the transmitted signal during periods where no message is transmitted. This situation has been analyzed in detail in chapter 4, where we train MNNs to reconstruct the dynamics of chaotic carriers defined by equation (6.2) for different values of β and τ. In the case of $\beta = 50$ and $\tau = 100$, the RMSE of the MNN(8:4) is around $5 \cdot 10^{-4}$ (see figure 4.11 in chapter 4) leading to a decoding error of $\epsilon_{nn} = 1 \cdot 10^{-3}$.

As explained above, we use the MNN model as an unauthorized receiver to decode the transmitted message. First, we consider sinusoidal and square periodic functions with zero mean and frequency 0.04 as information signals. The MCR is -17 dB for the sinusoidal function and -20 dB for the square one. These MCR are the highest ones that avoid the detection of $s(t)$ in the spectrum of $x_r(t)$.

For these cases, we analyze message recovery with the MNN when the information signal is injected into point I and II. The time series and spectrum of the original sinusoidal (square) message, the transmitted signal and the extracted message with the MNN, Δ_{nn}, are plotted in figure 6.5 (6.6) when the injection point is II (I). As can be seen, in both cases the original message is perfectly recovered with the MNN unauthorized receiver. The SNR of the extracted message is 53 (52) dB, whereas the original sinusoidal (square) message injected into point II (I) has a SNR=57 (59) dB. Furthermore, note that the message is concealed into the spectrum and time series of the transmitted signal in both cases.

There is a slight difference between the recovered message when $s(t)$ is injected into point I or II. When the message is injected into point II, $\Delta_{nn}(t)$ is directly the original message. However, when the message is injected into point I, $\Delta_{nn}(t)$ corresponds to the filtered message (see equation (6.7)). In the latter case, to properly recover the original message we have to calculate $\dot{\Delta}_{nn}(t)$ from the time series (for example with the method of local parabolic approximation) and add this to $\Delta_{nn}(t)$ to obtain $s(t)$. To illustrate this procedure, we plot in figure 6.7 a transmitted pseudo-random message with MCR = -20 dB and frequency 0.04 and the recovered message using the MNN when the information signal has been embedded into point I and II.

6.4.2 Training with message

In the previous subsection, we suppose the existence of periods where no message is transmitted and use them to train the MNN. However, the chaotic

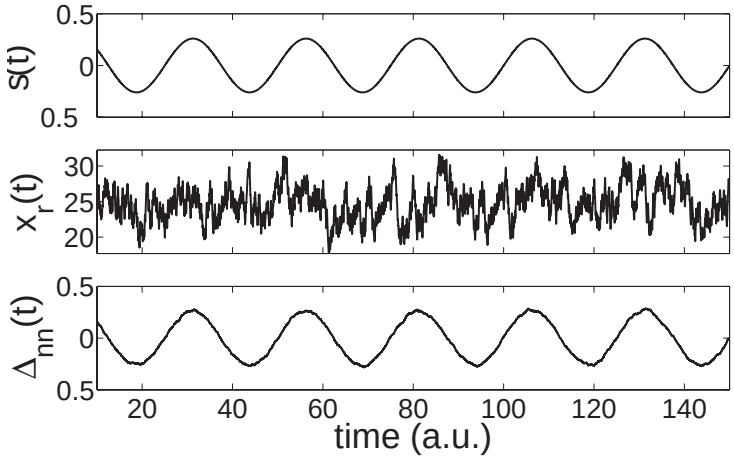

(a) Time series

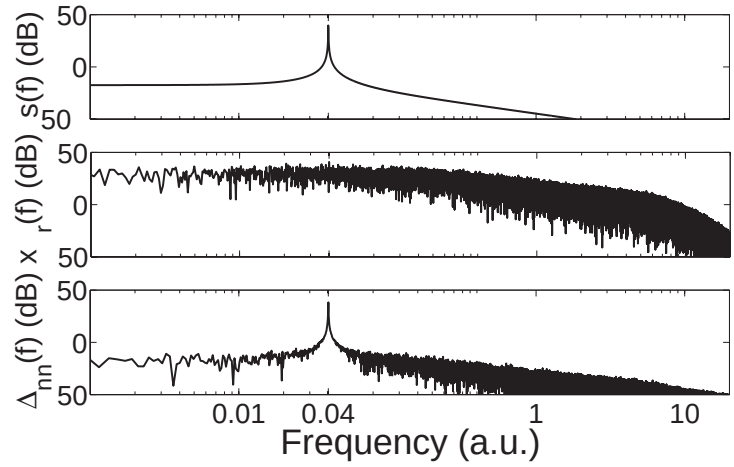

(b) Spectrum

Figure 6.5: From top to bottom it is plotted the original message, the transmitted signal and the recovered message in time (a) and frequency (b). The original message, s(t), is a sinusoidal function with MCR = -17 dB and frequency 0.04 injected into point II. The chaotic carrier has $\beta = 50$, $T = 1$, $\phi = 0.26\pi$ and $\tau = 100$. The MNN(8:4) has been trained without message.

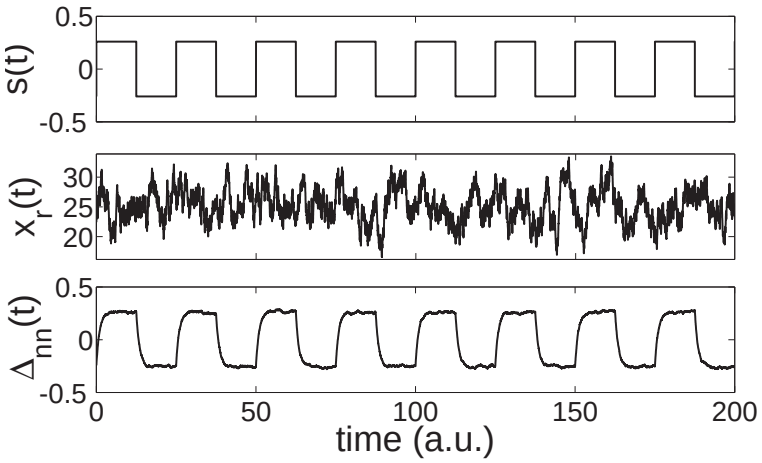

(a) Time series

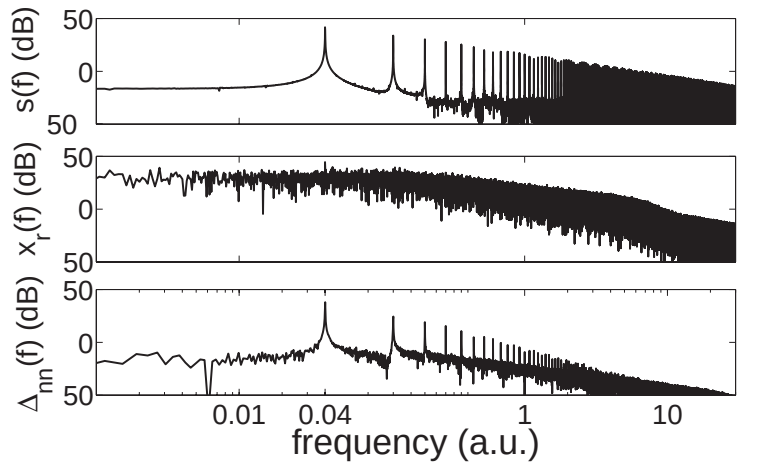

(b) Spectrum

Figure 6.6: From top to bottom it is plotted the original message, the transmitted signal and the recovered message in time (a) and frequency (b). The original message, s(t), is a square periodic function with a MCR = -20 dB and frequency 0.04 injected into point I. The chaotic carrier has $\beta = 50$, $T = 1$, $\phi = 0.26\pi$ and $\tau = 100$. The MNN(8:4) has been trained without message.

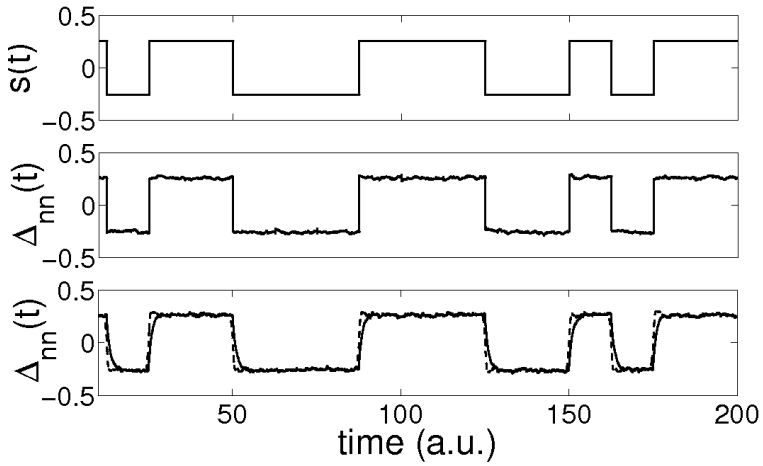

Figure 6.7: Top panel: The original square pseudo-random message with MCR = -20 dB and frequency 0.04. Middle (bottom) panel: Δ_{nn} when the information signal is injected into point II (I). The dashed line of the bottom panel corresponds to $\Delta_{nn} + \dot{\Delta}_{nn}$. The chaotic carrier has $\beta = 50$, $T = 1$, $\phi = 0.26\pi$ and $\tau = 100$. The MNN(8:4) has been trained without message.

communication system can be conceived so that a message is always transmitted.

The process to extract the nonlinear dynamics with NNs from $x_r(t)$ is the same regardless of the presence of the message in the transmitted signal. The message can be viewed as a perturbation. The nonlinear reconstruction with NNs is better when the injected message has low amplitudes and frequencies. The limit cases would be messages with zero frequencies or amplitudes, i.e. the NN would be trained from data without message. The effect of the shape of the message is negligible.

To illustrate the above points, we train a MNN from $x_r(t)$ with an injected NRZ (non return to zero) pseudo-random message with a MCR = -20 dB and frequency 0.04. We use the same MNN structure, number of inputs, training points and parameters that in the case without message. The RMSE (ϵ_{nn}) obtained is around $2 \cdot 10^{-3}$ ($9 \cdot 10^{-3}$), clearly higher that the RMSE (ϵ_{nn}) obtained when no message is injected (around $5 \cdot 10^{-4}$ ($1 \cdot 10^{-3}$)).

Regarding the message amplitude, higher amplitudes yield higher MNN RMSE and therefore, higher decoding errors, ϵ_{nn}. Nonetheless, the increment in the message amplitude compensates the worse decoding error and allows message recovery. To exemplify this point, we transmit a NRZ pseudo-random

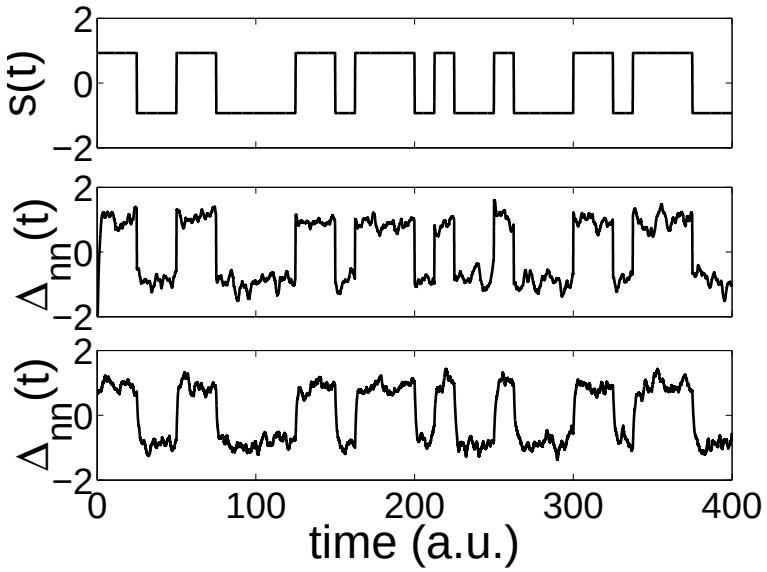

Figure 6.8: Top panel: The original message, s(t), is a square pseudo-random function with MCR = -9 dB and frequency 0.04. Middle (bottom) panel: Δ_{nn} when s(t) injected into point II (I). In both cases the MNN(8:4) has been trained from $x_r(t)$ with the information signal. The chaotic carrier has $\beta = 50$, $T = 1$, $\phi = 0.26\pi$ and $\tau = 100$.

message with MCR = -9 dB and frequency 0.04. In this case, the RMSE is around 0.02 yielding a $\epsilon_{nn} = 0.1$ for both injection points of the information signal. Therefore, the recovered message is similar for point I and II (see figure 6.8). The differences between Δ_{nn} when the message is injected into point I or II are here concealed by the higher decoding errors. Let us point out that the spectrum of the pseudo-random message allows that higher message amplitudes (until a MCR = -9 dB) are concealed into the spectrum.

Regarding the message frequency, this is limited by the first order filter (response time of the system $T = 1$) yielding a maximum transmission rate of the information signal around 0.1. We have found that the effect of the frequency on the recovered message is negligible for the allowed range of transmission frequencies.

Finally, let us point out that the MNN is able to filter the message to a certain extent in the same way that for a noisy time series. However, the filtering process is much more effective in the case of the message. For instance, the RMSE of a MNN trained from the transmitted signal without noise and an injected message with a MCR = -20 dB is around $2 \cdot 10^{-3}$. However, when

the MNN is trained from the transmitted signal with a CNR = -20 dB and without injected message the RMSE is $2 \cdot 10^{-2}$(see chapter 4, subsection 4.3.4).

6.4.3 Robustness to noise

In this subsection we study the robustness of message recovery to noise by adding a zero-mean Gaussian noise, $n(t)$, to the transmitted signal, $x_r(t)$. Different noise levels with a CNR from 40 dB (1%) to 20 dB (10%) are considered.

To recover the nonlinear dynamics from the transmitted time series with and without message, we use MNNs with the same structure, number of inputs, parameters and neurons as the ones used in chapter 4, subsection 4.3.4, for noisy time series.

When no message is transmitted, the MNN(10:5) trained from $x_r(t)$ with noise gives decoding errors from 0.08 for $CNR = 40$ dB to 0.27 for $CNR = 20$ dB. Clearly, lower noise levels (i.e. higher CNRs) lead to lower decoding errors and therefore better recovered messages. In figure 6.9 it is shown the extracted messages for different CNRs when $s(t)$ is injected into point I and II. The MNN has been trained from the transmitted time series without message.

In presence of noise, the recovered message using a MNN trained with or without message is very similar (see figure 6.10). As previously mentioned, the message in the chaotic transmitted signal can be viewed as a noise with respect the nonlinear dynamics reconstruction process. Hence, the effect of the message is overcome by the noise present in the transmitted signal.

Finally, let us point out that it is not possible to recover transmitted messages with amplitudes under the noise level of the system. Although we have shown in chapter 4, that the MNN is able to filter part of the input noise, ϵ_{nn} is always over the noise level.

We have demonstrated with numerical simulations that the chaotic communication system presented in figure 6.2 is vulnerable. An eavesdropper can train a MNN from the transmitted signal to reconstruct the nonlinear dynamics of the chaotic carrier. Next, the MNN can be used as an unauthorized receiver to extract the transmitted message. Therefore, the privacy of the communication system is compromised. In the next section we analyze if the above procedure is valid also when the chaotic generator has two delays.

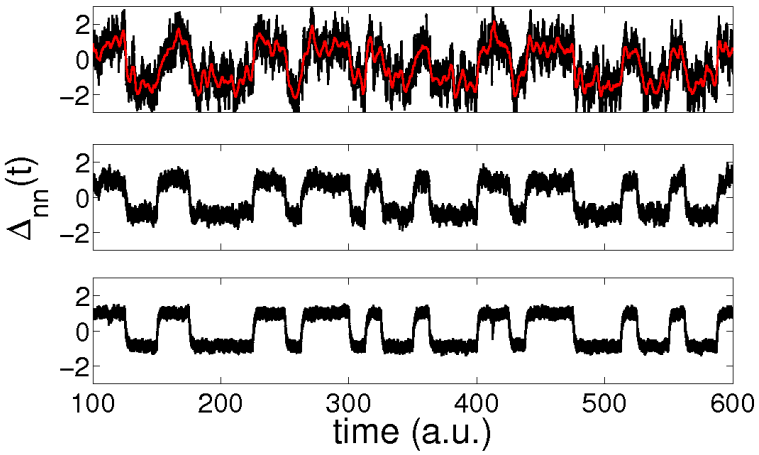

(a) Message injected into point I

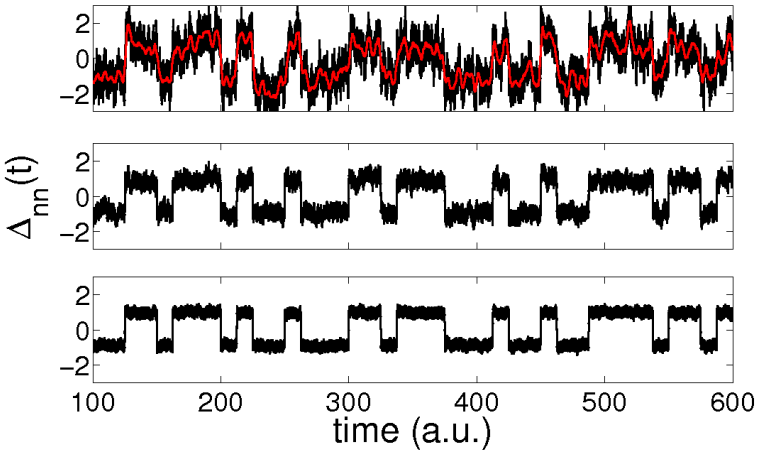

(b) Message injected into point II

Figure 6.9: (a,b): Recovered message with CNR= 20 (top), 30 (middle) and 40 (bottom) dB. The red line corresponds to the filtered extracted message. The original message, s(t), is a pseudo-random function with MCR = -9 dB and frequency 0.04. The chaotic carrier has $\beta = 50$, $\tau = 100$, $T = 1$ and $\phi = 0.26\pi$. The MNN(10:5) has been trained without message.

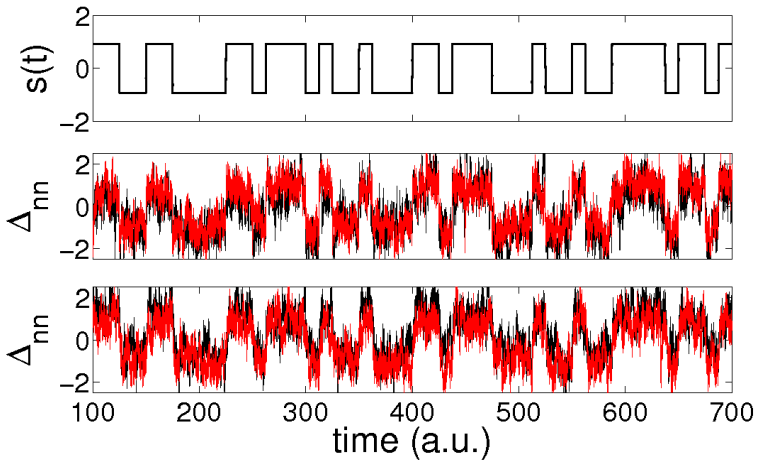

Figure 6.10: Top panel: The original pseudo-random message with MCR = -9 dB and frequency 0.04. Middle (bottom) panel: Δ_{nn} where the message is injected into point II (I). The black (red) lines correspond to Δ_{nn} when the MNN is trained from $x_r(t)$ without (with) message. The CNR = 23 dB. The chaotic carrier has $\beta = 50$, $\tau = 100$, $T = 1$ and $\phi = 0.26\pi$.

6.5 Two-delay system: Message extraction from simulations

Following the same technique used to encode a message in the single delay case, an information signal can be also embedded into a two delays chaotic generator described by:

$$x(t) + T\frac{dx(t)}{dt} = G(x(t-\tau_1), x(t-\tau_2)), \tag{6.12}$$

where τ_1 and τ_2 are the delay times, T is the response time of the system and G is the nonlinear function (see chapter 3, subsection 3.3.3 for more details).

The information signal can be injected into point I or II. In this section we only consider messages encoded inside the nonlinear function (point II). All the conclusions and results hold for messages injected into point I. Hence, the transmitted signal is giving by:

$$x_r(t) = x_c(t) + s(t), \tag{6.13}$$

where the chaotic part of the transmitter signal, $x_c(t)$, obeys the following equation,

$$T\frac{dx_c(t)}{dt} = -x_c(t) + G[x_r(t-\tau_1), x_r(t-\tau_2)] \tag{6.14}$$

The nonlinear function has two different implementations, serial and parallel. The nonlinear functions for the parallel, G_p, and serial, G_s, configuration are defined by:

$$\begin{aligned} G_p &= \beta_1 \sin^2\left(x_c(t-\tau_1) + s(t-\tau_1) - \phi_1\right) + \\ &\quad +\beta_2 \sin^2\left(x_c(t-\tau_2) + s(t-\tau_2) - \phi_2\right) \end{aligned} \tag{6.15}$$

$$G_s = \beta \sin^2\left(x_c(t-\tau_1) + x_c(t-\tau_2) + s(t-\tau_1) + s(t-\tau_2) - \phi\right) \tag{6.16}$$

The authorized receiver $y(t)$ is described by the following equation:

$$y(t) + T\frac{dy(t)}{dt} = G[x_r(t-\tau_1), x_r(t-\tau_2)] \tag{6.17}$$

The message is recovered by subtracting $y(t)$ from the transmitted signal $x_r(t)$, $\Delta(t) = x_r(t) - y(t)$.

Following the same approach as in the one delay case, an eavesdropper can decode the transmitted message by constructing a model that reproduces the nonlinear dynamics of the chaotic carrier subject to two delays. The message recovered by the eavesdropper is given by $\Delta_{nn}(t) = x_r(t) - y_{nn}(t)$. When the MNN is used to reconstruct the dynamics we have,

$$y_{nn}(t) = f_{nn}(\vec{y}_{nn}^{\,nf}(t)) + g_{nn}(\vec{x}_r^{\,f}(t)) \tag{6.18}$$

where f_{nn} and g_{nn} resemble the original linear and nonlinear functions of the chaotic carrier governed by equation (6.14). The vectors $\vec{y}_{nn}^{\,nf}(t)$ and $\vec{x}_r^{\,f}(t)$ are given by:

$$\vec{y}_{nn}^{\,nf}(t) = (y_{nn}(t-\tau_e), ..., y_{nn}(t-m_1\tau_e)) \tag{6.19a}$$

$$\begin{aligned} \vec{x}_r^{\,f}(t) = &(x_r(t-\tau_1-m_2\tau_e), ..., x_r(t-\tau_1), ..., x_r(t-\tau_1+m_2\tau_e), \\ &x_r(t-\tau_2-m_2\tau_e), ..., x_r(t-\tau_2), ..., x_r(t-\tau_2+m_2\tau_e)) \end{aligned} \tag{6.19b}$$

where τ_e is the embedding time and m_1 and $2(2m_2+1)$ are the numbers of non-feedback and feedback inputs, respectively.

To illustrate the procedure in the two delays case, the chaotic carrier, $x_c(t)$, ruled by (6.14) is used to transmit a pseudo-random NRZ message with

a MCR = -12 dB and frequency 0.04. The parameters of the chaotic carrier are $\beta = \beta_1 = \beta_2 = 15$, $\tau_1 = 100$, $\tau_2 = 215$, $T = 1$ and $\phi = \phi_1 = \phi_2 = 0.26\pi$. The amplitude and frequency of the message have been chosen so the information signal is not noticeable in the time series or spectrum of the transmitted signal, $x_r(t)$.

To recover the transmitted message, we reconstruct the nonlinear dynamics of the chaotic carrier using MNNs. Based on the results obtained in chapter 4, section 4.4, we use an adapted MNN for the parallel configuration and a non-adapted or standard MNN model for the serial configuration. In both cases, the MNN feedback modules have $14:7$ neurons.

First we consider the free noise case. The recovered message for both delays configuration when the MNN is trained with and without message is shown in figure 6.11(a). The RMSE of the MNN trained without message is around 10^{-5} (see chapter 4, section 4.4) whereas the RMSE of the MNN trained with message is around $9 \cdot 10^{-4}$. As in the one delay case, lower RMS errors lead to lower decoding errors, ϵ_{nn}, and therefore to better quality of the recovered message. In fact, the extracted message when the MNN is trained from $x_r(t)$ without information signal is practically identical to the original transmitted message (see figure 6.11(a)).

Now, we add white gaussian noise with a CNR = 30 dB to $x_r(t)$. The recovered message for both delays configuration when the MNN is trained with and without message is shown in figure 6.11(b). Evidently, the quality of the extracted message with noise is worse than without noise, specially when the MNN model is trained with the message (see figure 6.11(b) (right)). However, it is still possible to recover the original transmitted message.

Through this chapter, we have unmasked messages encoded by time-delay chaotic systems with one and two delays. Once the nonlinear dynamics is reconstructed by a model, we can also use this model to recover an encoded message. The more accurate is the extraction of the nonlinear dynamics, the higher is the quality of the message extraction. We have tested the message recovery under different noise levels and injection message points. In all the considered cases, the message can be recovered even when the model is constructed from the time series of the chaotic carrier with or without the transmitted message embedded. In the following section we will apply the same method to unmask messages from experimental time series.

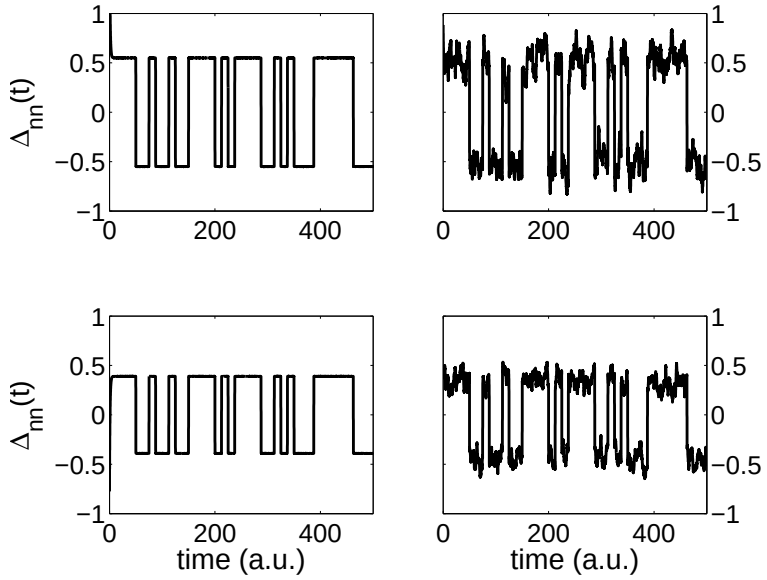

(a) Free noise case

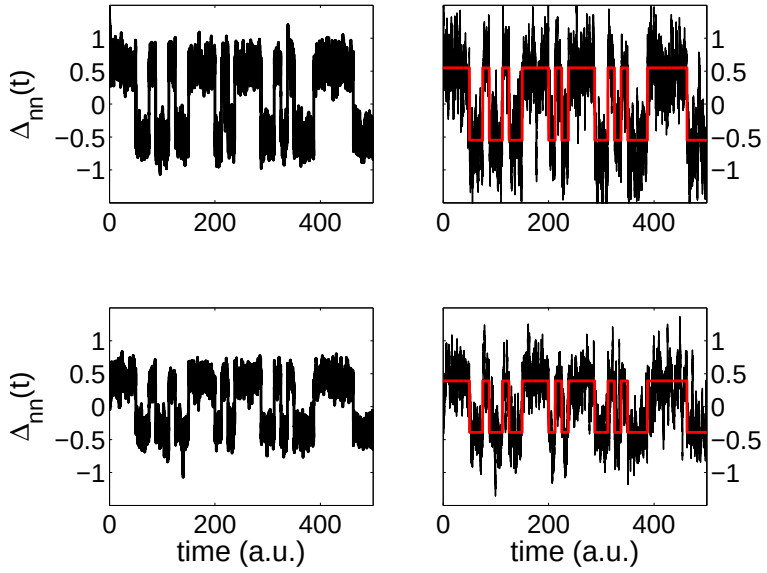

(b) CNR = 30dB

Figure 6.11: (a,b): Recovered message for the serial (top) and parallel (bottom) configurations. The MNN(14:7) has been trained from $x_r(t)$ without (left) and with (rigth) message. The original NRZ pseudo-random message is plotted in red and has MCR = -12 dB and frequency 0.04. The chaotic carrier has $\beta_1 = \beta_2 = \beta = 15$, $\tau_1 = 100$ and $\tau_2 = 215$.

6.6 Experiments: Optoelectronic feedback systems

The experimental chaos optical communication system analyzed in this section present chaos in wavelength. The experimental chaotic generator is explained in detail in chapter 3, section 3.4. The experimental receiver has not be implemented in the present case, however the complete optical chaos-based communication system (plotted in figure 6.2) has been demonstrated experimentally [Bavard et al. 2007, Larger et al. 1998a]. In the transmitter experimental setup, the message is injected into the feedback loop before the low pass filter and the amplifier that controls the nonlinearity of the system (see figure 6.12). This situation is equivalent to inject an effective message $\beta s(t)$ into the point I of the numerical simulations.

In this section we unmask messages encoded by the above experimental chaotic communication system. The procedure to extract the messages is the same as the one followed with the numerical simulations. We use a MNN model trained from the experimental time series as an unauthorized receiver. Here we only consider sinusoidal and square periodic messages injected before the low-pass filter and the amplifier (see figure 6.12) [Bavard et al. 2007].

The maximum frequency of the message analyzed is 4 KHz. The amplitudes of the message are similar to the ones used experimentally to achieve a good SNR at the experimental receiver [Bavard et al. 2007, Larger et al. 1998a]. This signal amplitude is around 10% of the amplitude of the transmitted signal without message. This leads to CNR much higher than the values analyzed with the numerical simulations.

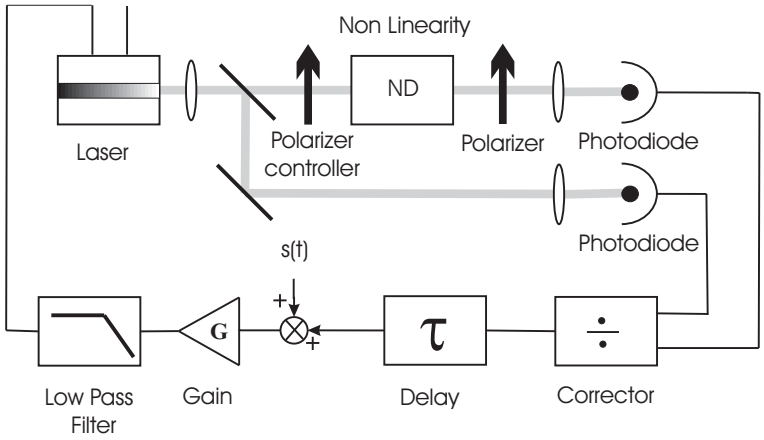

Figure 6.12: Experimental transmitter setup.

As previously mentioned (see chapter 4, section 4.5), chaotic time series with two different cut-off frequency of the low pass filter have been measured. The experimental time series, $x(t)$ (named as $\lambda(t)$ in chapter 4), is measured in volts that are proportional to the value of the wavelength deviation.

6.6.1 Long response time

In this subsection, the low pass filter has a cut-off frequency of 200 Hz that leads to a response time $T = 800\ \mu s$. For this case, we have reconstructed the nonlinear dynamics of the chaotic carrier by MNNs without message in chapter 4, subsection 4.5.1. The sampling period of the transmitted signal is 10 μs. The chaotic carrier has a nonlinear function with 5 extrema and the time delay of the system is 2.08 ms.

In this scenario, we have recovered square and sinusoidal periodic messages with a transmission rate of 50 and 100 Hz when the MNN is trained from the transmitted signal with and without message. Comparable results are obtained for sinusoidal and square messages. The amplitude of the messages is a 7% of the amplitude of $x_r(t)$ without message, that yields to a MCR = -7.7 dB. $x_r(t)$ and $\Delta_{nn}(t)$ are plotted in figure 6.13 when the original message is a square function with a transmission rate of 100 Hz and the MNN(6:3) is trained from $x_r(t)$ with message. Similar results are obtained when the MNN is trained from $x_r(t)$ without message.

For the above considered message amplitudes, a small peak at the basic frequency of the message is noticeable in the spectrum of the transmitted signal (see figure 6.13(b)), provided that the spectrum has been obtained with enough precision. We have demonstrated with numerical simulations that the quality of the recovered message is the same regardless the periodicity or pseudo-random nature of the transmitted message (see section 6.4). Therefore the experimental results obtained for the periodic messages can be extrapolated to pseudo-random messages. Pseudo-random messages with the same amplitude and frequency would not be noticeable in the spectrum of the experimental transmitted signal, assuring its concealment.

On the other hand, as previously mentioned (see subsection 6.3), there are other methods to extract the encoded message when the message is not affected by the nonlinear module of the transmitter. One of these methods recovers the transmitted message by using the MNN as simple predictor of the experimental time series. We use the same MNNs as in the previous case. The message is recovered by the difference between the transmitted signal and the result of the prediction with the MNN, i.e. $x_r(t) - x_{nn}(t)$. The recovered message smoothed by using a Savitzky-Golay (polynomial) filter is depicted in

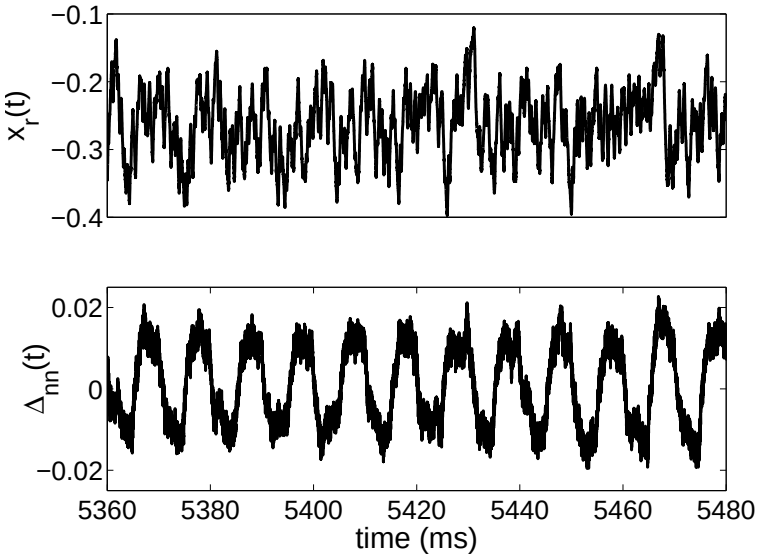

(a) Time series

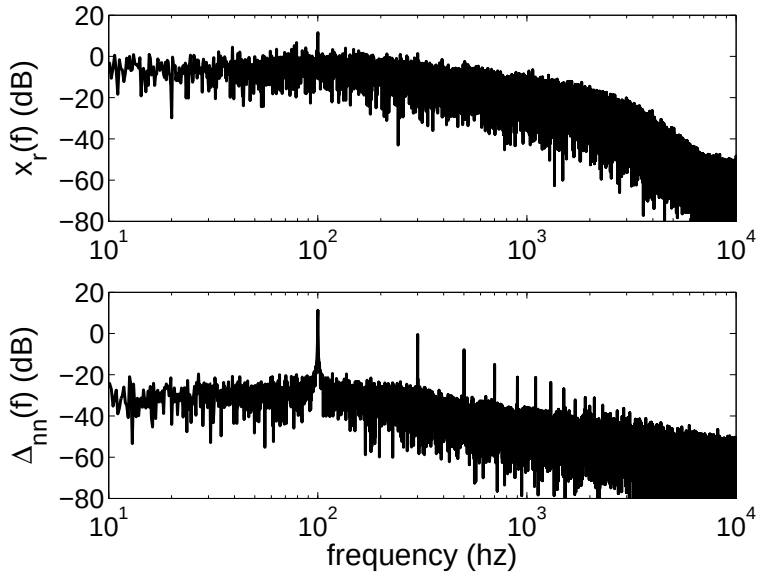

(b) Spectrum

Figure 6.13: The transmitted signal (top) and the recovered message (bottom) in time (a) and frequency (b). The original message, s(t), is a square periodic function with a MCR of -7.7 dB and frequency 100 Hz injected into point I. The chaotic carrier has a nonlinear function with 5 peaks, T = 800 μs and $\tau = 2.08$ ms. $x_r(t)$ is in volts.

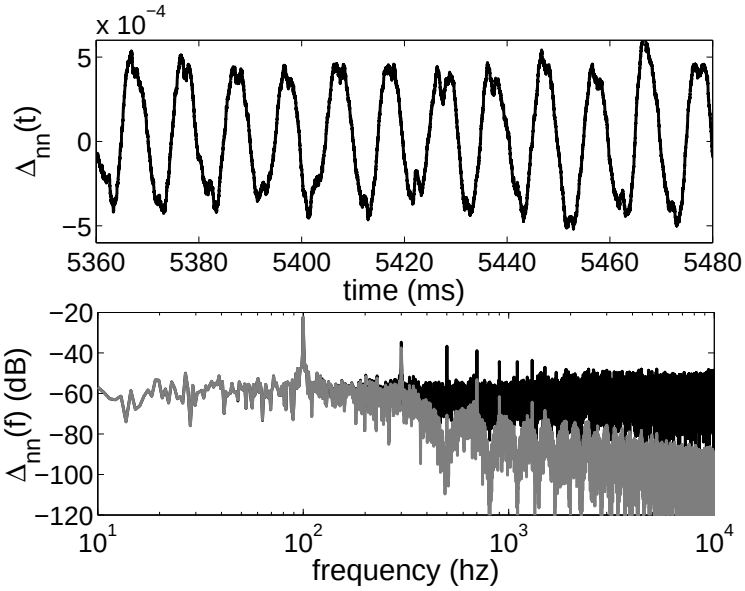

Figure 6.14: Top (Bottom): Recovered message using the MNN as a predictor in time (frequency). The message is smoothed by a Savitzky-Golay (polynomial) filter. The black spectrum corresponds to the non-filtered recovered message. The original message, s(t), is a square periodic function with a MCR = -7.7 dB and frequency 100 Hz injected into point I. The chaotic carrier has a nonlinear function with 5 peaks, T = 800 μs and τ = 2.08 ms.

figure 6.14 when the MNN is trained with message. The shape of the message is perfectly recovered whereas the amplitude of the extracted message is much smaller than the original one due to the method of extraction.

6.6.2 Short response time

Long response times of the system (T = 800 μs) are not appropriated for communications purposes as far as the maximum transmission rate of the message is very low. A second group of measures with a low pass filter with a cut off frequency of 20 KHz leading to a response time of 8 μs has been acquired.

For this case, in chapter 4, section 4.5.2 we have reconstructed the nonlinear dynamics of the system for three different values of the nonlinearity β that leads to nonlinear functions with 2, 5 and 6 extrema. The value of the parameter β can be estimated by comparing the normalized standard deviation and

the number of extrema of the nonlinear function of the numerical simulations with the experiment. In this case, the maximum feedback strength reached (6 peaks of the nonlinear function) corresponds to a value of the normalized parameter β around 15. The time delay of the system is 0.476 ms yielding a estimated attractor dimension of 357 (for an estimated $\beta = 15$). The nonlinear dynamics has been reconstructed from time series sampled each 1 μs (8 bits of resolution) and each 0.1 μs (12 bits of resolution). We use the MNN models to construct our unauthorized receiver to extract messages injected into point I following the same approach as in the numerical simulations. We have found that the extracted message has higher quality when the MNN is trained from $x_r(t)$ sampled each 1 μs (8 bits resolution). Next, we show some results obtained from data sampled each 1 μs (8 bits resolution).

We have extracted sinusoidal and square periodic messages with frequencies of 500 Hz, 1, 2 and 4 KHz. The amplitude of the messages is equal for all the cases and represents around a 10% of the amplitude of the $x_r(t)$ without message, yielding to a MCR = -8 dB. For this message amplitude, a small peak at the basic frequency of the message is noticeable in the spectrum of the transmitted signal. However, a pseudo-random message with the same amplitude and range of frequencies would be concealed in the spectrum.

We plot in figure 6.15 the transmitted signal and the recovered message in time and frequency for a square message with 4 KHz. The chaotic carrier has a nonlinear function with 5 peaks (moderate nonlinearity) and a time delay of 0.476 ms. The MNN has been trained in chapter 4, section 4.5.2 from the transmitted time series without message. The recovered message shows high oscillations, so a Savitzky-Golay (polynomial) filter is applied to the obtained message (red line in figure 6.15). Due to the filtering process, the amplitude of the extracted message is lower than the original one and its shape resembles more a sinusoidal than a square signal. The square-like appearance of the extracted message is more noticeable for smaller transmission rates (see for instance figure 6.16).

We can also train a MNN from the transmitted signal with message. Similar results are obtained when the MNN is trained from $x_r(t)$ with and without the message (see figures 6.17 and 6.18). These results are in agreement with the conclusions obtained from the numerical simulations (see section 6.4). In the cases presented in figures 6.17 (nonlinear function 5 peaks) and 6.18 (nonlinear function 6 peaks), the power spectrum of the recovered message displays a strong peak at 2 KHz with a SNR around 27 dB. In both cases the original message is a square periodic signal with a MCR= -8 dB and frequency 2 KHz.

Taking into account the results presented in this section, we conclude that chaos-based communication system based on optoelectronic feedback with one

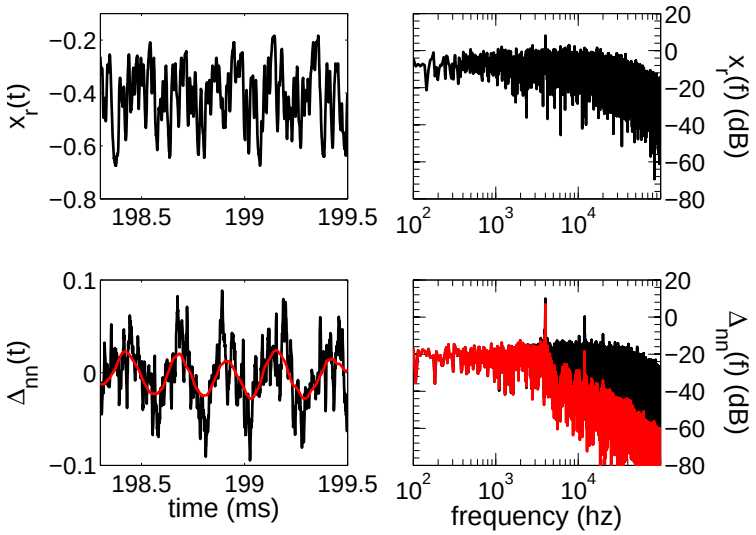

Figure 6.15: Top: time series (left) and spectrum (right) of the transmitted signal when s(t) is a square periodic function with a MCR = -8 dB and frequency 4 KHz. Bottom: The extracted message in time (left) and frequency (right). The red lines corresponds to the extracted message smoothed with a Savitzky-Golay filter. The chaotic carrier has a nonlinear function with 5 peaks, T = 8 μs and τ = 0.476 ms.

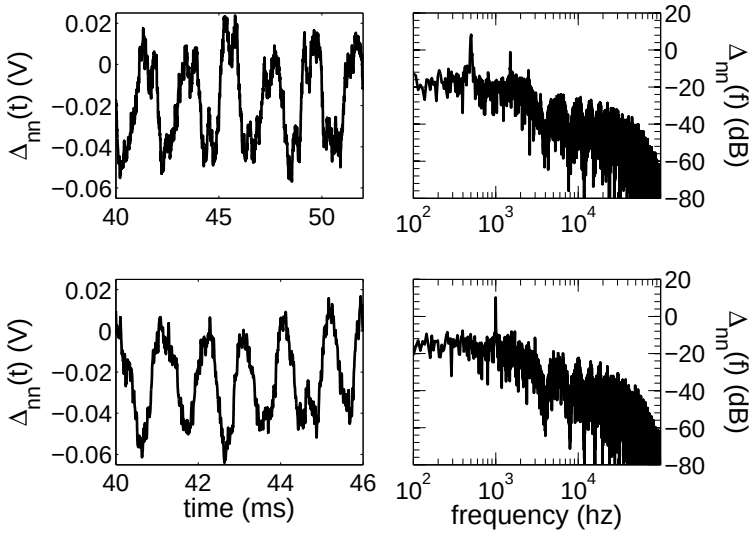

Figure 6.16: The extracted message with the MNN in time (left) and frequency (right) smoothed with a Savitzky-Golay filter. s(t) is a square periodic function with a MCR = -8 dB and frequency 500 Hz (top) and 1 KHz (bottom). The chaotic carrier has a nonlinear function with 2 peaks, T = 8 μs and τ = 0.476 ms.

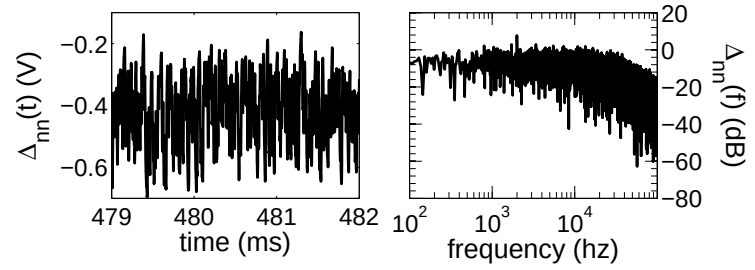

(a) Transmitted signal $x_r(t)$

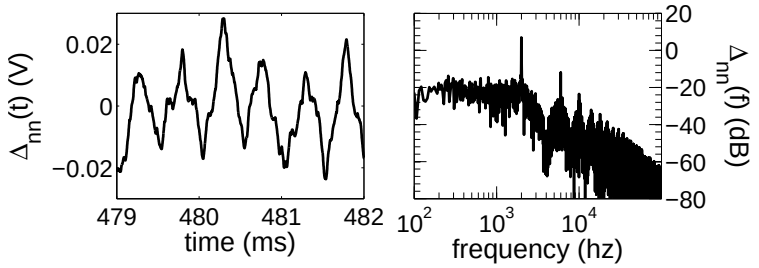

(b) Message recovered by using a MNN trained from $x_r(t)$ without including the message

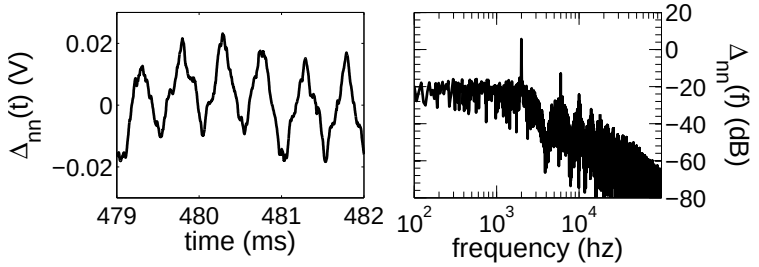

(c) Message recovered by using a MNN trained from $x_r(t)$ including the message

Figure 6.17: The chaotic carrier has a nonlinear function with 5 peaks, T = 8 μs and τ = 476 ms. The original message is a square periodic function with a MCR = -8 dB and a transmission rate of 2 KHz. The recovered message has been smoothed with a Savitzky-Golay filter.

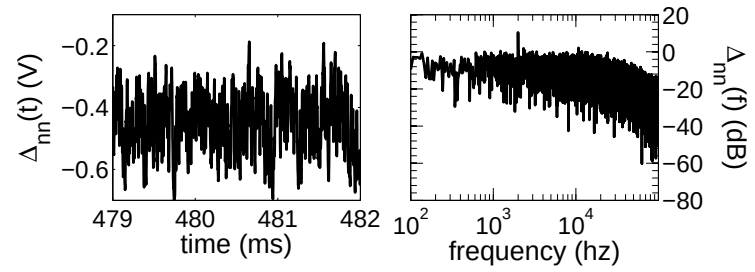

(a) Transmitted signal $x_r(t)$

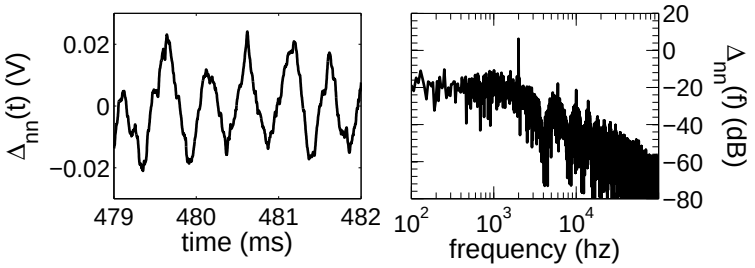

(b) Message recovered by using a MNN trained from $x_r(t)$ without including the message

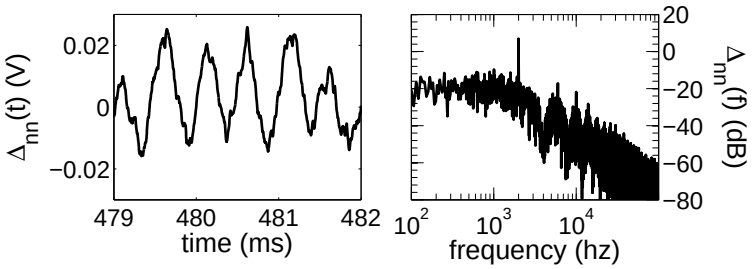

(c) Message recovered by using a MNN trained from $x_r(t)$ including the message

Figure 6.18: The chaotic carrier has a nonlinear function with 6 peaks, T = 8 μs and τ = 476 ms. The original message is a square periodic function with a MCR = -8 dB and a transmission rate of 2 KHz. The recovered message has been smoothed with a Savitzky-Golay filter.

fixed delay are not safe in spite of the very high dimension of the chaotic attractor. Although the experimental results are not so good as expected from the numerical simulations under similar parameters values and level of noise, we can extract the transmitted message. One possible cause to explain the difference between experiments and simulations can be the presence in the experiments of other sources of noise different of the additive gaussian noise considered in the numerical simulations.

6.7 Conclusions

The main conclusion of this chapter is that optical chaos-based communication systems based on optoelectronic feedback with several fixed delays are vulnerable.

In this chapter we have demonstrated with numerical simulations and experiments that MNN models can be used as unauthorized receivers to recover the transmitted original message. The MNNs are trained from the transmitted signal to reconstruct the nonlinear dynamics of the chaotic carrier. The quality of the extracted message depends on the quality of the obtained MNN. We have found that it is possible to recover the original message even from the transmitted signal with message and moderate noise. Moreover, in presence of noise the difference between messages extracted using MNN trained from transmitted signal with or without message is negligible. It seems that the noise overcomes the errors due to the presence of the message.

In the numerical case, we have analyzed the message extraction when the message is injected into two different points at the transmitter. Similar results are obtained in both cases. We have proved with numerical simulations that periodic and pseudo-random message can be recovered when the chaotic carrier is subject to one or two delays. For the two delays case the parallel and serial configuration have been analyzed yielding similar results.

Finally, experimental time series have been also studied. In all the analyzed experimental cases it is possible to retrieve the message using our unauthorized MNN receiver. However, the recovered message has worse quality than in the case of the numerical simulations. One reason could be that the experiment is affected by sources of noise different than the additional one considered in the numerical case.

In conclusion, the privacy of the above chaotic communication system is compromised. We have extracted the transmitted message with simple MNN with relative small number of parameters.

Chapter 7

General conclusions and open questions

The work presented in this thesis shows that the nonlinear dynamics of chaotic time-delay systems governed by scalar delay differential equations can be reconstructed by neural networks models. We have used an irregular embedding based on the time delay of the system. This procedure does not require a-priori knowledge of the structure of the equations that rule the system. It is only necessary to know the value of the time delay of the system.

Taking this into account we have first comprehensively studied the time delay identification from time series in semiconductor lasers subject to optical or optoelectronic feedback. These systems have been chosen because they are excellent candidates for optical chaos-based communications. We have found that the time delay of the system can be overestimated when using some standard identification techniques due to the response time of the system. As original contributions, we have developed customized techniques that permit the extraction of multiple fixed time delays and periodic time delays. We have applied these techniques to the numerical and experimental time series of an optoelectronic feedback system. Regarding the all-optical feedback systems, the time delay can be easily extracted except when low feedback rates are considered. This latter case is the only one in which the time delay identification has not been possible.

Once the time delay of the system is known, we have reconstructed the nonlinear dynamics of time-delay systems that have high dimensional attractors using the irregular embedding previously mentioned. A semiconductor laser subject to optoelectronic feedback that presents chaos in wavelength is

the prototype system used in our research to analyze the nonlinear dynamics reconstruction from experimental and numerical time series. We have found that the difficulty to model this system increases with the nonlinear strength of the system but not with the time delay. This is in agrement with the fact that the entropy of the system increases with the feedback strength while it does not depend on the delay time.

The special structure of time-delay systems has allowed us to model them using a new type of neural network: modular neural network. They give better models with less parameters than the standard feedforward neural networks. Using modular neural networks as unauthorized receivers, we have extracted messages encoded by a chaotic communication system based on semiconductor lasers subject to optoelectronic feedback. The higher is the quality of the neural model, the higher is the quality of the extracted message.

The above mentioned techniques are applicable to other scalar time-delay systems. In fact, we have successfully applied the same techniques to the Mackey-Glass system. Using this system, we have proven, both with numerical and experimental results, that the forecast horizon of time-delay systems obtained from anticipated synchronization can not be longer than the linear prediction time. This time is much smaller than the forecast horizon reached when using standard prediction methods. Cascades of non-identical replicas extracted from the time series can not significantly enlarge the forecast horizon based on anticipated synchronization due to the model errors. However, cascades of identical replicas of the original system reach longer prediction times than the characteristic ones. The problem of this configuration is the appearance of convective instabilities that reduce the obtained prediction times. Moreover, in this thesis we have proven that convective instabilities also appear in cascades of identical time-delays systems that are synchronized without anticipation. We have characterized these convective instabilities as a function of the parameters of the chaotic system. It remains to study convective instabilities in cascades of anticipated synchronized time-delay systems and extend this analysis to different time-delay systems, like the Ikeda one.

The foremost conclusion of this thesis is that chaotic communication systems based on laser diodes subject to optoelectronic feedback that present chaos in wavelength are not secure. Therefore, chaos-based communication systems have to evolve in order to meet the increasing demands for privacy of these systems. Not only the chaotic carrier dynamics must not be reconstructed by conventional methods, but all the stages of the design of a chaotic secure communication system must be considered and analyzed, such as appropriately choosing the transmitter and receiver system and the encoding/decoding schemes.

There are many interesting directions in which future research can be carried out to improve privacy of the chaotic communication systems based on time-delay systems. Next, we will mention some possible lines of future work.

It has been pointed out along the thesis that a successful nonlinear reconstruction lies in the identification of the time delay of the system. Therefore, a way to enhance the security of these systems could be the use of a chaotically variable time delay. This can lead to an additional level of confidence in the chaotic communication system. The chaotic time delay could be ruled by the own chaotic dynamics of the system or by an external chaotic system. In the latter case and additional channel of communication would be required to transmit the signal of the external chaotic system to the receiver. It is still an open question the identification of the chaotic time delay from the chaotic time series that governs it. Following a similar approach to the one used to identify the periodic time delay, we can try to map ranges of values of the chaotic time series with a constant time delay value.

In a similar way as for the case of one and two fixed time delays (see chapter 4), it can be expected that the identification of the time delay function will allow us to reconstruct the nonlinear dynamics. Once the time delay of the system is known, the nonlinear dynamic reconstruction is possible provided that the embedding vector contains the corresponding delayed values.

We have only lightly touched upon in this thesis the nonlinear dynamics reconstruction of time-delay system subject to several fixed time delays when they are multiples or take close values. It would be interesting in these cases to analyze the possibility of reconstructing the dynamics using only one of the time delays.

Another remarkable open question is the reconstruction of the nonlinear dynamics of semiconductor lasers subject to all-optical feedback and optoelectronic feedback that present chaos in intensity. These systems can reach high transmission rates. Moreover, the time scales involved in their dynamics can be very short. Nonlinear dynamics reconstruction proves challenging for these systems because it is difficult to directly measure and incorporate all of the relevant variables of the model. It is expected that high-end equipment will be necessary to acquire time series with the sampling rate and the precision required to reconstruct the nonlinear dynamics.

Appendix A

Resumen en castellano

Hoy en día un creciente tráfico de datos necesita un alto nivel de confidencialidad en su transmisión. La seguridad de la información en canales de transmisión públicos es uno de los grandes desafíos de las modernas redes de telecomunicaciones. Actualmente, la seguridad de los datos en los sistemas de comunicaciones convencionales esta basada en algoritmos matemáticos.

Uno de los motivos originales para el desarrollo de las comunicaciones caóticas fue la posibilidad de aumentar la privacidad y confidencialidad de la información transmitida. La privacidad aportada al sistema de comunicaciones gracias a las portadoras caóticas es a un nivel físico (hardware). Por lo tanto el uso de una portadora caótica que dinámicamente codifica la información no excluye la utilización de otras técnicas de software criptográfico más tradicional. La codificación dinámica con una portadora caótica puede ser considerada otra capa adicional de encriptado.

Aunque durante estos años se han diseñado un gran número de sistemas de comunicaciones caóticas, no existe todavía una forma sistemática para analizar la seguridad de estos sistemas similar a la desarrollada para la criptografía convencional. Es por lo tanto fundamental profundizar en la investigación sobre la privacidad de los sistemas de comunicaciones caóticas para ayudar a una futura aplicación práctica de estos sistemas.

Existen diversas formas de aplicar el caos en las comunicaciones. La privacidad aportada por el caos esta basada en la sensibilidad a las condiciones iniciales y el complejo comportamiento irregular que pueden presentar los sistemas caóticos. En esta tesis nos hemos centrado en las comunicaciones con portadora caótica basadas en sincronización. Estos sistemas fueron inicialmente propuestos por Pecora y Carroll a principios de los años noventa [Pecora

and Carroll 1990]. La idea consiste básicamente en "esconder" o "mezclar" el mensaje que se quiere transmitir con una portadora caótica. Una vez la señal transmitida llega al receptor, este sincroniza solo con la parte caótica de la señal transmitida. De esta manera se genera localmente la portadora caótica en el receptor y combinándola adecuadamente con la señal transmitida se puede recuperar el mensaje enviado.

El ancho espectro que caracteriza a las señales caóticas confiere a las comunicaciones caóticas robustez contra interferencias y otras ventajas asociadas hasta ahora con las comunicaciones de espectro ensanchado (sistema GPS, etc).

Los primeros experimentos de sistemas de comunicaciones caóticas basadas en sincronización fueron realizados con circuitos eléctronicos donde las velocidades de transmisión están limitadas al rango de los KHz [Cuomo and Oppenheim 1993, Cuomo et al. 1993, Halle et al. 1993, Kocarev et al. 1992, Parlitz et al. 1992, Volkovskii and Rul'kov 1993]. En los últimos años se han desarrollado sistemas de comunicaciones caóticas ópticas que ofrecen la posibilidad de alcanzar velocidades de transmisión del orden de Gbits [Argyris et al. 2005, Uchida et al. 2005]. Dentro de los sistemas de comunicaciones caóticas ópticas son especialmente interesantes los basados en laseres semiconductores ya que estos dispositivos son los emisores utilizados en los modernos sistemas de comunicaciones ópticas. Además, dentro de los laseres de semiconductor nosotros nos centraremos en esta tesis en aquellos sujetos a retroalimentación óptica o electro-óptica, ya que estos sistemas pueden presentar atractores con alta dimensión.

Hasta la fecha, se han desarrollado múltiples métodos para extraer el mensaje a partir de la señal transmitida por los sistemas de comunicaciones caóticas. Pronto se demostró que los sistemas de comunicaciones caóticas con baja dimensionalidad podían ser a menudo decodificados usando técnicas no lineales estándar basadas en los teoremas de embedding que permitían la reconstrucción de la dinámica no lineal del atractor caótico [Short and Parker 1998]. Sin embargo la aplicación de estas técnicas a sistemas caóticos con alta dimensión, especialmente aquellos que implican dinámicas hiper-caóticas, es computacionalmente difícil.

Los sistemas no lineales con retraso o retroalimentación pueden tener atractores caóticos cuya dimensión se incrementa con el tiempo de retraso alcanzando valores muy altos (Farmer, 1982). Estos sistemas están muy extendidos en la naturaleza. Entre otros ejemplos podemos destacar la ecuación de Ikeda [Ikeda 1979], que modela un resonador óptico pasivo, las ecuaciones de Lang-Kobayashi [Lang and Kobayashi 1980], que describen a los laseres de semiconductor con retroalimentación óptica o la ecuación del Mackey-Glass

[Mackey and Glass 1977] que modela la producción de células rojas en la sangre. Desde un punto de vista matemático, los sistemas no lineales con retraso son normalmente representados por ecuaciones diferenciales con retraso.

Es posible recuperar la ecuación que describe un sistema escalar con retraso y alta dimensionalidad explotando la particular estructura de estos sistemas sin tener en cuenta los teoremas de embedding, pero para ello es necesario conocer a priori la estructura de la ecuación que gobierna el sistema [Bezruchko et al. 2001, Bünner et al. 1997; 1996a;b, Ellner et al. 1997, Ponomarenko and Prokhorov 2002, Prokhorov et al. 2005, Robilliard et al. 2006, Udaltsov et al. 2003, Voss and Kurths 1997; 1999, Zhou and Lai 1999].

Sin embargo en muchos casos no se conoce la estructura de la ecuación que gobierna el sistema. Bünner y colaboradores [Bünner et al. 2000a;b, Hegger et al. 1998] han desarrollado un embedding especial que incluye componentes retrasadas y no retrasadas de la variable. Con este embedding especial, se puede recuperar la dinámica no lineal de sistemas escalares con retraso en un espacio con una dimensión más pequeña que la dimensión del atractor. En este caso no es necesario conocer la estructura de la ecuación que gobierna el sistema, siendo por lo tanto un enfoque mucho más flexible que no necesita tanta información a priori sobre el sistema analizado, únicamente el valor del retraso del sistema.

El objetivo principal de esta tesis es la reconstrucción de la dinámica no lineal de sistemas caóticos con retraso, basándonos en el método del embedding especial desarrollado por Bünner y colaboradores pero utilizando modelos globales no lineales que presentan un tiempo de computación mucho menor que los modelos locales lineales usados por ellos. Dentro de la variedad de modelos globales no lineales nosostros hemos escogido las redes neuronales artificiales (particularmente una de las más famosas, el perceptrón multicapa), que pueden teóricamente aproximar cualquier función con cualquier nivel de precisión [Cybenko 1989].

Nos vamos a centrar principalmente en la reconstrucción de la dinámica no lineal de los laseres de semiconductor con retroalimentación electro-óptica (o opto-electrónica) que presentan caos en longitud de onda. Este tipo de sistemas no alcanza grandes velocidades de transmisión, pero permiten estudiar la identificación del tiempo del retraso y la reconstrucción de la dinámica no lineal para atractores con altas dimensiones y entropía. Estos sistemas se pueden usar como test para determinar el efecto de estos factores en la reconstrucción de la dinámica no lineal y la identificación del tiempo de retraso. Además de simulaciones también presentaremos resultados experimentales. Los experimentos han sido llevados a cabo por el grupo del Prof. Laurent Larger (Universit de Franche-Comt, Besanon, France).

Aunque nos centramos principalmente en los sistemas con retroalimentación electro-óptica, las técnicas desarrolladas en esta tesis se pueden aplicar a cualquier sistema escalar no lineal con retraso que pueda ser representado como una ecuación diferencial retrasada. En concreto, nosotros también estudiamos el sistema Mackey-Glass con datos numéricos y experimentales, estos últimos obtenidos en el laboratorio del IFCA (Instituto de Física de Cantabria).

La tesis esta organizada de la siguiente manera:

Introducción (capítulo 2): Este capítulo describe el marco donde se lleva a cabo la investigación de esta tesis y presenta una serie de conceptos a los que nos vamos a referir en los capítulos posteriores. Parte de una descripción general de los sistemas caóticos y del fenómeno de la sincronización. A continuación describe los sistemas de comunicaciones caóticas, prestando especial atención a los basados en laseres de semiconductor con retroalimentación óptica o electro-óptica. Como hemos mencionado previamente estos sistemas pueden alcanzar altas velocidades de transmisión y presentar atractores caóticos con alta dimensión. Finalmente, se detallan los avances obtenidos en el estudio de la privacidad de los sistemas de comunicaciones caóticas. También se definen conceptos básicos relativos a las redes neuronales artificiales que son los modelos globales no lineales que vamos a usar en esta tesis para reconstruir la dinámica no lineal de sistemas con retraso.

Identificación del tiempo de retraso (capítulo 3): La identificación del tiempo de retraso es crucial para la reconstrucción de la dinámica no lineal de sistemas con retraso. Es a priori la única información necesaria para reproducir la dinámica no lineal de estos sistemas con el embeding especial. En este capítulo se analiza la identificación del tiempo de retraso en laseres de semiconductor sujetos a retroalimentación óptica y opto-electrónica a partir de la serie temporal con diferentes técnicas. Hemos mostrado como algunas de estas técnicas sobrestiman el tiempo de retraso debido al tiempo de respuesta del sistema. Por lo tanto en los casos donde el tiempo de respuesta tiene un valor significativo con respecto al del retraso se debe evitar usar dichos métodos para su identificación.

En el caso de la retroalimentación óptica, hemos encontrado que cuando la intensidad de la retroalimentación es alta, podemos identificar perfectamente uno y dos retrasos a partir de series numéricas y experimentales usando técnicas de identificación estándar. Sin embargo cuando la intensidad de la retroalimentación es baja y se escoge adecuadamente el resto de los parámetros operacionales del sistema, no es posible identificar el tiempo de retraso del láser de semiconductor con las técnicas estándar. Esta situación se da para un rango de parametros pequeño y regimes caóticos que en principio no son

los más adecuados para los sistemas de comunicaciones caóticas ya que la dimensión y entropía del caos no son muy altas.

Respecto al caso de laseres de semiconductor con retroalimentación opto-electrónica, el tiempo de retraso también puede ser extraído de series temporales numéricas y experimentales usando técnicas estándar, siempre que el sistema tenga un solo retraso o dos retrasos con configuración en paralelo. Cuando el sistema tiene dos retrasos y la configuración es en serie, hemos demostrado que los métodos estándar no permiten la identificación de ambos retrasos. En este caso hemos desarrollado técnicas basadas en los métodos estándar que permiten la correcta identificación de ambos retrasos. Dichas técnicas rastrean un espacio con la misma dimensión que el número de retrasos del sistema, lo que implica un mayor tiempo de computación.

Finalmente, en este capítulo investigamos la identificación del tiempo de retraso en un láser de semiconductor con retroalimentación opto-electrónica y tiempo de retraso variable de forma periódica. Los tiempos de retraso variables son una de las propuestas más interesantes para evitar la identificación del tiempo de retraso. En el caso que estudiamos, donde el retraso es periódico, hemos desarrollado una técnica basada en la información mutua y el factor de llenado que nos permite extraer el tiempo de retraso periódico a partir de series experimentales.

Reconstrucción de la dinámica caótica de sistemas no lineales con retraso (capítulo 4): En este capítulo hemos reconstruido la dinámica no lineal de laseres semiconductores sujetos a retroalimentación electro-óptica y el sistema Mackey-Glass a partir de series numéricas y experimentales usando redes neuronales. Las redes neuronales son entrenadas con datos procedentes de series temporales numéricas y experimentales que están retrasados el tiempo de embedding y el tiempo de retraso del sistema. Por lo tanto para reconstruir la dinámica no lineal de los sistemas con retraso usando redes neuronales solamente necesitamos conocer el tiempo de retraso del sistema que ha sido extraído de la serie temporal en el capítulo anterior mediante diversas técnicas.

Hemos logrado buenos resultados con las redes neuronales, pero dada la naturaleza del problema hemos estudiado también los resultados obtenidos usando redes neuronales modulares (MNN). Las MNN están basadas en el concepto de modularidad, que permite la división de un problema complejo en tareas más sencillas. Una de las principales ventajas de las MNN frente a las redes neuronales convencionales es que reducen el tamaño de la red (aportando más flexibilidad que las redes estándar) y por lo tanto reduciendo los tiempos de computación que dependen del número de neuronas y sus conexiones, así como mejorando los problemas de entrenamiento y convergencia. En nuestro caso la MNN es construida de acuerdo con la estructura de los sistemas

con retraso y tiene dos módulos: uno para la parte no retrasada con datos retrasados por el tiempo de embedding y otro módulo con datos de entrada retrasados por el tiempo de retraso. Hemos demostrado que este nuevo tipo de red neuronal modular genera mejores modelos con menos parámetros que las redes neuronales perceptrón multicapa. Los modelos obtenidos son validados gracias a la sincronización caótica idéntica. El número de parámetros de la red neuronal necesarios para obtener buenos modelos se incrementa con la intensidad de la retroalimentación del sistema pero no con el tiempo de retraso, a pesar de que al aumentar el tiempo de retraso aumenta la dimensión del atractor caótico. Estos resultados están en consonancia con el hecho de que la entropía del sistema se incrementa con la intensidad de la retroalimentación pero no con el tiempo de retraso.

También hemos reconstruido la dinámica no lineal de un sistema optoelectrónico con dos retrasos a partir de las series temporales numéricas. En este caso hemos estudiado dos configuraciones diferentes del retraso, serie y paralelo. Hemos encontrado que la configuración en paralelo requiere redes modulares adaptadas (cada función no lineal tiene un módulo diferente asociado) para obtener errores similares a la configuración en serie.

La principal conclusión que se puede extraer de este capítulo es que las portadoras caóticas basadas en sistemas con retraso escalares son vulnerables. Una vez que la dinámica no lineal del sistema ha sido reconstruida, esta se puede usar para predecir (capítulo 4) o para extraer los mensajes transmitidos cuando estos son encriptados con este tipo de portadoras caóticas como veremos en el capítulo 6.

Predicción de sistemas no lineales con retraso (capítulo 5): En este capítulo hemos estudiado la predictabilidad de los sistemas caóticos con retraso usando métodos de predicción estándar con redes neuronales y la sincronización anticipada. En los casos prácticos la situación más habitual es que el sistema original sea desconocido y modelos aproximados obtenidos a partir de los datos disponibles son usados para la predicción de la dinámica no lineal. En estos casos el horizonte de predicción depende no solo de la dinámica del sistema original sino también del error del modelo. Colocándonos en esta situación y una vez modelado el sistema con redes neuronales modulares a partir de datos de simulaciones numéricas y experimentales, hemos encontrado que en el caso de la predicción estándar el horizonte de predicción es del orden del inverso del mayor exponente de Lyapunov, es decir depende del valor del retraso del sistema. En cambio, en el caso de la predicción con sincronización anticipada hemos demostrado también para datos numéricos y experimentales que los tiempos de predicción máximos son independientes del tiempo de retraso pero el horizonte de predicción con un solo esclavo esta limitado por

el tiempo lineal del sistema. Estos tiempos de predicción no se incrementan significativamente usando una cadena de modelos esclavos sincronizados anticipadamente.

Si en lugar de modelos usamos cadenas de replicas idénticas sincronizadas anticipadamente, los tiempos de predicción del sistema son mayores que los característicos. Sin embargo en este caso la anticipación conlleva la aparición de inestabilidades convectivas. En el caso de sistemas con retraso nosotros hemos probado que debido al tiempo de retraso estas inestabilidades convectivas aparecen también en cadenas de esclavos identicos sincronizados sin anticipación. En este capítulo hemos caracterizado estas inestabilidades convectivas mediante el exponente de lyapunov convectivo, encontrando que para grandes valores del tiempo de retraso la amplificación de la perturbación en cada oscilador es independiente del tiempo de retraso. Esta amplificacin decrece de forma inversamente proporcional con el parámetro de acoplo.

Descodificación de mensajes en sistemas de comunicaciones caóticos con retraso(capítulo 6): Los sistemas de comunicaciones caóticas basados en laseres de semiconductor con retroalimentación electro-óptica con uno o varios retrasos son vulnerables. Los modelos de redes modulares neuronales obtenidos a partir de simulaciones numéricas y experimentales son usados como receptores no autorizados para recuperar el mensaje transmitido por el sistema de comunicaciones caótico. Las redes modulares neuronales son entrenadas a partir de la señal transmitida por el emisor para reconstruir la dinámica no lineal de la portadora caótica. La calidad del mensaje recuperado depende de la precisión con la que los modelos neuronales reproducen la dinámica caótica de la portadora. Nosotros hemos demostrado que es posible reconstruir la dinámica no lineal de la portadora caótica a partir de señales transmitidas con mensaje incluido y niveles de ruido moderados.

Conclusiones generales y trabajo futuro (capítulo 7): Cerramos esta tesis con una revisión de las conclusiones más relevantes obtenidas así como una discusión la investigación presentada que incluye las futuras líneas de trabajo.

Appendix B

List of abbreviations

AF	Autocorrelation Function
CC	coherence collapse
CMA	Chaos MAsking
CMO	Chaos MOdulation
CNR	Chaotic carrier to Noise Ratio
CSK	Chaos Shift Keying
DDE	Delay Differential Equation
DMI	Delayed Mutual Information
ECSL	semiconductor-based External Cavity Surface Lasers
FF	Filling Factor
FFNN	Feed-Forward Neural Network
GLM	Global Linear Model
GNLM	Global Non Linear Model
HL	Hidden Layers
KS	Kolmogorov-Sinai
LFF	Low Frequency Fluctuations
MCR	Message to Chaos Ratio
MG	Mackey-Glass
MNN	Modular Neural Network
NN	Neural Network
NRZ	Non Return to Zero
QKD	Quantum Key Distribution
RMSE	Root Mean Squared Error
SNR	Signal to Noise Ratio
TDE	Time Distribution of Extrema

Appendix C

Publication list

Articles

- Damien Rontani, Alexandre Locquet, Marc Sciamanna, David S. Citrin and Silvia Ortín.
  Time-Delay Identification in a Chaotic Semiconductor Laser With Optical Feedback: A Dynamical Point of View. *IEEE Journal of Quantum Electronics*, Volume 45, Issue 7, Pages: 879 - 1891 (2009).

- Marzena Ciszak, José Manuel Gutiérrez, Antonio Cofiño, Claudio Mirasso, Raúl Toral, Luis Pesquera and Silvia Ortín.
  Approach to predictability via anticipated synchronization. *Physical Review E*, Volume 72, Issue 4, Article Number: 046218 (2005).

- Silvia Ortín, José Manuel Gutiérrez, Luis Pesquera and Hernando Vasquez.
  Nonlinear dynamics extraction for time-delay systems using modular neural networks synchronization and prediction. *Physica A - Statistical Mechanics and its applications*, Volume 351, Issue 1, Pages: 133-141 (2005).

- Min W. Lee, Alan Shore, Silvia Ortín, Luis Pesquera and Ángel Valle.
  Dynamical characterization of laser diode subject to double optical feedback for chaotic optical communications. *IEE Proceedings-Optoelectronics*, Volume 152, Issue 2, Pages:97-102 (2005).

International Proceedings

- Silvia Ortín, Maxime Jacquot, Luis Pesquera, Michael Peil and Laurent Larger.
  Time delay extraction in chaotic cryptosystems based on opto-electronic feedback with variable delay. *Proceedings of the society of photo-optical instrumentation engineers (SPIE)*, Volume 6997, Pages: E9970-E9970 (2008).

- Silvia Ortín, Luis Pesquera, José Manuel Gutiérrez, Ángel Valle and Antonio Cofiño.
  Nonlinear dynamics reconstruction with neural networks of chaotic time-delay communication systems. *AIP Conference Proceedings*, Volume 887, Pages: 249-256 (2007).

- Alexandre Locquet, Silvia Ortín, Vladimir Udaltsov, Laurent Larger, David S. Citrin, Luis Pesquera and Ángel Valle.
  Delay-time identification in chaotic optical systems with two delays. *Proceedings of the society of photo-optical instrumentation engineers (SPIE)*, Volume 6184, Pages: L1840-L1840 (2006).

- Ángel Valle, Silvia Ortín and Luis Pesquera.
  Current modulation of multi-transverse mode vertical-cavity surface-emitting lasers. *Proceedings of the 7th International Conference on Transparent Optical Networks*, Volume 2, Pages: 126-131 (2005).

- Silvia Ortín, Luis Pesquera, Ángel Valle and José Manuel Gutiérrez.
  Nonlinear Dynamics Reconstruction for Time-Delay Systems using Modular Neural Networks. *Fifth EUROMECH Nonlinear Dynamics Conference*, (ISBN 9038626673), Pages: 1090-1099 (2005).

- Silvia Ortín, Luis Pesquera, Antonio Cofiño, Ángel Valle and José Manuel Gutiérrez.
  Extraction of nonlinear dynamics for laser diodes with feedback in chaotic regime. *Proceedings of the society of photo-optical instrumentation engineers (SPIE)*, Volume 5452, Pages: 273-282 (2004).

National Proceedings

- Silvia Ortín, Maxime Jacquot, Luis Pesquera, Michael Peil and Laurent Larger
  Security analysis of chaotic communication systems based on delayed optoelectronic feedback. *Proceedings 5th Reunión nacional de optoelectrónica*, Pages: 429-434 (2007).

Bibliography

Abarbanel, H. D. I., Carroll, T. A., Pecora, L. M., Sidorowich, J. J., and Tsimring, L. S. (1994). Predicting physical variables in time-delay embedding. *Phys. Rev. E*, 49(3):1840–1853.

Aguirre, L. A., Furtado, E. C., and Torres, L. A. B. (2006). Evaluation of dynamical models: Dissipative synchronization and other techniques. *Phys. Rev. E*, 74.

Ahlers, V., Parlitz, U., and Lauterborn, W. (1998). Hyperchaotic dynamics and synchronization of external cavity semiconductor lasers. *Phys, Rev. E*, 58:7208–7213.

Alvarez, G. and Li, S. J. (2006). Some basic cryptographic requirements for chaos-based cryptosystems. *Int. J. of Bifurcation and Chaos*, 16:2129–2151.

Annovazzi-Lodi, V., Donati, S., and Scire, A. (1996). Synchronization of chaotic injected-laser systems and its application to optical cryptography. *IEEE J. Quantum Electron*, 32:953–959.

Argyris, A., Syvridis, D., Larger, L., Annovazzi-Lodi, V., Colet, P., Fischer, I., Garcia-Ojalvo, J., Mirasso, C. R., Pesquera, L., and Shore, A. K. (2005). Chaos-based communications at high bit rates using commercial fibre-optics links. *Nature*, 438:343–346.

Ashwin, P., Buescu, J., and Stewart, I. (1994). Bubbling of attractors and synchronisation of chaotic oscillators. *Physics Letters A*, 193(2):126 – 139.

Bavard, X., Locquet, A., Larger, L., and Goedgebuer, J. P. (2007). Influence of digitisation on master-slave synchronisation in chaos-encrypted data transmission. *IET Optoelectronics*, 1:3–8.

Bennett, C. H. and Brassard, G. (1984). Quantum cryptography: Public-key distribution and coin tossing. In *Proc. of IEEE International Conference on Computers, Systems and Signal Processing*, pages 175 – 179.

Bezruchko, B. P., Karavaev, A. S., Ponomarenko, V. I., and Prokhorov, M. D. (2001). Reconstruction of time-delay systems from chaotic time series. *Phys. Rev. E*, 64(5):056216.

Briggs, R. J. (1964). *Electron-stream interaction with plasmas*. M.I.T. Press Cambridge,.

Brown, R., Rulkov, N. F., and Tracy, E. R. (1994). Modeling and synchronizing chaotic systems from time-series data. *Phys. Rev. E*, 49(5):37843800.

Bünner, M. J., Ciofini, M., Giaquinta, A., Hegger, R., Kantz, H., Meucci, R., and Politi, A. (2000a). Reconstruction of systems with delayed feedback: I. theory. *The European Physical Journal D*, 10(2):165–176.

Bünner, M. J., Ciofini, M., Giaquinta, A., Hegger, R., Kantz, H., Meucci, R., and Politi, A. (2000b). Reconstruction of systems with delayed feedback: II. application. *The European Physical Journal D*, 10(2):177–187.

Bünner, M. J., Kittel, A., Parisi, J., Fischer, I., and Elsäβer, W. (1998). Estimation of delay times from a delayed optical feedback laser experiment. *Europhysics Lett.*, 42(4):353–358.

Bünner, M. J., Meyer T., Kittel, A., and Parisi, J. (1997). Recovery of the time-evolution equation of time-delay systems from time series. *Phys. Rev. E*, 56(5):5083–5089.

Bünner, M. J., Popp, M., Meyer, T., Kittel, A., and Parisi, J. (1996a). Tool to recover scalar time-delay systems from experimental time series. *Phys. Rev. E*, 54(4):R3082–R3085.

Bünner, M. J., Popp, M., Meyer, T., Kittel, A., Rau, U., and Parisi, J. (1996b). Recovery of scaler time-delay systems from time series. *Physics Letters A*, 211(6):345 – 349.

Casdagli, M., Eubank, S., Farmer, J., and Gibson, J. (1991). State space reconstruction in the presence of noise. *Physica D: Nonlinear Phenomena*, 51(1-3):52 – 98.

Castillo, E., Cobo, A., Gutiérrez, J. M., and Pruneda, R. E. (1999). *Introducción a las redes funcionales con aplicaciones*. Editorial Paraninfo, Santander (España).

Chen, G., Chen, Y., and Ogmen, H. (1997). Identifying chaotic systems via a wiener-type cascade model. *IEEE Control Systems*, page 2936.

Ciszak, M., Gutiérrez, J. M., Cofiño, A. S., Mirasso, C., Toral, R., Pesquera, L., and Ortín, S. (2005). Approach to predictability via anticipated synchronization. *Phys. Rev. E*, 72(4):046218.

Cohen, A. B., Ravoori, B., Murphy, T. E., and Roy, R. (2008). Using synchronization for prediction of high-dimensional chaotic dynamics. *Phys. Rev. Lett.*, 101:154102.

Cuenot, J. B., Larger, L., Goedgebuer, J. P., and Rhodes, W. T. (2001). Chaos shift keying with an optoelectronic encryption system using chaos in wavelength. *IEEE J. Quantum Electron.*, 37:849–855.

Cuomo, K. M. and Oppenheim, A. V. (1993). Circuit implementation of synchronized chaos with applications to communications. *Phys. Rev. Lett.*, 71:65–68.

Cuomo, K. M., Oppenheim, A. V., and Strogatz, S. H. (1993). Synchronization of lorenz-based chaotic circuits with applications to communications. *IEEE Trans. Circuits Syst. I*, 40:626–633.

Cybenko, G. (1989). Approximation by superpositions of a sigmoidal function. *Mathematics of Control, Signals, and Systems*, 2:304–314.

Deissler, R. J. (1987). Spatially growing waves, intermittency, and convective chaos in an open-flow system. *Phys. D*, 25(1-3):233–260.

Deissler, R. J. and Kaneko, K. (1987). Velocity-dependent lyapunov exponents as a measure of chaos for open-flow systems. *Physics Letters A*, 119(8):397 – 402.

Ekert, A. K. (1991). Quantum cryptography based on bell's theorem. *Phys. Rev. Lett.*, 67(6):661–663.

Ellner, S. P., Kendall, B. E., Wood, S. N., McCauley, E., and Briggs, C. J. (1997). Inferring mechanism from time-series data: Delay-differential equations. *Physica D: Nonlinear Phenomena*, 110(3-4):182 – 194.

Farmer, J. D. (1982). Chaotic attractors of an infinite dimensional system. *Physica D*, 4:366–393.

Fowler, A. C. and Kember, G. (1993). Delay recognition in chaotic time series. *Physics Letters A*, 175(6):402 – 408.

Genay, R. and Liu, T. (1997). Nonlinear modelling and prediction with feedforward and recurrent networks. *Physica D: Nonlinear Phenomena*, 108(1-2):119 – 134.

Giacomelli, G., Hegger, R., Politi, A., and Vassalli, M. (2000). Convective lyapunov exponents and propagation of correlations. *Phys. Rev. Lett.*, 85(17):3616–3619.

Goedgebuer, J. P., Larger, L., and Porte, H. (1998a). Optical cryptosystem based on synchronization of hyperchaos generated by a delayed feedback tunable laser diode. *Phys. Rev. Lett.*, 80:2249–2252.

Goedgebuer, J.-P., Larger, L., Porte, H., and Delorme, F. (1998b). Chaos in wavelength with a feedback tunable laser diode. *Phys. Rev. E*, 57(3):2795–2798.

Goedgebuer, J. P., Levy, P. Larger, L., Chen, C. C., and Rhodes, W. T. (2002). Optical communication with synchronized hyperchaos generated electrooptically. *IEEE J. Quantum Electron.*, 38:1178–1183.

Gouesbet, G., Meunier-Guttin-Cluzel, S., and Mènard, O. (2003). Global reconstruction of equations of motion from data series, and validation techniques: a rewiev. In Gouesbet, G., Meunier-Guttin-Cluzel, S., and Mènard, O., editors, *Chaos and Its Reconstruction*, chapter 1, pages 1–160. Nova Science, New York.

Hagan, M. T., Demuth, H. B., and Beale, M. (1996). *Neural Network design*. PWS Publishing Company, Boston, USA.

Haken, H. (1975). Analogy between higher instabilities in fluids and lasers. *Phys. Lett. A*, 53:77–78.

Halle, K. S., Wu, C. W., Itoh, M., and Chua, L. O. (1993). Spread spectrum communication through modulation of chaos. *Int. J. Bifurcation Chaos*, 3:469–477.

Happel, B. and Murre, J. (1994). Design and evolution of modular neural network architectures. *Neural Networks*, 7:985–1004.

Haykin, S. (2001). *Neural Networks. A comprehensive foundation*. Pearson Education, Singapore (India).

Hegger, R., Bünner, M. J., Kantz, H., and Giaquinta, A. (1998). Identifying and modeling delay feedback systems. *Phys. Rev. Lett.*, 81(3):558–561.

Hernández-García, E., Masoller, C., and Mirasso, C. R. (2002). Anticipating the dynamics of chaotic maps. *Physics Letters A*, 295(1):39 – 43.

Hilborn, R. C. (2000). *Chaos and nonlinear dynamics*. Oxford University Press, New Work, USA.

Ikeda, K. (1979). Multiple-valued stationary state and its instability of the transmitted light by a ring cavity system. *Opt. Commun.*, 30:257–261.

Ikeda, K. and Matsumoto, K. (1987). High-dimensional chaotic behavior in systems with time-delayed feedback. *Physica D: Nonlinear Phenomena*, 29(1-2):223 – 235.

Jones, A. J., Tsui, A. P. M., and Oliveira, A. G. (2002). Neural models of arbitrary chaotic systems: construction and the role of time delayed feedback in control and synchronization. *Complexity International*, 9.

Kantz, H. and Schreiber, T. (1997). *Nonlinear time series analysis*. Cambridge University Press, Cambridge, UK.

Kaplan, D. T. and Glass, L. (1993). Coarse-grained embeddings of time series: random walks, gaussian random processes, and deterministic chaos. *Physica D: Nonlinear Phenomena*, 64(4):431 – 454.

Kecman, V. (2001). *Learning and soft computing*. The MIT press.

Kocarev, L., Halle, K. S., Eckert, K., Chua, L. O., and Parlitz, U. (1992). Experimental demonstration of secure communications via chaotic synchronization. *Int. J. Bifurcation Chaos*, 2:709–713.

Kocarev, L. and Parlitz, U. (1995). General approach for chaotic synchronization with applications to communication. *Phys. Rev. Lett.*, 74(25):5028–5031.

Kouomou, Y. C., Colet, P., Gastaud, N., and Larger, L. (2004). Effect of parameter mismatch on the synchronization of chaotic semiconductor lasers with electro-optical feedback. *Phys. Rev. E*, 69(5):056226.

Kurkova, V. (1992). Kolmogorov's theorem and multilayer neural networks. *Neural Networks*, 5:501–506.

Kye, W.-H., Choi, M., Rim, S., Kurdoglyan, M. S., Kim, C.-M., and Park, Y.-J. (2004). Characteristics of a delayed system with time-dependent delay time. *Phys. Rev. E*, 69(5):055202.

Lang, R. and Kobayashi, K. (1980). External optical feedback effects on semiconductor laser properties. *IEEE J. Quantum Electron.*, QE-16:347–355.

Larger, L., Goedgebuer, J. P., and Delorme, F. (1998a). Optical encryption system using hyperchaos generated by an optoelectronic wavelength oscillator. *Phys. Rev. E*, 57:6618–6624.

Larger, L., Goedgebuer, J. P., and Merolla, J. M. (1998b). Chaotic oscillator in wavelength: a new setup for investigating differential difference equations describing non linear dynamics. *IEEE J. Quantum Electron.*, 34:594–601.

Larger, L., Udaltsov, V. S., Poinsot, S., and Genin, E. (2005). Optoelectronic phase chaos generator for secure communication. *Journal of optical technology*, 72:378–382.

Lee, M. W., Larger, L., Udaltsov, V., Genin, E., and Goedgebuer, J.-P. (2004). Demonstration of a chaos generator with two time delays. *Opt. Lett.*, 29(4):325–327.

Lee, M. W., Rees, P., Shore, K. A., Ortin, S., Pesquera, L., and Valle, A. (2005). Dynamical characterisation of laser diode subject to double optical feedback for chaotic optical communications. *IEE Proceedings - Optoelectronics*, 152(2):97–102.

Lepri, S., Giacomelli, G., Politi, A., and Arecchi, F. T. (1994). High-dimensional chaos in delayed dynamical systems. *Physica D: Nonlinear Phenomena*, 70(3):235 – 249.

Liu, Y., Takiguchi, Y., Davis, P., Aida, T., Saito, S., and Liu, J. M. (2002). Experimental observation of complete chaos synchronization in semiconductor lasers. *Applied Physics Letters*, 80(23):4306–4308.

Locquet, A., Ortin, S., Udaltsov, V., Larger, L., Citrin, D. S., Pesquera, L., and Valle, A. (2006). Delay-time identification in chaotic optical systems with two delays. In Lenstra, D., Pessa, M., and White, I. H., editors, *Proceedings of the SPIE*, volume 6184, pages L1840–L1840. SPIE, SPIE.

Ma, Q.-L., Zheng, Q.-L., Peng, H., Zhong, T.-W., and Xu, L.-Q. (2007). Chaotic time series prediction based on evolving recurrent neural networks. *Machine Learning and Cybernetics, 2007 International Conference on*, 6:3496–3500.

Mackey, M. C. and Glass, L. (1977). Oscillation and chaos in physiological control systems. *Science*, 197:287–289.

Mendoza, C., Boccaletti, S., and Politi, A. (2004). Convective instabilities of synchronization manifolds in spatially extended systems. *Phys. Rev. E*, 69(4):047202.

Mirasso, C. R., Colet, P., and Garcia-Fernandez, P. (1996). Synchronization of chaotic semiconductor lasers: Application to encoded communications. *IEEE Photonics Technol. Lett.*, 8:299–301.

Mulet, J. (2003). *Semiconductor Laser Dynamics: Compound-cavity, polarization and transverse modes*. PhD thesis, Universidad de las Islas Baleares.

Müller, K., Smola, A., Rätsch, G., Schölkopf, B., Kohlmorgen, J., and Vapnik, V. (1997). Predicting time series with support vector machines. *Artificial Neural Networks ICANN'97*, pages 999–1004.

Ohira, T. and Sawatari, R. (1997). Delay estimation from noisy time series. *Phys. Rev. E*, 55(3):R2077–R2080.

Ohtsubo, J. (2007). *Semiconductor lasers. Stability, Instability and Chaos.* Springer, Berlin (Germany), second edition.

Olbrich, E. and Kantz, H. (1997). Inferring chaotic dynamics from time-series: On which length scale determinism becomes visible. *Physics Letters A*, 232(1-2):63 – 69.

Ortín, S., Gutiérrez, J., Pesquera, L., and Vasquez, H. (2005). Nonlinear dynamics extraction for time-delay systems using modular neural networks synchronization and prediction. *Physica A: Statistical Mechanics and its Applications*, 351(1):133 – 141.

Ortín, S., Pesquera, L., Gutiérrez, J. M., Valle, A., and Cofiño, A. (2007). Nonlinear dynamics reconstruction with neural networks of chaotic communication time-delay systems. In Marro, J., Garrido, P., and Torres, J., editors, *Cooperative behavior in neural systems*, volume 887, pages 249–258, New York. AIP Proceedings.

Ott, E. (2002). *Chaos in dynamical systems.* Cambridge University Press, Cambridge, UK.

Packard, N. H., Crutchfield, J. P., Farmer, J. D., and Shaw, R. S. (1980). Geometry from a time series. *Phys. Rev. Lett.*, 45(9):712–716.

Papoff, F. and Zambrini, R. (2005). Convective instability induced by nonlocality in nonlinear diffusive systems. *Phys. Rev. Lett.*, 94:243903.

Parlitz, U., Chua, L. O., Kocarev, L., Halle, K. S., and Shang, A. (1992). Transmission of digital signals by chaotic synchronization. *Int. J. Bifurcation Chaos*, 2:973–977.

Pazó, D. (2009). private communication.

Pecora, L. M. and Carroll, T. L. (1990). Synchronization in chaotic systems. *Phys. Rev. Lett.*, 64:821–824.

Pecora, L. M. and Carroll, T. L. (1991). Driving systems with chaotic signals. *Phys. Rev. A*, 44:2374–2383.

Peng, J. H., Ding, E. J., Ding, M., and Yang, W. (1996). Synchronizing hyperchaos with a scalar transmitted signal. *Phys. Rev. Lett.*, 76(6):904–907.

Pérez, G. and Cerdeira, H. A. (1995). Extracting messages masked by chaos. *Phys. Rev. Lett.*, 74(11):1970–1973.

Pikovsky, A., Rosenblum, M., and Kurths, J. (2001). *Synchronization. A universal concept in nonlinear sciences*. Cambridge University Press, Cambridge, UK.

Ponomarenko, V. I. and Prokhorov, M. D. (2002). Extracting information masked by the chaotic signal of a time-delay system. *Phys. Rev. E*, 66(2):026215.

Press, W. H., Flannery, B. P., Teukolsky, S. A., and Vetterling, W. T. (1992). *Numerical Recipes*. Cambridge University Press, Cambridge, UK.

Principe, J. C., Rathie, A., and Kuo, J. M. (1992). Prediction of chaotic time series with neural networks and the issue of dynamic modeling. *Int. J. of Bifurcation and Chaos*, 2(4):989–996.

Prokhorov, M., Ponomarenko, V., Karavaev, A., and Bezruchko, B. (2005). Reconstruction of time-delayed feedback systems from time series. *Physica D: Nonlinear Phenomena*, 203(3-4):209 – 223.

Prokhorov, M. D. and Ponomarenko, V. I. (2008). Encryption and decryption of information in chaotic communication systems governed by delay-differential equations. *Chaos, Solitons and Fractals*, 35:871–877.

Pyragas, K. (1993). Predictable chaos in slightly perturbed unpredictable chaotic systems. *Phys. Lett. A*, 181:203–210.

Quiñonero Candela, J. and Hansen, L. K. (2002). Time series prediction based on the relevance vector machine with adaptive kernels. In *Proceedings of the International Conference on Acoustics, Speech and Signal Processing Conference*, pages 985–988.

Robilliard, C., Huntington, E., and Webb, J. (2006). Enhancing the security of delayed differential chaotic systems with programmable feedback. *Circuits and Systems II: Express Briefs, IEEE Transactions on*, 53(8):722–726.

Rontani, D., Locquet, A., Sciamanna, M., and Citrin, D. S. (2007). Loss of time-delay signature in the chaotic output of a semiconductor laser with optical feedback. *Optics Lett.*, 32(20):2960–2962.

Rontani, D., Locquet, A., Sciamanna, M., Citrin, D. S., and Ortín, S. (2009). Time-delay identification in a chaotic semiconductor laser with optical feedback: A dynamical point of view. *IEEE Journal of Quantum Elect.*, 45(7):879–891.

Rosenblum, M. G., Pikovsky, A. S., and Kurths, J. (1996). Phase synchronization of chaotic oscillators. *Phys. Rev. Lett.*, 76:1804–1807.

Roy, R. and Thornburg, J. K. S. (1994). Experimental synchronization of chaotic laser. *Phys. Rev. Lett.*, 72:2009–2015.

Rulkov, N. F., Sushchik, M. M., Tsimring, L. S., and Abarbadel, H. D. I. (1995). Generalized synchronization of chaos in directionally coupled chaotic systems. *Phys. Rev. E*, 51:980–994.

Sauer, T., Yorke, J. A., and Casdagli, M. (1991). Embedology. *Journal of Statistical Physics*, 65(3-4):579–616.

Shor, P. W., editor (1994). *Algorithms for quantum computation: Discrete logarithms and factoring*. Proc. 35nd Annual Symposium on Foundations of Computer Science, IEEE Computer Society Press.

Short, K. M. (1994). Steps toward unmasking secure communications. *Int. J. Bifurcation Chaos*, 4:959–977.

Short, K. M. (1996). Unmasking a modulated chaotic communications scheme. *Int. J. Bifurcation Chaos*, 6:367375.

Short, K. M. and Parker, A. T. (1998). Unmasking a hyperchaotic communication scheme. *Phys. Rev. E*, 58(1):1159–1162.

Siefert, M. (2007). Practical criterion for delay estimation using random perturbations. *Phys. Rev. E*, 76:026215.

Small, M. and Tse, C. K. (2002). Minimum description length neural networks for time series prediction. *Phys. Rev. E*, 66(6):066701.

Strogazt, S. H. (1994). *Nonlinear Dynamics And Chaos: With Applications To Physics, Biology, Chemistry, and Engineering*. Perseus book Publishing.

Sugawara, T., Tachikawa, M., Tsukamoto, T., and Shimizu, T. (1994). Observation of synchronization in laser chaos. *Phys. Rev. Lett.*, 72:3502–3506.

Suykens, J. A. K. and Vandewalle, J. (1995). Learning a simple recurrent neural state space model to behave like chua's double scroll. *IEEE Transactions on Circuits and Systems-I*, 42(8):499–502.

Takens, F. (1981). Detecting strange attractors in turbulence. *Lecture Notes in Math*, 898:366–381.

Tenny, R. and Tsimring, L. (2004). Steps towards cryptanalysis of chaotic active/passive decomposition encryption schemes using average dynamics estimation. *Int. J. Bifurcation Chaos*, 14:3949–3968.

Tian, Y.-C. and Gao, F. (1997). Extraction of delay information from chaotic time series based on information entropy. *Physica D: Nonlinear Phenomena*, 108(1-2):113 – 118.

Uchida, A., Rogister, F., Garcìa-Ojalvo, J., and Roy, R. (2005). Synchronization and communication with chaotic laser systems. In Wolf, E., editor, *Progress in Optics, volume 48*, chapter 5, pages 203–341. Elsevier Science Amsterdam.

Udaltsov, S. V., Goedgebuer, J. P., Larger, L., and Rhodes, W. T. (2001). Communicating with optical hyperchaos: Information encryption and decryption in delayed nonlinear feedback systems. *Phys. Rev. Lett.*, 86(9):1892–1895.

Udaltsov, V. S., Goedgebuer, J.-P., Larger, L., Cuenot, J.-B., Levy, P., and Rhodes, W. T. (2003). Cracking chaos-based encryption systems ruled by nonlinear time delay differential equations. *Physics Letters A*, 308(1):54 – 60.

Udaltsov, V. S., Larger, L., Goedgebuer, J. P., Locquet, A., and Citrin, D. S. (2005). Time delay identification in chaotic cryptosystems ruled by delay-differential equations. *Journal of optical technology*, 72:372–377.

Van Wiggeren, G. D. and Roy, R. (1998). Communication with chaotic lasers. *Science*, 81:1198–1200.

Vicente, R., Dauden, J., Colet, P., and Toral, R. (2005). Analysis and characterization of the hyperchaos generated by a semiconductor laser subject to a delayed feedback loop. *IEEE Journal of Quantum Electronics*, 41(4):541–548.

Volkovskii, A. R. and Rul'kov, N. (1993). Synchronous chaotic response of a nonlinear oscillator system as a principle for the detection of the information component of chaos. *Tech. Phys. Letter*, 19:1197–1204.

Voss, H. and Kurths, J. (1997). Reconstruction of non-linear time delay models from data by the use of optimal transformations. *Physics Letters A*, 234(5):336 – 344.

Voss, H. and Kurths, J. (1999). Reconstruction of nonlinear time-delayed feedback models from optical data. *Chaos, Solitons and Fractals*, 10:805–809.

Voss, H. U. (2000). Anticipating chaotic synchronization. *Phys. Rev. E*, 61(5):5115–5119.

Voss, H. U. (2001a). Dynamic long-term anticipation of chaotic states. *Phys. Rev. Lett.*, 87(1):014102.

Voss, H. U. (2001b). Real-time anticipation of chaotic states of an electronic circuit. *Int. J. of Bifurcation and Chaos*, 12:1619–1625.

Wolf, A., Swift, J. B., Swinney, H. L., and Vastano, J. A. (1985). Determining lyapunov exponents from a time series. *Physica D: Nonlinear Phenomena*, 16(3):285 – 317.

Yang, T., Yang, L.-B., and Yang, C.-M. (1998a). Breaking chaotic secure communication using a spectrogram. *Physics Letters A*, 247(1-2):105 – 111.

Yang, T., Yang, L. B., and Yang, C. M. (1998b). Breaking chaotic switching using generalized synchronization: Examples. *IEEE Trans. on Circuits and Systems-I: Fundamental Theory and Applications*, 45:1062–1067.

Yang, T., Yang, L.-B., and Yang, C.-M. (1998c). Cryptanalyzing chaotic secure communications using return maps. *Physics Letters A*, 245(6):495 – 510.

Zhou, C. and Lai, C. H. (1999). Extracting messages masked by chaotic signals of time-delay systems. *Phys. Rev. E*, 60(1):320–323.